FY21 STATUS REPORT: SNF INTERIM STORAGE CANISTER CORROSION AND SURFACE ENVIRONMENT INVESTIGATIONS

Spent Fuel and Waste Disposition

Prepared for
US Department of Energy
Spent Fuel and Waste Science and Technology

Charles Bryan, Andrew Knight, Brendan Nation, Timothy Montoya, Erin Karasz, Ryan Katona, Rebecca Schaller

Sandia National Laboratories

September 24, 2021

M2SF-21SN010207056
SAND21-xxxx

DISCLAIMER

This information was prepared as an account of work sponsored by an agency of the U.S. Government. Neither the U.S. Government nor any agency thereof, nor any of their employees, makes any warranty, expressed or implied, or assumes any legal liability or responsibility for the accuracy, completeness, or usefulness, of any information, apparatus, product, or process disclosed, or represents that its use would not infringe privately owned rights. References herein to any specific commercial product, process, or service by trade name, trade mark, manufacturer, or otherwise, does not necessarily constitute or imply its endorsement, recommendation, or favoring by the U.S. Government or any agency thereof. The views and opinions of authors expressed herein do not necessarily state or reflect those of the U.S. Government or any agency thereof.

Prepared by
Sandia National Laboratories
Albuquerque, New Mexico 87185 and Livermore, California 94550

Sandia National Laboratories is a multimission laboratory managed and operated by National Technology and Engineering Solutions of Sandia, LLC, a wholly owned subsidiary of Honeywell International, Inc., for the U.S. Department of Energy's National Nuclear Security Administration under contract DE-NA0003525.

SUMMARY

This progress report describes work performed during FY21 at Sandia National Laboratories (SNL) to assess the localized corrosion performance of canister materials used in the interim storage of spent nuclear fuel (SNF). Of particular concern is stress corrosion cracking (SCC), by which a through-wall crack could potentially form in a canister outer wall over time intervals that are shorter than possible dry storage times. In FY21, modeling and experimental work was performed that further defined our understanding of the potential chemical and physical environment present on canister surfaces at both marine and inland sites. Research also evaluated the relationship between the environment and the rate, extent, and morphology of corrosion, as well as the corrosion processes that occur. Finally, crack growth rate testing under relevant environmental conditions was initiated.

In FY21, work to define dry storage canister surface environments included several tasks. First, dust specimens were analyzed from the surface of in-service canisters at two inland independent spent fuel storage installation (ISFSI) site locations. These samples represent the first that have been collected from inland sites and provide insights into the chemistry and mineralogy of dust and salts on canisters at those sites. The results showed that nitrates, sulfates, and carbonates dominated the soluble salts, but small amounts of chloride, mostly in the form of halite (NaCl), were present. The probable halite sources are cooling tower emissions (both sites have cooling towers), or road salts used during winter months. Second, SNL continued to evaluate the stability of $MgCl_2$ brines on heated surfaces. $MgCl_2$-rich brines are the first to form when sea-salts deliquesce, and understanding their behavior is critical to the prediction of canister corrosion and the potential occurrence of SCC. Work in FY21 focused on development of a consistent thermodynamic model for magnesium hydroxides, chlorides, and hydroxychlorides. This model is necessary for understanding and predicting when deliquescent $MgCl_2$ brines are stable on canister surfaces, and, also in understanding corrosion processes in those brines. Additional work focused on experimental measurement of the stability of $MgCl_2$ brines as a function of temperature and RH. Finally, several support activities were initiated for the Canister Deposition Field Demonstration (CDFD). These included developing a preliminary plan for sampling canister surface deposits; developing a method for measuring canister surface roughness on the macro-micro scale; evaluating techniques for marking sampling grids onto the canister surfaces; and developing specifications for site monitoring of atmospheric gases and aerosols at the CDFD site.

In FY21, corrosion testing and modeling was performed in more canister-relevant environments. Two large scale pitting exposures; one under cyclic diurnal conditions and a second exploring the influence of inert dust, were initiated. Initial results of these exposures are presented herein and have helped elucidate influences of the canister surface environment on pit growth and extent of damage. These exposures also explore material influences, including the effects of material composition and surface finish on pitting susceptibility. In addition to testing in more relevant scenarios, FY21 continued to expand modeling efforts for the maximum pit size model. Efforts focused on accounting for non-static brine/corrosion conditions, including changes in brine layer composition, thickness, and mineral precipitation, to better predict pitting and SCC initiation. Major observations from FY20 were furthered in FY21 through three studies; 1) brine influence on the controlling cathodic kinetics that lower the predicted maximum pit size, 2) evolution of brine pH due to anode-cathode separation, and the subsequent influence on predicted maximum pit sizes, and 3) the controlling role of brine layer thickness, specifically under natural convection boundary layer conditions, and the implications for atmospheric corrosion. Further developing the roles these phenomena play in the maximum pit size model helps to better predict SCC initiation and enhances our determination of the susceptibility of SNF canisters to SCC. FY21 has also focused on how these factors influence the transition of a pit to a SCC crack. Both experimental and modeling efforts are being developed to capture the influence of canister-relevant brine conditions on pitting, the role these play in pit damage and morphology, and how this in turn effects crack initiation. While FY21 saw major advancements in understanding the relationship between brine properties and corrosion, it is still unknown how cracks, once initiated, will behave in canister-relevant conditions. SNL

has continued its program for crack growth rate measurement through initial crack growth rate tests of stainless steel materials. This supports development of new crack growth rate data in more relevant brine compositions, and eventually, under atmospheric conditions. These data will expand the existing SNL literature database and should reduce the large uncertainties associated with use of the existing data. It will also be compared to the model developed for use in flaw disposition for the American Society of Mechanical Engineers (ASME) code case N-860. Finally, in collaboration with Pacific Northwest National Laboratory (PNNL), SNL has helped to examine the corrosion properties of cold spray as a mitigation and repair strategy for SNF canisters. Initial results in FY21 have focused on accelerated corrosion testing to help optimize the cold spray coatings and determine potential deleterious features. In FY22, SNL will continue this collaboration to evaluate the performance of these coatings under relevant conditions.

To summarize, in FY21, SNL characterized soluble salt chemistries at inland ISFSI sites for the first time; worked to refine our understanding of brine and Mg-hydroxychloride stabilities on heated canister surfaces; and initiated several studies in support of the CDFD project. Experiments and modeling in FY21 helped parameterize the SNL probabilistic SCC model, and elucidated potentially significant influences of $MgCl_2$-dominated brines on corrosion processes and damage morphology; these brines may also govern crack initiation (pit to crack transition) and crack growth rates. Crack growth rate experiments have also been initiated at SNL; these early experiments focus on developing the methods and expertise for reliable and repeatable crack growth rate measurements but will transition into testing in relevant environments in FY22. Finally, corrosion testing of cold spray coatings provided by PNNL has been started and will continue into FY22; these experiments will aid in material/process optimization and will evaluate the potential effectiveness of cold spray as a mitigation and repair tool. The work in FY21 enables better predictions of timing and location of SCC occurrence, to minimize risk of release, to inform canister inspections, and to develop and apply enhanced repair and mitigation strategies. Work in FY22 will continue this effort, expanding upon information gained and skills developed in FY21.

ACKNOWLEDGEMENTS

The authors would like to acknowledge the following people for their contributions to the work documented in this report: Sandians Sara Dickens, Carlos Jove-Colon, Luis Jaregui, Jay Taylor, Greg Koenig, Sam Durbin, Philip Noell, Jake Carpenter, Makeila Maguire, Andres Sanchez, Laura Lemieux, Robert Reese, Nichole Garcia, John Walter; also Alana Parey, Jay Srinivasan, Jenifer Locke, and Eric Schindelholz of the Ohio State University; Rob Kelly of the University of Virginia; John Plumley of the University of New Mexico; Shohel Mohammad of the University of Iowa; Orano staff members Ray Phan, Roger Maggi, Jeffery Gagney, and Jason Billard; Jamie Beard of Robotic Technologies of Tennessee; Ramgopal Thodla of DNV-GL; and Ned Larson of DOE:NE.

This page is intentionally left blank.

CONTENTS

This page is intentionally left blank.

LIST OF FIGURES

LIST OF TABLES

ACRONYMS

AED	aerodynamic equivalent diameter
AHSM	advanced horizontal storage module
ASME	American Society of Mechanical Engineers
ASTM	American Society of Testing and Materials
BLM	Bureau of Land Management
CASTNET	Clean Air Status and Trends Network
CDFD	Canister Deposition Field Demonstration
CGR	crack growth rate
CISCC	chloride-induced stress corrosion cracking
CS	cold spray
CT	compact tension
DCPD	direct current potential drop
DI	deionized [water]
DIC	dissolved inorganic carbon
DIC	digital image correlation
DNV-GL	Det Norske Veritas Group
DOE	US Department of Energy
DPC	dual-purpose canister
DRH	deliquescence relative humidity
EBSD	electron backscatter diffraction
EDM	electrical discharge machining
EDS	energy-dispersive [X-ray] spectroscopy
EPA	Environmental Protection Agency
FEM	finite element modeling
FTIR	Fourier transform infrared spectroscopy
FY	fiscal year
GTAW	gas tungsten arc welding
HAZ	heat affected zone
HE	hydrogen embrittlement
HEAC	hydrogen environment assisted cracking
HER	hydrogen evolution reaction
HLW	high-level radioactive waste
IC	ion chromatography

ISFSI	independent spent fuel storage installation
LAP	laser aerosol particle [spectrometer]
LD	loading density
LLW	low-level radioactive waste
LT	longitudinal transverse
MW	molecular weight
NDE	non-destructive evaluation
NEUP	Nuclear Energy University Program
NPS	National Park Service
NRC	Nuclear Regulatory Commission
ORR	oxygen reduction reaction
OSU	Ohio State University
PM_{10}	particulate matter, ≤10 μm
PNNL	Pacific Northwest National Laboratories
PP	potentiodynamic polarization
RD	rolling direction
RH	relative humidity
SCC	stress corrosion cracking
SEM	scanning electron microscope
SENT	single edge notched tension specimen
SFWST	Spent Fuel and Waste Science and Technology
SNF	spent nuclear fuel
SNL	Sandia National Laboratory
SRNL	Savannah River National Laboratory
SS	stainless steel
ST	short transverse
ToF-SIMS	time-of-flight secondary ion mass spectrometry
TSP	total suspended particulate
UT	ultrasonic phase array
UTS	ultimate tensile strength
UNM	University of New Mexico
UVA	University of Virginia
VCC	vertical concrete canister
WL	water layer
XCT	X-ray computed tomography

XRD	X-ray diffraction
YS	yield strength

This page is intentionally left blank.

SPENT FUEL AND WASTE SCIENCE AND TECHNOLOGY

FY21 STATUS REPORT: SNF INTERIM STORAGE CANISTER CORROSION AND SURFACE ENVIRONMENT INVESTIGATIONS

1. INTRODUCTION

In dry storage, spent nuclear fuel (SNF) is commonly stored in welded stainless steel (SS) canisters enclosed in passively ventilated overpacks. Over time, dust accumulates on the canister surfaces, and as the SNF cools, salts within that dust will deliquesce to form concentrated brines. If the salts contain aggressive species such as chloride, then the resulting brine can cause localized corrosion, and if sufficient tensile stresses are present in the metal, stress corrosion cracking (SCC) can occur. Over time, SCC cracks could penetrate the canister wall. The risk of corrosion and SCC is greatest in near-marine settings, where chloride-rich sea-salt aerosols are deposited on the canister surface. Developing an improved understanding of the occurrence and risk of SNF storage canister SCC is considered to be critical to demonstrating the safety of long-term dry storage of SNF. For this reason, the Department of Energy (DOE) is funding a large effort to evaluate the occurrence and potential consequences of storage canister SCC as well as to develop prevention, mitigation, and repair technologies for this degradation mechanism, if it should occur.[1] This effort includes work at several different national laboratories and a large DOE-funded effort at universities, as part of the Nuclear Energy University Program (NEUP) (Figure 1).

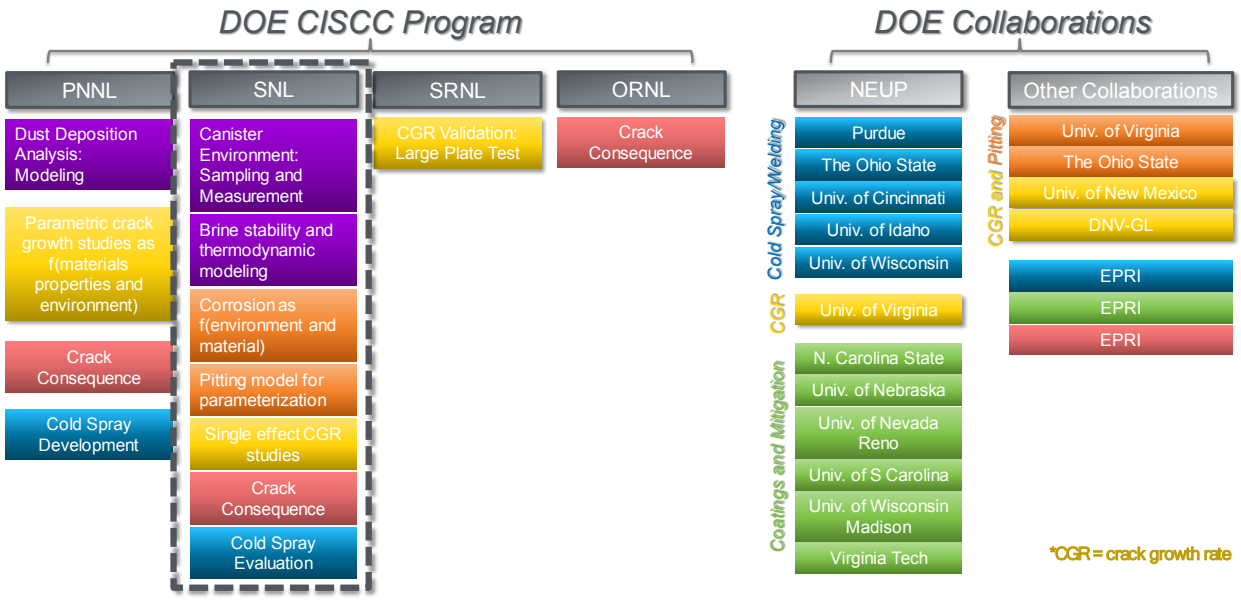

Figure 1. Experimental work on canister SCC currently being carried out by SNL, other national laboratories, and collaborators.

Sandia National Laboratory (SNL) plays a major role in this effort, leading work to develop a scientific basis for understanding canister corrosion and SCC initiation and growth, and work to evaluate the potential consequences of canister SCC. This work also involves development of a probabilistic model for canister stress corrosion cracking. Pacific Northwest National Laboratories (PNNL) has a supporting role in many of these activities. In turn, SNL is performing corrosion experiments to support work to develop cold spray repair technologies at PNNL. Finally, SNL is evaluating potential coatings for prevention and mitigation of canister corrosion and SCC. It should be noted that the DOE has large NEUP efforts in both SCC mitigation and repair and corrosion coating development.

This report documents work done by SNL to develop a scientific basis for canister SCC—to define the canister surface environment and corrosion phenomena, including the occurrence and growth of canister pitting and SCC. Work by other national laboratories and by other parts of the SNL program, shown in Figure 1, are documented in other Spent Fuel and Waste Science and Technology (SFWST) reports.

Over the past few years, SNL has worked to develop a probabilistic model for SCC which utilizes mechanistically-based sub-models to describe individual processes and events that occur during canister aging and that could eventually lead to canister SCC (Figure 2). The current model framework contains numerous assumptions and oversimplifications, many with insufficient scientific basis. Current SCC work at SNL focuses on acquiring data for improved sub-model development, concentrating mostly on determining the underlying mechanisms that govern (1) brine evolution, both before and after initiation of corrosion; (2) the corrosion processes of pitting, SCC crack initiation, and SCC crack growth. This includes developing high-quality data for salt compositions and deposition rates at ISFSI sites and for brine compositions in the evolving canister surface environment, and statistical pitting and SCC initiation and growth data for canister-relevant conditions. By improving sub-model parameterization and validation, this work will reduce uncertainty in our estimates of the timing and occurrence of SCC.

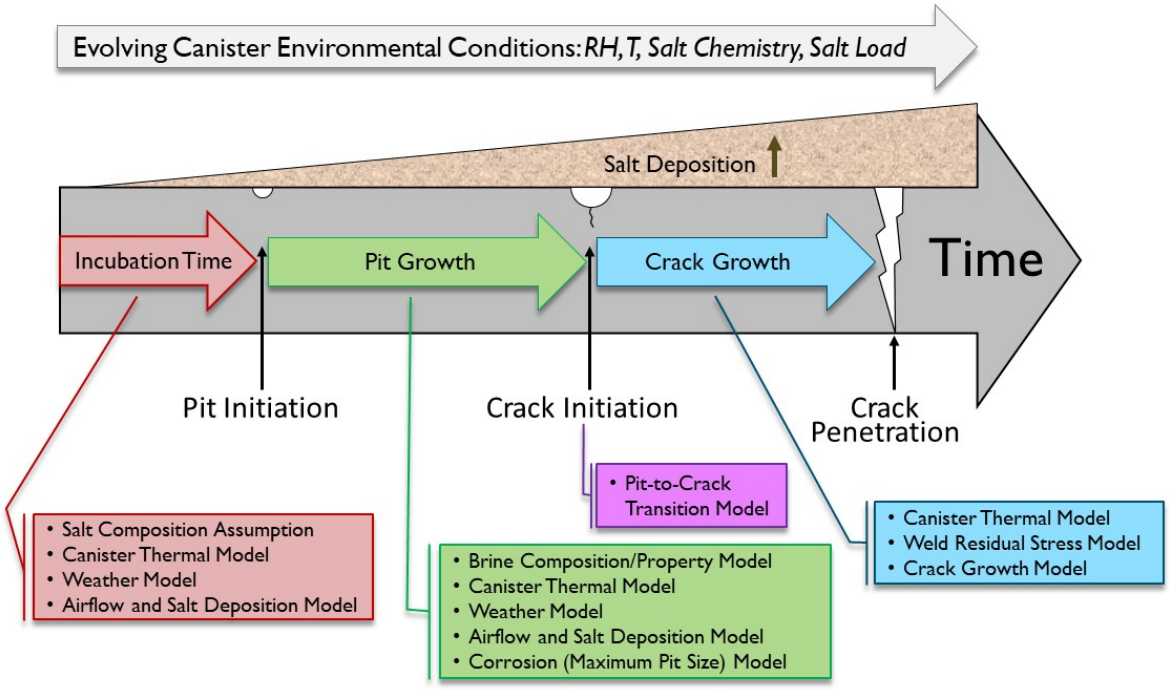

Figure 2. Probabilistic model for SNF dry storage canister SCC.

1.1 Background

A timeline for SCC of SNF dry storage canisters is shown in Figure 2. Several important events and processes occur during the development of through-wall SCC and understanding the timing of event initiation and the rates of these processes is critical to accurate prediction of possible SCC penetration times. These parameters are highly dependent upon the evolving physical and chemical environment on the canister surface and on the canister material properties, including composition, surface finish, and weld-related microstructure and residual stress levels. SNL and collaborators are working to understand these dependencies, and their effect on potential canister penetration rates by SCC.

Once a canister is placed in a ventilated overpack, dust and salt aerosols begin to be deposited on the canister surface. Determining the composition of those salts is critical to understanding the risk of canister corrosion, and SNL has participated in several dust sampling campaigns over the last several years. Section 2.1 presents the results of the dust sampling carried out at two anonymous inland Independent Spent Fuel Storage Installations (ISFSI) sites in Fall of 2020. These two sampling campaigns were carried out by Orano, with SNL performing the dust analyses. They represent the first time that inland ISFSI sites have been sampled and provide insights into canister surface dust and salt aerosol compositions and size distributions at sites far from the ocean. These sampling campaigns show that chloride salts are still present at inland sites, probably derived from road salts and cooling tower emissions. However, chloride is present only in small amounts, soluble salts are dominated by nitrates, sulfates, and carbonates. The inland site dust characterization work performed by SNL is documented in two SAND reports [2], and is summarized here.

Initially, canister surface temperatures may be too high to permit salt deliquescence or even development of adsorbed water layers on salts, and localized corrosion cannot occur. But as the canister cools, surface relative humidity (RH) values increase; eventually, salts will deliquesce and a brine forms on the metal surface, permitting corrosion to occur. Once a brine is present, corrosion may be delayed for a time, but this period is likely to be insignificant relative to storage time intervals. The period following emplacement and prior to corrosion is known as the incubation period and is a function of the physical environment—the temperature, RH, and salt load on the canister surface. One important conclusion in last-year's status report [3] concerns the prediction of the evolution of canister surface RH values as the canister cools over time. The evaluation presented shows that initial sea-salt deliquescence, forming $MgCl_2$-rich brines, may occur relatively soon after canister emplacement, deliquescence of NaCl in the sea salts will not occur for hundreds of years. This means that over time periods relevant to canister corrosion, brines formed by sea-salt deliquescence will be magnesium chloride rich. Because of this, the long-term stability of $MgCl_2$-rich brines on the heated canister surface, and the effect of atmospheric exchange and corrosion reactions is of particular interest. SNL has performed experimental and modeling studies of the stability and properties of $MgCl_2$-rich brines for several years, and an update on the current research into the brines is presented in Section 2.2.

Once deliquescence occurs, if the deliquescent brine is chemically aggressive (e.g., chloride-rich), then pitting corrosion will initiate. One important factor controlling the timing and extent of corrosion, and possibly the initiation of SCC cracks, is the salt and dust load deposited on the canister surface. Salt and dust deposition rates on dry storage canisters are known only from surface sampling. However, only a small number of ISFSI sites have been sampled, the degree of canister surface coverage assessed has been limited, and the range of canister heat loads examined has been relatively narrow. For this reason, the Canister Deposition Field Demonstration (CDFD) is being planned to evaluate salt and dust deposition on heated canister surfaces [4]. In this experiment, three canisters with different heat loads will be placed in overpacks at an ISFSI site, and deposited dusts and salts will be periodically sampled over several years. SNL will perform sampling and analysis of the dusts. In FY21, we have begun CDFD support studies (Section 2.3). These include developing initial plans for CDFD canister and overpack surface sampling; developing methods for measurement of canister surface roughness, which may impact dust deposition or

canister corrosion; and developing equipment and testing procedures for monitoring of ambient weather and aerosol sampling at the test site.

SNL research into corrosion pitting and the phenomenon of pit to crack transition is discussed in Section 3. Pitting initiation, pit growth rates, pit morphology, and possible limitations on pit growth, are strongly controlled by environmental factors such as temperature, RH, brine composition, and salt load, but also by material properties, including metal composition, surface finish, microstructure, and stress level. SNL has several collaborations with university groups evaluating aspects of pitting initiation and growth as a function of environmental conditions and material properties. SNL is collaborating with the University of New Mexico (UNM) to evaluate the effect of stress on pit growth rates. SNL is working with Ohio State University (OSU) to evaluate pit initiation and growth on unstrained samples with different surface finishes and in different brine chemistries (e.g., NaCl-rich and $MgCl_2$-rich). SNL is also evaluating the effect of brine composition on the cathodic current generated in the region surrounding the pit, and the anodic current demand due to dissolution within the pit. This work is being carried out in collaboration with the University of Virginia (UVA), and results to date have been incorporated into the SNL probabilistic SCC model, where they are used to determine the maximum pit size that can occur for a given set of environmental conditions.

In the presence of tensile stresses, the current assumption is that pits that grow sufficiently large will eventually initiate SCC cracks. Existing models relate pit depth to crack initiation through the calculated crack tip stress intensity factor [5, 6]. However, this approach must be implemented stochastically, and makes broad assumptions about the shape of the pit. Experimental work in FY21 has shown that pit morphology, and the development of shallow surface cracks that may develop into SCC cracks, is strongly controlled by brine chemistry. To develop a more realistic relationship between brine composition, pitting, and crack initiation, SNL is working with OSU to experimentally evaluate conditions of pit to crack transition under controlled conditions (Section 3.3).

Once a SCC crack initiates, the rate of crack growth will be controlled by the temperature and chemical environment, as well as, possibly, the salt surface load. The tensile stress profile through the metal is also important, as it is combined with the depth of the crack to determine the crack tip stress intensity factor [7, 8]. SNL is working with colleagues at PNNL and SRNL to measure crack initiation and growth rates as a function of canister surface environment (brine composition and temperature). Prior to FY20, SNL's role was largely to define the appropriate environments for testing, and to help interpret test results. In FY21, SNL installed load frames and began testing. These early experiments focused on developing the methods and expertise for reliable and repeatable crack growth rate measurements and will transition into testing in relevant environments in FY22. Sandia's crack growth rate measurement work is described in Section 4.

Finally, as industry begins to move towards strategies for mitigation and repair of SCC cracks, should they be observed on SNF dry storage canisters, SNL is supporting work to develop repair strategies. SNL is working with PNNL to evaluate cold spray repairs for material compatibility and corrosion resistance (Section 5). This work is presented in detail in a FY21 report from PNNL[9], and is summarized here. Moreover, SNL is also working as a collaborator in a NEUP project led by Purdue University to evaluate the corrosion properties of cold-spray repairs. This funding does not come from the SFWST program, but the collaboration will allow us to leverage our funding for both projects.

2. CANISTER SURFACE ENVIRONMENT

In FY21, several efforts focused on understanding the canister surface environment and how it evolves over time. First, SNL analyzed dust samples collected from SNF dry storage canisters at two inland ISFSIs. These data are the first from inland sites and offer insights into chloride deposition and potential SCC at those sites. Also, experiments and calculations to evaluate $MgCl_2$ stability on heated surfaces were continued. Over the first few hundred years for canister storage, canister surface temperatures are sufficiently high that only $MgCl_2$-rich brines can form by sea-salt deliquescence, so these experiments are critical for determining the risk of canister SCC at near-marine sites. Finally, SNL performed several studies in support of the planned CDFD project. These include developing initial plans for CDFD canister and overpack surface sampling; developing methods for measurement of canister surface roughness, which may impact dust deposition or canister corrosion; and developing equipment and testing procedures for monitoring of ambient weather and aerosol sampling at the test site. Each of these efforts is described in the following sections.

2.1 Analysis of Dust Samples Collected from Canisters at Inland Spent Nuclear Fuel Storage Installations

In FY21, for the first time, dust samples were collected from SNF dry storage canisters at two inland ISFSI sites. Previous sampling episodes had concentrated on near-coastal sites, where the risk of chloride induced SCC (CISCC) is considered greater. However, as NRC-mandated ISFSI canister inspections after twenty years of service become increasingly common, opportunities for sampling at inland sites have become available. In the fall of 2020, nuclear services vendor Orano performed inspections at two inland sites, referred to as "Site A" and "Site B" to preserve the anonymity of the sites. As part of that work, Orano collected dust samples from canister surfaces, and the samples were provided to SNF for analysis. The results of those analyses are documented in two SNL reports *Analysis of Dust Samples Collected from an Inland ISFSI Site ("Site A")* [2], and *Analysis of Dust Samples Collected from an Inland ISFSI Site ("Site B")* [2]. Those results are summarized here; for more detail, the reader is referred to the two parent reports. Comparing these two data sets offers insights into the potential range of variability of dust and salt compositions at inland sites as the settings varied (one was more industrial, and the other, somewhat more rural); the local bedrock also varied, as was evident from the mineralogy of the detrital mineral grains in the dust. As discussed below, the soluble salt load and composition also varied from site to site.

2.1.1 Sample Descriptions

Horizontal storage systems are in use at both sites, and the same strategy was used to collect the samples. A remote crawler (Figure 3) was placed on the canisters within their overpacks, and moved over the surface on rubber treads, using a blower to create a Bernoulli effect to keep the robot on the canister surface. Samples were collected with a sampler on the underside of the crawler (Figure 4). The sampler held a rotatable sampling block with two samples, located 180° from each other. Each sample consisted of a glass fiber filter sandwiched between two Scotch-brite® pads, through which a vacuum was drawn. To collect a sample, the sampler would rotate the sampling block until one of the sampling pads was facing downwards and in contact with the canister surface. Then, the robot would move a specified distance in order to sample a known area. Each sample pad was ½″ (1.27 cm) wide, and the robot was moved 6″ (15.2 cm), collecting a sample from 3 square inches (19.35 cm^2). When not actively collecting the sample, the sample block was rotated such that the sample pads were protected from contamination while the robot moved. Each sampling block could collect two samples, minimizing trips into and out of the canister overpack. Samples were collected at several circumferential locations, from the top centerline of the canister down the sides to locations just above the support rails.

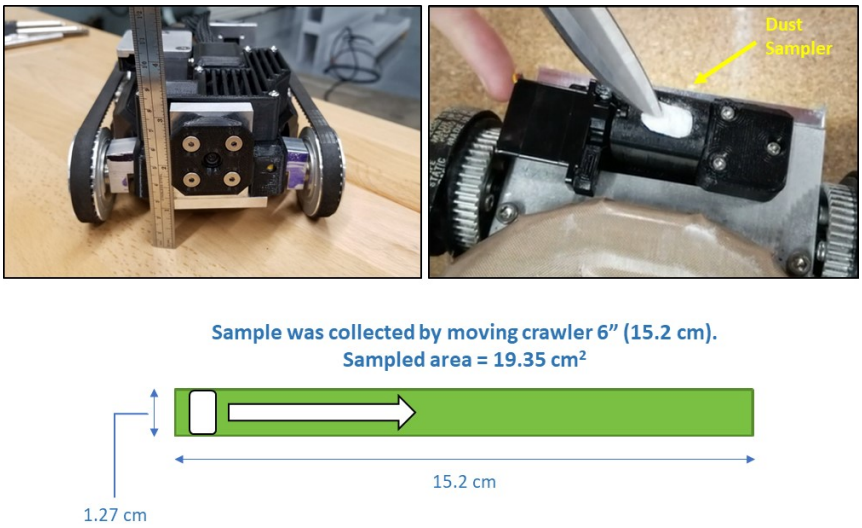

Figure 3. Remote crawler with mounted sampling block. Samples were collected by translating the crawler 6 inches across the canister surface.

Once collected, the samples were shipped to SNL, where they were analyzed by gamma spectroscopy to ensure they weren't radioactive and then disassembled for analysis. Each sample consisted of the Scotch-brite® pads and the glass fiber filter that was sandwiched between them (Figure 4). Upon receipt, each of the sample heads were photographed to document the visible dust load, and then the upper Scotch-brite® pad was removed, and the exposed filter was photographed. Typical examples are shown in Figure 5. Visible dust levels varied, with heavier dust corresponding to samples higher on the surface of the canister.

For Site A samples, loose-fitting pads and filters were used; there was evidence of dust and air travelling around the filter. It is possible that dust collection efficiency may have been inefficient at this site. The equipment was modified for sampling at Site B, with tighter-fitting pads and filters. Collected dust loads were much higher at Site B, but it is not clear how much sampling inefficiencies at Site A may have contributed to this.

After photographing, each sample (consisting of the two Scotch-brite® pads and the filter) was removed from the sample block and retained for leaching to determine soluble salts. A dry dust sample was collected from the outer surface of each sample block for scanning electron microscope/energy dispersive X-ray spectroscopy (SEM/EDS) analysis. Then, each sample, and each of the sample blocks, was leached with deionized water and the leachate analyzed to determine soluble salts. The pad/filter samples provide quantitative information on salt loads per unit area on the canister surface; the block samples cannot be related to any given sampled area but do provide additional information on the soluble salt chemistry in the dust. In addition to the samples, glass fiber filter and Scotch-brite® blanks were analyzed.

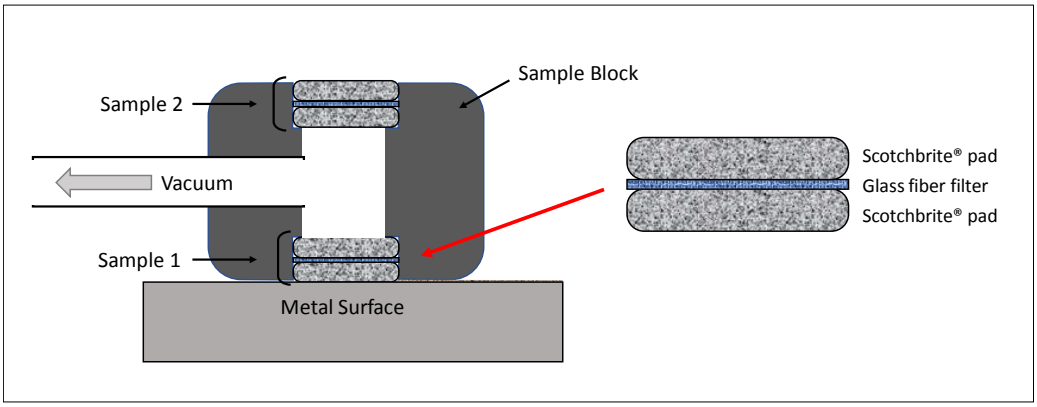

Figure 4. Schematic of a sampling block with two samples, each consisting of a glass fiber filter sandwiched between two porous Scotch-brite® abrasive pads. After using one sample pad, the block would be rotated, and the second pad would be used.

Figure 5. Photographs of Sample F-1, Site B, within the polymer sample head, before (left) and after (right) removal of the upper Scotch-brite® pad.

2.1.2 Methods

Once the samples were extracted from the sample blocks, dust samples were taken from the blocks for characterization by SEM/EDS analysis. Then, the pad/filter samples and the sample blocks were leached to extract the soluble salts for analysis. The following analytical methods were used:

Chemical analysis of soluble salts by ion chromatography (IC). The soluble salts were leached from the Scotch-brite® pads and glass fiber filters with deionized (DI) water. Analysis of the leachate provides soluble salt compositions and concentrations in the samples. The samples were analyzed for major cations and anions by IC. An Apollo Scitech® total dissolved inorganic carbon (DIC) analyzer was used for analysis of inorganic carbon (carbonate/bicarbonate/dissolved CO_2).

SEM imaging and EDS element mapping. SEM/EDS analysis of the dry dust samples provides textural and mineralogical information of dust and soluble salt species and allows visual identification of organic matter (floral/faunal fragments). For this work, two different SEMs were used, a Tescan Vega III Scanning Electron Microscope, and a Zeiss GeminiSEM 500 Variable Pressure Field Emission Scanning Electron Microscope equipped with a Bruker XFlash 6|60 SDD Energy Dispersive Spectrometer.

For a detailed description of the equipment and the analytical procedures used, see Bryan and Knight (2020) [2], and Knight and Bryan (2020) [2].

2.1.3 Results and Discussion

2.1.3.1 Leaching and Chemical Analysis

Analysis procedures for Sites A and B were identical, and both the actual samples and leachate from the sample blocks were analyzed. The sampling material used (the glass fiber filters and the Scotch-brite®) at each site were the same. Testing showed that the glass fiber filters were inert; contributing no appreciable soluble salts to the leachate for each sample. The Scotch-brite® pads, however, leached small amounts of salts, and also, relatively high levels of Li^+. As Li^+ is not a contaminant that is likely to occur naturally in any significant concentration, and is not a contaminant of interest, this had no effect on the analytical results.

These two sets of analyses also provided, for the first time, direct analysis of carbonate, resulting in considerably better cation/anion charge balances than were seen in previous sampling episodes where carbonate was not analyzed. This confirms that the poor charge balances previously observed were due to lack of carbonate data.

The results of the leachate chemical analyses for samples and sample blocks from Site A are shown graphically in Figure 6 and the results for Site B are given in Figure 7. The sample data are reported in units of mg/m^2 because the area sampled is known; however, the sample block data cannot be associated to a known surface area, so are reported in terms of µg extracted. In samples from Site A, cations are dominantly Ca^{2+} and Na^+, with much lower amounts of K^+, NH_4^+ and Mg^{2+}; these same trends hold for the sample block data. As discussed previously, measured Li^+ values represent leachate from the Scotch-brite® pads; that is why Li^+ only appears in the samples, and not in the leachate from the sample blocks. Anions are dominantly SO_4^{2-} and HCO_3^-, with lesser NO_3^-, and only trace Cl^-. Soluble cations at site B are also dominated Ca^{2+} and Na^+, with much lower amounts of K^+, NH_4^+ and Mg^{2+}. However, in contrast to Site A, the anions are dominated by SO_4^{2-} and NO_3^-, with only minor amounts of HCO_3^- — frequently less carbonate than Cl^-, which was also present in only minor amounts. As discussed in the Section 2.1.3.2, detrital mineral grains at Site A were dominated by minerals (calcite and dolomite), while detrital mineral grains at Site B were dominated by silicates, although calcite was also present. It is possible that the elevated carbonate in the "soluble salt" fraction from Site A represents, in part, dissolution of very fine-grained detrital carbonate grains.

At both sites, charge balance errors were ~+15% for most samples, indicating a deficiency of anionic species. These errors are much smaller than those measured in previous sampling episodes, because for the first time, the leachate samples were analyzed for total inorganic carbon (e.g. bicarbonate), which is commonly a large component of the anion load. Peaks corresponding to organic acid ligands (acetate, formate, and oxalate) were observed in the anion chromatography spectra, suggesting that these species accounted for the missing anionic charge. These species have not been observed in previous sampling of near-marine canister dust samples, suggesting that organic acid ligands are characteristic of inland sites.

Total soluble salt loads as a function of location on the canister surface are shown for both Site A and Site B in Figure 8. In both cases, salt loads were highest on the top of the canister and decreased going down the sides. In the case of Site A, the salt loads were symmetric, but on the Site B canister, one side was significantly more heavily loaded than the other. This may be due to an overpack vent orientation with respect to dominant wind direction. Soluble salt loads were much heavier at Site B than at Site A. However, it is not clear if this reflects the canister surface conditions or if it is due to inefficient sampling of the canister surface deposits at Site A, as discussed in Section 2.1.1.

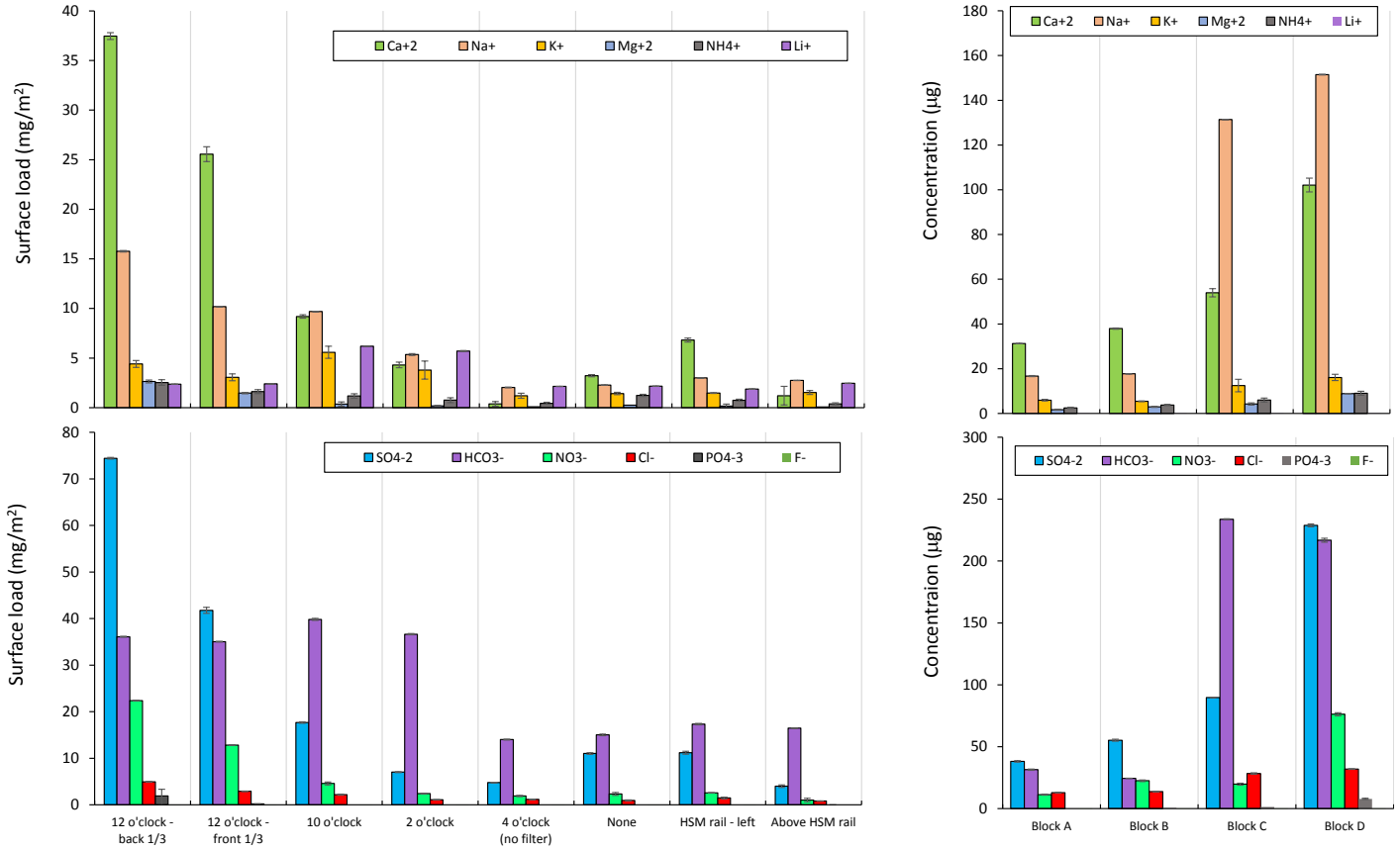

Figure 6. Soluble salt anion and cation concentrations in dust samples collected from spent nuclear fuel dry storage canisters at Site A. Samples (left) and sample blocks (right).

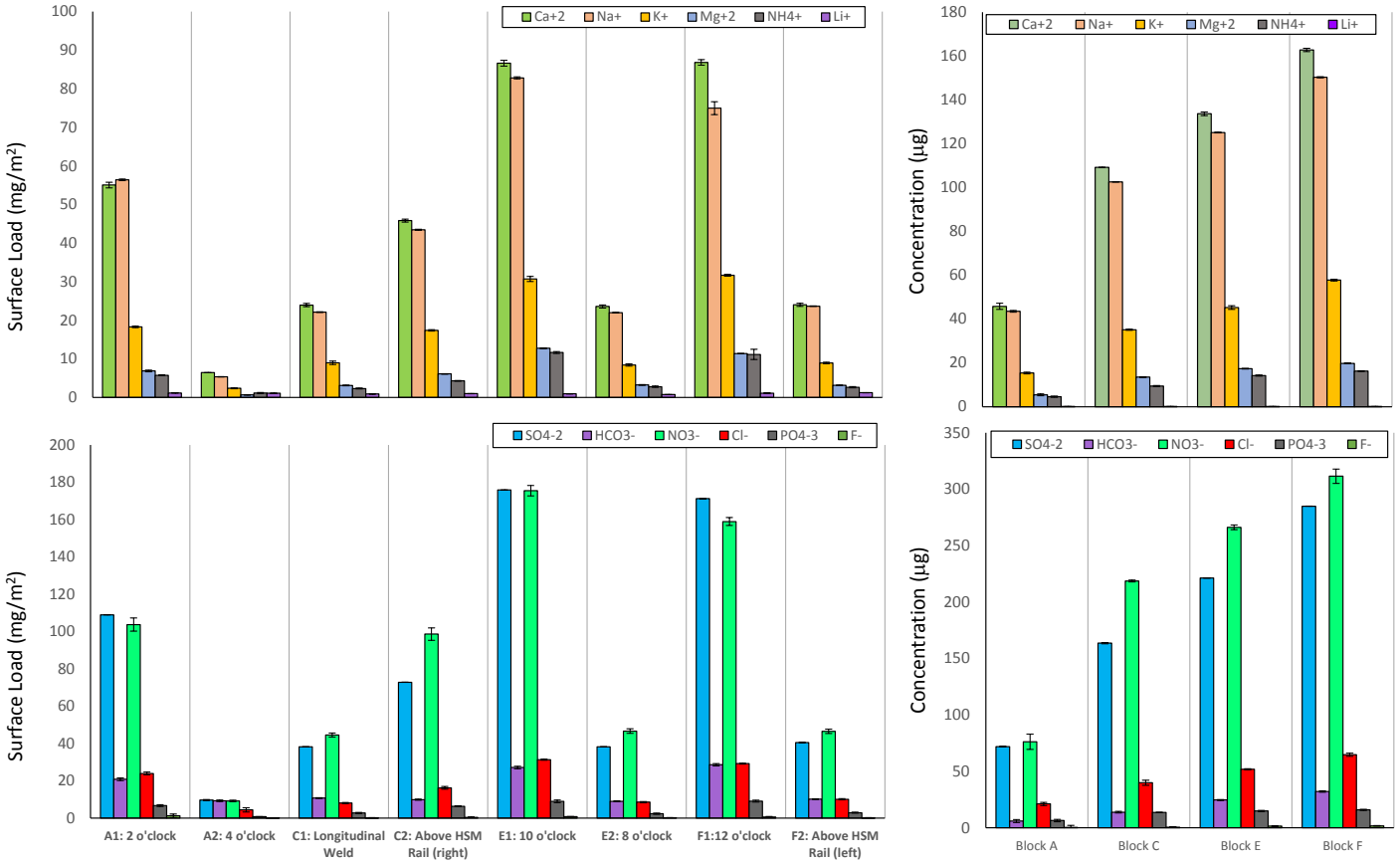

Figure 7. Soluble salt anion and cation concentrations in dust collected from the sample blocks at Site B. Samples (left) and sample blocks (right).

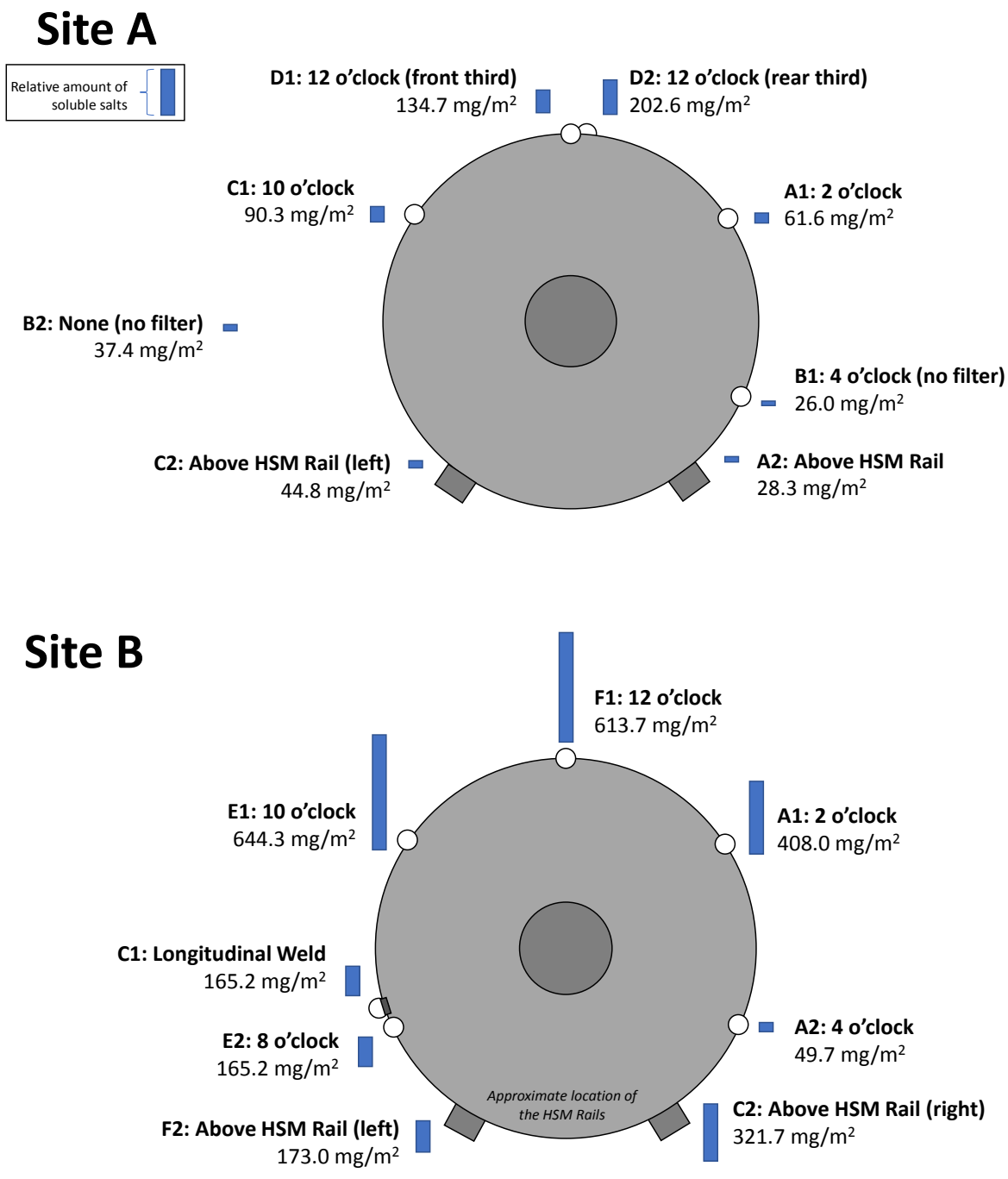

Figure 8. Soluble salt load as a function of sampling location on the canister surfaces, at Site A (upper) and Site B (lower). Soluble salt loads are highest on the top of the canister, and at any given canister location, are higher at Site B than at Site A.

2.1.3.2 SEM/EDS analysis

SEM imaging and EDS analyses were performed to determine the composition and morphology of the insoluble phases and soluble salts in the dust from Site A, and also to determine particle size distributions at each site. At both sites, detrital mineral phases comprised the majority of the dust, and identifiable salt phases were dominantly sulfates.

Site A

At Site A, the dust was dominantly quartz (SiO_2), and dolomite ($CaMg(CO_3)_2$), but potassium feldspar ($KAlSi_3O_8$), calcite ($CaCO_3$), and calcium sulfate (gypsum ($CaSO_4$:$2H_2O$) or anhydrite ($CaSO_4$)), and iron oxides were also common. Other silicates and sulfates were present in minor or trace amounts. Salt aerosols at Site A are mostly finely particulate calcium sulfate, but trace amounts of Na-sulfate as very fine particles were also present. these probably formed by reaction of NaCl or $NaCO_3$ with atmospheric sulfuric acid (or SO_2, which reacts with water form sulfuric acid) via a reaction such as:

$$2NaCl(s) + H_2SO_4(g) \rightarrow Na_2SO_4(s) + 2HCl(g)$$

In addition to sulfates and carbonates, other soluble salt phases were observed in small amounts. Chloride was sparse, but when identified, was halite. In a few cases, it was spatially associated with Mg and K, but due to the prevalence of Mg- and K-rich minerals, definitive identification of chloride phases other than NaCl was not possible. In one case, a NaCl grain was found with a thick $NaNO_3$ rim. This may have formed by the common atmospheric particle-to-gas conversion reaction of NaCl with nitric acid, which forms by reaction of atmospheric NO_x species with water. This reaction, which is similar to the reaction with sulfuric acid described previously, can be written as:

$$NaCl(s) + HNO_3(g) \rightarrow NaNO_3(s) + HCl(g)$$

Nitrogen may also have been present as ammonium but could not be distinguished as such on the plastic Biotape® slide.

SEM images of dust from Site A, with EDS element maps, are shown in Figure 9 and Figure 10. These images were selected to show chloride salts but capture the characteristics (composition/particle sizes) of the dust in general. The figures illustrate the dominance of carbonate and silicate/aluminosilicate detrital grains. In Figure 9, discrete grains of NaCl are visible. The grains are euhedral, suggesting they formed by dryout of NaCl brine aerosols. In contrast, the large NaCl grain in Figure 10 is rimmed with $NaNO_3$, indicating reaction with atmospheric gases, probably prior to deposition on the heated canister surface.

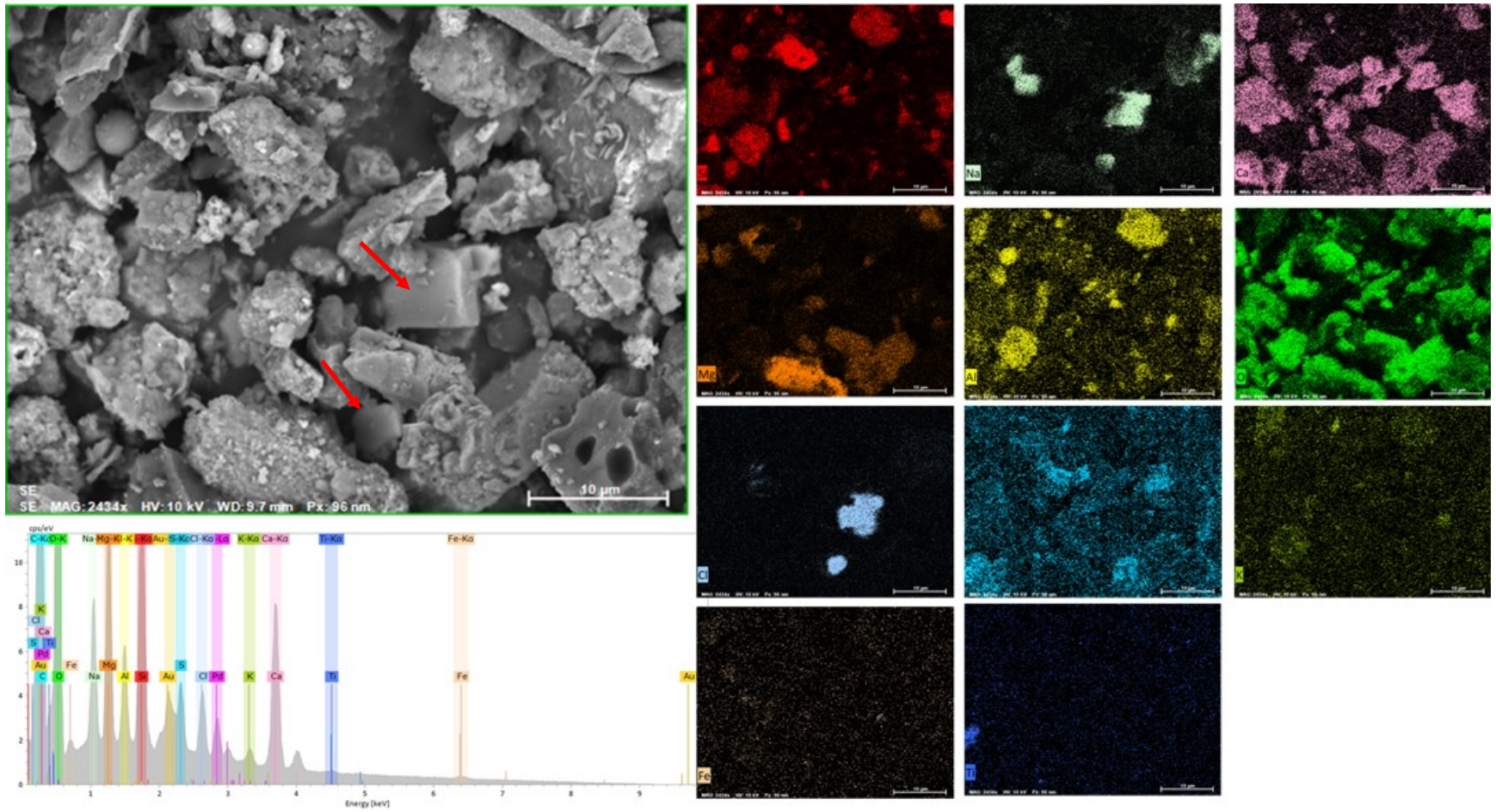

Figure 9. SEM BSE image and EDS element maps of dust from Block D, Site A. Particles are mostly calcite and dolomite, and aluminosilicates. Two well-formed NaCl crystals (arrows) are also present.

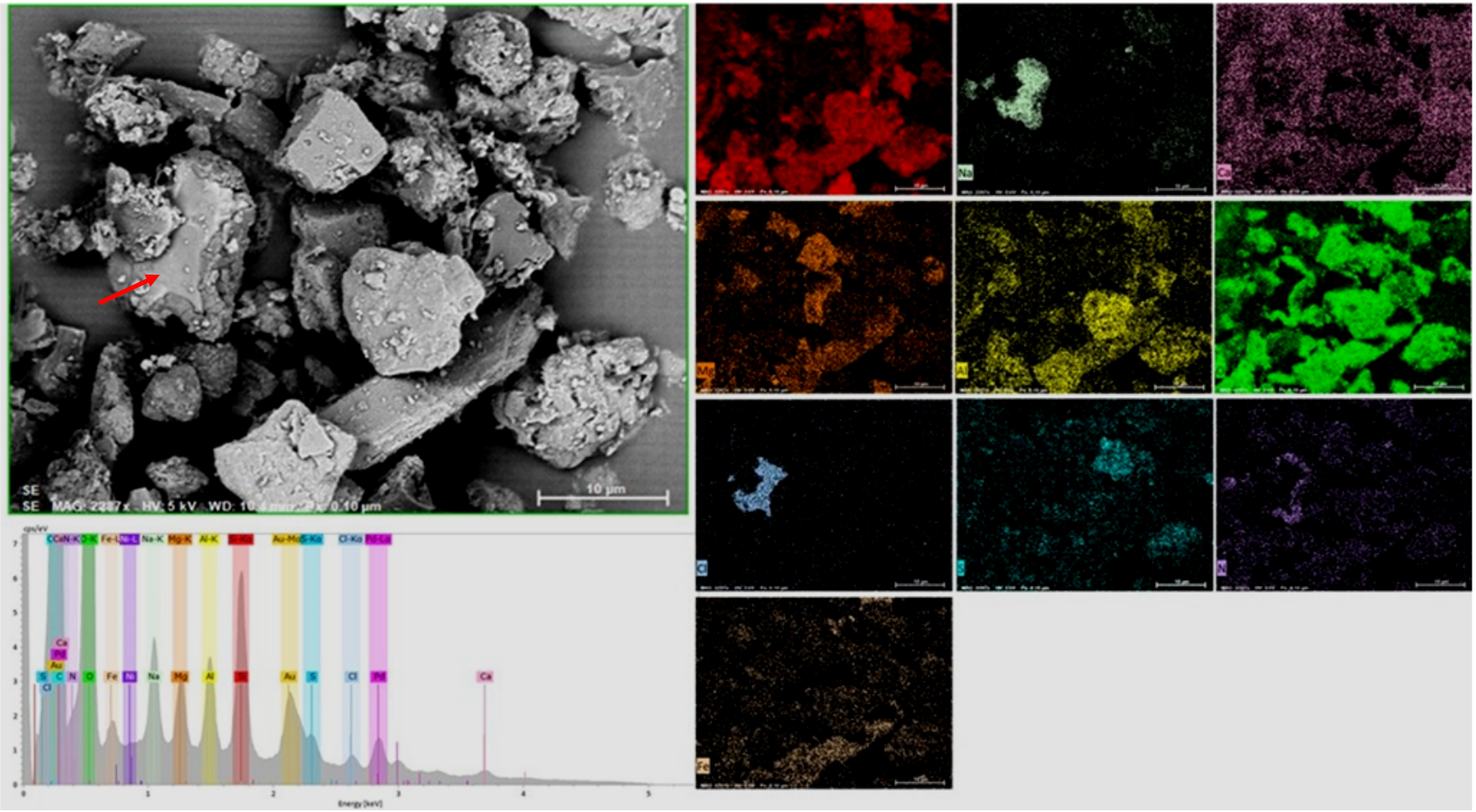

Figure 10. SEM BSE image and EDS element maps of dust from Block D, Site A. Particles are largely carbonates and aluminosilicates. A single large grain of NaCl with a rim of soda niter ($NaNO_3$) is present (arrow).

Site B

At Site B, the dust was dominantly quartz, and aluminosilicates (feldspars and mica). Iron and aluminum oxides/hydroxides were also relatively common. Detrital calcite was common, but dolomite was rare at this site. For soluble salts, sulfate minerals were very common; calcium sulfate was the most abundant, but sulfate was also present as phases that are common components in fertilizers, such as potassium sulfate (potash of sulfur) and an organo-sulfate phase. Sodium sulfate was also observed and may have originated via atmospheric reactions with NaCl as discussed previously. In addition to sulfates and carbonates, other soluble salt phases were observed in small amounts. Chloride was commonly present as halite, but on one occasion, was present as sylvite (KCl), adhering as small crystals to the surface of a large particle of plant matter. Sylvite, also know as muriate of potash, is a common component of fertilizers. $NaNO_3$ was frequently spatially associated with NaCl. In some examples, the NaCl particles appeared to have nitrate-rich rims, indicating partial conversion of the halite to nitrate via particle-to-gas conversion reactions. Pure $NaNO_3$ grains were also observed.

In addition to nitrates, the IC results showed that nitrogen was also present as ammonium species—these cannot readily be identified by SEM/EDS, and no clear examples were observed. Phosphate occurred as discrete detrital mineral grains, commonly associated with Ca^{2+} (as apatite). Phosphate was also present in forms likely associated with fertilizers, such as aggregates containing K and SO_4, possibly as ammonium phosphate or organic phosphate compounds.

The dust also contained a significant amount of organic matter. This material was mostly plant matter such as pollen and stellate trichomes (plant fibers produced by oak trees) and other plant fibers, and possibly insect parts.

SEM images of dust from Site B, with EDS element maps, are shown in Figure 11 and Figure 12. These images were selected to show chloride salts but capture the characteristics (composition/particle sizes) of the dust in general. The figures illustrate the dominance of silicate/aluminosilicate detrital grains in the dust. In Figure 11, discrete grains of NaCl are visible. The grains are euhedral, suggesting they formed by dry-out, of NaCl brine aerosols. They are co-located with concentrations of nitrate and sulfate, possibly indicating the effects of particle-to-gas conversion reactions. The large skeletal NaCl grain in Figure 12 is not directly associated with nitrate or sulfate, but smaller Na-nitrate and Na-sulfate grains are present in the surrounding region.

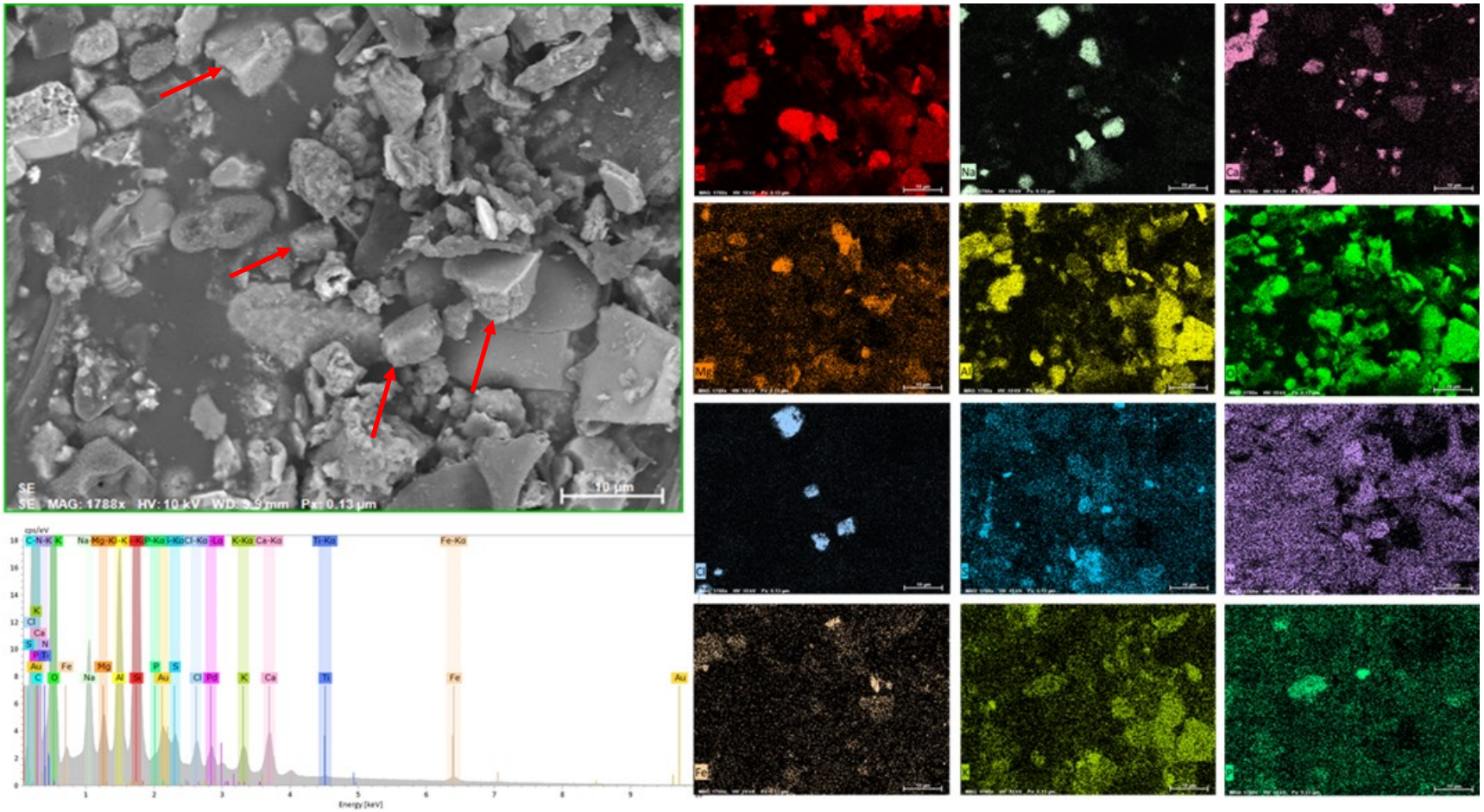

Figure 11. SEM BSE image and EDS element maps of dust from Block A, Site B. The particles are dominantly silicates and aluminosilicates, but pollen is also present. Several halite (NaCl) particles are visible (arrows), occurring as euhedral blocky crystals. The co-location of NaCl particles with S and N, may indicate that atmospheric conversion reactions are converting NaCl to nitrates and sulfates.

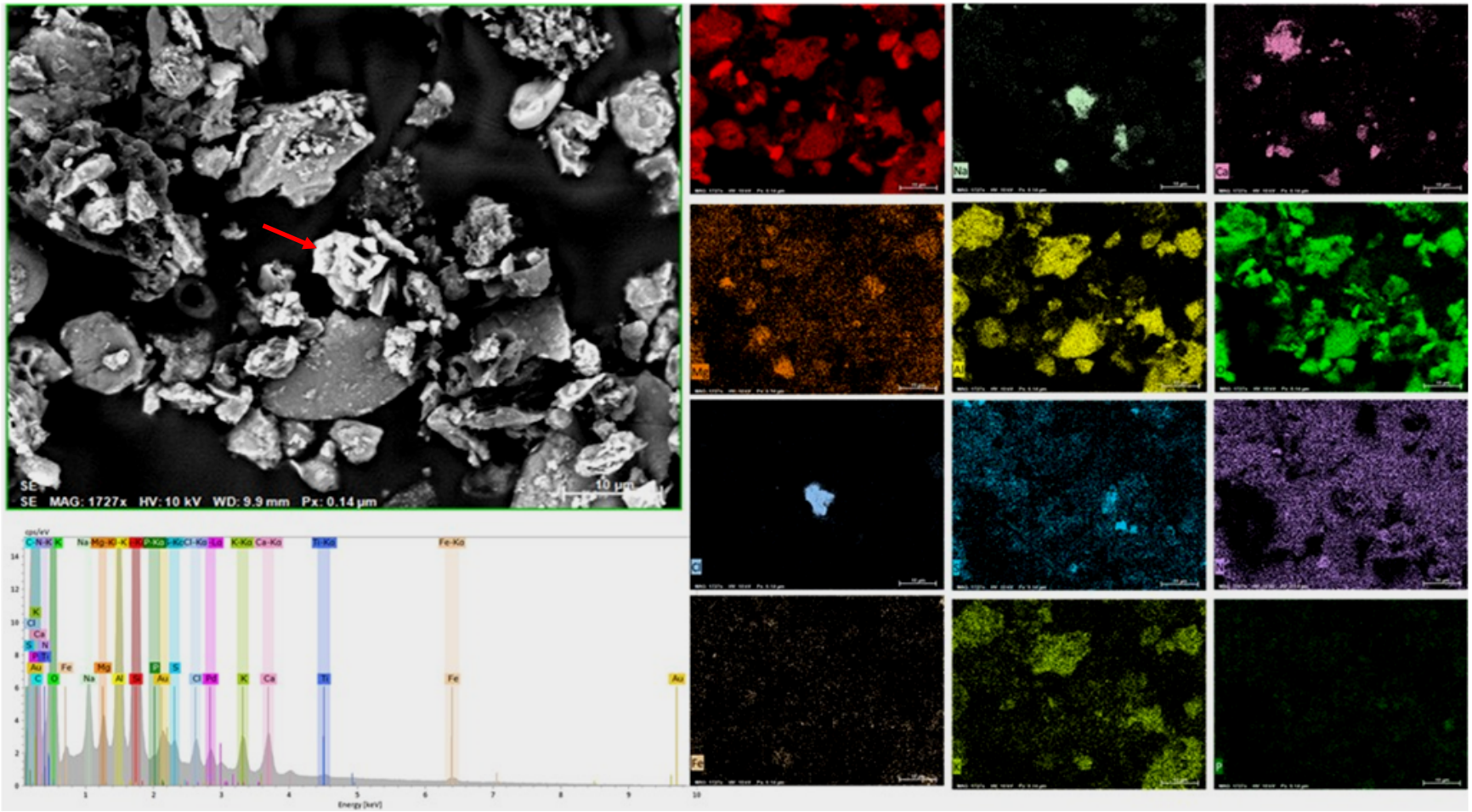

Figure 12. SEM BSE image and EDS element maps of dust from Block C, Site B. Most dust particles are silicates and aluminosilicates. A single large skeletal NaCl grain (arrow) and smaller Na-sulfate and Na-nitrate grains are scattered throughout.

Dust particle sizes

SEM images were also used to evaluate the particle size distribution of the dust deposited on the canister surfaces at Sites A and B. The particle size distributions are provided in Figure 13, and are compared with dust particle sizes at other sites in Figure 14. The peaks of the particle size distributions are slightly higher in the samples from the inland Sites A and B relative to the coastal sites previously sampled, but the maximum particle sizes are consistent over all sites. It should be noted that the sampling methods used at Sites A and B were more effective and less likely to result a sampling bias (undercounting large particles) than the previous sampling methods. Hence, it is not clear that the measured differences between the inland sites and the previously sampled near-marine settings reflect the actual dust.

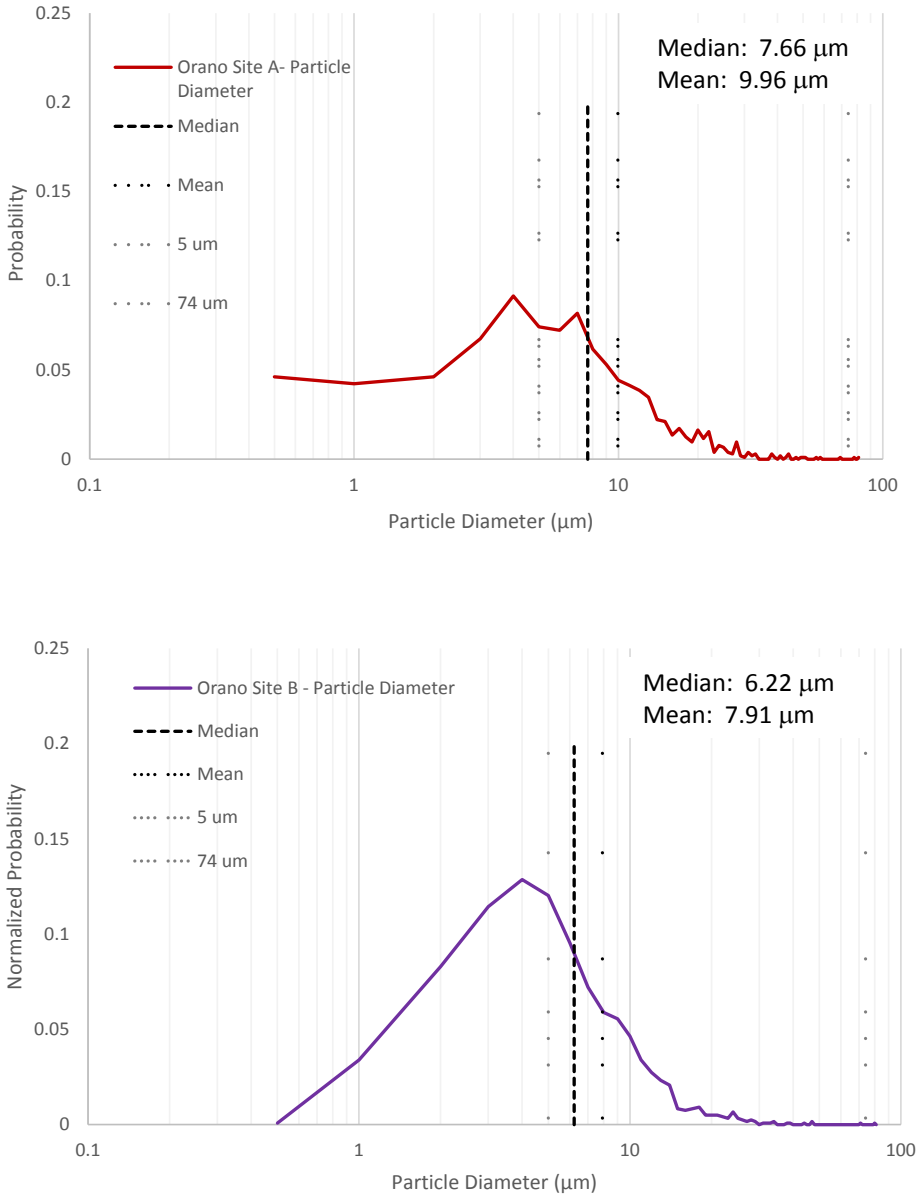

Figure 13. Particle Size distributions for dust from Site A (upper) and Site B (lower). Also shown are the 5 µm and 74 µm lines.

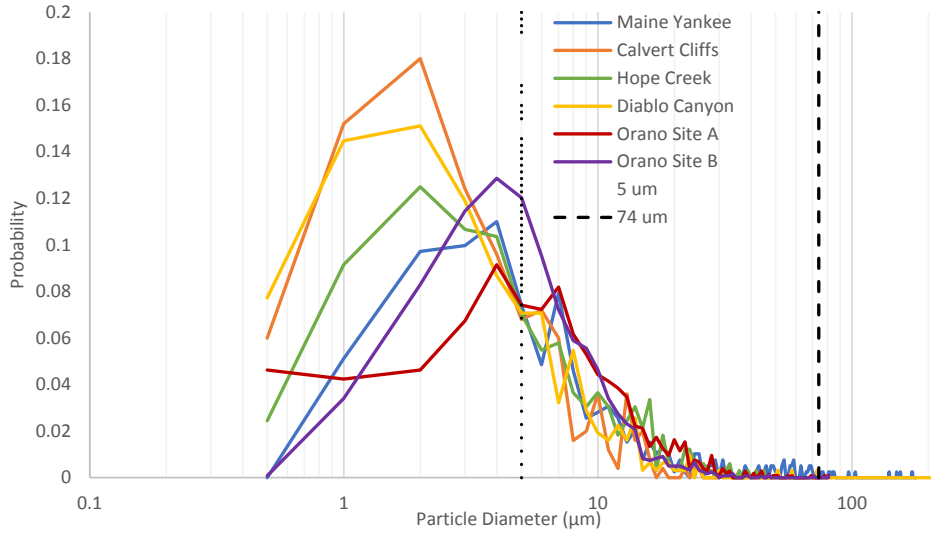

Figure 14. Particle Size distributions for dust from Site A and Site B, compared to particle size distributions from previously sampled near-marine sites.

2.1.4 Summary

The chemical and textural characterization of the dust samples from inland Sites A and B has yielded a great deal of information. The canister surface coverage for these two sites was more extensive that at any other horizontal storage canister site, and for these sites, dust and salt loads were highest on the top of the canister and decreased going down the canister sides. Overall, gravitational settling appeared to be the dominant mode of deposition; the lower the angle of the surface (the closer to horizontal), the greater the deposition. However, even the lower parts of the canister, with overhanging surfaces, had significant dust/salt loads.

SEM analysis indicated that the dust consisted largely of detrital mineral fragments. The local geology had an influence on the composition of the detrital grains; at Site A, quartz, aluminosilicates (feldspars) calcite, and dolomite were abundant, while at Site B, quartz and aluminosilicates were abundant, but detrital carbonates were sparse. Chloride was most commonly present as NaCl, which was frequently associated with nitrates or sulfates. The association of these chemical species suggests that reactions with atmospheric acid gases (SO_2, NO_x) may play a role in converting NaCl to other phases, before, and possibly after, deposition onto the canister surface. In a few rare cases, Cl^- was also present as KCl, or muriate of potash, which is a common component of agricultural fertilizers.

The soluble salts present in the dust from Site A are dominated by Ca^{2+} Na^+, SO_4^{2-}, CO_3^{2-}, and to a lesser extent, NO_3^- species, with minor contributions from K^+, NH_4^+, CO_3^{2-}, and Cl^-. At Site B, the soluble salts are dominated by Ca^{2+} Na^+, SO_4^{2-}, and NO_3^- species, with minor contributions from K^+, NH_4^+, CO_3^{2-}, and Cl^-. Relative to expected continental salt compositions at an inland site, this distribution of ions was not entirely expected. Na^+ is generally only a minor component in inland salts, and ammonium, NH_4^+, is typically the most abundant cation. However, ammonium minerals (NH_4NO_3, NH_4Cl, and possibly $(NH_4)_2SO_4$) have been shown to be unstable at even slightly elevated temperatures [10-12], decomposing to form ammonia (NH_3) and an acid gas (e.g., $HCl_{(g)}$); this may explain the relatively low amounts of ammonium measured in the samples. It is possible that the abundance of Na^+ can be sourced to NaCl from industrial applications (e.g. cooling tower aerosols) or from road salts. NaCl will react with atmospheric acid gases (NO_x or SO_2), produced by industrial and agricultural processes, and will partially or fully convert to nitrates and sulfates.

Chloride is the driving contaminant for CISCC. Major sources of chloride salt aerosols at inland sites are road salts and salts derived from cooling tower emissions. Both Site A and Site B are located in states that make use of road salts during winter months (Site A is in a state that uses exceptional amounts), and both sites have reactor cooling towers. However, in these samples, chloride was only present in trace quantities. At Site A, the maximum surface load of chloride present was about 5 mg/m^2. At Site B, the chloride surface load was >20 mg/m^2 on the upper surfaces of the canister (samples at 10, 12, and 2 o'clock), and achieved a maximum value of about 31 mg/m^2. These chloride concentrations are quite low, suggest that the risk of CISCC is probably low at these two ISFSI sites.

2.2 Magnesium Chloride Brine Stability

$MgCl_2$ brines and their stability play an important role in understanding the risk of CISCC on SNF dry storage canisters for several reasons [3, 13-15]. $MgCl_2$-rich brines are the first to form by deliquescence of sea-salts on the surface of SNF dry storage canisters as the temperature decreases and the RH increases. Moreover, $MgCl_2$ brines have been shown to lead to irregularly-shaped pits on SS, which may promote pit to crack transition by affecting stress distributions around the pit (Section 3.1). Finally, in cathodic regions supporting pit growth, $MgCl_2$ brines suppress oxygen transport to the surface via precipitation of Mg-hydroxides/hydroxychlorides, that suppress the oxygen reduction reaction (ORR) by forming a surface film that blocks oxygen diffusion to the surface. The dominant cathodic reaction becomes the hydrogen reduction reaction (HER), which may promote hydrogen embrittlement (HE) and stress corrosion cracking of the near-surface SS (Section 3.1).

While the presence of $MgCl_2$ brines on the canister surface may be detrimental, these brines have been shown to be unstable at elevated temperatures, readily degassing $HCl_{(g)}$ to convert to Mg-hydroxide or Mg-hydroxychloride phases. The deliquescence RH values of these phases are significantly higher than that of bischofite ($MgCl_2{:}6H_2O$). When these phases form, the brine will dry out, stifling corrosion until the temperature drops and RH rises sufficiently for other phases in the salts (e.g., NaCl) to deliquesce, thus delaying SCC for decades or even hundreds of years. This phenomenon of brine dry-out from conversion of $MgCl_2$ brines to less deliquescent Mg phases has been demonstrated previously by experiments at SNL. $MgCl_2$ brine conversion can occur for two reasons. First, at elevated temperatures, the brine can degas $HCl_{(g)}$, while simultaneously precipitating Mg-hydroxide or hydroxychloride. This has been observed for $MgCl_2$ brine droplets deposited on an inert substrate and heated to 80 ºC at 35% RH [13, 14]. Second, corrosion results in hydroxide production in the cathode region surrounding the corroding area (the anode), resulting in Mg-hydroxide/hydroxychloride precipitation in the cathode area [16]. This has been observed in both driven corrosion tests (Section 3.1.4) and in corrosion testing. For example, on a SS plate from the Sandia canister mockup, coated with $MgCl_2$ and kept under static deliquescent conditions for several months, the brine completely dried out when the 2-1-4 Mg-hydroxychloride phase precipitated around the corroding regions [13]. Understanding the stability of $MgCl_2$ brines as a function of T, RH, and ambient HCl gas concentrations allows prediction of when a corrosive brine can exist on the canister surface, and when initiation and growth of pitting and stress corrosion cracks can occur.

SNL continued to evaluate the stability of $MgCl_2$ brines as a function of environment in FY21 through geochemical modeling and experimental efforts. SNL completed work developing an updated, consistent thermodynamic Pitzer database for modeling the $Mg(OH)_2 – MgCl_2 – H_2O$ ternary system as a function of temperature. This database was updated to include the formation of the Mg-hydroxychloride phases from 25 °C to 200 °C (See Section 2.2.1). Experimental work continued investigations into the stability of $MgCl_2$ droplets on an inert substrate, aged in an environmental chamber with continuous airflow to evaluate the conversion of $MgCl_2$ to Mg-hydroxychloride and Mg-carbonate phases. In FY21, the droplets were deposited using a nebulizer system to generate smaller droplets with higher surface areas,

increasing the rate of reaction and the ease of observing and quantifying reaction products. Sampling has been completed on these experiments, sample analysis is in progress, and will be completed in FY22.

2.2.1 Thermodynamic Modeling

Efforts by SNL to create an internally consistent Pitzer thermodynamic database (built off the Yucca Mountain Project Database *data0.ypf.R2*; [17]) that includes a suite of Mg-hydroxychloride phases were completed in FY21, and the results are being prepared for publication. This work builds upon the previous modeling work performed by SNL in FY19 and FY20 [3, 14]. The resulting thermodynamic database incorporates (1) updates made to the Mg^{++} basis species (referred to here as Mg^{2+}_CODATA) to be consistent with those reported by CODATA and recent publications [18, 19]; (2) updates to brucite ($Mg(OH)_2$), bischofite ($MgCl_2:6H_2O$), $MgCl_2:4H_2O_{(s)}$, 3-1-8 ($Mg_2(OH)_3Cl:4H_2O$), and $MgOH^+_{(aq)}$ to match available solubility data and be consistent with Mg^{2+}_CODATA; and (3) incorporation of additional Mg-hydroxychloride phases, including the 2-1-4 ($Mg_3(OH)_4Cl_2:4H_2O$), 2-1-2 ($Mg_3(OH)_4Cl_2:2H_2O$), and 9-1-4 ($Mg_{10}(OH)_{18}Cl:4H_2O$) phases into the database. These were accomplished by derivation of new thermodynamic data for the phases and adjustment of Pitzer interaction parameters for the $MgOH^+$—Cl^- ion pair, using available experimental data on phase stability and solubility to calculate LogK values as a function of temperature.

The derived thermodynamic data are shown in Table 1; the derived Pitzer interaction parameters for the $MgOH^+$—Cl^- ion pair, in Table 2; and the derived logK/temperature grid, in

Table 3. The derivation of these values is discussed in the rest of this section.

Table 1. Thermodynamic values (ΔG_f^0, ΔH_f^0, and S^0; Top) and C_P with coefficients (*a, b, c, d,* and *e*; bottom) calculated from this study for several magnesium solid species and $MgOH^+_{(aq)}$.

Phase	Short Name	ΔG_f^o (kJ mol^{-1})	ΔH_f^o (kJ mol^{-1})	S^o (J mol^{-1}K^{-1})
$Mg(OH)_{2(s)}$	Brucite	-831.798	-922.826	63.199
$MgCl_2:6H_2O_{(s)}$	Bischofite	-2115.074	-2499.458	366.083
$MgOH^+_{(aq)}$	-	-626.503	-706.391	-67.36
$MgCl_2:4H_2O_{(s)}$	-	-1624.923	-1900.649	263.982
$Mg_2(OH)_3Cl:4H_2O_{(s)}$	3-1-8 Phase	-2554.73	-2942.309	313.700
$2Mg(OH)_2$-$MgCl_2:2H_2O_{(s)}$	2-1-2 Phase	-2815.800	-3158.670	309.170
$2Mg(OH)_2$-$MgCl_2:4H_2O_{(s)}$	2-1-4 Phase	-3306.055	-3762.785	393.890
$9Mg(OH)_2$-$MgCl_2:4H_2O_{(s)}$	9-1-4 Phase	-9136.206	-9602.377	842.430

Table 1, continued.

Phase	Short Name	C_P (J g^{-1} mol^{-1} K^{-1})	*a* (J g^{-1} mol^{-1} K^{-1})	*b* (J mol^{-1} K^{-2})	*c* (*J K* mol^{-1})	*d* (*J K*^{2} mol^{-1})	*e* (*J K*$^{-2}$ mol^{-1})
$Mg(OH)_{2(s)}$	Brucite	74.99	80.764	$1.57x10^{-3}$	$-5.50x10^5$	-	$-5.77x10^{-7}$
$MgCl_2:6H_2O_{(s)}$	Bischofite	389.74	300	$3.87x10^{-1}$	$-5.05x10^5$	-	$-2.24x10^{-4}$
$MgOH^+_{(aq)}$	-	129.1	131.969	1.36e-3	-	-	$-3.33x10^{-5}$
$MgCl_2:4H_2O_{(s)}$	-	255.44	255.44	-	-	-	$-1.04x10^{-10}$
$Mg_2(OH)_3Cl:4H_2O_{(s)}$	3-1-8 Phase	286.07	204.93	$2.86x10^{-1}$	$-2.72x10^5$	-	$-1.22x10^{-5}$
$2Mg(OH)_2$-$MgCl_2:2H_2O_{(s)}$	2-1-2 Phase	293.73	243.72	$2.75x10^{-1}$	$-2.30x10^6$	-	$-6.85x10^{-5}$
$2Mg(OH)_2$-$MgCl_2:4H_2O_{(s)}$	2-1-4 Phase	362.08	336.37	$2.62x10^{-8}$	-	-	$-6.76x10^{-5}$
$9Mg(OH)_2$-$MgCl_2:4H_2O_{(s)}$	9-1-4 Phase	885.06	766.40	$8.34x10^{-1}$	$-1.07x10^7$	-	$-1.08x10^{-4}$

Table 2. Pitzer interaction parameters for the [$MgOH^+$—Cl^-] interaction, including $\beta^{(0)}$, $\beta^{(1)}$, $\beta^{(2)}$, c^{φ}, $\alpha^{(1)}$, and $\alpha^{(2)}$ along with temperature dependent values, c1- c5.

Pitzer Interaction Parameter			c1	c2	c3	c4	c5
$MgOH^+$ — Cl^-	$\beta^{(0)}$	-0.0125	1.644×10^{-6}	22.168033	3.442×10^{-9}	0	0.1343
	$\beta^{(1)}$	-0.3000	8.134×10^{-5}	2783.7256	1.725×10^{-7}	0	16.830
	$\beta^{(2)}$	0	0	0	0	0	0
	c^{φ}	0	0	0	0	0	0
	$\alpha^{(1)}$	2	0	0	0	0	0
	$\alpha^{(2)}$	12	0	0	0	0	0

Table 3. Derived LogK grid [0-25-60-100-150] for the dissociated reaction of various Mg-bearing mineral phases calculated using CHNOSZ and the adjusted values to fit the experimental data. Unless otherwise stated, the uncertainty in the LogK value is ± 0.2%

Reaction	Short Name	0 °C	25 °C	60 °C	100 °C	150 °C	200 °C	Source
$Mg(OH)_{2\,(s)} + 2H^+_{(aq)} \leftrightarrow Mg^{++}_{(aq)} + 2\,H_2O$	Brucite	19.02	17.16	15.04	13.15	11.32	9.89	This study
$MgCl_2{:}6H_2O_{(s)} \leftrightarrow Mg^{++}_{(aq)} + 2Cl^-_{(aq)} + 6\,H_2O$	Bischofite	4.76	4.55	4.17	3.69	3.03	2.26	This study
$MgOH^+_{(aq)} + H^+_{(aq)} \leftrightarrow Mg^{++}_{(aq)} + H_2O$	$MgOH^+$	12.81	11.68	10.33	9.22	8.06	7.14	This study [18, 20]
$Mg_2(OH)_3Cl{:}4H_2O_{(s)} + 3\,H^+_{(aq)} \leftrightarrow 2\,Mg^{++}_{(aq)} + Cl^-_{(aq)} + 7\,H_2O$	3-1-8	28.42	25.86	22.94	20.34 ± 0.17*,[a]	17.83 ± 0.07*,[c]	15.81[d]	This study
$Mg_3(OH)_4Cl_2{:}2H_2O_{(s)} + 4\,H^+_{(aq)} \leftrightarrow 3\,Mg^{++}_{(aq)} + 2\,Cl^-_{(aq)} + 6\,H_2O$	2-1-2	45.97[c]	41.35[c]	35.92[c]	30.88[c]	25.75 ± 0.25*	21.46[d]	This study
$Mg_3(OH)_4Cl_2{:}4H_2O_{(s)} + 4\,H^+_{(aq)} \leftrightarrow 3\,Mg^{++}_{(aq)} + 2\,Cl^-_{(aq)} + 8\,H_2O$	2-1-4	42.70[c]	38.56[c]	33.78 ± 0.22*	29.41	25.07 ± 0.08*	21.51[d]	This study
$Mg_{10}(OH)18Cl_2{:}4H_2O_{(s)} + 18\,H^+_{(aq)} \leftrightarrow 10\,Mg^{++}_{(aq)} + 2\,Cl^-_{(aq)} + 22\,H_2O$	9-1-4	174.39[c]	157.35[c]	137.79[c]	120.08*	102.70	88.78[d]	This study

* LogK used to fit the experimental data was > 0.02% different than the than the LogK calculated using Equation 3.

[a] Phase formed metastably in the experiment at this temperature [21]

[c] Did not form during the experiment at the temperature given [21]

[d] Extrapolated from lower temperatures; no experimental data exist to fit

2.2.1.1 Updates to Mg^{++}, $Mg(OH)_2 + H_2O$, and $MgCl_2 + H_2O$ Systems

Recent studies regarding systems containing Mg^{2+} have shifted toward using a ΔG_f^o for Mg^{2+} of -455.4 ± 1.8 kJ mol^{-1}, which is consistent with the values used for CODATA [18, 19]. This value of ΔG_f^o is ~2 kJ mol^{-1} more negative than the previously value used in SUPCRT92 [22] and in the *data0.ypf.R2* database. To maintain consistency, the changes made to Mg^{2+} were propagated through to all Mg-bearing species (aqueous and mineral species) in this system and then refit with available experimental data.

For brucite, several $LogK_{brucite}$ values exist in the literature ranging from 16.3, consistent with SUPCRT92 [22], to 17.1 [23-25]. When compared to experimental data [25-27], $LogK_{brucite}$ values consistent with SUPCRT92 generally underestimate the experimental solubility data as a function of temperature. Using Mg^{2+}_CODATA and the high enthalpy estimates for brucite derived from Robie and Hemingway (1995) [28] (G_f^o = -831.798 kJ mol^{-1}; H_f^o = -922.826 kJ mol^{-1}; S_o = 63.199 J mol^{-1} K^{-1}) and CP from Helgeson et al. (1978) [29] (C_P =74.99 J g^{-1} mol^{-1} K^{-1}), the resulting $LogK_{brucite}$ as a function of temperature more closely agrees with previously reported $LogK_{brucite}$ values derived from experimental solubility data

(Figure 15a) [23, 25, 26]. For this work, the calculated standard $LogK_{brucite}$ was 17.159 (25 °C, 1 bar), and the temperature grid (

Table 3) was calculated with CHNOSZ.

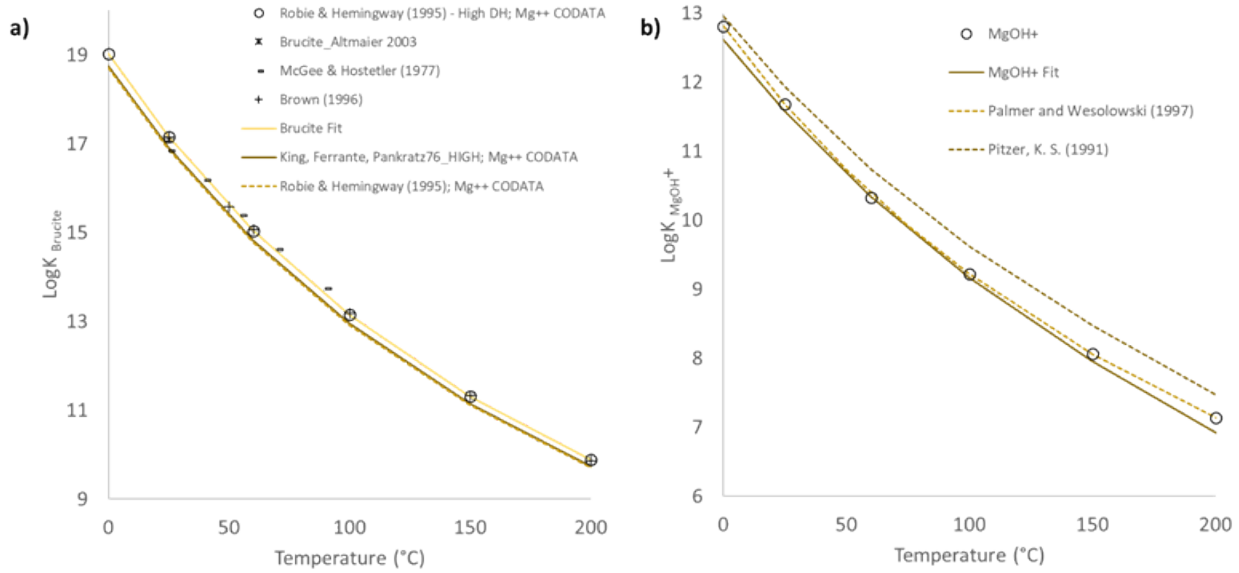

Figure 15. LogK versus temperature plots for a) brucite shown with experimental data and several calculated values. The values selected for this study originated from [28] high enthalpy values and consistent with [18]; b) $MgOH^+_{aq}$ shown with LogK values consistent with [18, 20].

The literature ΔG_f^o, ΔH_f^o, and S^o values for brucite varied; specifically, there are large discrepancies in S^o values from 50.6 J $mol^{-1}K^{-1}$ to 64.4 J $mol^{-1}K^{-1}$. The generally accepted value of S^o= 63.18 J K^{-1} mol^{-1} is derived from experimental heat capacity data [23, 30-32], however some studies have suggested that a lower entropy value, 50.6 J mol^{-1} K^{-1}, is more representative [19, 23]. Here, the accepted value of S^o for brucite was used, along with a high estimation of the ΔH_f^o, as described by Robie and Hemingway (1995) [28] – which was shown to fit the experimental data in Figure 15-a. The resulting thermodynamic values are shown in Table 1 and are calculated using Mg^{2+} CODATA and the high ΔH_f^o value from by Robie and Hemingway (1995) [28]. These values agree with the bulk of the literature values, except for the low value of S^o mentioned previously [23]. The C_p was calculated to be 76.17 J $g^{-1}mol^{-1}K^{-1}$ using the Mostafa method [33] described previously by SNL [3, 14] and was in agreement with the literature reference value of 77.03 J $g^{-1}mol^{-1}K^{-1}$ [34]. These thermodynamic values were used to generate the $LogK_{brucite}$ grid, and were further adjusted to better match experimental data [25, 26]. The resulting standard $LogK_{brucite}$ and $LogK_{MgOH+}$ are shown in Table 1 and Figure 15. Then, C_P was re-calculated to be 74.99 J g^{-1} $mol^{-1}K^{-1}$ by fitting the $LogK_{brucite}$ data with C_P coefficients (*a, b, c, d, e*) from Equation 1.

$$C_p = a + bT + \frac{c}{T^2} + dT^2 \qquad \text{(Eq. 1)}$$

This value is slightly lower than the value derived via the Mostafa method and the literature reference value [34], however deviations were expected since the basis species Mg^{2+} was modified.

The modeled solubility of brucite as a function of temperature using the calculated $LogK_{brucite}$ is compared with the most comprehensive available set of experimental data [27, 35]. Recent modeling efforts suggested that the experimental solubility data at elevated temperatures are inconsistent with the thermodynamic data [36], when compared with the most comprehensive set of experimental data [27, 35]. To accurately model experimental data in the $Mg(OH)_2$-H_2O system, previous work included the

$MgOH^{+}_{(aq)}$, with a pK_d value of 2.19 [25, 37, 38]. Therefore, the SNL model includes the following species: $H_2O_{(l)}$, Mg^{2+} CODATA, $OH^{-}_{(aq)}$, and $MgOH^{+}_{(aq)}$, along with the brucite mineral phase.

The $LogK_{MgOH+}$ values in the Pitzer *data0.ypf.R2* database are from Pitzer (1991) [39], are consistent with the Mg^{2+} data from SUPCRT92 [22], and are based on predictions that utilize correlations between standard state properties of ions and of $MgOH^{+}$ [18, 22]. For the SNL model, the $LogK_{MgOH+}$ values were fitted to available experimental data [20] and consistent with the use of the Mg^{2+}_CODATA (Figure 15b). The thermodynamic parameters were calculated to be ΔG_f^o = -626.503 kJ mol^{-1}; ΔH_f^o = -706.391 kJ mol^{-1}; and S^o = -67.36 J $mol^{-1}K^{-1}$ (Table 1). The resulting $LogK_{MgOH+}$ values as a function of temperature are shown in

Table 3. The $MgCl_2$+H_2O binary system has also been previously studied through modeling and experimental methods evaluating the solubility of bischofite and the high temperature phases ($MgCl_2$:$4H_2O$ and $MgCl_2$:$2H_2O$) [40-43]. The thermodynamic data, LogK values, and solubility of $MgCl_2$:$2H_2O$ were not calculated in this study because this phase only forms under temperature conditions (> ~180 °C) [43]) above the range of interest for this work. The standard state $LogK_{bischofite}$ and $LogK_{MgCl2:4H2O}$ values needed to be updated because of the change of the Mg^{2+} thermodynamic data to match Mg^{2+} CODATA. SNL re-evaluated the thermodynamic data and solubility of these two phases as a function of temperature to maintain consistency with the Mg^{2+}_CODATA data, and to better match the available experimental solubility data. The calculated $LogK_{bischofite}$ and $LogK_{MgCl2:4H2O}$ values are shown in Figure 16 as a function of temperature along with LogK values proposed by others.

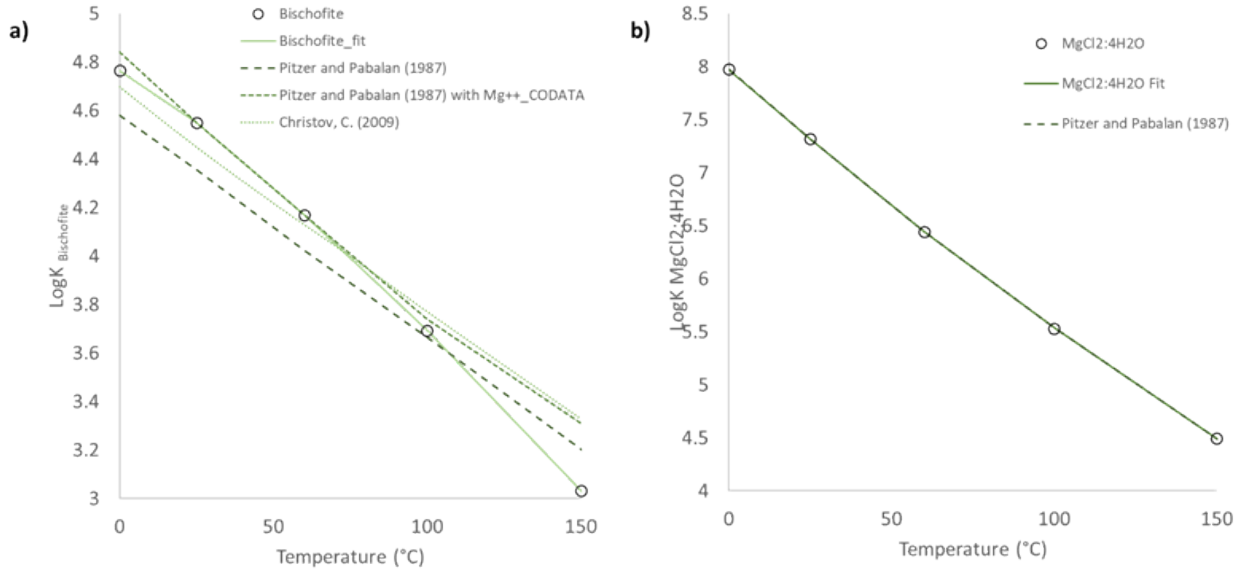

Figure 16. LogK trends versus temperature for a) bischofite, showing LogK trends calculated by SNL along with those of others [41, 43]; and b) $MgCl_2$:$4H_2O$ showing LogK trends consistent with those of [18] and [43].

The literature thermodynamic values for bischofite were relatively consistent, the range of ΔG_f^o was -2115.196 to -2114.64 kJ mol^{-1}; H_f^o from -2499.02 to 2507.43 kJ mol^{-1}; and S^o from 339.73 to 366.1 J $mol^{-1}K^{-1}$. Initial $LogK_{bischofite}$ values as a function of temperature [43] were derived by fitting experimental data [40] from 0 ºC to 200 ºC, which included the formation of $MgCl_2$:$4H_2O$ and $MgCl_2$:$2H_2O$ ($0 < m_{MgCl2} < 14$) [40]. Due to the large fitting window, the bischofite solubility was generally underestimated when 25 ºC < T < 100 ºC and overestimated when T> 100 ºC. For this reason, and to reflect the changes made

to Mg^{2+}, it was necessary to refit bischofite solubility [21, 40, 42-44]. Recent literature updated the $MgCl_2$+H_2O system [41]. While the results did improve the fit to experimental data, SNL did not incorporate these values into the thermodynamic database, because of uncertainties in how changes made to the $A_{\varphi b}$ term and other Pitzer interaction parameters might impact the solubilities of other species in the database. Changes to Pitzer parameters were kept to a minimum, due to concerns that too many changes to Pitzer interaction parameters could have unintended consequences to the predicted solubilities of other species in the database. The SNL refit of the data to improve the agreement between modeling and experiments of the $MgCl_2$-H_2O system was accomplished by changing fewer parameters. The resulting $LogK_{bischofite}$ values are shown in

Table 3 and Figure 16-a. Using the adjusted $LogK_{bischofite}$ values and Mg^{2+}_CODATA, new values of ΔG_f^o, ΔH_f^o, S^o, and C_P were derived (Table 1). The resulting values of ΔG_f^o , ΔH_f^o , and S^o are within the range of literature values [34, 37, 45]. A C_P value of 389.74 J g^{-1} mol^{-1} K^{-1} was derived by fitting $LogK_{biscofhite}$ as a function of temperature with Equation 1. While this value differs significantly from the previously reported value of 315.06 J g^{-1} mol^{-1} K^{-1} [34] and from the value calculated using the Mostafa method, 289.43 J g^{-1} mol^{-1} K^{-1} [33], this lack of consistency in the calculation of the C_P is likely driven by the large deviation in the $LogK_{bischfite}$ at elevated temperatures (Figure 16-a), which may be a result of the limited amount of data that exists at higher temperatures, and of uncertainty in the location of the phase boundary between bischofite and $MgCl_2$:$4H_2O$ (Figure 17).

The $LogK_{MgCl2:4H2O}$ values remained unchanged due to lack of experimental data to confidently fit; however, ΔG_f^o, ΔH_f^o, S^o, and C_P were updated to reflect changes to Mg^{2+} in the thermodynamic database (Table 1), therefore ΔG_f^o and ΔH_f^o shifted ~4 kJmol^{-1}. The $MgCl_2$:$4H_2O$ phase does not precipitate in the calculated results shown in Figure 17-b, it requires higher temperatures and concentrations of $MgCl_2$ to precipitate.

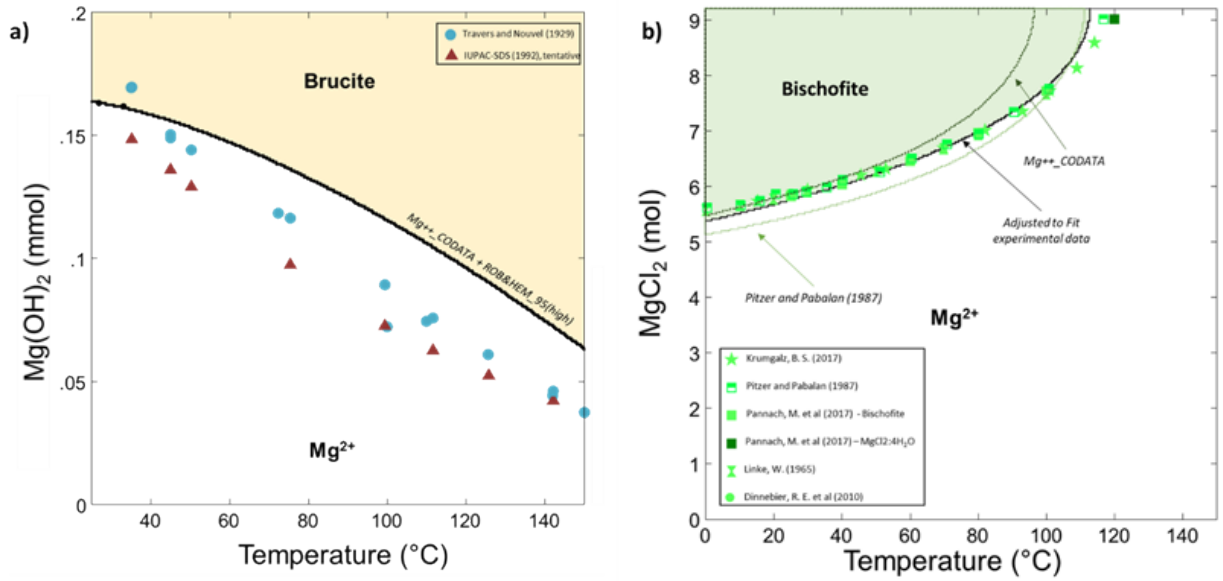

Figure 17. a) Plot of experimental and predicted brucite solubilities versus temperature. Experimental data [27, 35, 36]; modeled data, using thermodynamic values that are consistent with [18, 28]. b) plot of bischofite solubility versus temperature comparing SNL values to literature models [18, 43] and experimental data [21, 40, 42-44].

2.2.1.2 Updates to Mg-hydroxychloride Phases

Updated LogK values for the phases in the binary $Mg(OH)_2$+H_2O and $MgCl_2$+H_2O systems, consistent with Mg^{2+}_CODATA, were used to constrain the number of variables required to fit the experimental data in the ternary $Mg(OH)_2$-$MgCl_2$-H_2O system. When fitting the experimentally measured phase boundaries, only the LogK values for the Mg-hydroxychloride phases were adjusted. While there have been several recent publications describing the solubilities of the phases in the $Mg(OH)_2$-$MgCl_2$-H_2O system, the bulk of this work was collected or calculated for this system at room temperature [23, 24, 37, 46, 47] and therefore most of the data is limited to phase equilibria of room temperature phases—brucite, 3-1-8, 5-1-8 (metastable), and bischofite. Moreover, other than a few studies describing the existence of high temperature phases, such as the 2-1-4 and 2-1-2 phases [48], and the 9-1-8 phase [44], only three studies referenced describe the phase stabilities and measured solubilities extending to elevated temperatures [21, 49, 50]; these references were prioritized in fitting the data.

The initial estimated values of ΔG_f^o , ΔH_f^o, S^o and C_p for each Mg-hydroxychloride phase, determined using stoichiometric equivalents of MgO, $MgCl_2$, and H_2O in a Mg-salt structure, were used to approximate LogK values [0-25-60-100-150-200] for the $Mg(OH)_2$-$MgCl_2$-H_2O system using CHNOSZ as described previously in FY19 and FY20 [3, 14]. These preliminary LogKs, with updated values for Mg^{2+}_CODATA, brucite, bischofite, $MgOH^+$, and $MgCl_2$:$4H_2O$, were used to calculate solubility diagrams using Phase2 in Geochemist's Workbench (GWB) [51] at 25 ºC, 40 ºC, 60 ºC, 80 ºC, 100 ºC, and 120 ºC. The model was refined via trial and error to improve the agreement between the calculated solubilities and experimental data [21, 44, 47-50]. These refinements were done by adjusting the LogK values of the Mg-hydroxychloride phases to match the experimental phases boundaries, and then adjusting the Pitzer binary interaction parameters ($\beta^{(0)}$ and $\beta^{(1)}$) for the cation-anion pair of $MgOH^+$ and Cl^-. Effort was made to minimize changes to Pitzer interaction parameters, but in this case, because the thermodynamic data for the Mg^{2+} basis species was changed to Mg^{2+}_CODATA, the $MgOH^+$—Cl^- binary interaction parameters needed to be updated. The temperature-dependent virial coefficients, c_1-c_5, for the $MgOH^+$—Cl^- binary interaction parameters were not defined in the *data0.ypf.R2* database; as a result, initial estimations of the $Mg(OH)_2$-$MgCl_2$-H_2O system poorly reflected the experimental data at elevated temperatures. A given Pitzer interaction parameter as a function of temperature can be described through the terms c_1-c_5 via:

$$\beta_T = \beta_{25} + c_1(T_K - T_r) + c_2\left(\frac{1}{T_K} - \frac{1}{T_r}\right) + c_3\, ln\left(\frac{T_K}{T_r}\right) + c_4\left(T_K^2 - T_r^r\right) + c_5\left(\frac{1}{T_K^2} - \frac{1}{T_r^2}\right) \quad \text{(Eq. 2)}$$

where, β_T is the temperature dependent Pitzer interaction value and β_{25} is the value at 25 ºC; T_K is the absolute temperature and T_r is the reference temperature of 298.15 K (25 ºC). This equation describes the temperature dependence of each Pitzer interaction parameter.

The identity and solubility of the stable Mg-hydroxychloride phase is dependent upon both Mg^{2+} solution concentration and temperature, and using a graphical trial and error method to adjust LogK values to match experimental data is only possible at temperatures when a given phase forms. To mitigate any inconsistencies caused from this limitation, the entire LogK-temperature grid was refit using adjusted LogK values, when applicable, to minimize the squared difference between calculated values and the values determined through fitting. The output resulted in a new value of ΔG_f^o and a set of C_P coefficients (Eq. 1); the value for S_f^o, calculated as described above, was not changed. Then $\Delta G_f^o(T)$ was calculated via equation 3 [29]:

$$\Delta G_f^o(T) = \Delta G_f^o - S_f^o(T - T_r) + \int_{T_r}^{T} C_{P_r} dT - T\int_{T_r}^{T} C_{P_r} d\, ln\, T + \int_{P_r}^{P} V_T\, dP \quad \text{(Eq. 3)}$$

Where T_r and P_r are the temperature and pressure at 25 ºC, and T and P are the temperature and pressure of interest. For this case, $P=P_r$ for all calculated values, therefore $\int_{P_r}^{P} V_T \, dP = 0$. The calculated values of $\Delta G_f^o(T)$ were used to calculate new LogK values via equation 4:

$$\text{LogK} = \frac{-\Delta G_f^o(\text{T})}{2.302\ RT} \qquad \text{(Eq. 4)}$$

where R is the ideal gas constant (8.314403 J mol^{-1} K^{-1}). This process was continued in an iterative fashion, graphically fitting the experimental data with the calculated LogK values, and then re-calculating ΔG_f^o and C_p. To maintain consistency, ΔH_f^o was re-calculated from ΔG_f^o.

Following calculation of the LogK values for each of the Mg-hydroxychloride phases to match the experimentally observed phase boundaries, the measured phase solubilities were fit by adjusting the [$MgOH^+$—Cl^-] binary interaction parameters $\beta^{(0)}$ (c_1-c_5) and $\beta^{(1)}$ (c_1-c_5) in a graphical trial and error process to match the experimentally measured solubilities. First, the temperature-dependent parameters (c_1-c_5) were set to 0 so that $\beta_{25} = \beta_T$. Then $\beta^{(0)}$ and $\beta^{(1)}$ were adjusted to fit the solubility data at 25 ºC, 40 ºC, 60 ºC, 80 ºC, 100 ºC, and 120 ºC. The temperature-dependent parameters c_1-c_5 in Equation 2 were calculated by minimizing the sum of the squared difference between the graphically determined qualitative "best fit" value and the measured values at each temperature point. This process was included in the iterative process with the LogK calculations in order to converge upon best graphical representation of the data with an internally consistent database.

Fitting at 25 °C

The most widely studied Mg-hydroxychloride phase is the 3-1-8 phase. This largely due to its formation over a wide range of $MgCl_2$ molalities at room temperature. Initial $LogK_{3\text{-}1\text{-}8}$ values were limited to a small number of datasets [52], however, recent studies have provided a more detailed experimental data, allowing for greater confidence in identifying the $LogK_{3\text{-}1\text{-}8}$ and thermodynamic properties [21, 23, 49, 53]. At 25° C, the stable phases are brucite, the 3-1-8 phase, and bischofite. Since brucite and bischofite solubilities were already determined as a function of temperature in this study, only the $LogK_{3\text{-}1\text{-}8}$ and [$MgOH^+$—Cl^-] binary interaction parameters ($\beta^{(0)}$ and $\beta^{(1)}$) were adjusted to match the experimental phase boundaries (Figure 18). There is a large spread in the experimental data [21, 47]. However, the more recent work [21] states that the earlier solubility results [47] underestimate the [OH^-] in solution, because [OH^-] was determined by direct titration with a phenolphthalein indicator—which the authors [47] assert was a "necessarily poor" method to determine [OH^-]. Other experimental data [54] indicated brucite formation at >2 *m* $MgCl_2$, however, it has been noted that these results are likely due to meta-stable brucite formation because the equilibrium times were relatively short [21]. Related data showing very high brucite solubilities, even when the molality of $MgCl_2$ is > 2, were likely due to addition of NaOH to the system to help precipitate solids at higher $MgCl_2$ molalities, or to the solutions only being equilibrated 3-4 days [54, 55]. For this reason, SNL adjusted the $LogK_{3\text{-}1\text{-}8}$ to match the phase boundaries corresponding to the experimental data from Pannach et al. (2017) [21], which allowed solutions to equilibrate up to 3 years and measured $[OH^-]_{equilibrium}$ by a potentiometric method.

The initial $\beta^{(0)}$ and $\beta^{(1)}$ in the *data0.ypf.R2* database [39] were -0.1 and 1.658 for $\beta^{(0)}$ and $\beta^{(1)}$, respectively, and were determined by fitting the experimental data available at the time [47, 54]. Here, $\beta^{(0)}$ was determined to be -0.0125 and $\beta^{(1)}$ was determined to be -0.3 (Table 2). The impact of these changes significantly altered the calculated solubilities, especially as the ionic strength increased. Using the initial values, the model underestimated the experimental data at low ionic strength, but then sharply increased and overpredicted the solubility at higher ionic strength. The alterations made to the $\beta^{(0)}$ and $\beta^{(1)}$ binary interaction parameters for [$MgOH^+$—Cl^-] were made to dampen the impact of the $MgOH^+$—Cl^- ion pair to more accurately match the experimental data at intermediate $MgCl_2$ molalities where the 3-1-8 phase is the stable phase.

The modeled results of the $Mg(OH)_2$-$MgCl_2$-H_2O system using best fit values at 25 °C are shown in Figure 18. The $LogK_{3-1-8}$ was determined to be 25.8558, resulting in a ΔG_f^o = -2554.73 kJ mol^{-1}; ΔH_f^o = -2942.309 kJ mol^{-1}; and S^o = 313.700 J mol^{-1} K^{-1}. The calculated ΔG_f^o is in agreement (~1.4 kJ mol^{-1} lower) with the previously determined value [37]. The $LogK_{3-1-8}$ is slightly lower, but within the uncertainty, relative to previously reported value of 26.0 ± 0.2 [23, 56]. Experimental data collected since the determination of the original LogK values used in the *data0.ypf.R2* database provide an expanded dataset for fitting the system solubility.

Fitting at elevated temperatures

The methodology to fit the experimental data at elevated temperatures resembled the process at 25 °C; however, there were a few significant differences:

1. Since the thermodynamic database quantizes the LogK grid at select temperatures, [0-25-60-100-150-200], only LogK values at those temperatures could be adjusted directly. Therefore, fitting at 40 °C and 80 °C were performed by extrapolation; where 40 °C was fit indirectly by fitting 25 °C and 60 °C data, and 80 °C was fit indirectly by fitting 60 °C and 100 °C.
2. Not all Mg-hydroxychloride phases form under all temperature conditions, therefore adjusting LogK values can only be performed when the phase of interest is present at a specific temperature. For example, the 2-1-2 phase, only occurs under 1 temperature condition evaluated, and therefore there is more uncertainty in the calculation of its LogK values and thermodynamic properties than phases where more temperature dependent data is available. To maintain internal consistency, Equations 3 and 4 were used to generate a set of thermodynamic data based upon adjustments made to LogK values to fit experimental data.
3. The temperature dependent [$MgOH^+$—Cl^-] binary interaction parameters $\beta^{(0)}$ and $\beta^{(1)}$ are determined by making coefficients c_1 through $c_5 = 0$, then $\beta_T = \beta_{25}$. Then the fit at each temperature and each coefficient could be calculated by fitting with Equation 2.

There is less experimental data at elevated temperatures than at room temperature, therefore, the accuracy of the resulting thermodynamic values are dependent on the quality of data from a limited dataset. Given this limitation, the proposed thermodynamic values of the phases that form in the $Mg(OH)_2$-$MgCl_2$-H_2O system are internally consistent and fit the experimental data relatively well.

At 40 °C, the same assemblages are present as at 25 °C. Because 40 °C cannot be fit directly, LogK values at 25 °C and 60 °C were evaluated first. In addition to the assemblages at 25 °C and 40 °C, the experimental data at 60° C identify the presence of the 2-1-4 phase. The $LogK_{3-1-8}$ and Log_{2-1-4} at 60 °C were adjusted to provide a match to the experimentally determined phase boundaries [21, 57]. The resulting $LogK_{3-1-8}$ and $LogK_{2-1-4}$ at 60 °C are shown in

Table 3. The [$MgOH^+$—Cl] $\beta^{(0)}$ and $\beta^{(1)}$ parameters were adjusted to capture the solubilities indicated by the experimental data (Figure 18). Using these values, the model fits the experimental data well at 40 °C; however, at 60 °C, the model was not able to accurately capture the single 2-1-4 phase data point (Figure 18) – the solubility is overestimated by about 5 mmolal $Mg(OH)_2$. Although the solubility differs, the phase boundaries at 60° C are in good agreement. The model does predict the observed solubility decrease at the onset of the 2-1-4 phase precipitation; however the magnitude is not fully accounted for. At 60 °C, there are two datasets present [21, 57], and while these datasets generally agree, there is a systematic shift of ~ 2 mmolal of $Mg(OH)_2$ at which precipitation of the 3-1-8 phase occurs and the 2-1-4 phase only occurs in one dataset [21]. Given these discrepancies, no additional effort was made to adjust to the 2-1-4 phase, as more experimental data are needed.

At 80 °C, brucite, the 3-1-8 phase, the 2-1-4 phase, and bischofite all precipitate and the data is limited to one dataset [21]. These were fit indirectly by interpolating between the values in the temperature grid at 60 °C and 100 °C. At 100 °C, the 9-1-4 phase replaces the 3-1-8 phase as the phase that exists at

intermediate $MgCl_2$ molalities. $LogK_{9\text{-}1\text{-}4}$ and $LogK_{2\text{-}1\text{-}4}$ were altered to fit the phase boundaries of the experimental data at 100 °C. This is the first temperature that the 9-1-4 phase precipitated – and therefore $LogK_{9\text{-}1\text{-}4}$ at T < 100 °C could be not adjusted by fitting experimental data, but rather calculated using the trend defined by the adjusted $LogK_{9\text{-}1\text{-}4}$ at 100 °C and 120 °C, using Equations 3 and 4. The $LogK_{3\text{-}1\text{-}8}$ for T < 100 °C were estimated in a similar way by fitting the adjusted $LogK_{3\text{-}1\text{-}8}$ values derived at 25 and 60 °C). The 3-1-8 phase is reported to exist as a metastable phase at this temperature, these data were not used because this model represents the equilibrium solubility [21]. The resulting solubility diagrams for the $Mg(OH)_2$ — $MgCl_2$ — H_2O system at 80 °C and 100 °C using the adjusted LogK values and the $[MgOH^+—Cl^-]$ binary Pitzer parameters are shown in Figure 18. At 80 °C, the shape of the solubility diagram represents the experimental data and matches the phase boundaries. One discrepancy was the solubility near the 3-1-8|2-1-4 phase boundary at ~ 5 *m* $MgCl_2$. The model unpredicted the solubility of the 3-1-8 phase by ~10 mmolal $Mg(OH)_2$. Again, considering the limited availability of the experimental data and the general spread of the available experimental data when multiple data sets are available, the overall model fits the system well.

At 100 °C, the model is in good agreement with the experimentally determined 9-1-8|2-1-4 and 2-1-4|bischofite phase boundaries. However, the brucite|9-1-8 phase boundary is predicted to occur at lower $MgCl_2$ molalities than the experimental data indicate. Experimental datasets [21, 57, 58] agree for $MgCl_2$ concentrations between ~3*m* and ~5 *m*; however, not all experimental studies observed formation of the 9-1-4 phase [57, 58]. One reason for this is that the first reported identification of the 9-1-4 phase was years after these earlier studies [44]. In addition to phase boundary discrepancies between the model and the experimental data, the model does not always agree with phase solubilities respect to $Mg(OH)_2$. Here, the model over-predicted the brucite solubility when the molality of $MgCl_2$ is low; under-predicted the solubility at the 9-1-4 phase|2-1-4 phase boundary; and overpredicted the 2-1-4 phase solubility at high $MgCl_2$ molalities. To reconcile these differences, the $[MgOH^+—Cl^-]$ interaction parameters were adjusted, however, without making dramatic changes, no combinations of $\beta^{(0)}$ and $\beta^{(1)}$ fit the experimental data over the entire range. One explanation is the uncertainty in the experimental data at high temperatures. The experimental data takes great care to quantify the $[OH^-]_{equilbrium}$ via addition of HCl and back potentiometric titration with NaOH – to account for bound OH^- as $MgOH^+$[21]; however, at temperatures near or above the boiling point of water, it is possible that the water volume could have changed due to evaporation or that the solution pH (and therefore $[OH^-]$) could have changed from temperature changes over the course of the experiment.

Lastly at 120°C, brucite, the 9-1-4 phase, the 2-1-4 phase, the 2-1-2 phase, and $MgCl_2$:$4H_2O$ precipitate and were fit to experimental data indirectly by using the LogK-temperature grid values from 100 °C and adjusting the values at 150 °C. As no experimental data exist for 150 °C, the uncertainty in the model at 120 °C is much greater than at other temperatures and represents a bounding case. LogK values for the 9-1-4 phase, the 2-1-4 phase, and the 2-1-2 phase were adjusted to fit the experimental data. When possible, the LogK (e.g. 2-1-4 phase) values at 150 °C were determined via Equation 3 by calculation from the values determined at lower temperatures. Since this was the first time that the 2-1-2 phase precipitates, the $LogK_{2\text{-}1\text{-}2}$ was determined by matching the 2-1-4 phase|2-1-2 phase and 2-1-2 phase| $MgCl_2$:$4H_2O$ boundaries. The results are shown in Figure 18, and generally fit the experimental data; however the model systematically overestimates the solubility of the 2-1-2 phase over its entire stability range. One possibility is the experimental uncertainty, as discussed with respect to the data at 100 °C. The lack of bounding data at higher temperatures may also make accurate data fitting impossible. Should additional, higher temperature data become available, this model should be revisited.

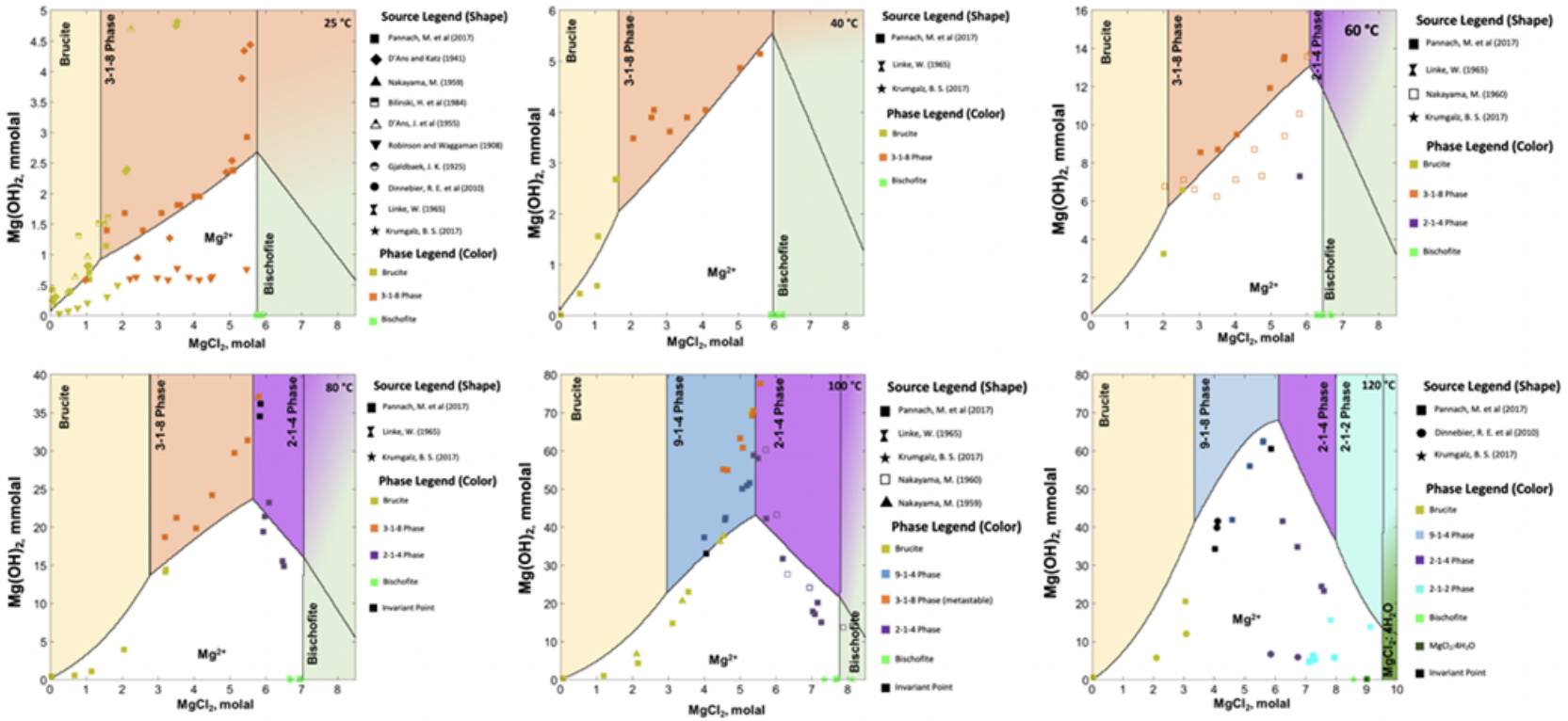

Figure 18. Phase diagrams of the $Mg(OH)_2$ – $MgCl_2$ – H_2O ternary system from 25 °C to 120°C showing the final modeled result versus the available experimental data where symbol colors represent the precipitated phases (brucite – yellow; 3-1-8 phase – orange; bischofite – green; 2-1-4 phase – purple; 9-1-4 phase – blue; 2-1-2 phase – teal) and symbols shapes refer to different experimental datasets.

2.2.1.3 Final Reported Values

The final adjusted LogK values for each phase are shown in Figure 19 and

Table 3. The dotted lines in Figure 19 represent the initial calculated value (using the contributions of MgO, $MgCl_2$, and H_2O described in previous reports [3, 14]), the solid line is the line fit to the LogK values at 0-25-60-100-150 °C using Equation 3. This comparison demonstrates that estimating the LogK values from group contributions provides a great starting value when limited or no data exist. Apart from the 3-1-8 phase (and metastable 5-1-8 phase – not included in this study), no thermodynamic data existed previously for the Mg-hydroxychloride phases. For the 3-1-8 phase, the initial calculation slightly underestimated the LogK values that were determined by fitting. Following adjustments to fit experimental data, the $LogK_{3\text{-}1\text{-}8}$ at 25 °C agrees with the previously determined value [23]. For the remaining Mg-hydroxychloride phases, the initial calculation overestimated the LogK values as a function of temperature – most dramatically with the 2-1-2 and 2-1-4 phases. One potential explanation for this is that the stoichiometric equivalents of MgO, $MgCl_2$, and H_2O for these phases are larger [3, 14], which means any uncertainty in the calculated values would be propagated into the calculation for these phases. Another explanation is that the calculated values of MgO, $MgCl_2$, and H_2O are more influenced by phases where there is sufficient experimental data (brucite, bischofite, 3-1-8 phase), therefore the initial calculation of these phases is based upon the assumption that the contribution of each of these components in the mixed salts systems is the same – which is likely not the case. Using the adjusted LogK values as a function of temperature and Equation 3, the thermodynamic properties of the Mg-hydroxychloride phases were re-calculated (Table 1). The proposed values here are the first reported thermodynamic values for the elevated temperature Mg-hydroxychloride phases (the 2-1-4, 2-1-2, and 9-1-4 phases).

Estimates of the [$MgOH^+$—Cl^-] binary Pitzer interaction parameters, $\beta^{(0)}$ and $\beta^{(1)}$, as a function of temperature are shown in Figure 20. These parameters were determined through a trial and error process by altering the $\beta^{(0)}$ and $\beta^{(1)}$, keeping c_1 through $c_5 = 0$, and identifying which combination of $\beta^{(0)}$ and $\beta^{(1)}$ fit the experimental dataset best at each temperature. Those estimated values were then fit using Equation 2 to determine the values of the coefficients that best represent the interaction parameters. The resulting Pitzer interactions parameters ($\beta^{(0)}$ and $\beta^{(1)}$) and temperature dependent coefficients for [$MgOH^+$—Cl^-] are shown in Table 2. Overall, the impact is dampened as the temperature increases and the relationship is non-linear. No adjustments were made to $\beta^{(2)}$, c^{φ}, $\alpha^{(1)}$, $\alpha^{(2)}$, though introducing additional parameters would improve the model's ability to fit the experimental data; however, there does not currently exist a justification to change these additional parameters. The $\beta^{(0)}$ and $\beta^{(1)}$ values differ from those previously derived [39]; however, these changes largely reflect the availability of more experimental data. In addition, this work presents the first reported values for c_1-c_5 and therefore there are no data with which to compare.

Using the thermodynamic values that were derived from fitting the experimental data, the thermodynamic values of the components (MgO, $MgCl_2$, and H_2O) were re-calculated. These results agree with previous work [59] in which the average error was ~0.2 %. Based on this understanding in the calculation, it is considered that the expected uncertainty in the presented values, unless otherwise stated, is reflected in this calculation and therefore is ± 0.2% of the value. Under a few circumstances the LogK had to be adjusted more than 0.2% of the calculated value to fit the experimental data – these circumstances are noted in

Table 3. All but one of these LogK values that were adjusted beyond 0.2% of the calculated value were at elevated temperature (≥100 °C) – and primarily occurred in Mg-hydroxychloride phases ≥ 150 °C, which were adjusted to match solubility data at 120 °C. The one exception is that the $LogK_{2\text{-}1\text{-}4}$ at 60 °C needed to be adjusted >0.2% for GWB to converge. Interestingly the calculated solubility diagram poorly reflects the single experimentally measured solubility datapoint of the 2-1-4 phase at 60 °C. More experimental data at 60 °C in the stability field of the 2-1-4 phase may be required to refine the $LogK_{2\text{-}1\text{-}4}$.

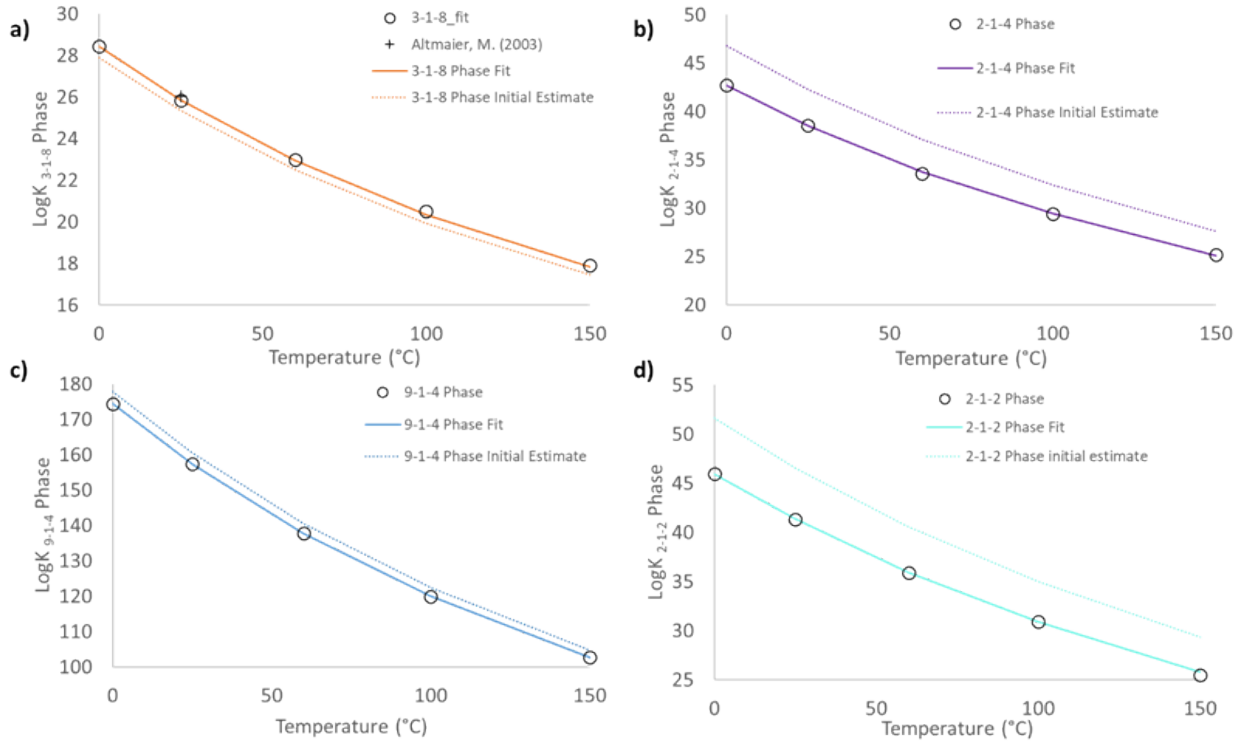

Figure 19. a) $LogK_{3\text{-}1\text{-}8}$ as a function of temperature shown with initial estimate, fit values, and compared to [23]; b) $LogK_{2\text{-}1\text{-}4}$ as a function of temperature shown with initial estimate and fit values; c) $LogK_{9\text{-}1\text{-}4}$ as a function of temperature shown with initial estimate and fit values; d) $LogK_{2\text{-}1\text{-}2}$ as a function of temperature shown with initial estimate and fit values.

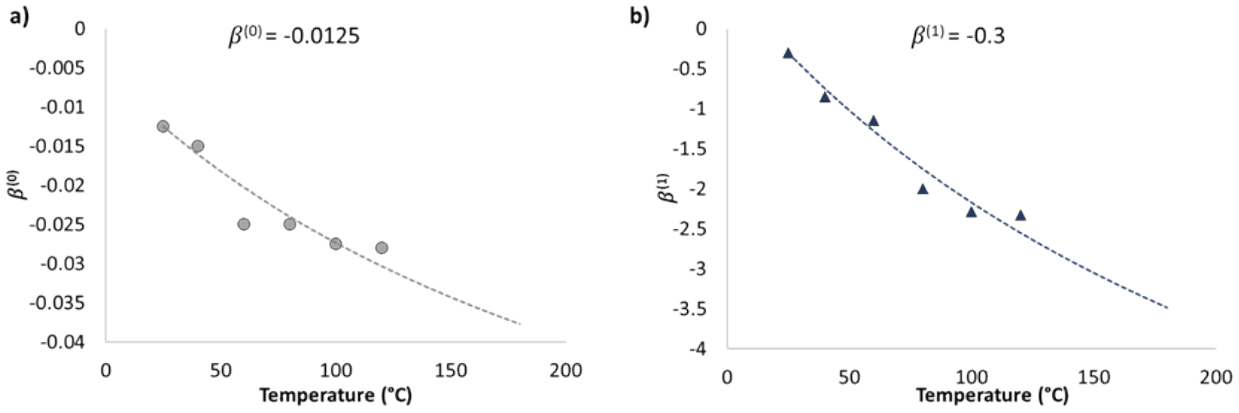

Figure 20. The Pitzer parameters (a) $\beta^{(0)}$ and (b) $\beta^{(1)}$ for the [$MgOH^{+}$—Cl^{-}] binary interaction as a function of temperature. The datapoints were determined via graphical trial and error process to fit the experimental data (with c_1-c_5 = 0), the best fit line was generated by fitting the datapoints using Equation 2.

2.2.1.4 Future Work

With a consistent, accurate thermodynamic database that incorporates the formation of Mg-hydroxychloride species as a function of temperature, SNL can develop a more predictive understanding of brine $MgCl_2$ brine stability on heated SNF dry storage canister surfaces. In FY22, SNL plans to incorporate the effects of the Mg-hydroxychloride species and of acid gas species to model the interactions of seawater brines with atmospheric acid gases. As discussed in Section 2.1.3, acid gas reactions with $NO_{x\,(g)}$, $SO_{2\,(g)}$, and $HCl_{(g)}$ can occur; therefore additional work is needed to better understand brine stability under canister-relevant conditions with acid gas interactions. This will allow for a better understanding of chemical factors that could lead to increased brine stability (e.g. some nitrate salts have low DRH values) or brine dry out (e.g. Mg-hydroxychloride or hydroxysulfate precipitation).

2.2.2 $MgCl_2$ degassing experiments

Experimental efforts at SNL to further evaluate the stability of $MgCl_2$ brines, adding to previous experiments performed in FY17 – FY20 [3, 13-15], continued $MgCl_2$ degas studies in FY21. Previous and ongoing work from SNL has demonstrated the importance of understanding the stability of $MgCl_2$ brines due to their impact on canister corrosion and potential CISCC. The presence of a stable $MgCl_2$ brine will not only cause irregular pitting, which may be more susceptible to pit to crack transition, but also would increase the amount of time that a brine can exist on the canister surface. Since bischofite ($MgCl_2 \cdot 6H_2O$) is the first sea-salt aerosol to deliquesce on the canister surface as the RH increases from a decreasing canister temperature, a $MgCl_2$-rich brine could potentially exist on the canister surface, depending on the initial heat load and local weather data, as soon as 20-30 years after the fuel is loaded [3, 13, 14]. Conversion to Mg-hydroxychloride (as shown in Section 2.2.1), Mg-hydroxide, or Mg-carbonate phases can occur by degassing Cl^- and/or absorbing CO_2 from the atmosphere, and their formation would lead to brine dry-out under deliquescent conditions for bischofite.

Similar to previous experiments, in FY21 $MgCl_2$ was deposited onto an inert substrate (25 mm diameter silicon wafer), and placed in an environmentally controlled chamber (T and RH) with continuous airflow, generated with a Zero Air Generating system that removes all contaminants (acid gases, organics) from the air stream (importantly CO_2 is not removed by the Zero Air Generating system), and periodically sampled over 16 weeks (sampled at 4 weeks, 8 weeks, and 16 weeks). The exposure conditions for this experiment were 48 °C, 40 % RH and an air flow rate of 9 L/min. These conditions were the same as in FY20, however the $MgCl_2$ droplets were smaller. This modification made in FY21 was due to the deposition of $MgCl_2$ not with the ink jet printer [60], but rather with a nebulizer in an aerosol chamber. This one was done for two reasons, highly concentrated $MgCl_2$ brines are viscous and can clog the ink jet print, but more importantly the nebulizer deposited $MgCl_2$ in smaller droplets than the ink jet printer. Figure 21 shows the $MgCl_2$ droplet sizes using the ink jet printer in FY20 and the nebulizer in FY21. The exposure condition (48 °C, 40 % RH) represent conditions close to the highest temperatures where bischofite could deliquesce in a real canister environment. Previous work under these conditions resulted in minimal conversion over the experimental duration, where the calculated Cl^- loss was <10% in 16 weeks and the carbonate gain was ~0.1 µmol/µmol of Mg [3]. SEM/EDS analyses demonstrated the formation of Mg-CO_3 and Mg-hydroxychloride species, which was preferential to smaller droplets (where the surface area to volume ratio is largest) – however X-ray diffraction (XRD) analyses only showed the presence of bischofite (XRD is not sensitive to minor phase contributions). This was the motivation to perform the experiment with smaller $MgCl_2$ droplets in FY21. In addition to experiments under these conditions, previous studies were also performed at 80 °C and 35 % RH, which represent accelerated conditions where significant Cl^- degassing can occur [14]. Under these conditions, more Cl^- was lost over the experiment. Nearly 20% Cl^- was lost within 4 weeks and upwards of 40% was lost over 8 weeks. XRD experiments demonstrated the formation of a high temperature Mg-hydroxychloride phase (2-1-4 phase), confirming predictive stabilities in the geochemical modeling (Section 2.2.1) and agreed with other studies where 2-1-4 phase was observed under similar conditions [13, 14].

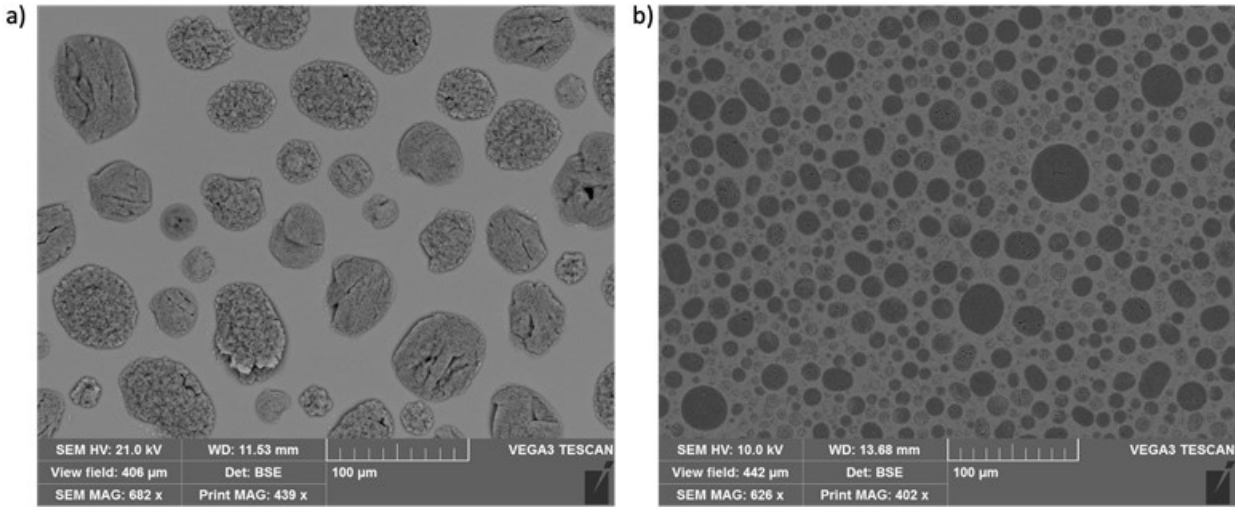

Figure 21. $MgCl_2$ droplets on silicon wafer deposited by a) ink jet printer in FY20 and b) nebulizer in FY21, showing that the nebulizer produced smaller droplets.

In FY21, the 16-week exposure period ended, and sample analysis has begun. Sample analyses include TOF-SIMS, vibrational spectroscopy (Raman and FTIR), XRD, SEM/EDS, IC, and DIC. In FY22, the experimental analyses will be completed, and the data will be compiled and compared with previous results. These experiments will allow for a better understanding of the degree of $MgCl_2$ as a function of droplet size under canister relevant exposure conditions and aid in the developing a clearer understanding of $MgCl_2$ stability. Furthermore, in FY22 studies will begin investigating the stability of seawater relevant brines when exposed to atmospheric acid gases. As discussed in Section 2.1.3, acid gas reactions with the salts present on the canisters can occur, and their implications on the corrosion and potential for CISCC are not fully understood. To begin, experimental analysis of the stability of $MgCl_2$ brines under atmospheric conditions with $HCl_{(g)}$, $SO_{2(g)}$, and/or $NO_{x(g)}$ will be performed and the results will be compared with advancements in the thermodynamic modeling to include acid gas reactions.

2.3 Canister Deposition Field Demonstration Studies

The SCC group has performed several studies in support of the CDFD project. These include developing a preliminary sampling plan for dusts on the canisters, evaluating and developing specifications for on-site sampling of atmospheric aerosols, evaluating methods for measuring canister surface roughness on a submillimeter-to-micron scale, and evaluating methods for marking the canisters for sample grids. A summary of each of these is discussed below.

2.3.1 Canister Sampling

A preliminary plan for sampling the dust on the surface of the three dry storage canisters that will be used in the CDFD has been developed, and was published as a Level 4 Milestone, *Surface Sampling Techniques for the Canister Deposition Field Demonstration*, in March 2021 [61]. A short summary is provided here.

The CDFD project will use three commercial 32PTH2 NUHOMS welded SS storage canisters, which will be stored at an ISFSI site in Advanced Horizontal Storage Modules (AHSMs). One canister will be unheated and the other two will have heaters to achieve canister surface temperatures that match, to the degree possible, loaded SNF canisters with heat loads of 10 kW and 40 kW. Surface sampling campaigns will take place on a yearly or bi-yearly basis. The goal of the planned dust sampling and analysis is to determine important environmental parameters that impact dust and salt accumulation on canister

surfaces, and hence, the potential occurrence of canister stress corrosion cracking. Specifically, the size, morphology, and composition of the deposited dust and salt particles will be quantified, as well as the soluble salt load per unit area and the rate of deposition, as a function of canister surface temperature, location, time, and orientation. In addition, atmospheric monitoring will be carried out to monitor weather and the ambient atmospheric aerosol particle size distributions and particle densities (Section 2.3.2). The ambient data provide boundary conditions at the inlet vents for modeling aerosol deposition within the overpacks, while the measured canister surface deposits will be used to calibrate and validate the deposition models.

Current sampling plans are that the canister will be allowed to cool and then pulled from the AHS. Sampling will be accomplished by hand at specific locations on the canister surface. Proposed sampling locations are shown in Figure 22. There will nominally be 25 locations, corresponding to 5 circumferential locations at each of the 5 longitudinal locations. However, surface access limitations due to the frame supporting the extracted canister will probably limit sampling to fewer locations. At each sampling location, a 2×2 sampling grid (containing 4 sample cells, each 7.5 × 7.5 cm) will be painted onto the metal surface. The locations have been chosen such that there is little temperature variation between the four cells—the cells can be considered equivalent with respect to dust deposition processes. During each sampling campaign, two samples at each location will be collected, in a specific routine to measure both periodic (yearly or bi-yearly) and cumulative deposition rates. It is important to capture both, to assess the possible effects of accumulated dust on further deposition; as dust loads increase, impacting dust particles are more likely to knock off previously deposited particles, resulting in a decrease in deposition efficiency with time. However, this effect is highly dependent upon the angle of the surface and the mode of deposition (e.g., collision vs. gravitational settling). One possible sampling schedule is shown in Figure 23; the actual sampling interval (yearly or bi-yearly) has not been determined, so the actual number of sampling episodes may vary.

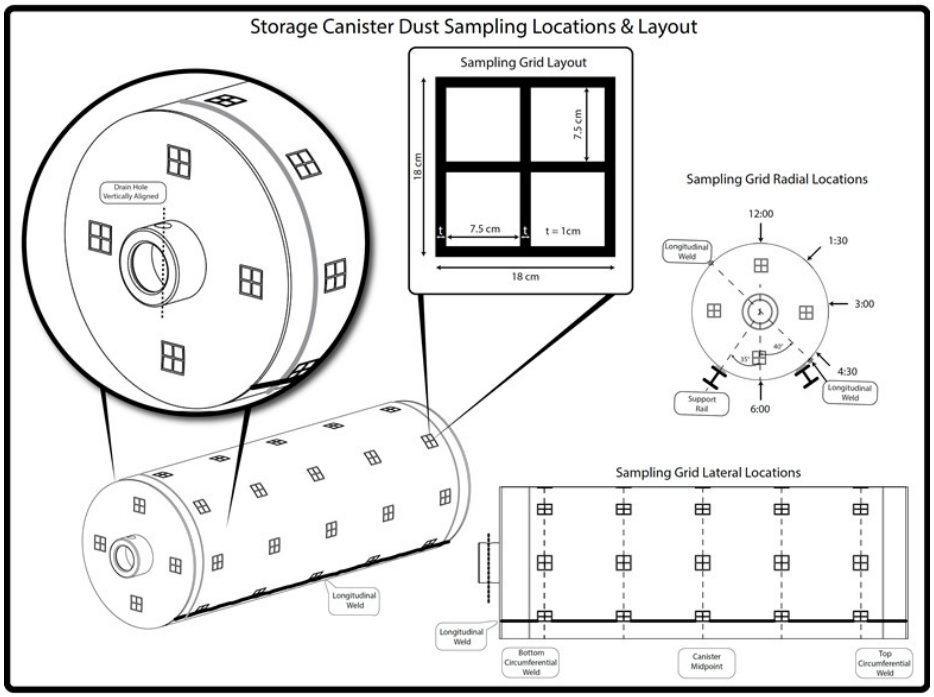

Figure 22. Proposed sampling locations on the canister surface. A total of 25 sampling grids will be used, with 5 circumferential locations at each of the 5 locations along the longitudinal axis of the canister.

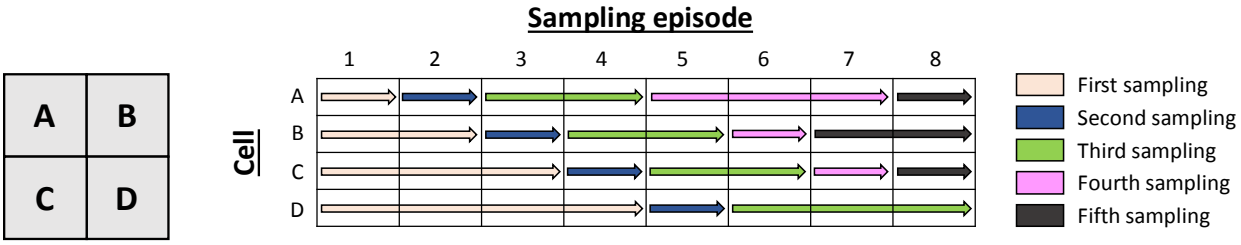

Figure 23. Sampling grid and possible sampling schedule.

For each sample, a wet and a dry sample will be collected (Figure 24). Wet filters will be used to quantitatively remove dust and salts from the entire surface within a single cell of the sampling grid, using a template to constrain the area sampled. The wet samples will be leached and analyzed to determine the composition of the soluble salt fraction and to estimate salt loading per unit area. Dry samples will be collected using an adhesive tape (Biotape®) from the canister surface adjacent to the cell sampled, and will be analyzed to assess particle size, morphology, mineralogy, and identity (e.g. for floral/faunal fragments).

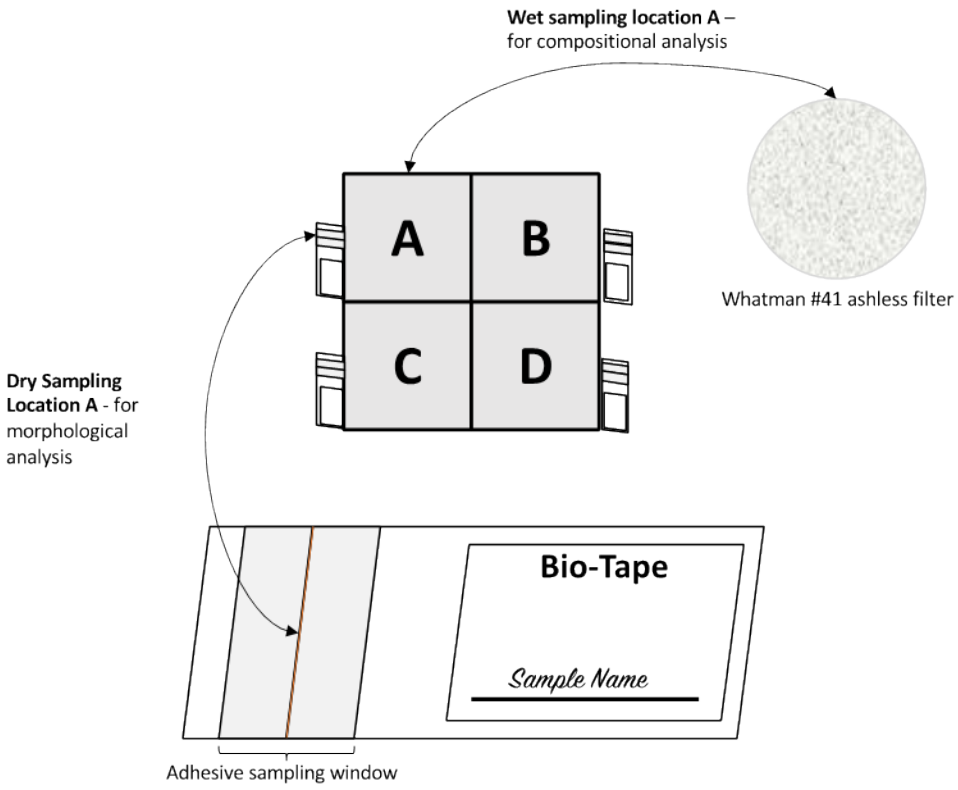

Figure 24. Schematic showing the sampling locations of the wet and dry samples, along with their collection media.

To the degree possible, other surfaces within the AHSM, including surfaces within the inlet and outlet vents, rails and canister support structures, and heat shields, will also be sampled. However, access

restrictions may limit sampling in these areas. Also, each canister and overpack must be sampled within a single day; this may limit the extent of sampling additional surfaces.

Following collection, the samples will be transported to SNL. Once received at SNL, the wet filter samples will be leached to extract the soluble salts for analysis. The leachate will be analyzed by IC and DIC analyzer. The dry samples, collected using Biotape® from the canister surface, will be characterized by SEM/EDS analysis. Sample analysis techniques will include:

- Chemical analysis of soluble salts by IC. The soluble salts will be leached from the filters with DI water. Analysis of the leachate provides soluble salt compositions and concentrations in the samples.
- Analysis of inorganic carbon by DIC. Like the IC, soluble salts will be leached from the filters with DI water. Analysis of the leachate provides the total amount of inorganic carbon in the samples. It is important to note that, since the samples were collected wet, there is a potential for CO_2 to degas, or to be adsorbed by the samples. This could result in inorganic carbon measurements that differ from the actual value.
- SEM imaging and EDS element mapping. SEM/EDS analysis of the dry dust samples provides particle size, textural and mineralogical information of dust and soluble salt species and allows visual identification of organic matter (floral/faunal fragments).

The data generated by the CDFD sampling, periodic quantifiable sampling of three canisters of varying heat loads, will allow for an in-depth understanding of cumulative dust and salt aerosol deposition, and of salt deposition rates as a function of salt load, and canister surface location, orientation, and temperature. This information is critically needed to parameterize and validate the dust deposition models that are being developed at PNNL [61-63]; to provide input conditions for future and ongoing corrosion studies; aiding ongoing efforts to develop a detailed understanding of the potential occurrence and timing of stress corrosion cracking on SNF dry storage canisters.

2.3.2 Environmental Monitoring at the CDFD Site.

In addition to analysis of canister surface deposits, parameterization of the PNNL canister dust deposition model requires knowledge of the ambient conditions external to the AHSM, which define the boundary conditions at the overpack inlets and outlets, as well as at the overpack walls. Environmental monitoring at the site is required to characterize the ambient weather conditions and aerosol characteristics.

2.3.2.1 Weather Monitoring

Weather data are critical parameters for both thermal and dust deposition models of the CDFD canisters. Standard, readily available stations collect the following data, most of which are required model inputs, currently estimated or evaluated parametrically:

- Wind speed
- Wind direction
- Temperature
- Humidity (relative humidity, absolute humidity, or dewpoint - if temperature and pressure are known, each can be converted to the other)
- Barometric pressure
- Rainfall (cumulative amount, duration, intensity)

Additional information that is provided by some weather stations includes:

- Solar radiation (this affects canister and overpack temperatures)

- Wind gust data (this is important for modeling aerosol particle transport to, and entry into, the AHSM)

A weather station has not yet been chosen for the site; many commercially available weather stations are capable of collecting the necessary data. The power requirements for weather stations are very low, on the order of mA to tens of mA. They are frequently solar-powered, but a hard-wired power source or battery as a backup may be necessary. A data logger and/or data transmitter capable of wireless communications from the site is also required.

2.3.2.2 Aerosol Sampling

Specific parameters that need to be collected include the following:

- Particle size distribution, from >10 μm to 0.1 μm in at least 7 size fractions
- Particle density per unit volume of air (e.g., $\mu g/m^3$)
- Particle composition, as a function of particle size
- Chloride density per unit volume of air (e.g., $\mu g/m^3$)

Note that for the dust deposition model developed at PNNL, the required particle sizes are that of the aerosol particles that will enter the overpack. Depending upon the RH, these particles may be deliquesced or partially deliquesced. Also, a fraction—perhaps the majority—of the dust particles will not be salt aerosols. Experience has shown that the majority of dust deposited on the SNF dry storage canisters may be detrital mineral grains. In many areas, these are silicate minerals such as quartz, feldspars, and clays; in other areas where the surrounding bedrock is limestone or dolomite, carbonate mineral grains may be abundant.

It would be best to sample as close to the storage systems as possible; nearby topography could have a significant effect on atmospheric dust loads. Given the proximity to the ocean, it is likely that there will be significant variation in aerosol size distributions and composition as a function of elevation.

Is it necessary to sample at the elevation of the inlet vents? Outlet vents?

Will the atmospheric dust bedload this close to a beach be so high that sampling near the ground is impossible?

Background—Expected Salt Aerosols

In selecting the appropriate aerosol sampling equipment, it is important to consider the size and nature of the aerosol particulates that will be sampled. Dried sea-salt particles observed on canisters at Diablo Canyon were generally in the 5-15 μm range (Figure 25) [64]. Deliquescence plays a direct role in particle sizes; a 10 μm particle corresponds to an initial seawater droplet that is about 37 μm across. However, assuming that the aerosol droplets equilibrate at the ambient T/RH, these droplets will generally be significantly smaller than the initial seawater droplet but larger than the fully-dried salt particles. Hourly temperature and RH values over an entire year from an airport near a proposed site for the CDFD are shown in Figure 26. To the degree that these data are applicable to the site (which is on the shoreline), this figure indicates that sea-salt particles will almost always be at least partially deliquesced (>35% RH) and will frequently be fully deliquesced (> 74% RH). However, they will rarely encounter an RH as high as seawater deliquescence (98.1%), and hence will be smaller than the original seawater droplet. Particle diameters as a function of RH are given in Figure 27. For instance, assume an RH of 80%; in this case, a 10 μm salt particle corresponds to a brine droplet about 18 μm in diameter.

It is important to note that that particle sizers segregate particles based upon aerodynamic equivalent diameter (AED), not actual diameter. A particle density of 1.0 g/cm^3 (pure water) is assumed. Actual particle densities will vary from ~1.03 g/cm^3 for unevaporated seawater to ~2.05 g/cm^3 for completely dried salts. Thus, the particle AED will vary from the physical diameter, and the relative difference will

increase as the particle dries out and the density increases. In addition to the physical diameters, AED values calculated using the equations in Raabe (1976) are shown in Figure 27. Note that the physical diameters in Figure 27 all evolve along parallel pathways with evaporation, but the AEDs do not. That is because the calculated AEDs include particle drag effects, which increase as the particles become smaller.

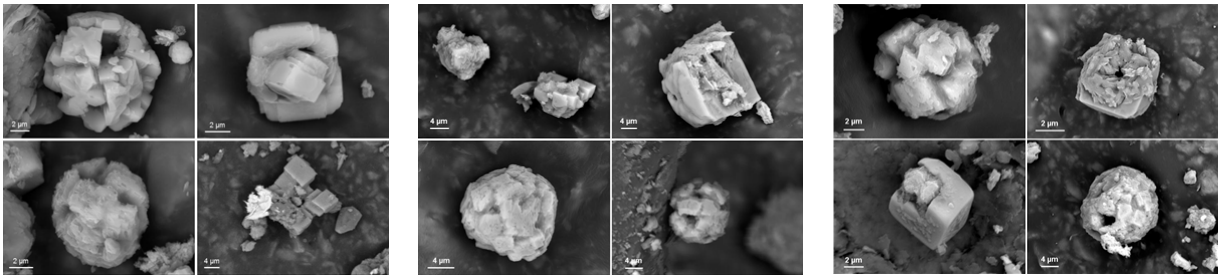

Figure 25. SEM images of sea-salt aggregates collected from the tops of canisters from the Diablo Canyon ISFSI.

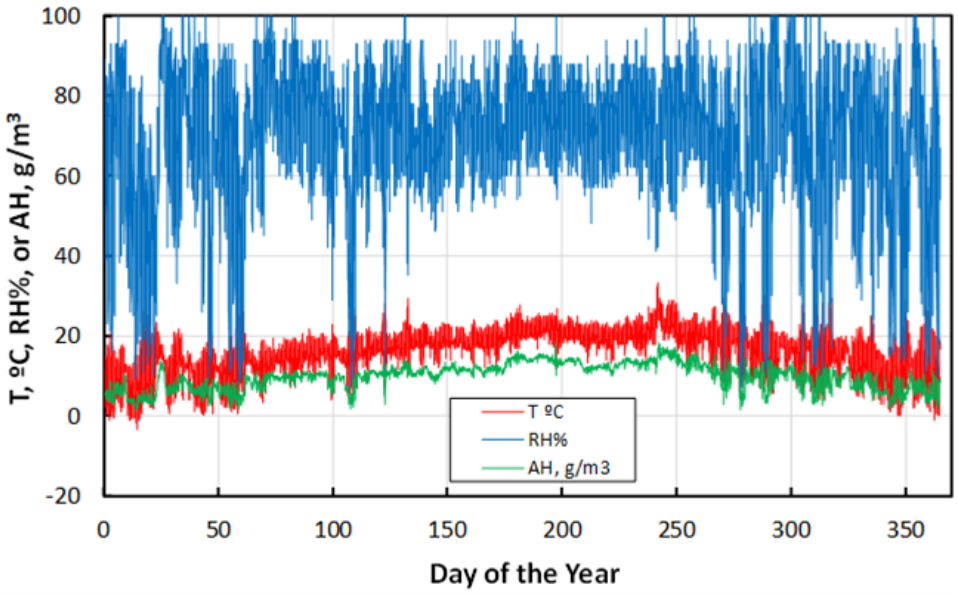

Figure 26. Weather data from an airport near one proposed CDFD site.

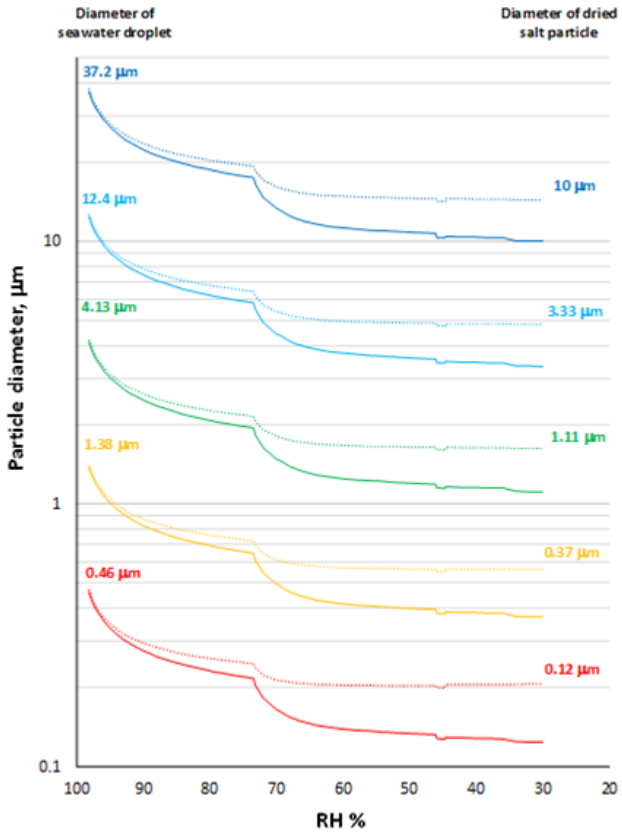

Figure 27. Sea-salt aerosol particle diameters as s function of RH. Solid lines are physical particle diameters (assuming a spherical particle). Dotted lines are AEDs, accounting for changes in density and drag as the particle dries out.

Unevaporated seawater aerosol particle sizes generated by sea-foam bubble bursting are shown in Figure 28. Median particle sizes are in the 0.05-0.2 µm range (Figure 28; [65]), but the vast majority of the mass is associated with larger particles, in the 1-20 µm range. While the masses associated with the smaller particles will be small, the ability to sample and discriminate these may be necessary, as the smaller particles may be preferentially deposited on canister surfaces.

It is important to note, too, that sea foam is only one source of seawater aerosols. Surf also produces seawater aerosols, which are shifted to larger sizes relative to sea-foam aerosols. The actual aerosol size is a function of wave intensity, which is a function of the seafloor slope. At the proposed site, the slope is low.

Ideally, we would be able to sample and size particles with aerodynamic diameters at least as large as few tens of µm. Most sea-salt aerosols will be significantly smaller, but the large particles are especially important because they carry most of the mass. A minimum particle size cutoff in the 0.05-0.2 µm range would be potentially useful.

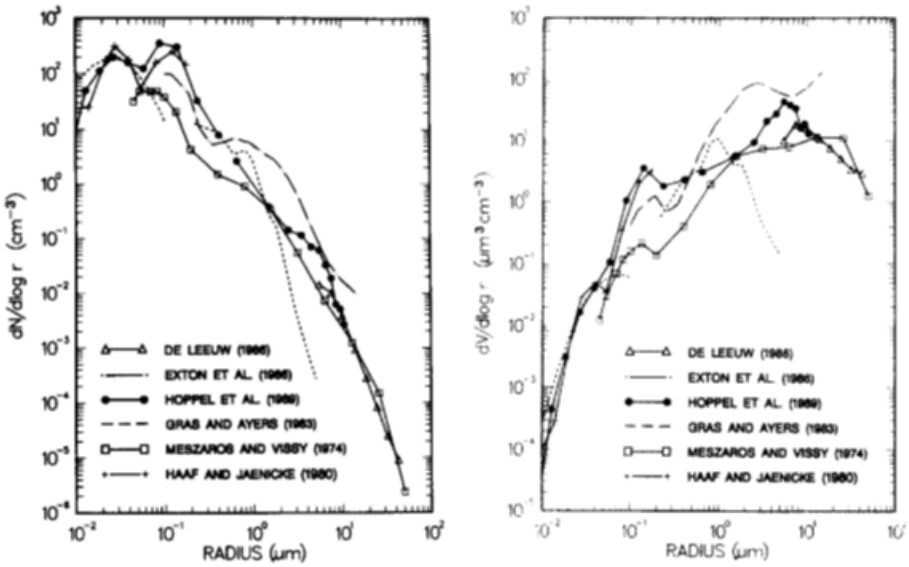

Figure 28. Seawater aerosol particle sizes generated by sea-foam bubble bursting [65].

Required equipment

There are several options for aerosol sampling. Real-time particle sizing can be done using several different methods (e.g., light scattering laser photometry), but these do not allow retention of samples for chemical analysis. They also do not offer any chemical discrimination—it is not possible to differentiate salt or brine aerosols from detrital silicate mineral grains. Only a cascade impactor discriminates between different particle sizes and collects the particles for later analysis, allowing assignment of particle mineralogy/composition as a function of particle size. Cascade impactors consist of a series of stages, each of which captures progressively smaller aerosol particles from an airstream passing through it. This allows a particle size distribution to be determined.

Cascade Impactor

A few considerations for cascade impactors include the following:

- *Do they work with deliquesced particles?* Yes. In fact, partially deliquesced particles adhere better to the targets. However, if wet aerosols are collected, they may undergo conversion/ degassing reactions as they sit on the impactor targets. Also, impactors don't work under condensing conditions, and are generally limited to <90% ambient RH. Incoming air stream can be passed through a dryer to mitigate both of these; however it is important to note that the measured particle sizes will be the dry particle size, not the deliquesced or partially deliquesced particle size that is actually present in the ambient air. Finally, the instrument must be sheltered from rain.
- *What particle size range can be sampled?* Impactors are generally used to study particulate matter, ≤10 μm (PM_{10}) or smaller particles, that are readily suspended, transported, and inhaled. Most have an engineered inlet that rejects particles 10 μm or larger, but one instrument has an optional inlet that provides a 15-20 μm precut. The material rejected by the inlet cannot be quantitatively removed for analysis. The first stage in all systems is a 10 μm cut, with progressively smaller particles being retained by subsequent stages. The final stages vary with the instrument but can be as small as 0.05 - 0.06 μm; smaller particles are retained by HEPA filter, which may or may not be removable for analysis. All the cut sizes are based on aerodynamic equivalent diameter.

- *What are the mass limitations?* As mass accumulates on each target, the collection efficiency decreases, because the likelihood increases of an impacting particle knocking loose previously collected particles. All manufacturers recommend the maximum surface load on any impactor plate to be 1 mg. The accumulation rate on any impactor plate is a function of the aerosol density in the environment, and it is the limitation on accumulated mass that determines how frequently the impactors have to be replaced.
- *How is the mass of each size fraction determined?* For standard impactors, each target is carefully weighed at a fixed RH prior to use. After sample collection, the target is then equilibrated at the same RH and reweighed to determine accumulated mass. One company uses a different approach, imparting a static charge to the particles as they enter the cascade impactor, separating the particles aerodynamically, and then measuring the current generated as the dust deposits on each impactor target to get the particle size distribution. This allows for both individual particle counting, and estimation of the total mass deposited on each target, if a particle density is assumed.
- *How is the chemistry determined?* Once the aerosol particles have been separated into different particle sizes, the impactor is disassembled, and the targets are extracted. The chemistry of the deposited dusts on each target is determined via leaching and chemical analysis. X-ray fluorescence analysis of the targets is also sometimes used.

Cascade impactors are used for many different industry applications. Many are designed for specific tasks (e.g., pharmaceuticals, monitoring of bacteria/fungal spores in buildings) and are not appropriate for our application. For the CDFD, an impactor is required that is suitable for outdoor environmental monitoring, that retains the samples for later chemical analysis, and that can collect material over a significant amount of time, requiring less frequent exchanges of the impactor targets. Equipment from several different manufacturers was evaluated, and an impactor offered by Dekati Ltd. has been chosen.

The impactor is a Dekati® HRELPI+ instrument. It is a 14-stage impactor covering a size range from 0.016 μm to 10 μm, with a flow rate or 10 L/min. It has an absolute filter at the exit to capture all particles less than 0.016 μm. The collection plates in each stage accept 25 mm collection foils which can be any material that is thin and smooth; for chemical analysis, polycarbonate foils are used. In this system, aerosol particles pass through a unipolar corona charger where a known positive charge is applied. In the impactor, the particles are size classified into 14 size classes onto the impactor plates. The charge deposited in each stage is measured, allowing the instrument to measure the particle number size distribution and concentration in real-time. To convert to a mass distribution, a density must be assumed for the particles. Alternatively, the targets can be weighed at a known RH before and after use, as with a standard cascade impactor. The high-resolution version of the instrument offers 100 particle size channels instead of 14 channels; the extra cuts are achieved through software. Collection of particles on polycarbonate or Teflon® for post-measurement analysis is possible just like a regular cascade impactor. It should be noted that for the Dekati®, the 10 μm cut in the first impactor stage is collected, but not monitored electronically. The weight of the 10 μm cut is important and must be determined by the weight difference between the clean target and the target after use, at a known RH. Particles too small to be captured by the final target are collected by a HEPA filter after the final target. This filter is fixed—it cannot be removed for sample retrieval.

Mass limits on the targets for quantitative chemical analysis are still 1 mg for the heaviest loaded target; this requirement determines how often the targets have to be removed and replaced. That limit may well be reached first by the 10 μm target, as it accumulates the most massive particles. One alternative is to use a sintered plate for this target; this plate can hold up to 50 mg prior to becoming overloaded. This plate is not generally used for chemical analysis, but may be an option, if high aerosol loads in the ambient air require too frequent replacement of the targets.

Several accessories are either required to run the cascade impactor or provide benefits for this use.

Pump—Air will be pulled through the instrument by a dry scroll pump, which was chosen because it is quieter than oil piston pump and does not exhaust oil vapors, which could be an issue on an ISFSI pad.

Inlet—An engineered inlet for omnidirectional sampling of the ambient air is also required. Dekati offers both PM_{10} and TSP (total suspended particle) inlets. PM_{10} are used in ambient measurements as pre-separators to prevent particles larger than 10 μm in aerodynamic diameter from entering the sampling line and thus the particle measurement instrument. The operating principle of the inlet is based on impaction; particles larger than 10 μm are separated from the aerosol flow and collected inside the sampling inlet. The Dekati® PM_{10} inlets are specified for either 10, 30, or 70 Lpm sampling flow rate. The Dekati® TSP inlets have a larger cutpoint of around 15–20 μm for sample flow rates of either 10 or 30 Lpm; this is desirable, as the goal is to capture as much of the coarser salt aerosols as possible, and deliquesced sea-salt particles may be even coarser than this (Figure 28). Hence, the TSP inlet has been purchased. In continuous use, the inlet is recommended to be cleaned periodically, so that the particles that deposit inside the inlet don't affect the calibrated cutpoint for that inlet. The cleaning can be done with a cloth saturated with isopropanol solution. The frequency depends upon the aerosol load in the environment—Dekati® has stated that at other marine sites, cleaning was required every 1-2 months.

Dryer: An air stream dryer is placed below the inlet to remove water from aerosols prior to entering the cascade impactor to deposit on the impactors. It important for the real-time reading to best correlate with post-measurement analysis, if the particle-borne water is allowed to evaporate between collection and analysis. In terms of aerodynamic particle sizes entering the inlet of the overpack, *for this project, we are interested in the particle size distributions of the deliquesced particles*. This information is lost when the particles are dried. However, the dry particle sizes measured can be used to calculate the particle sizes as a function of RH (Figure 27), which may be the best approach for the modeling. Advantages of collecting dried samples are several: (1) dried salts do not undergo particle/gas exchange reactions on the impactor targets—they are not modified between collection and analysis; (2) the collected mass is less, so that collection times can be longer without exceeding the mass limit of the targets; (3) in the case of deliquesced particles, it is likely that a majority of the mass will deposit on the particle impactors for the largest particles—drying the particles first may be a better way of obtaining a complete size distribution for the sea-salt aerosols; and (4) it prevents deliquescence of salts on the impactor plates, which could potentially result in exceeding the mass limit for the plates.

The Dekati® dryer is not a heated dryer; instead, it uses a Nafion filter to remove water vapor from the sample. It generally requires a dry air source (10-60 Lpm), which may not be readily accessible on the ISFSI pad; however, an alternative is to use a vacuum, requiring only a vacuum pump. The scroll pump is purchased with the HRELPI+ is sufficient to support the dryer as well as the cascade impactor.

Diluter: The frequency of target replacement depends on the aerosol load in the air but is likely to be hours to a day under normal circumstances. Software can be used to turn the impactor on for 5-10 minutes an hour, increasing the collection times to provide a sample representing longer time periods, but this may result in bias. For example, if aerosol concentrations vary over short intervals (e.g., gusty conditions exist), then this method may not adequately average those variations. The best alternative is to use a diluter, a device that dilutes the air stream so that a continuous sample may be collected while increasing the sampling time greatly. Common dilution ratios are 1/10 or 1/100, so representative sampling for one or more samples could be done for days or weeks without replacing the targets. Two different types of diluters are possible. The first type uses compressed air and requires an air source, but for the second type, no second air source is needed—the inlet air stream is split, and a fraction of it is filtered and then added back in to accomplish dilution. The TOPAS diluters available for the Dekati® instrument can dilute up to a factor of about 1:200, greatly extending the target replacement time. Dilution ratios are fixed by the manufacturer; in order to determine the appropriate dilution ratio (maximize sampling time without falling below the HRELPI+ sensitivity), it is necessary to run the

instrument without a diluter at the site and determine accumulation rate, and then order a diluter with the appropriate ratio.

Impactor cassettes: The unit comes with one cascade impactor cassette. If two cassettes are purchased, the targets can be replaced rapidly and easily onsite by swapping out a complete deck. One huge advantage of the HRELPI+ unit is that the accumulated mass is determined real-time via the charge transferred to each plate—hence, the target does not need to be pre-conditioned, pre-weighed, or post-weighed. It should be noted that the mass of the finest size fraction, collected on the HEPA filter, is not calculated, because particles smaller than 0.006 μm do not accumulate enough charge to be measured. Also, the mass of the particles that collect on the 10 μm cut is not monitored; to determine this, the 10 μm target will have to be weighed before and after use, as with a standard impactor.

Targets: Aluminum filters, coated with grease, are commonly used for the impactor targets. However, for chemical analysis, polycarbonate or Teflon® filters are recommended. They still must be greased to minimize particle bounce, and Apiezon-L grease, which is free of inorganic contaminants, is the best option. This can be purchased as a grease and diluted with acetone for application by painting or spraying on, or can be purchased as a pressurized spray can for convenient use. A template is also supplied, to avoid spraying the edges of the targets.

The system components and their power needs are listed in Table 4. A schematic of the assembled system is shown in Figure 29.

Table 4. Cascade impactor components and power needs.

Item	Function	Power needs
HRELPI+	Cascade Impactor (electrostatic)	110 V (200 watts) power pack AC-DC
Spare impactor and charger unit	For easily changing out impactor disks.	
Pump (dry scroll pump)	Required to pump air through the Impactor	100-127V (10 amp fuse); 700-800 watts at startup, <350 watts continuous
Dekati® Dryer (DD-603) setup for ELPI+ (runs off vacuum pump); TSP inlet replacing standard PM_{10} inlet. Includes roof flange for mounting inlet to instrument shelter	**Required.** ELPI+ unit requires RH <90%, to keep condensation from occurring in impactor. Also keeps targets from overloading as quickly.	Runs off of the vacuum pump
Diluter (Topas DIL 540 series with automatic dilution ratio adjustment to maintain set dilution ratio)	Dilutes the air stream to allow longer collection times without replacing impactor target.	110V low wattage (12 V DC via AC adapter).
Impactor targets (IPR-200, 100x25 mm) plus Apiezon-L spray (DS-515) Price for 5 packages of 100 each plus 1 DS-515 can of spray and 1 DS-125 spraying stencil.	Polycarbonate targets for chemical analysis of dust. Requires grease (DS-515) to prevent particle bounce.	—

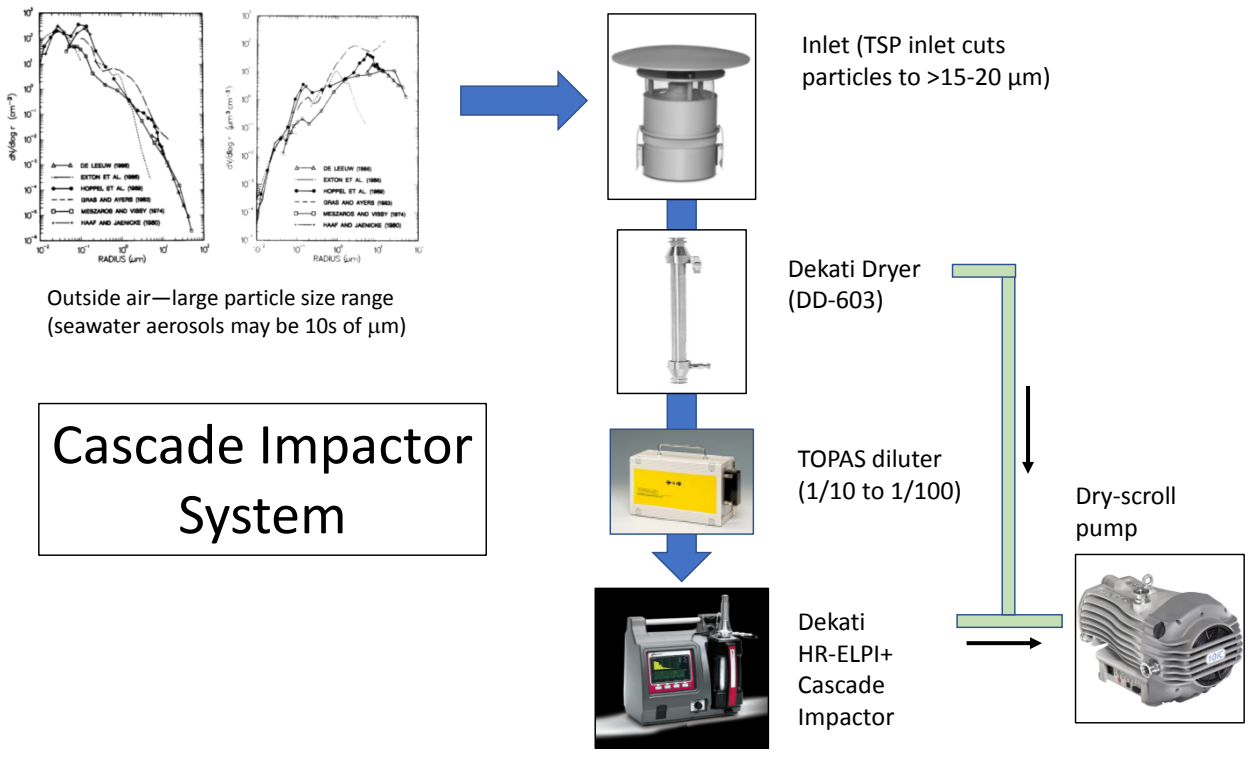

Figure 29. Schematic of cascade impactor system, with dryer and diluter accessories installed.

Onsite use/maintenance: Onsite use and maintenance will be performed by site personnel; frequency of maintenance is as yet unknown, as it will vary with site-specific parameters that have not yet been determined; however, the goal is to limit hands-on maintenance to weekly or biweekly events. Two impactor cassettes are purchased. An outside lab will prepare the targets, load one cassette, and ship to the site, where site personnel will switch the new cassette for the used one and send the used cassette back to the analysis laboratory. The laboratory will remove targets for analysis and replace with new ones, and then ship back to the CDFD site for next use. Additional maintenance that will need to be performed at the site includes periodically (potentially on a monthly basis) rinsing or wiping the inlet clean to avoid particle buildup, which would result in coarser particles entering the impactor. In high salt environments, the dryer will also have to be rinsed clean on a monthly basis. Rinsing the inlet and the dryer may require detaching and then re-attaching the tubing to the impactor.

Particle size spectrometer

Cascade impactors don't cover the full particle size range of interest for many applications. The range of particles that can enter the inlet for the cascade impactor is limited to 15-20 μm at the 10 Lpm flow rate of the impactor, and the size distributions will be for the dried equivalents of those. Because of the size limitations, cascade impactors are frequently coupled with other instruments that do particle sizing and particle density measurements. To complement the cascade impactor, a TOPAS LAP 322 Laser Aerosol Particle (LAP) Spectrometer will be used. It can size particles from 0.2 μm to 40 μm (0.2 to 5 μm or 0.7 to 40 μm) in 64-128 channels. This unit is ruggedized for environmental monitoring studies. Although it can sample relatively large aerosols, an inlet to remove extremely coarse particles is still required, and an additional Dekati® TSP inlet will be used. This inlet normally has a 15-20 μm cut size; however, because of the low flow rate through the LAP, it will have a larger cut size, estimated by Dekati to be 40-50 um. This is sufficient to entrain all anticipated sea-salt aerosols. The TOPAS LAP has its own internal pump, and so does not need a separate pump.

An automated switching valve is available for the TOPAS LAP, allowing sampling of two different air streams. We will use the switching value to sample the air stream below the TSP inlet, and then will run the air stream through a Dekati® dryer, which will dry out deliquesced sea-salt particles. The dryer is sufficient to dry out brine particles potentially as large as 40-50 μm at the relatively low flow rate (and hence, long residence time in the dryer) associated with the LAP. Then, the switching valve will be used to sample the air stream and dried aerosols below the dryer. This provides a complete particle size distribution for both the ambient air and for the dried particles. The scroll pump for the HR-ELPI+ is sufficient for the dryer on the LAP as well, so a separate pump is not necessary, as long as the two instruments are co-located. A humidity sensor will be installed at the outlet of the dryer to monitor the dryer performance. A list of the LAP spectrometer system components provided in Table 5, and a schematic of the system is given in Figure 30.

It should be noted that laser scattering spectrometers measure a "scattered light equivalent diameter", which is the diameter of a spherical particle with the same light scattering characteristics as the actual aerosol particles. This parameter is strongly affected by particle shape.

Onsite use/maintenance: As with the cascade impactor, the TSP sampling inlet will have to be periodically wiped clean to avoid overloading. The dryer must also be disconnected from the LAP and rinsed periodically.

Table 5. Laser particle spectrometer components and power needs.

Item	Function	Power needs
Laser particle sizer (TOPAS LAP 322 or 323)	Particle sizer capable of measuring particle sizes from 0.2 μm to 40 μm	110 - 230 VAC, 50-60 Hz; 12 VDC, 4.2 A
TOPAS SYS 520 automated switching valve	Would allow the LAP to sample more than one location (e.g., upstream and downstream of the dryer)	External AC adapter: 100-240 VAC / 24 VDC
Dekati® Dryer (DD-603) vacuum pump for cascade impactor); TSP inlet replacing standard PM_{10} inlet. Includes roof flange for mounting inlet to instrument shelter	Dries out deliquesced particles, allowing sampling of size distributions for deliquesced vs dry particles sizes	Requires vacuum pump for the cascade impactor.

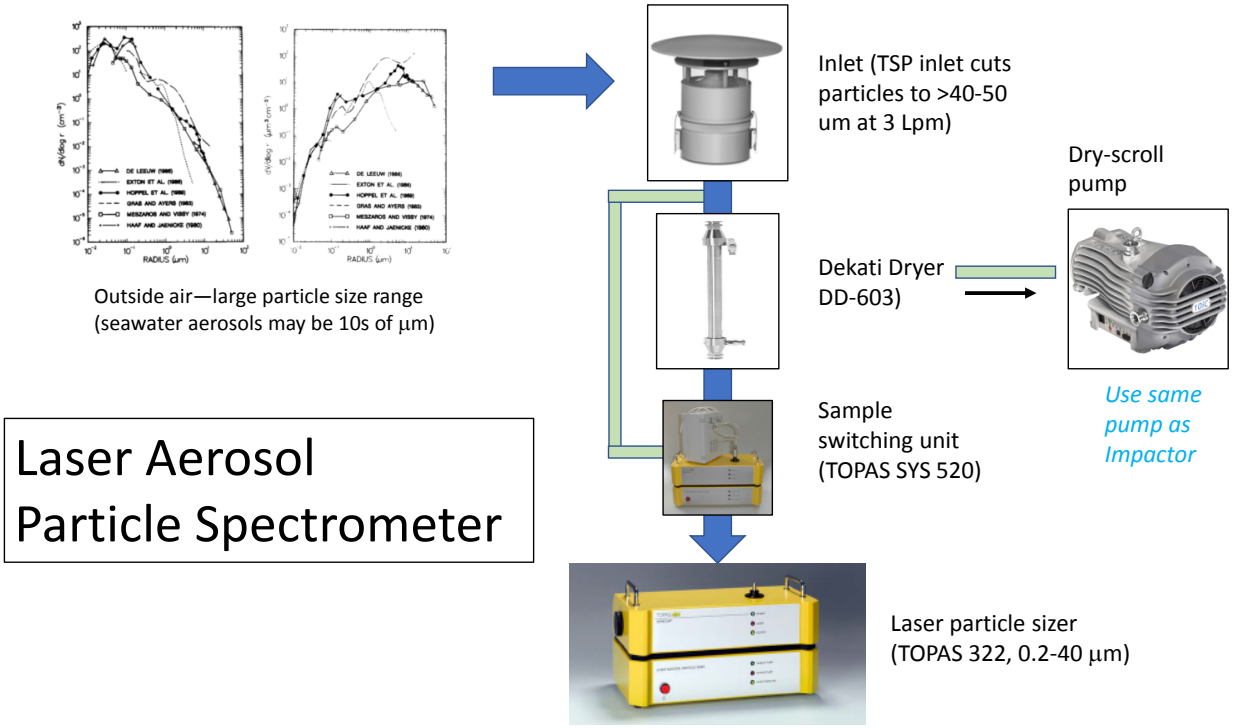

Figure 30. Schematic of laser aerosol particle spectrometer system, with dryer and sample switching unit installed.

The cascade impactor and LAP spectrometer will be co-located and must be protected from the weather; they will be housed within a small shelter. Because of the anticipated large particle sizes, horizontal tubing must be avoided; the particles could settle out within the tubing. Airflow will be vertically down from the inlets on the roof of the shelter to the cascade impactor and LAP spectrometer. The requirement for a vertical flow path limits how close to ground level the sample inlets can be placed.

Chloride Candle

The wet candle method, ASTM-G140-02 [66] is a widely used method for qualitatively measuring the corrosiveness of an environment by measuring chloride deposition rates onto a wet wick. The measured results are quantitative but can only be compared to other wet candle measurements because the deposition rates are a function of the geometry and the collection method; they are not representative of deposition onto any other surface. The design of a wet candle is described in ASTM-G140-02 and is shown in Figure 31. Exposure times vary, but 1-month intervals are frequently used. Following exposure, the salts are leached from the wick and other components of the wet candle and analyzed to determine chloride content. The results not only allow comparison with other sites, but also capture seasonal variations in chloride deposition. Chloride wet candle setups are commonly custom-made, using specifications outlined in the ASTM procedure or an equivalent ISO procedure.

Onsite use/maintenance: Site personnel will be required to switch out the wet candle with a fresh one on a periodic basis, probably monthly. The candle and flask will have to be disassembled, sealed, and shipped to Sandia for leaching and analysis.

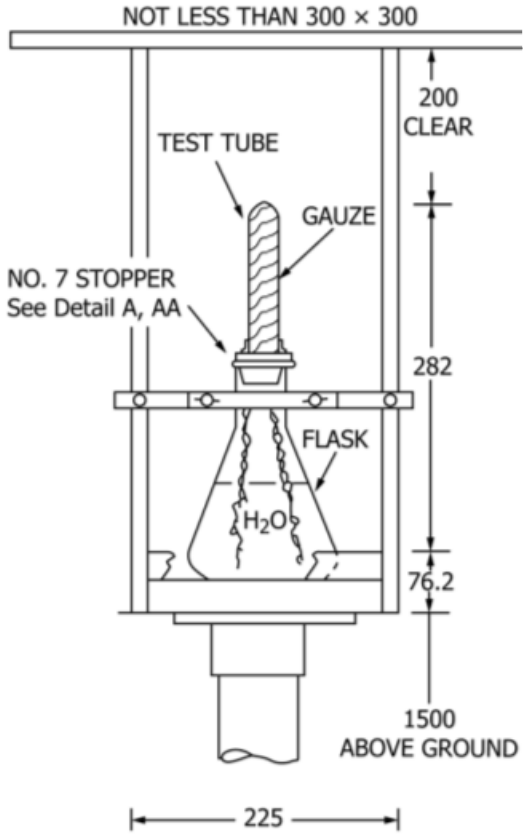

Figure 31. Schematic of a chloride wet candle.

2.3.2.3 CASTNET Atmospheric Monitoring

The Clean Air Status and Trends Network (CASTNET) is a long-term atmospheric monitoring program that is managed and operated by the U.S. Environmental Protection Agency (EPA) in cooperation with the National Parks Service (NPS), Bureau of Land Management (BLM), and many local partners. There are currently ~100 sites in operation across the U.S. (Figure 32). We have asked the CASTNET organization if they are interested in collecting data from our potential site, and they have tentatively accepted.

CASTNET sites use filter packs to measure the ambient concentrations of atmospheric gaseous sulfur and nitrogen species and particulate composition on a weekly basis; in addition, ozone can potentially be measured on an hourly basis. These analyses provide total suspended particle bulk compositions (no size discrimination) and acid gas concentrations via analysis of the filter pack collection system. The sample analytes for the CASTNET system are commonly the bulk cations (Ca^{2+}, Na^{+}, Mg^{2+}, K^{+}, NH_4^{+}), bulk anions (Cl^{-}, NO_3^{-}, SO_4^{2-}), acid gases ($HNO_{3(g)}$, $H_2SO_{4(g)}$, $SO_{2(g)}$), and ozone. As part of the CASTNET network, filter pack preparation and sample analysis activities will be carried out by CASTNET partners. Filter pack analysis will be provided by John Wood Group PLC (Wood). The data collected by this system will be analyzed using standardized measurement methods and will provide highly accurate information regarding composition of the atmosphere near the proposed ISFSI site.

Critical information that CASTNET will provide is the composition and concentration of acid gases in the atmosphere. The acid gas data provided by CASTNET monitoring will be used for thermodynamic modeling of salt and brine stabilities on heated canister surfaces; both particle/gas conversion reactions and brine acid degassing are dependent upon the background acid gas concentrations.

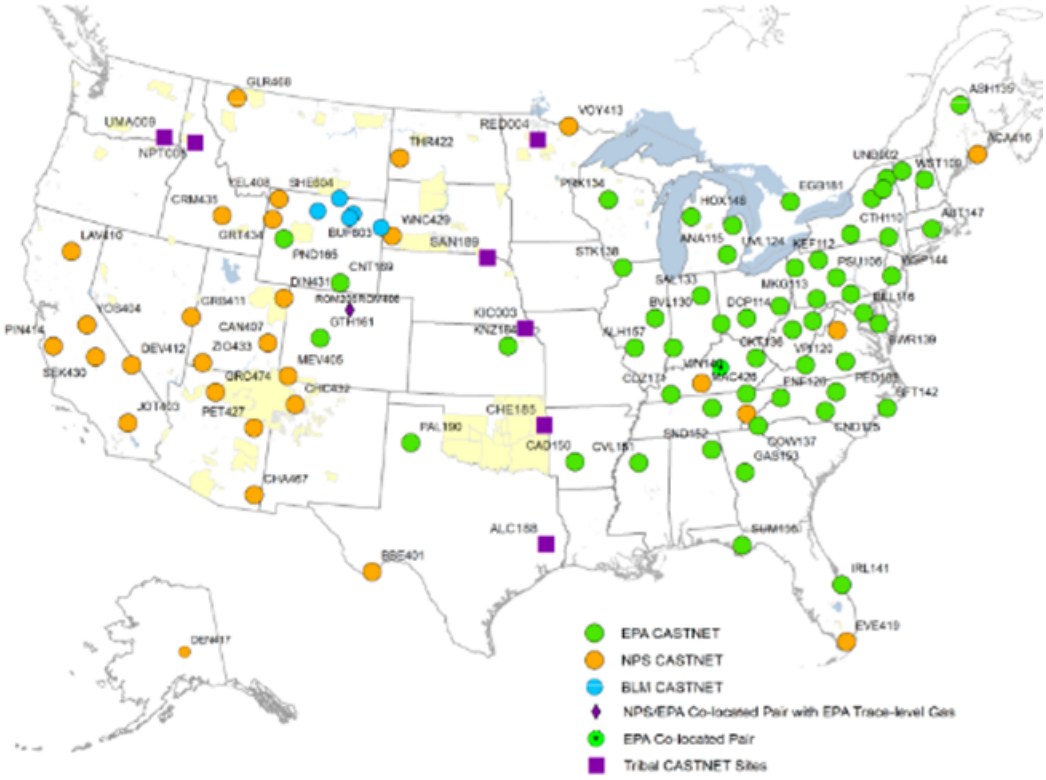

Figure 32. Map showing the location of CASTNET sites across the US.

At a typical site, the CASTNET towers are 10 meters high, with a 1-meter mast on top (Figure 33). The filter packs are installed at the top of the tower and are open-ended. To prevent the filters from getting wet, there is a rain shield installed and the filter packs face downwards. To replace the filters, the tower is hinged at a height of ~5 feet and can be tilted down to ground level. Power is required for operation of the pump to draw the air through the filters; the specific power needs for the tower are a few amps (110V).

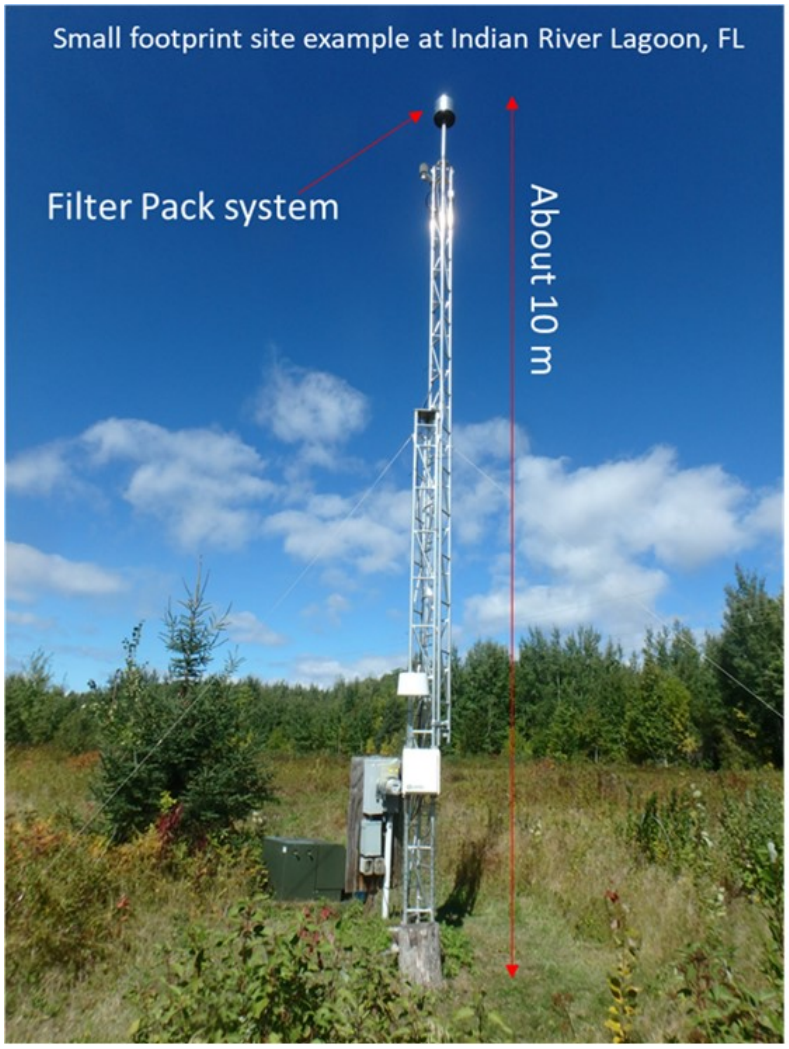

Figure 33. Photo of a CASTNET collection tower at Indian River Lagoon, FL.

The filter packs must be changed once per week, and this task will be performed by a local operator, who must first be trained by CASTNET/Wood. This task is easy and takes about 30 minutes. The CASTNET group will send out fresh filters every week, along with a return label. The operator will replace the used filter pack with the fresh filter pack, and then mail the used filter packs to Wood. There are no special storage or transportation requirements for these routine analyses; however, if additional analytes are desired, CASTNET/Wood can accommodate special storage/shipping requirements (e.g. ice) if necessary.

For analysis, the CASTNET sample/filter pack utilizes three different filters to provide the chemical composition and concentrations of the total suspended particulates and atmospheric gases. Specifically, the CASTNET filter pack consists of three sequential filters; typically, a Teflon filter, a nylon filter, and a Whatman filter impregnated with potassium bicarbonate and glycerol. Each filter has a specific purpose, targeting the collection of various analytes (Figure 34). The Teflon filter collects particulates and is analyzed for bulk cations (Ca^{2+}, Na^{+}, Mg^{2+}, K^{+}, NH_4^{+}) and bulk anions (Cl^{-}, NO_3^{-}, SO_4^{2-}). The nylon filter collects the acid gases HNO_3 and H_2SO_4. The Whatman filter collects residual gaseous SO_2. Cations are analyzed by ICP, while anions are analyzed by IC. Figure 35 shows an example CASTNET data set (truncated here to only show the ions), generated by analysis of the filter packs. Wood claims to be able to accurately analyze sample sizes as little as 1 µg.

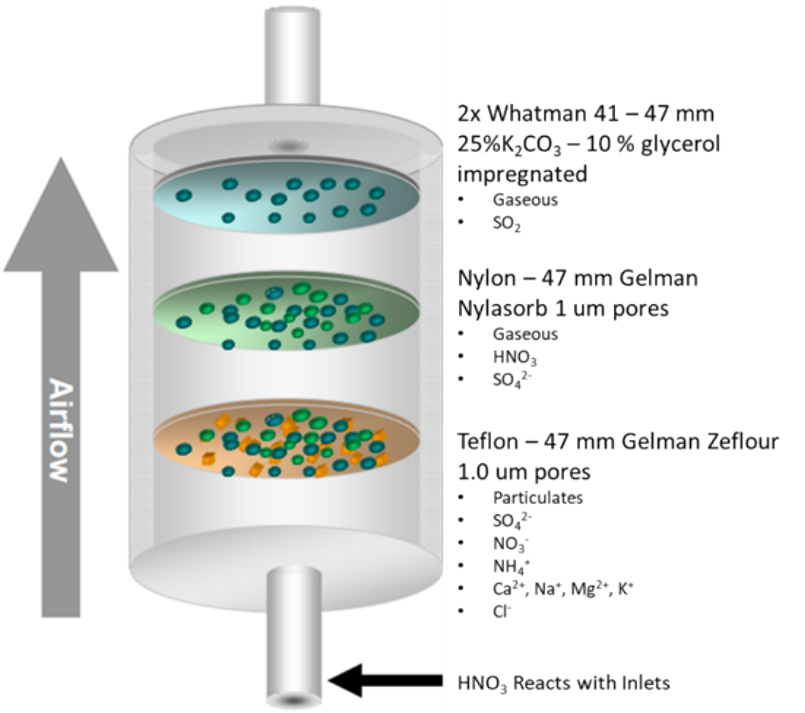

Figure 34. Schematic showing the analytes collected on each filter of the filter pack used in the CASTNET system.

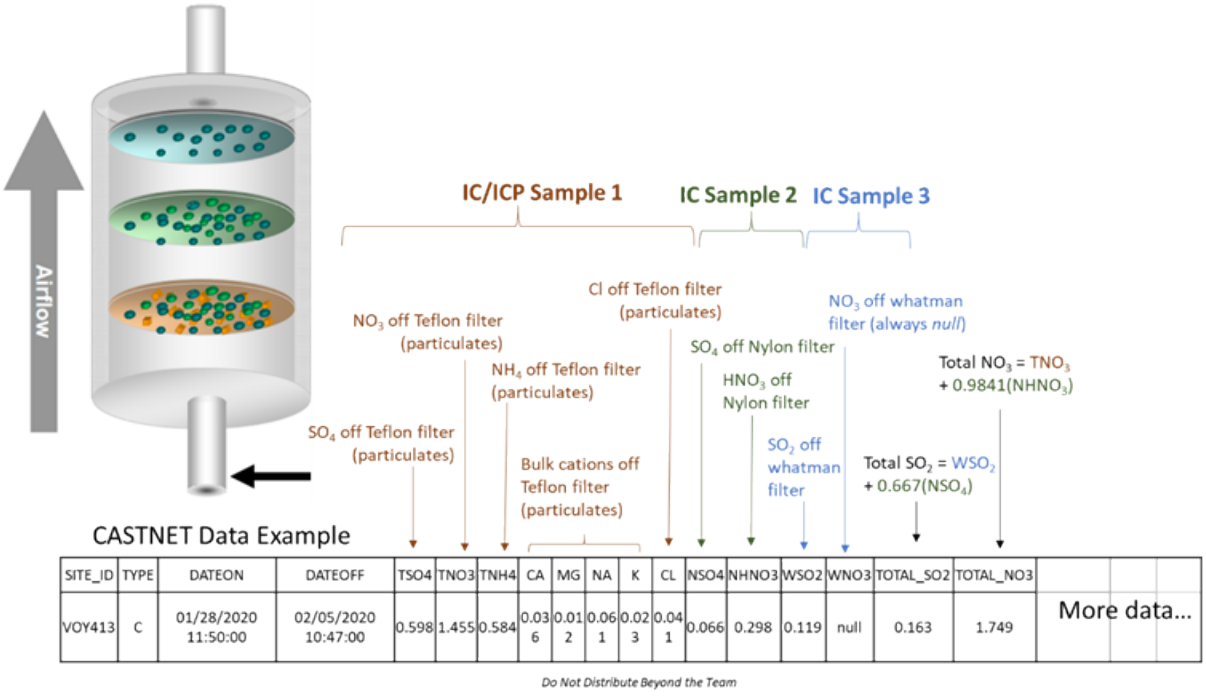

SITE_ID	TYPE	DATEON	DATEOFF	TSO4	TNO3	TNH4	CA	MG	NA	K	CL	NSO4	NHNO3	WSO2	WNO3	TOTAL_SO2	TOTAL_NO3	
VOY413	C	01/28/2020 11:50:00	02/05/2020 10:47:00	0.598	1.455	0.584	0.036	0.012	0.061	0.023	0.041	0.066	0.298	0.119	null	0.163	1.749	More data...

Do Not Distribute Beyond the Team

Figure 35. Example CASTNET output shown with sample analyses.

The CASTNET system and tower are built to order. The overall material and lead costs are about $20K, and the sample analysis costs about another $20K per year. The typical lead time for the tower is ~10-12 weeks and they must be shipped from Florida to the sampling site. In addition to analysis of the CASTNET filters, Wood are willing to consider preparation of cascade impactor cassettes, and analysis of the used impactor targets; discussions are ongoing.

Onsite use/maintenance: Onsite personnel must be trained by CASTNET/Wood on how to remove and replace the filter packs from the CASTNET tower and must be available to do so on a weekly basis. The spent filter pack must be then sent to Wood for analysis.

2.3.3 Measuring Canister Surface Roughness

In preparation for use, prior to initiation of the CDFD, all three of the CDFD canisters were inspected for possible SCC using non-destructive examination (NDE) techniques, including dye penetrant and eddy current array techniques. In addition, the entire surface of one canister was photographically mapped on a fine scale, and the surface topology of the same canister was mapped using laser line surface scanning, to produce a 3D map of the upper 2/3 of the canister, with a feature resolution of approximately 100 μm. However, the surface of the canister had many visible grind areas, that were not adequately discriminated by the laser mapping. To evaluate the macro-level features on the canister surface at a higher resolution, the local surface roughness of the canister will be measured. Conventional methods to measure the roughness of a surface, such as profilometry, generally require the sample to be placed on a sample stage. For the SNF canisters, due to apparent size limitation, this is not possible; instead, SNL is working to develop a method to produce replicas of selected areas of the surface using surface casting materials. These surface replicas can then be analyzed by profilometry to determine the surface roughness of the canister. The goal of this test is to evaluate both the nominal surface roughness of the canister and that in select areas (e.g., weld regions and ground areas) to correlate canister roughness to visible features. If surface sampling or inspections carried out for the CDFD project determine that surface roughness plays a role in dust deposition or corrosion, these data may be necessary for developing or parameterizing models for those processes.

2.3.3.1 Sample Cell for Canister Measurements

In order to make casts at any possible location on the canister surface, a sample cell was designed that would adhere to the canister surface, and then be filled with the molding material *in situ*. Based upon the surface features of interest for this sampling technique (to supplement the laser line scan mapping), the sample cell window was created to be 25.4 mm (1 inch) in diameter. This allows for profilometry methods that can determine micron-sized features to measure the entire area within a reasonable amount of time (e.g., several days). A Solidworks drawing of the sample cell is shown in Figure 36. During use, an adhesive gasket with a cutout for the sampling window is applied to the bottom the cell, and it is adhered to the canister surface. Then, the molding material is mixed and transferred to a 10 mL syringe. The syringe is connected to the sample cell inlet via tubing, and the molding material is injected into the sample cell until the sample cell is filled and a small amount escapes through the overflow outlet. The material is allowed to fully cure in place, and then the gasket and sample cell are carefully peeled off the canister surface and the puck with a negative replica of the surface in the sample window is removed (Figure 37).

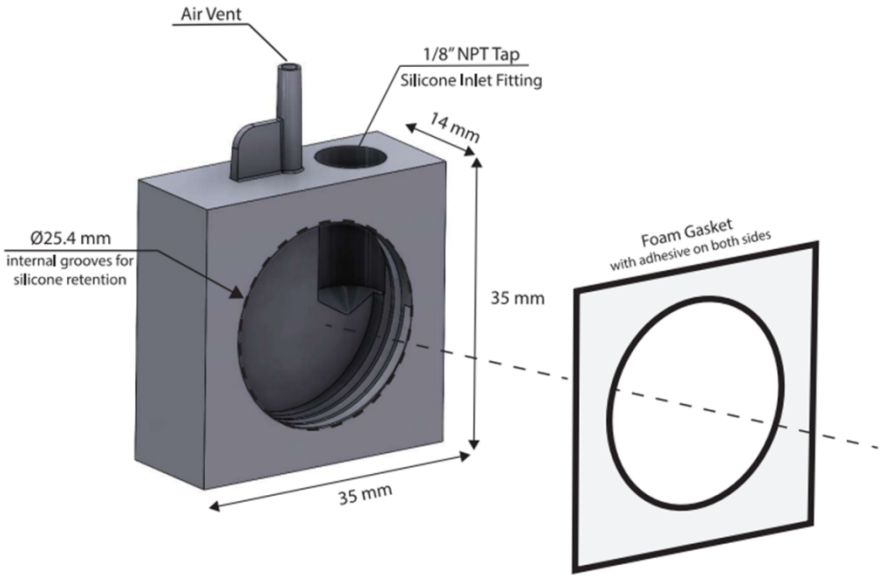

Figure 36. Solidworks rendering of the surface replicator cell showing the features and dimensions.

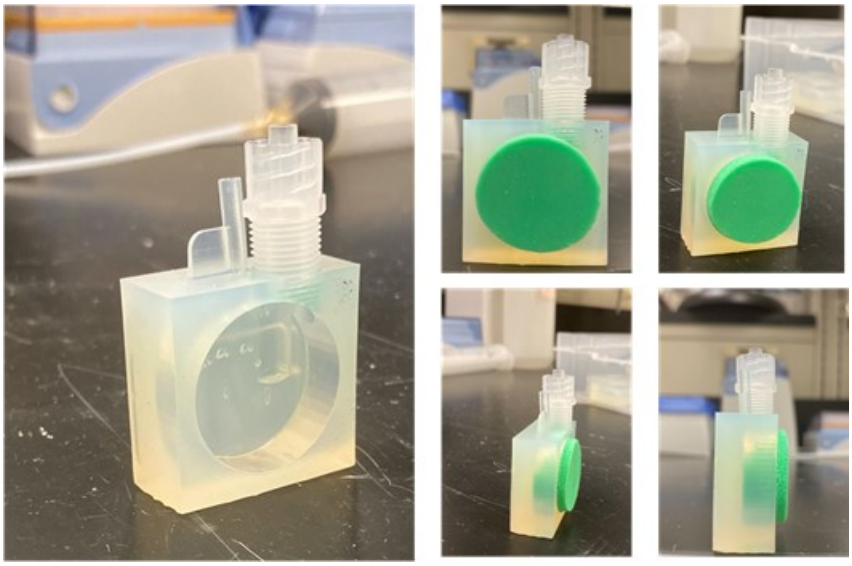

Figure 37. Images of the surface roughness sampling cell. Shown empty (left) and with PlatSil 73-25 silicone rubber following 24 hours of curing on a SS surface.

2.3.3.2 Initial Material Testing

Several materials from Polytek and 3M were tested as possible molding materials (Table 6). Initial testing evaluated both usability and ability to replicate the surface. It was immediately obvious that the Polytek Brush-on 35 Rubber was not effective for this application. When it was applied by brushing it onto the surface, it did not successfully replicate the surface; therefore, it was eliminated from consideration. PlatSil 73-25 is a 2-part silicone that, when mixed, forms a viscous fluid that can be poured into a retaining structure (such as the cell in Figure 37) on the metal surface. After curing (~5 hours), PlatSil 73-25 was easy to remove from the surface; a release agent was not needed. Experiments

were carried out to determine the impact of a thickening agent on the PlatSil 73-25 and demonstrated that the more thickening agent used, the softer the resulting cured silicone rubber. Also, the resulting surface mold contained bubbles, and the number of bubbles increased with the percent of the thickening agent added. Overall, PlatSil 73-25 performed best when no thickening agent or release agent was added (Table 6). The last material evaluated was 3M Express STD VPS Impression Material Putty. This material was extremely easy to use, as it could be mixed by hand and cures rapidly (~5 mins), and after curing, the putty was easy to peel off the metal surface. Following initial testing, two materials were considered for further analysis, the PlatSil 73-25 silicone rubber (Polytek) with no release agent or thickening agent, and the Express STD VPS impression Material Putty (3M).

Table 6. Description of the materials considered for the surface replication for determining surface roughness.

Product	Material	Color	Release Agent	Thickening Agent	Shore Hardness	Pour Time	Mixed Viscosity	Result
Polygel Brush-On 35 Rubber	Polyurethane	Light Blue	Pol-Ease 2300	N/A	A35	10-15 min	Medium Thixotropic	Poor surface replication
Polytek PlatSil 73-25 Silicone Rubber	Silicone	Lime Green	N/A	N/A	A25	15 min	6000 cP	Good
Polytek PlatSil 73-25 Silicone Rubber	Silicone	Lime Green	Pol-Ease 2500	N/A	A25	15 min	6000 cP	No need for release agent
Polytek PlatSil 73-25 Silicone Rubber	Silicone	Lime Green	N/A	PlatThix	A25	15 min	6000 cP + thickening	Thickening agent caused softening and bubbles
Polytek PlatSil 73-25 Silicone Rubber	Silicone	Lime Green	Pol-Ease 2500	PlatThix	A25	15 min	6000 cP + thickening	No need for release agent and thickening agent caused bubbles
3M Express STD VPS Impression Material Putty Refill	Vinyl polysiloxane	Light Brown/Off white	N/A	N/A	?	3-5 min	Variable	Good

2.3.3.3 Initial Profilometry Assessment

After down-selecting to the two most promising candidates, the next step was to determine if the samples could be analyzed by profilometry and to quantify how well the two materials replicated the SS surface. For these tests, a small piece from the SNL mockup canister was analyzed by both laser confocal microscopy (Keyence VK-X150 Laser Scanning Microscope) and stylus profilometry (DekTak) to determine the average surface roughness ($R_{a)}$ value and map the surface. The molding materials were applied to the SS surface, allowed to cure, and peeled off. Then the molded replicas were analyzed using the two characterization techniques. The results for the PlatSil 73-25 and Express STD VPS materials are compared to the original coupon in Figure 38. The molds are the negative of the actual surface, shown by the differences between the positive and negative features in the SS coupon and the molding materials. While both molding materials successfully captured the surface features, the Express STD VPS material exhibited large numbers of bubbles that had formed on the metal surface. These artifacts, in addition to incorrectly representing the surface, impact the estimation of the R_a; therefore, the Express STD VPS material was ruled out from consideration. The PlatSil 73-25 performed better, replicating the surface well and forming no bubbles. It was carried forward for further testing with a surface roughness calibration standard.

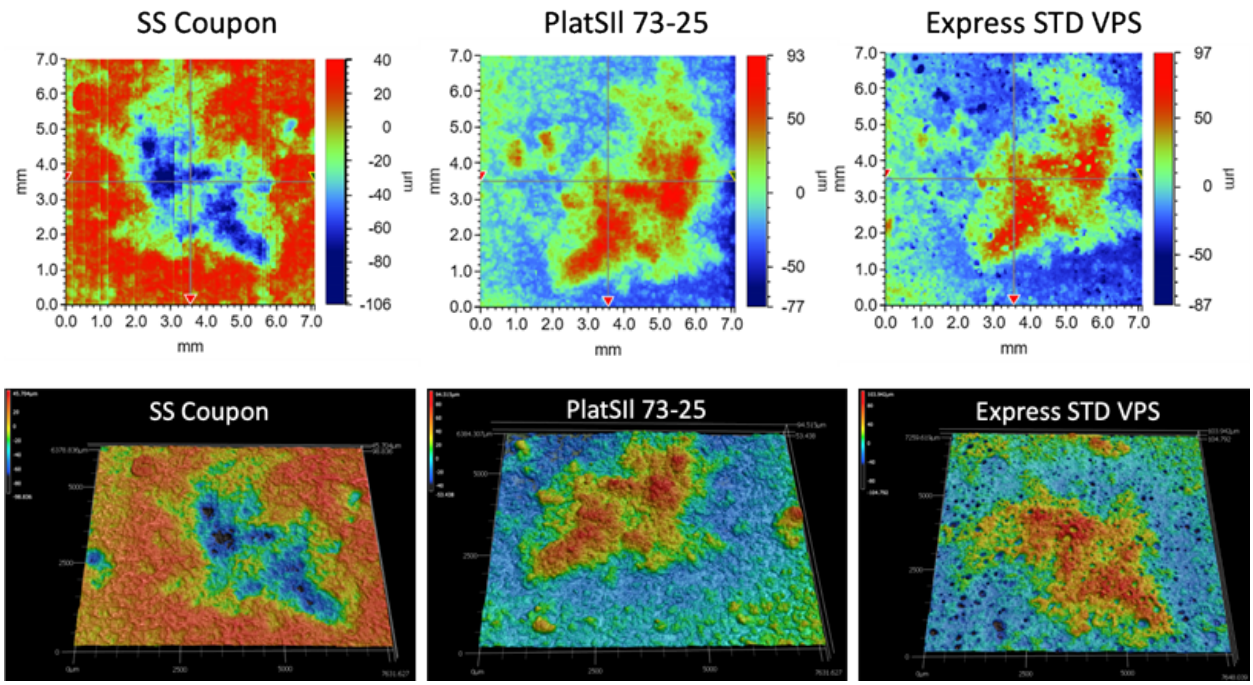

Figure 38. Results of stylus profilometry (top) and laser profilometry (bottom) showing the SS coupon compared to the negative impressions made by PlatSil 73-25 and Express STD VPS.

2.3.3.4 Verification of the Effectiveness of PlatSil 73-25 with a Surface Roughness Standard

The ability of PlatSil 73-25 silicone rubber to replicate a surface was verified using a surface roughness standard (SPI Microsurf 326- Linishing). The standard had six regions, each with a different surface roughness. The surface roughness standard is a 2-D standard with grooves in one direction; therefore, the roughness was measured perpendicular to the grooves. The analysis was performed using a 658 nm laser with a Z-resolution of 5 nm and spatial resolution of 230 nm. For analysis, the 20X objective lens was used to characterize the roughness, and the roughness was determined via a line analysis at several transects across the grooves. PlatSil 73-25 was applied across two sections corresponding to R_a = 1.60 µm and R_a = 3.2 µm (Figure 39), and both the standard and the replica were analyzed by laser profilometry and compared.

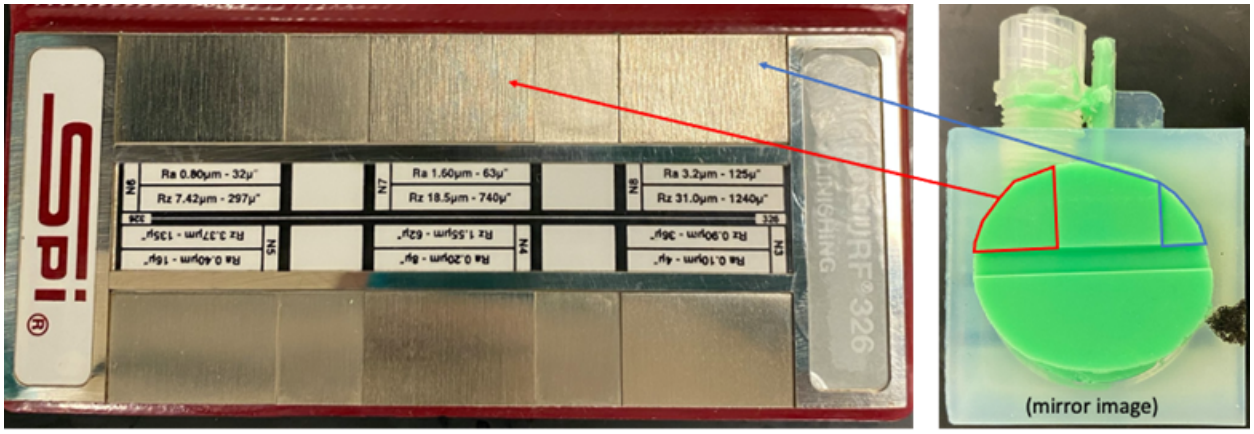

Figure 39. Verification test of the PlatSil 73-25 using the SPI Mircosurf 326 (Linishing) standard replicating the R_a = 1.60 µm (circled in red) and R_a = 3.2 µm (circled in blue).

Overall, the PlatSil 73-25 performed adequately in replicating the two surfaces to a nominal degree of accuracy (Figure 40). The surface roughness standard was measured directly, at the R_a = 1.6 µm and R_a = 3.2 µm locations as a calibration check of the Keyence microscope. The measured values systematically higher than the expected value listed on the standard. The measured value for the R_a = 1.60 µm region was 2.42 µm; this was less accurate than the measured value for the R_a = 3.2 µm surface, which was 3.878 µm. The source of these differences is unclear; however, analysis settings may need to be adjusted, or the number of measurements may need to be increased to improve the accuracy. The PlatSil 73-25 measured values were systematically higher than the measured surface roughness standard; for the R_a = 3.2 µm surface, the measured value for the silicone rubber was 4.18 um. For the R_a = 1.60 µm surface, the measured value was 2.89 um. It is not unexpected that the PlatSil 73-25 was able to more accurately replicate a rougher surface, as the viscosity of the mixed rubber (~6000 cp – similar to molasses) may not be low enough to fully penetrate the smaller surface features.

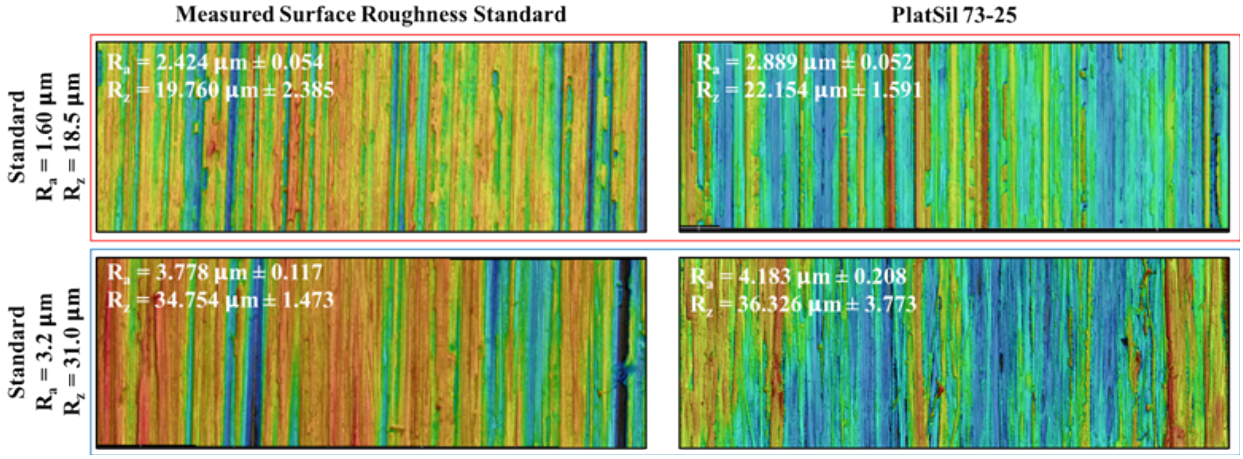

Figure 40. Laser profilometry measurements of the surface roughness standard and PlatSil 73-25.

Overall, the PlatSil 73-25 systematically overestimated the surface roughness by a significant amount, with the error increasing as the Ra decreases (Figure 41). However, on a surface with coarser features like the canister, it should give a good estimate of the surface roughness. It is expected that features on the milled metal surface and in ground areas on the canister surface are > 3.2 µm deep; therefore, the PlatSil 73-25 should be effective at documenting the surface roughness in sufficient detail for future incorporation into corrosion or dust deposition models.

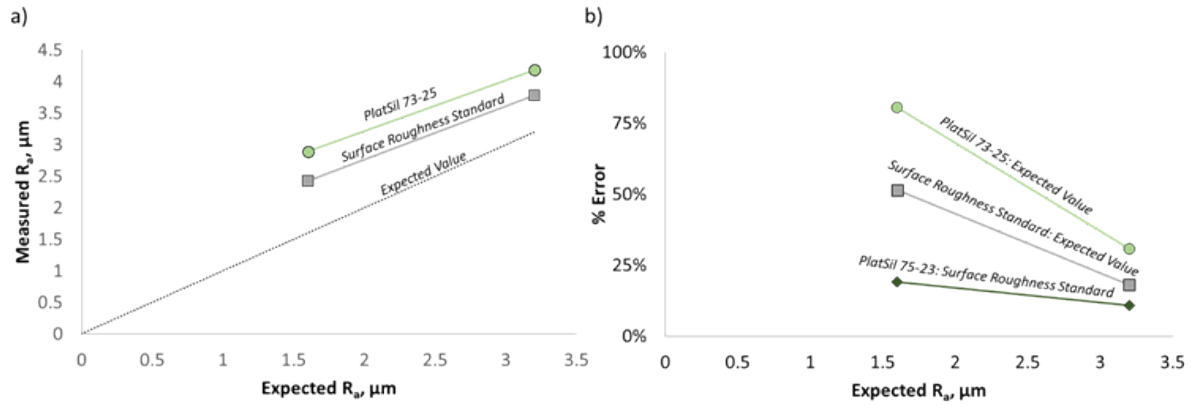

Figure 41. a) Measured R_a versus the expected R_a (as determined from the surface roughness standard) for the measured surface roughness standard and for PlatSil; b) the %error in the roughness measurement of the measured surface roughness standard and PlatSil 73-25 relative to the expected value, and the PlatSil73-25 relative to the measure surface roughness standard.

2.3.3.5 Canister Measurements

In FY22, SNL will collect surface molds from one of the SNF canisters used for the CDFD campaign. The locations will be carefully documented (measured and photographed) to track location to surface roughness. No effort will be made to collect roughness samples that correspond to dust sampling locations – that is not the goal of the surface roughness measurements. Instead, several locations will be chosen on the canister surface to (1) represent the normal mill-finish surface roughness, and (2) surface roughness differences caused by grinding or other mechanically-induced surface damage; these are frequently associated with welded regions. This information will eventually be used to support canister corrosion or dust deposition models.

2.3.4 Canister Markings

As described in Section 2.3.1, the surfaces of the three dry storage canisters used in the CDFD project will be sampled for dust and salts (Figure 22). At each sampling location, a grid will marked on the metal surface, and over several years, different squares within the grid will be sampled according to a predetermined sampling plan (Figure 23). In order to accurately locate the sampling locations and grid cells over several years, the canister surface must be marked. The most appropriate marking method for the canister surfaces is currently being evaluated. The mark must meet the following requirements:

- It must be able to withstand high temperatures, up to 200 ºC, for up to 10 years on the heated canister surfaces.
- It should not actively promote corrosion or decrease the corrosion resistance of the metal surface.
- It should not significantly affect air flow over the surface, which could have an effect on dust deposition rates.

One possible solution is to mark the sampling areas by scribing the metal surface. However, such a mark will change metal surface stresses and is likely to promote corrosion and possibly SCC. Scribing is not an ideal solution, but may be the default method, if an alternative permanent marking method cannot be identified. Two alternative approaches are currently being evaluated. The first is a spray-on high-temperature epoxy primer used for automotive engines, designated VHT® Hi-Temp Engine Enamel 550°F (288°C). The second is a SS blackening agent made by Caswell Inc. (part number SSB370); this material is a gel-like liquid that is brushed onto the metal surface. After application and removal of the

gel, a sealer (Caswell Sealer), must be applied. The blackening agent contains corrosive compounds (HCl), so the steel surface must be carefully cleaned after application to ensure that all chloride is removed.

Each marking material will be exposed to three different environments to determine if it is effective: (1) at 200 °C in an oven, observing periodically to determine if the marking degrades or peels; (2) in a RH chamber at a temperature of 50 °C and an RH of 40%, to evaluate marking degradation or potential marking-related corrosion; and (3) coated with sea-salt aerosols, and then aged at 50°C and 40% RH. Under these conditions, the metal will corrode; the goal of the test is to evaluate potential enhancement of corrosion due to the markings (e.g., crevice corrosion under the enamel), and to further evaluate potential marking degradation or peeling.

2.3.4.1 Test Samples

In order to test the marking materials, two sections of the SNL canister mockup [67] are being used. The mockup materials are arcuate sections of SS304L with a mill finish—similar to the CDFD canisters. Prior to use, the metal sections were thoroughly cleaned with soap and water, rinsed with deionized water, and then cleaned with isopropanol, and allowed to dry overnight. There was still some minor brown staining on the metal, probably due to corrosion that had occurred during years in storage (Figure 42-a). For the CDFD canisters, the sampling grid will be applied using a template, so the same approach was used here. A test template of open squares was made by laser cutting adhesive-backed printer paper, and two copies of the template were then applied to the each of the mockup sections (Figure 42-b). In addition to the mockup plates, each marking material was applied to two polished SS304 coupons (four total); these provide a smoother surface for assessing possible coating-related corrosion damage (Figure 42-c).

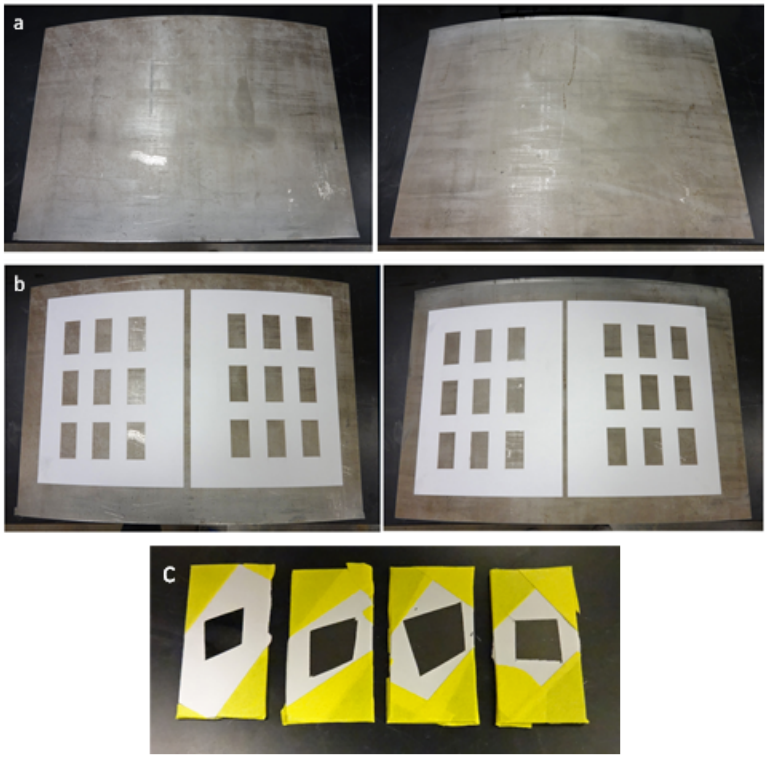

Figure 42. Metal Sections of the Sandia Mockup used to test marking materials for the CDFD field project. a) cleaned plate; b) applied templates; c) hand-masked SS304 coupons.

2.3.4.2 *Applying the Marking Materials.*

After applying the templates, a plastic skirt was added to isolate one side of the first mockup plate for testing the spray enamel. The plastic prevented over-spraying, protecting the second template for testing the blackening agent. The spray enamel was applied using the recommended procedure. One light coat was applied, followed by a 10-minute wait. Then, a second light coat was applied and after another 10-minute wait, a final medium coat was applied, followed by at least a 30-minute drying period; the actual drying period was one hour. Two of the four masked coupons were also sprayed. The engine enamel applied easily and uniformly and dried to form a smooth gray layer.

The second template, and the two additional coupons, were coated with the blackening agent. The blackener resulted in immediate darkening of the metal surface on the mockup plates but did not darken the polished coupons. After allowing to react for 1-5 minutes (each line of rectangles in the template was subjected to a different treatment time), the blackening agent was washed off and the sealer was applied. After thoroughly washing off the sealer, the plate and coupons were allowed to dry, and the adhesive templates were removed.

Removal of the adhesive template proved to be problematic; the adhesive adhered strongly to the metal (especially the polished coupons) and was not readily removed. The plate and coupons are shown in Figure 43, immediately after removing the templates. The overall quality of the sprayed markers was very good. The spraying was even, and the paint appeared to stick to the metal plates well, with very sharp edges to the applied marks. The blackened areas were also sharp-edged—perhaps surprising, since the blackening agent wetted the mask thoroughly. Apparently, it did not penetrate the adhesive underneath. The entire plate was scrubbed with a sponge in an effort to remove the remaining adhesive from the template. Scrubbing did not affect the enamel, but did remove some of the blackening agent, revealing shiny, etched metal underneath (Figure 44-a). The scrubbing was ineffective at removing the adhesive.

For the polished coupons, the enamel adhered well. However, the blackening agent did not blacken the metal, and after thoroughly cleaning with acetone to remove the template adhesive, it was apparent that the blackening agent, even after a short contact time, had pitted the SS304 (Figure 44-b). Because of the evidence of etching on the mockup plate material and on the coupons, the blackening agent is no longer considered a possible choice for marking the CDFD canisters.

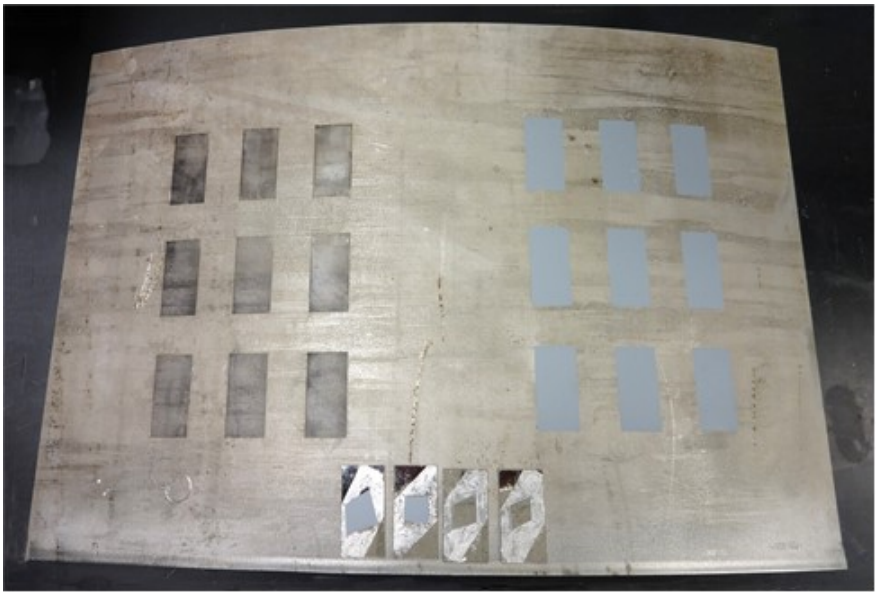

Figure 43. Coatings, immediately after removing the templates.

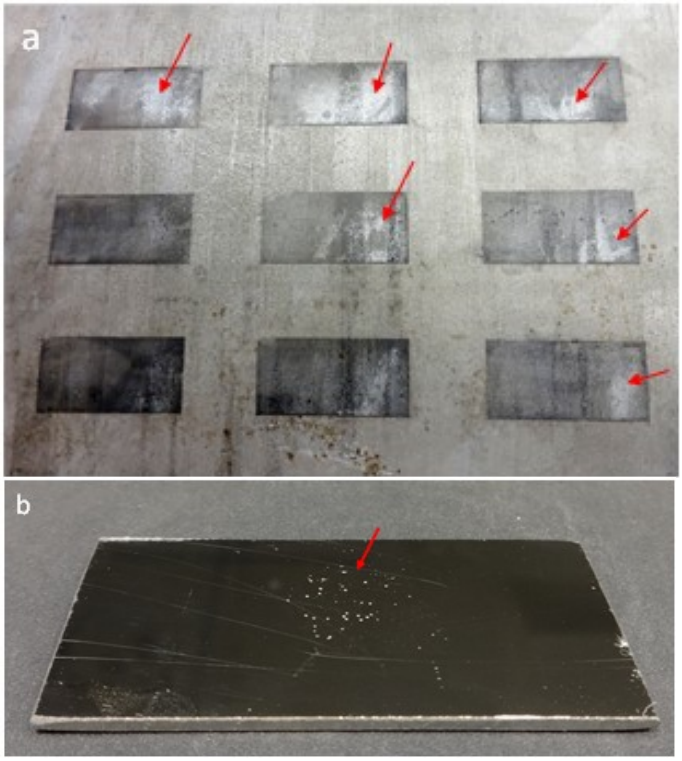

Figure 44. Effect of using the Caswell blackening agent. a) mockup plate: blackened marks were partially removed upon scrubbing, revealing shiny, etched areas underneath. b) polished coupon: showing pitting on the surface that had been exposed to the blackener.

Removal of the adhesive proved to be extremely difficult. Water and soap had little effect, and even alcohols proved ineffective. Ultimately, a citrus oil-based cleaner was used, which required heavy scrubbing, and appeared to slightly react with the engine enamel.

Templates were also applied to a second plate and spray enamel markings were applied. The blackening agent was not applied to this second plate, given the damage it caused to the first plate.

After cleaning, the mockup plate containing the patterns of both markers was placed in a 200 ºC oven for two weeks—modeling suggests that surface temperatures of the hottest of the three CDFD canisters will be in this range. The results are compared with the second plate in Figure 45. The marks made by the blackening agent, already eliminated from consideration, had completely faded. The engine enamel, although rated for higher temperatures than 200 °C, showed evidence of degradation, and had changed color, becoming much paler. Upon rubbing with a finger or a wad of paper, much of the mark was enamel and was easily removed from the surface (Figure 46).

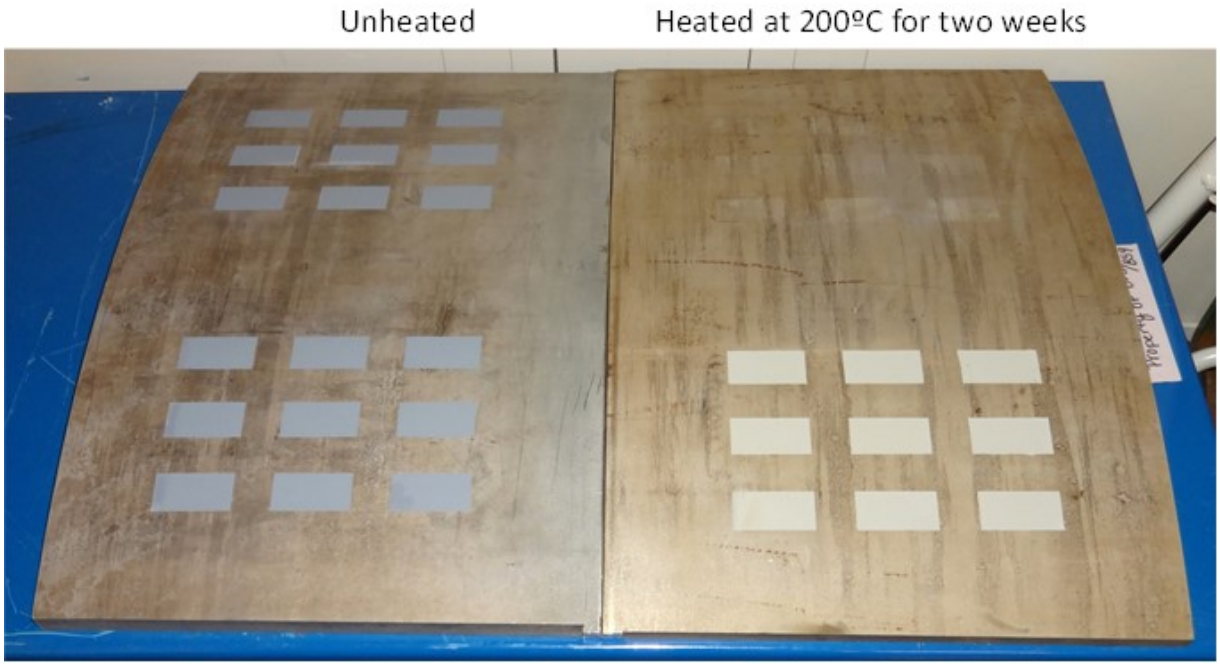

Figure 45. Comparison of marks on unheated mockup plate with marks on a plate after 2 weeks of aging at 200 ºC.

Figure 46. Degradation of the enamel markings after two weeks at 200 ºC.

It was speculated that the citrus-oil based cleaner may have damaged the enamel, so a second plate was sprayed. This time, removable ID labeling paper (Avery 6470) was used to make the template rather than the adhesive printer paper. This worked well—the paper peeled readily off the metal surface, leaving no residue behind. The new plate was aged in the oven at 200 ºC for two weeks, and the enamel markings fared better. They still lightened, and it was still possible to wipe off some of the paint with mild rubbing, but much less was removed.

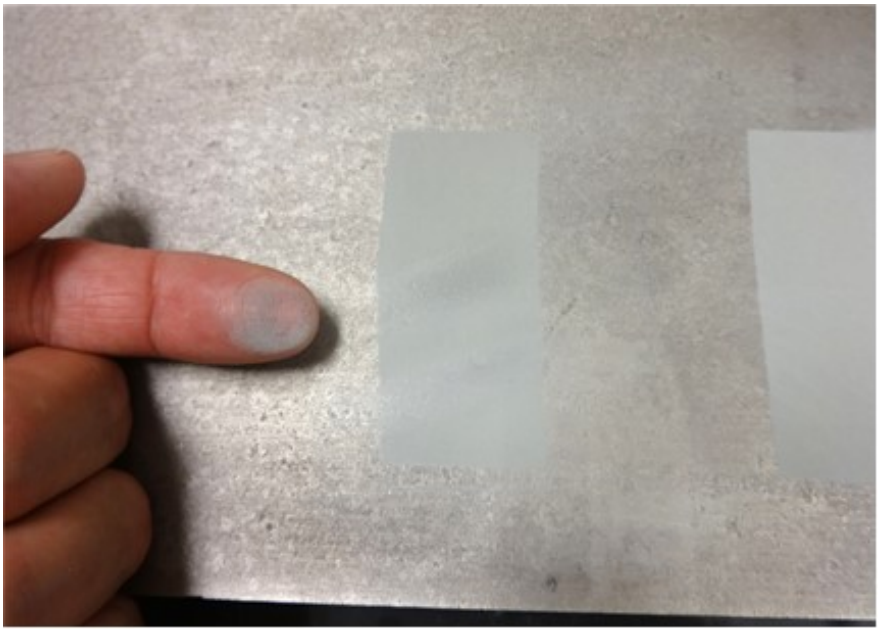

Figure 47. Degradation of the enamel markings after two weeks at 200 ºC.

Future testing: At this point, it is not clear if the engine enamel is sufficiently robust to withstand the maximum expected canister surface temperatures of ~200 ºC. Additional, longer term testing is required. Moreover, additional testing is necessary to determine if the enamel markings cause or contribute to corrosion processes on the metal surface. Should the engine enamel prove unacceptable, other marking methods will be considered.

3. Canister Corrosion: Pitting and Pit to Crack Transition

As discussed in the sections below, much effort in FY21 focused on refining our understanding of environmental factors controlling pitting and on the factors controlling the transition an actively growing pit to a stress corrosion crack.

3.1 Effect of Brine Composition on Pitting and Pit to Crack Transition

As reported in FY20, Weirich et al. [68] and Srinivasan et al. [69] explored SS304 pitting under sea-salt brine droplets for one year in controlled atmospheric exposures, and found that pit morphology was highly dependent on the exposure RH. At a lower exposure RH (40 %) pits displayed an irregular, cross-hatched morphology with fissures resembling microcracks. However, at higher RH (76 %) pits displayed crystallographically faceted ellipsoids with no associated microcrack-like fissures or irregular morphology. As brine composition is highly dependent on RH, it was suggested this played an influential role in determining susceptibility to pitting, microcracking, and possible eventual SCC. In FY21, a manuscript exploring pit morphology at longer exposure times was published (Appendix A) [69]. Further research continued to explore the driving force for variations in pit morphology as well as microcrack initiation and formation, including influences of brine composition, morphology (water layer thickness and distribution), and evolution with corrosion. The current research has elucidated some of the contributing factors, such as specific components of the brine that influence microcracking, and will be discussed herein. Also, in FY21, investigations into potential brine influences on pit to crack transition, in part through morphological effects on pitting, were initiated and detailed below.

3.1.1 Effects of Brine Composition on Pit Morphology

From work carried out in FY19 and FY20, it became apparent that SS304 specimens exposed at a lower relative humidity exhibit more irregular pits, crosshatching, and increased microcracking which was hypothesized to be due to the presence of high concentrations of Mg^{2+} ions in the brine. In FY20, full immersion experiments on SS304 coupons were explored to isolate the effects of brine composition, by essentially removing the cathodic limitations observed in atmospheric exposures [3]. In bulk exposures, potential cathode limitations may arise due to changes of the brine composition/conductivity, whereas in atmospheric exposures, cathode limitations are due to water layer thickness or droplet size, and brine distribution, although changes in brine composition and conductivity may also occur. Isolating some of the exposure variables by use of full immersion exposures helped to better understand the controlling factors for pit morphology development, especially in the $MgCl_2$ - rich brines of interest. This was continued in FY21, and, formed the basis of a manuscript under preparation that explores the effects of surrogate and equivalent sea-salt brines on pitting in SS304 coupons. Sample coupons (with a #4 uni-directional mechanical surface finish) were exposed for 24 hours to 7 weeks at 35 ^{o}C in surrogate brines to explore the potential roles of the cations in the brine compositions provided in Table 7 and Table 8.

Table 7. Composition of NaCl-rich brines examined in this study. pH values and ionic concentrations indicated were calculated using the EQ 3/6 software.

Solution	pH	$[Cl^-]$/M	$[HCO_3^-]$ /M	Relevance to sea-salt brine
76% RH sea-salt brine	7.61	5.009	5.73×10^{-3}	76% RH brine
5.22 M NaCl	5.18	5.22	5.09×10^{-6}	Concentration of NaCl matching that in 76% RH sea-salt brine
5.22 M NaCl + 0.1 M $MgCO_3$	8.61	5.22	7.29×10^{-3}	Concentration of NaCl matching that in 76% RH sea-salt brine, excess $MgCO_3$ added and equilibrated with air.

Table 8. Composition of $MgCl_2$-rich brines examined in this study. pH values and ionic concentrations indicated were calculated using the EQ 3/6 software.

Solution	pH	$[Cl^-]$/M	$[HCO_3^-]$ /M	Relevance to sea-salt brine
40% RH sea-salt brine	6.85	9.003	9.79×10^{-2}	40% RH brine-- EQ3/6 predicted concentration of $MgCO_3$ added (0.1M) but most did not dissolve and was filtered out.
40% RH sea-salt brine without $MgCO_3$ addition	3.39	9.003	2.82×10^{-5}	40% RH brine, no added $MgCO_3$, carbonate species only from atmospheric CO_2 uptake.
0.566 M $MgCl_2$	5.42	1.132	1.37×10^{-5}	Concentration of $MgCl_2$ matching that in 76% RH sea-salt brine
2.61 M $MgCl_2$	4.90	5.22	1.60×10^{-5}	Concentration of $MgCl_2$ that provides same total $[Cl^-]$ as is present in 76% RH sea-salt brine
4.47 M $MgCl_2$	3.51	8.94	3.08×10^{-5}	Concentration of $MgCl_2$ matching that in 40% RH sea-salt brine
4.47 M $MgCl_2$ + 0.1 M $MgCO_3$	7.07	8.94	4.55×10^{-2}	Concentration of $MgCl_2$ in 40% RH brine with 0.1M $MgCO_3$ added (most did not dissolve and was filtered out)

Following exposure and corrosion product removal, SEM analysis of the coupon surfaces showed that concentrations of Mg^{2+}, Cl^-, and HCO_3^- primarily controlled the differences observed in pit morphology and microcracking seen in sea-salt brines at low (40%) and high (76%) RH. As with previous exposures, ellipsoidal pits with faceted bases were the common morphology observed in NaCl-rich solutions representative of high RH conditions (Figure 48-a & b). However, additional, similar morphological features were also seen on SS304 exposed to solutions with no NaCl but containing $MgCl_2$ at lower concentrations (Figure 49). Cross-hatching in pits was specifically seen only on SS304 exposed to solutions of $MgCl_2$ concentrations representative of low RH, close to saturation for bischofite

($MgCl_2$:$6H_2O$) (Figure 48-c). These results, again, suggest that pit morphology is critically influenced by $MgCl_2$ concentration.

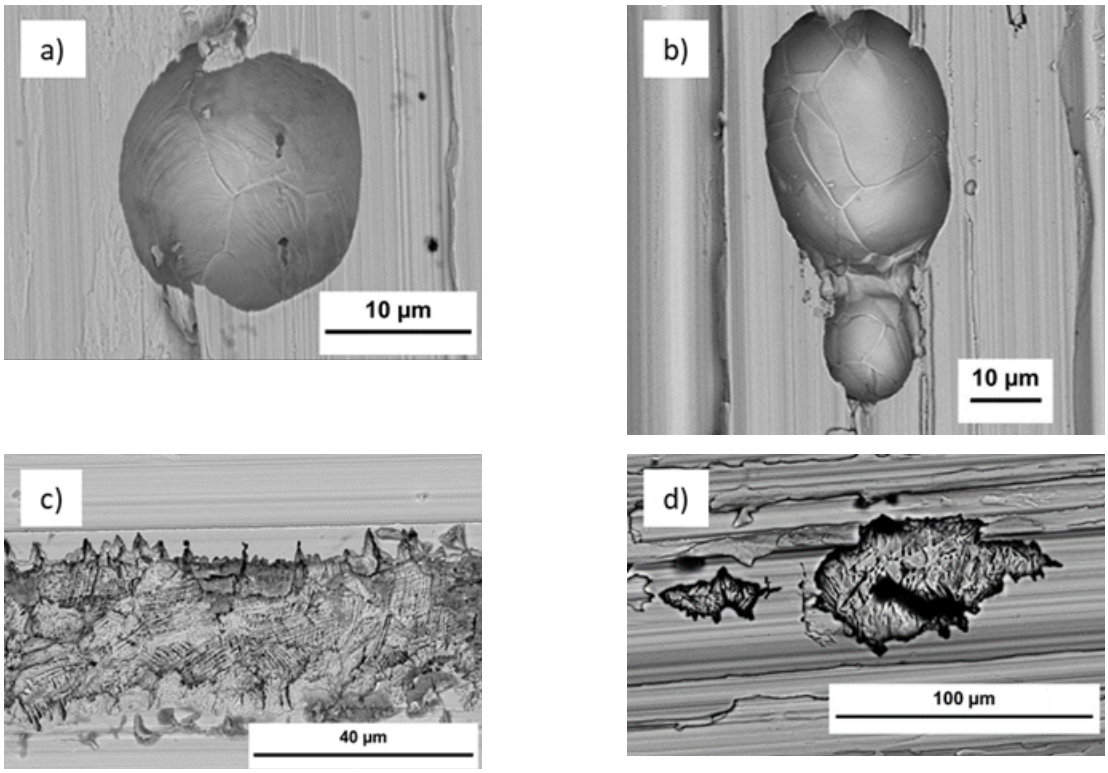

Figure 48. Pit morphology observed on samples exposed for 2 weeks to a) sea-salt brine equilibrated to 76% RH, b) 5.22 M NaCl, c) sea-salt brine equilibrated to 40% RH, and d) 4.47 M $MgCl_2$.

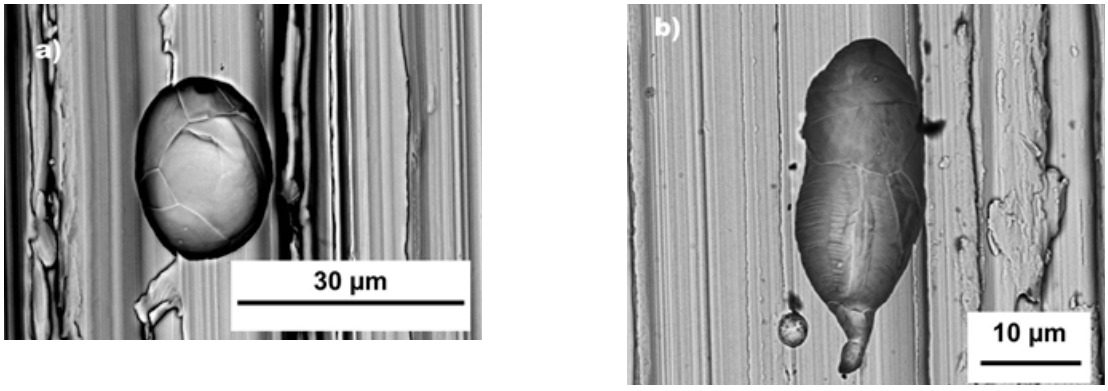

Figure 49. Pit morphology observed in samples exposed to solutions containing only $MgCl_2$ at different concentrations. a) 0.566 M $MgCl_2$ for 7 weeks and b) 2.61 M $MgCl_2$ for 2 weeks.

Exposures in solutions with and without specific brine components were carried out to try to determine what components govern the microstructural etching, irregular shaped pits, and observed microcracking. The frequency of microcracking was observed to correlate with the presence of $MgCO_3$, but only in solutions that also contained high concentrations of $MgCl_2$, as shown in Figure 49. A possible hypothesis for this observation is hydrogen environment assisted cracking (HEAC). This may be due to the enhanced hydrogen evolution reaction kinetics observed in $MgCl_2$ rich brines[70]. The enhanced HER kinetics are due to buffering of the near-surface pH. In the presence of residual stresses and potentially strain-induced martensite from grinding (as these coupons were all exposed with a #4 surface finish produced through uni-directional machine grinding), the surface microcracking observed may be due to HEAC. Further work in FY22 will seek to quantify the near surface residual stresses and/or potential microstructural changes due to the effects of surface finishing procedures.

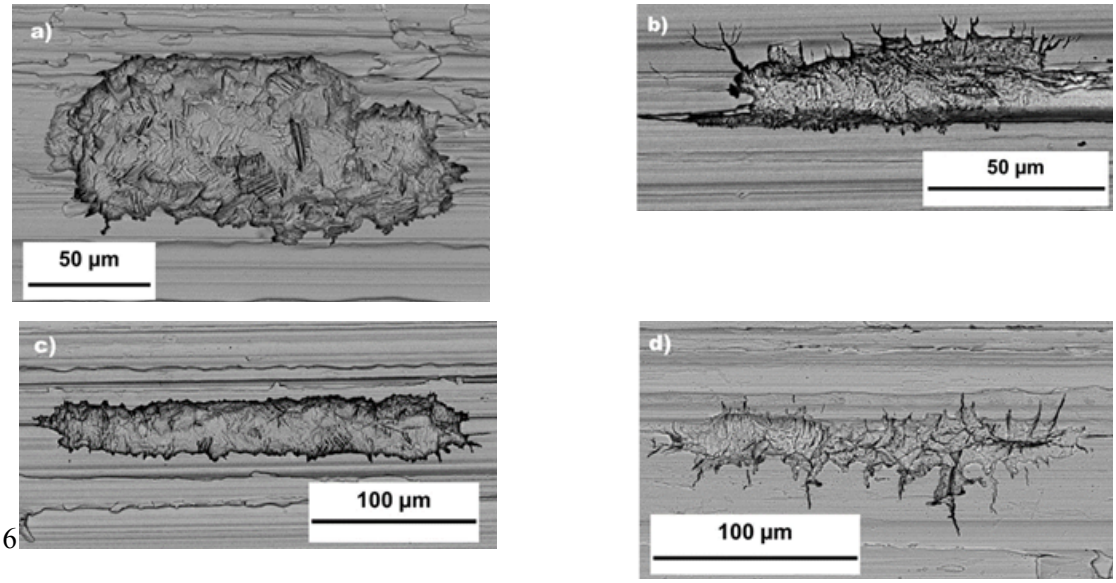

Figure 50. Effect of $MgCO_3$ addition on pit morphology. One-week exposures in a) 4.47 M $MgCl_2$, b) 4.47 M $MgCl_2$ with $MgCO_3$, c) 40% RH sea-salt brine without $MgCO_3$, and d) complete 40% RH sea-salt brine.

3.1.2 Quantitative Assessment of Environmental Phenomena on Maximum Pit Size Predictions in Marine Environments

In FY21, a manuscript, "Quantitative assessment of environmental phenomena on maximum pit size predictions in marine environments", was published in Electrochimica Acta. This paper applied the Chen and Kelly model (Figure 51-a) to evaluate the effects of brine evolution that occur with corrosion and is provided in Appendix B [71]. This paper provides a basis, specifically in terms of available cathodic current supply, for the differences in morphologies observed in the pits in 3.1.1. As shown in FY20 and in [70, 72], the aspects of solution conductivity are significant for accurate predictions in the maximum pit model. Not only do initial brine compositions and properties influence corrosion, but brine evolution throughout the corrosion process also plays a role. When there are solid products/precipitates on the material surface or in the electrolyte, such as insoluble hydroxides or carbonates, flow pathways become more tortuous, and the conductivity decreases in the solution. In addition, cathodic sites can be physically blocked by solid precipitates (Figure 51-a). Also, precipitation will remove brine components, resulting in a decrease in brine volume and hence brine layer thickness at constant RH. A decrease in conductivity and reduction in cathode size will decrease the overall cathodic current available for dissolution; thus, the

maximum achievable pit size will decrease, all else being held constant. An example of how the effects of precipitation were explored in this manuscript is presented in Figure 51. A schematic is shown in Figure 51-a of how precipitates might affect the cathodic radius, and thus current, along with a description (flowchart) of how precipitation was accounted for within the model (Figure 51-b). The inclusion of precipitation reduced the available cathodic current, as show in Figure 51-c, thus reducing the maximum predicted pit size. Inclusion of other potential influences on the maximum pit model are also shown in Figure 51-d for $MgCl_2$ brines.

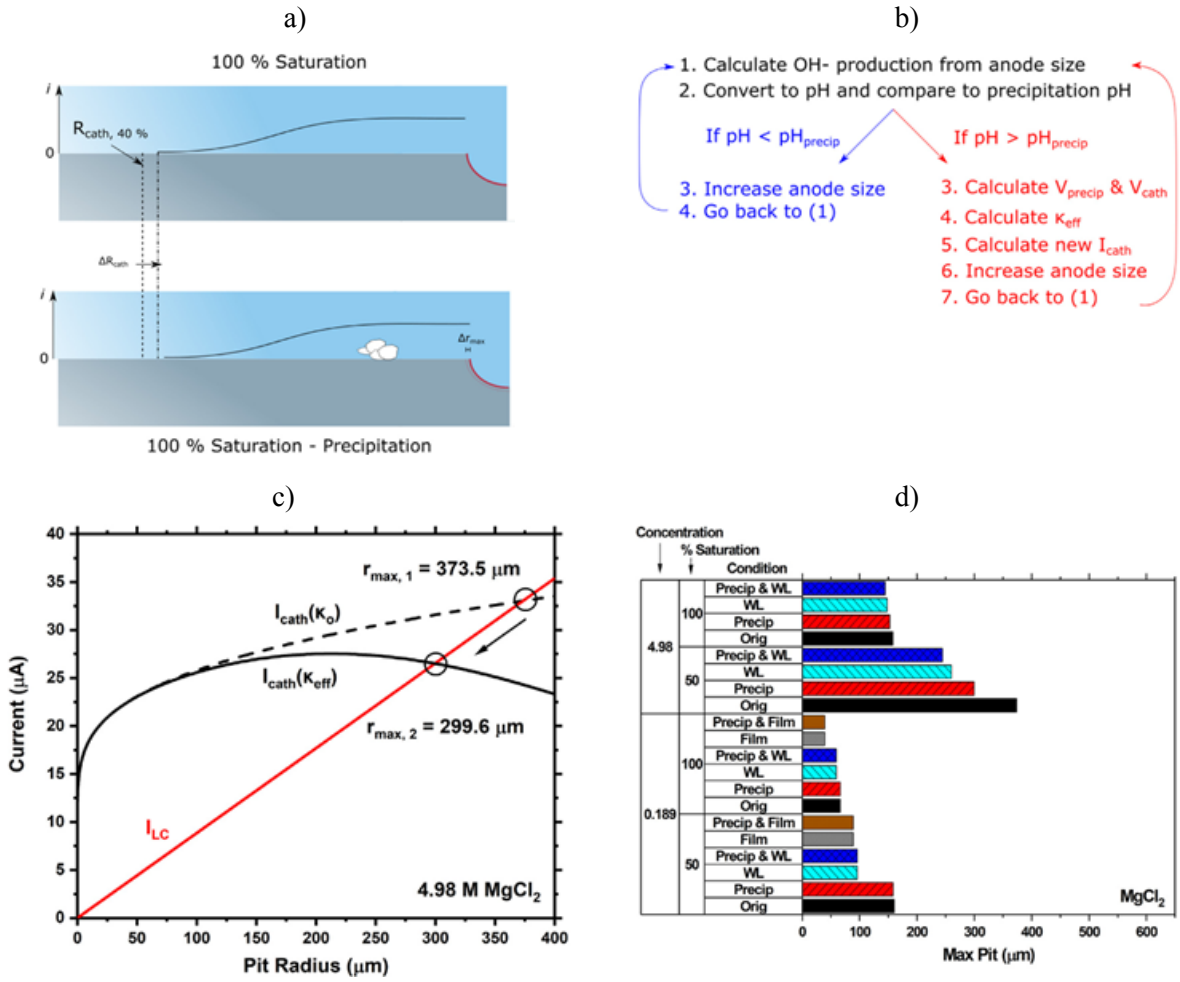

Figure 51. a) Governing factors for maximum pit size predictions when considering precipitation, b) flowchart for calculation of maximum pit sizes when accounting for cathode precipitation, c) maximum pit predictions shown both with and without the consideration of precipitation in the cathode for 4.98 M $MgCl_2$, and d) influence of all cathode evolution scenarios explored for $MgCl_2$ electrolytes on pit size.[73]

As seen in Figure 51, another phenomenon that can occur in these $MgCl_2$ solutions is dry-out of the cathode. As pointed out by Bryan and Schindelholz [74], highly deliquescent $MgCl_2$ can be replaced with a non-deliquescent solid and the brine will dry out as reactions on the surface (corrosion) progress to completion. This means one of two things can happen: (1) brine coverage (the equivalent cathode size) can decrease or (2) the water layer thickness will decrease (Figure 51-d). In both cases, the maximum current will decrease, and the maximum attainable pit on the surface will be smaller.

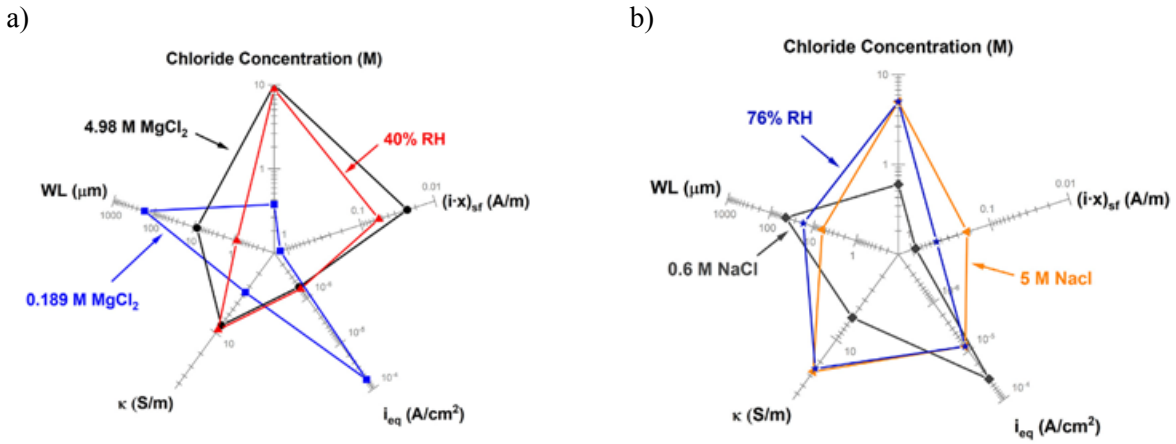

Figure 52. Radar plots comparing properties for (a) $MgCl_2$ solutions and sea-salt at 40% RH and (b) NaCl solutions and sea-salt at 76% RH. Examined in the plots are chloride concentration, water layer thickness, pit stability product under a salt film, equivalent current density, and conductivity of the solution.

The influence of brine composition on anodic and cathodic reactions in general was also evaluated in several brine compositions, including 0.6 and 5 M NaCl, 0.189 and 4.98 M $MgCl_2$, and the equivalent sea-salt brines at 40 and 76% RH. Comparison of the results of the implications on the predicted maximum pit size for all brines are shown in Figure 52. This shows the effect of brine chemistry on parameters in the maximum pit size model. Inclusion of the influences of non-static brine properties in the maximum pit size model reduces the maximum pit sizes predicted. This is of particular significance to potential predictions for risk of SCC as SCC initiation is dependent on pit size. This brings up not only the significance of considering precipitation reactions for $MgCl_2$-dominated brines, which could lead to a potential reduction in timing or severity for SCC, but also the influence that use of surrogate brines may have on the accuracy of predictions. As seen in Figure 52, while the more concentrated brines of $MgCl_2$ and NaCl solutions are better representations of their respective equivalent RH sea-salt brines, they still display discrepancies in the influences of brine properties on parameters significant for the maximum pit model. Understanding maximum pit size predictions under more relevant conditions (and specifically more representative brines) is key to forming accurate predictions for SCC.

3.1.3 Influence of NaOH on Pitting

As corrosion occurs, brine compositions evolve, with development of established pH regions due to the separation of the anode and cathode. This phenomenon was further explored in a manuscript published in FY21 entitled "Cathodic Kinetics on Platinum and Stainless Steel in NaOH Environments" and is presented in Appendix C[75]. When atmospheric corrosion scenarios are modeled, the change in electrolyte chemistry, due to both corrosion and evolution over time, influences the potential and the current density. Under typical atmospheric conditions, cathodic reduction reactions produce hydroxyl ions leading to an increased pH in the cathodic region (example pH vs NaOH solutions are given in Table 9 along with electron transfer numbers). In the case of the maximum pit size model, for example, in 0.6 M NaCl, the repassivation potential (E_{RP}) is roughly −0.265 V_{SCE}, whereas in 0.6 M NaOH (pH=13.6), the open circuit potential (E_{OCP}) is lower than the repassivation potential (Figure 53), indicating that the cathode would no longer be able to supply the necessary current for cathodic kinetics, and would also be limited by an increase in the pH dropping the E_{OCP} below E_{RP}. In all cases, utilizing NaCl polarization curves (rather than NaOH, with higher pHs) will be conservative as higher cathodic currents, and thus larger maximum pit sizes, would be predicted. Additionally, it was determined that at even higher pHs (16.5), the cathodic reduction reaction is no longer due to the oxygen reduction reaction but rather to the

reduction of the oxide on the SS surface (Figure 53-c). *Note:* To achieve a prediction of a pH of 16.5, this is the predicted activity of the hydrogen ion, and in concentrated NaOH solutions, the activity coefficients are much larger than 1, so the activity is much higher than concentration.

Table 9. Calculated electron transfer numbers as a function of NaOH solution pH and electrode material. [75]

NaOH Concentration (M)	NaOH pH	Platinum	Stainless Steel 304 l
0.6	13.6	1.8	1.5
3.6	14.5	1.7	1.3
5.4	14.9	1.5	1.3

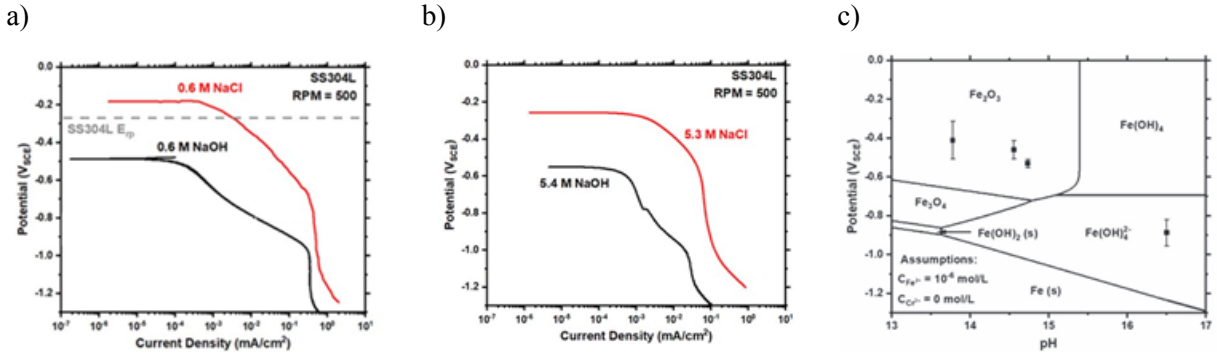

Figure 53. Comparison of cathodic kinetics of SS304L exposed to (a) 0.6 M NaOH and 0.6 M NaCl and (b) 5.4 M NaOH and 5.3 M NaCl. (c) Overlay of SS304L Fe-H_2O Pourbaix diagram and average E_{OCP} in each NaOH solution.

This modeling again highlights the significance of understanding the impact of studying surrogate brines in place of real, relevant brine compositions for predictions of pitting and SCC. In this case, the use of NaCl brine properties instead of brines with true cathodic pHs will overestimate the corrosion damage and potentially lead to overestimations of SCC susceptibility.

3.1.4 *In Situ* Raman of $MgCl_2$ and Seawater Brines

In FY21, SNL continued work to identify and characterize the precipitating phases that form on SS in $MgCl_2$ brines during cathodic polarization scans. In FY19, cathodic polarization scans of SS in $MgCl_2$ brines using rotating disc electrode experiments (RDE) demonstrated the absence of an oxygen diffusion limiting step, suggesting ORR is inhibited and HER is promoted. *Ex situ* characterization of the coupon following the polarization scans identified a precipitating film in $MgCl_2$ brines, however, phase identification of that film remained elusive [76-78]. In FY20, SNL developed an *in situ* method for identifying precipitating surface films during electrochemical polarization using an Raman flow cell (Figure 54) and applied the technique to relevant SNF exposure conditions (e.g. dilute $MgCl_2$ – similar to the $MgCl_2$ content in high RH seawater brines, e.g. 76 % RH) [3, 79]. This seminal study identified the formation of brucite ($Mg(OH)_2$) on the SS304L coupon surface *in situ*, and also confirmed details of brine evolution properties as a function of time, potential, and pH [79] – which helped inform model inputs for the enhanced prediction of maximum pit sizes [80]. The *in situ* identification of brucite during a polarization scan helped link the modeling and synthesis efforts directly with the rotating disc electrode polarization scans as shown in Figure 55.

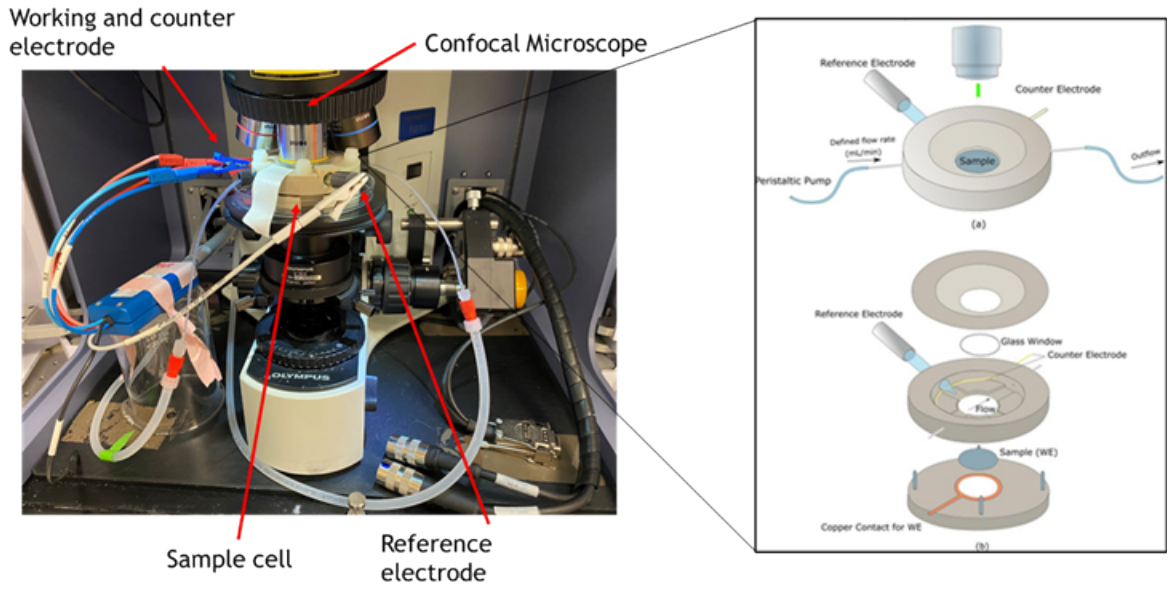

Figure 54. Experimental set up for *in situ* measurements using the electrochemical Raman flow cell (left), and schematic showing the components of the flow cell (right).

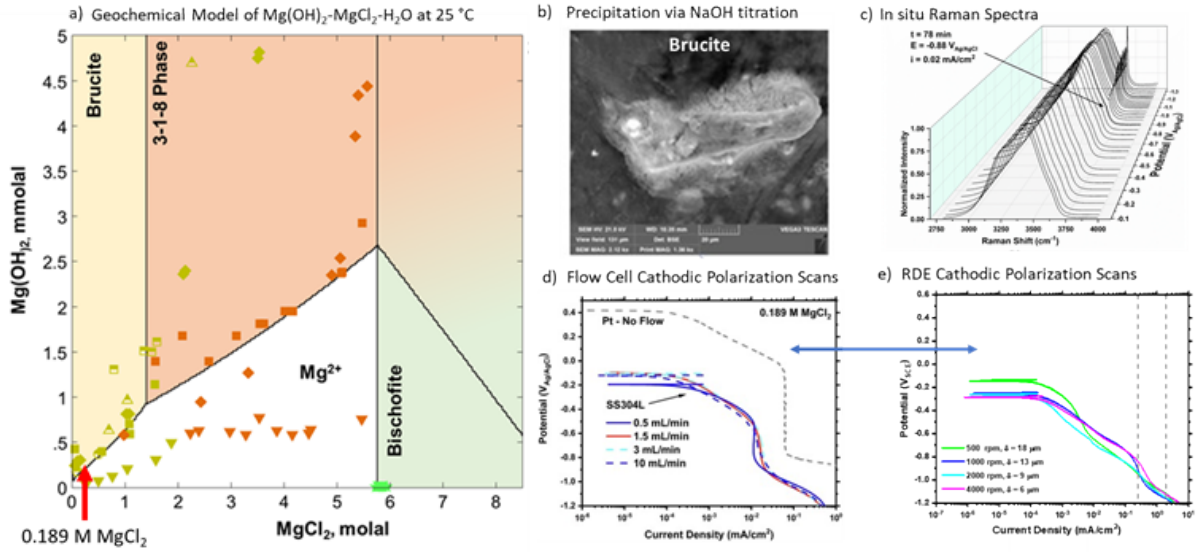

Figure 55. a) Geochemical model at 25 °C of the $Mg(OH)_2$-$MgCl_2$-H_2O ternary system; b) precipitation of brucite by adding NaOH to 0.189 M $MgCl_2$ [3]; c) *in situ* Raman measurement showing the formation of brucite as a function of potential during cathodic polarization in 0.189 M $MgCl_2$ at 1.5 mL/min [3, 79]; d) electrochemical cathodic polarization scan using the Raman flow cell in 0.189 M $MgCl_2$ as a function of flow rate; and e) RDE cathodic polarization curves in 0.189 M $MgCl_2$ as a function of rotation speed [77].

Building on the work in FY20, in FY21 SNL applied the electrochemical Raman flow cell technique to different relevant exposure conditions; including $MgCl_2$ brines (0.189 M, 0.5 M, 1.0 M, 2.0 M, and 3.3 M) and seawater brines (76 % RH and 40 % RH). The goal of this work was to characterize the precipitating phases and develop a link between the chemistry and electrochemistry – as this can aid in

understanding corrosion, pitting, and the potential for cracking. As predicted by geochemical modeling (Section 2.2), at 25 °C the precipitating Mg-phases as a function of concentration are brucite, 3-1-8 Mg-hydroxychloride, and bischofite, respectively. This work aimed to identify the impact of the precipitating phase on the electrochemical behavior, as these phases differ in their pH of precipitation, morphology, and their ability to scavenge Cl^- — all of which could impact corrosion pitting.

3.1.4.1 Flow Rate Dependencies

Cathodic polarization scans of SS304L in $MgCl_2$ were collected as a function of the solution flow rate through the electrochemical cell (Figure 56). The features of the cathodic scans resemble RDE experiments [77] where an activation controlled region occurs from E_{OCP} of ~ -0.4 to -0.5 $V_{Ag/AgCl}$ followed by a quasi-mass-transport controlled region (indicative of SS304 in dilute $MgCl_2$ brines) from ~ -0.5 to -0.9 $V_{Ag/AgCl}$, after which HER is the dominant cathodic reaction. Additionally, as with the RDE experiments in Figure 55-d, independent of flow rate, the diffusion-limited current density measured on Pt was not achieved. This result suggests that in 0.189 M to 3.3 M $MgCl_2$ something is occurring that prohibits ORR, likely the presence of a surface precipitating film.

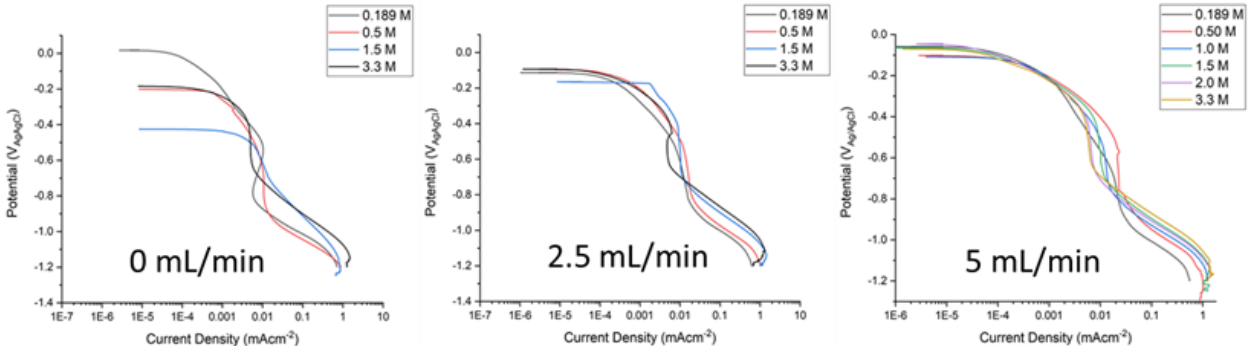

Figure 56. Cathodic polarization scans on SS304L in different concentrations of $MgCl_2$ solutions collected at flow rates; 0 mL/min, 2.5 mL/min, and 5 mL/min.

Shown in Figure 57 are the cathodic polarization scans in 76 % RH and 40 % RH sea-salt brines as a function of flow rate through the electrochemical cell. The 76 % RH brine is primarily an NaCl brine and contains ~ 0.189 M $MgCl_2$, while the 40 % RH brine is primarily a $MgCl_2$ dominated brine. The polarization curve in the 76 % RH brine contains an activation-controlled region from E_{OCP} to ~ 0.4 $V_{Ag/AgCl}$ followed by a short period of mass-transport control, which appears to be flow rate dependent, and finally a region where HER becomes dominant. This behavior is unique to the 76 % RH brine and resembles a combination of NaCl and $MgCl_2$ rich brines. For the 40 % RH brine, an activation-controlled region is dominant for roughly the entire polarization scan and is similar to RDE polarization scans for saturated $MgCl_2$ [70].

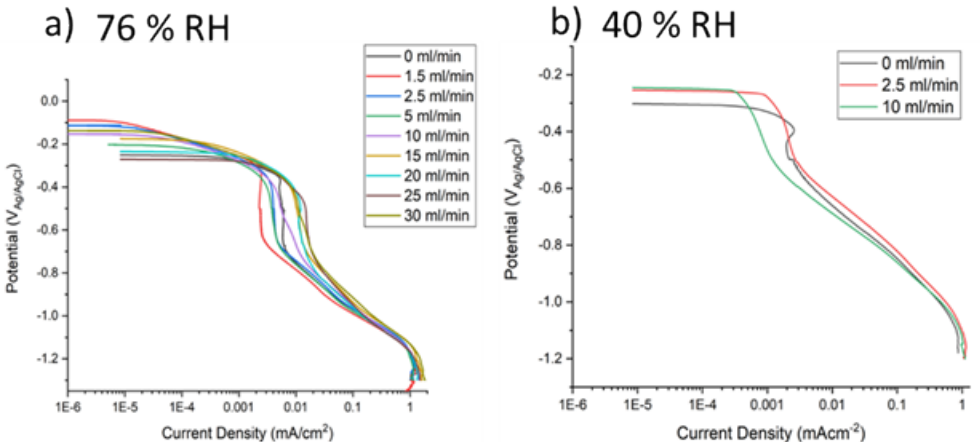

Figure 57. Cathodic polarization scans on SS304L taken at different flow rate of a) 76% RH equivalent sea-salt and b) 40% RH equivalent sea-salt.

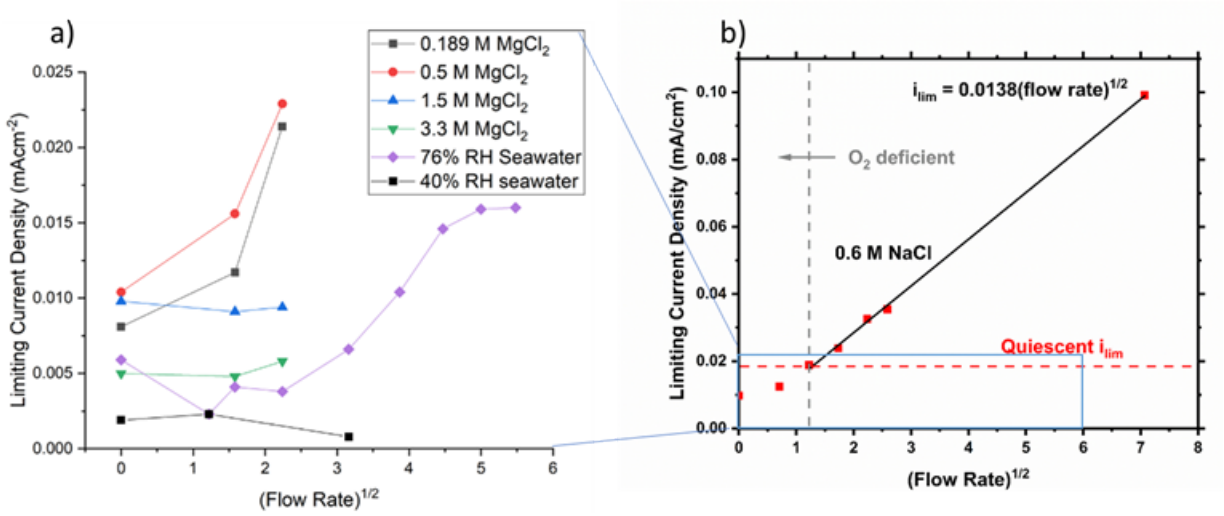

Figure 58. a) Limiting current density vs flow rate for all solutions used in polarization experiments, shown with b) determined flow rate dependence of 0.6 M NaCl brines [79] and the corresponding axis window.

The relationship between flow rate and the limiting current density (i_{lim}) for each of the $MgCl_2$ solutions and for the two sea-salt brines are shown in Figure 58-a. Previous work by SNL identified a relationship between i_{lim} and flow rate in 0.6 M NaCl and how that could be applied to estimate the boundary layer thickness for oxygen diffusion in ORR [79] –similar to how rotation speed controls the boundary layer thickness in RDE experiments [77-79]. However, the presence of $MgCl_2$ eliminates the relationship between flow rate and i_{lim}, consistent with initial studies in 0.189 M $MgCl_2$ [79], suggesting that the flow rate does not change the boundary layer thickness. This could be explained by the formation of a thin precipitating film that controls oxygen diffusion to the SS surface. The 76 % RH sea-salt brine may have a slight flow rate dependence when the flow rate is between 5 mL/min and 25 mL/min; however, when compared to the result from 0.6 M NaCl, the possible relationship was weak, and i_{lim} never exceeds that of i_{lim} for the quiescent study. However, when the relationship between i_{lim} and flow rate (or rotation speed for RDE) for 76 % RH equivalent sea-salt brine is compared to that of saturated NaCl, good agreement

was obtained [71]. This suggests that the flow cell is potentially a suitable technique for evaluating atmospheric corrosion and is comparable to an RDE experiment.

3.1.4.2 *In Situ Raman Spectroscopy*

Raman spectra were collected periodically during the cathodic polarization scans. For each experiment, after calibration using a Si wafer, the sample surface was focused using a 10X objective lens with numerical aperture (n_a) of 0.25. The Raman spectra were collected *in situ* during the cathodic polarization using a 532 nm wavelength laser utilizing 75% of the maximum 100 mW power. High resolution Raman spectra were collected every 120 seconds with 3 second exposure times, averaged over 5 scans from 2955 to 3800 cm^{-1}. This region corresponds to the O-H stretching vibrational frequency, which is a dominant feature in brucite and in 3-1-8 Mg-hydroxychloride, which thermodynamic models predict to precipitate at higher $MgCl_2$ concentrations. For brucite, a single sharp peak is centered around 3646 cm^{-1} and corresponds with the A_{1g} O-H stretch for microcrystalline brucite [79, 81]. Similarly, the 3-1-8 Mg-hydroxychloride phase has O-H stretch vibrational frequencies in this region. For this phase, there are two sharp peaks centered at 3639 cm^{-1} and 3657 cm^{-1} [81-83]. A spectrum for dried synthesized 3-1-8 Mg-hydroxychloride phase is shown in Figure 59; this phase was precipitated by mixing $MgCl_2$ with NaOH, using the procedure described in the FY20 status report [3]. Although the O-H stretch peaks for brucite and the 3-1-8 phase are very close to each other, because the 3-1-8 peak is a doublet, it should be possible to discern them. Also, the major peak in the $O\text{-}H_{3\text{-}1\text{-}8\ phase}$ is 11 cm^{-1} blue shifted relative to $O\text{-}H_{brucite}$; this shift is large enough to differentiate between the two. To compare among collected Raman spectra, the spectra were normalized using the intensity at 3411 cm^{-1}, associated with maxima of $O\text{-}H_{water}$ stretching for H_2O molecules [79].

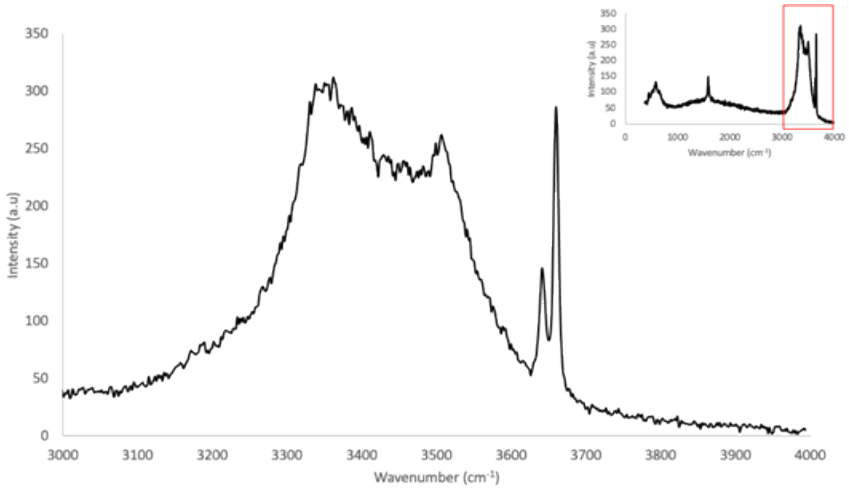

Figure 59. *Ex situ* Raman of synthesized, dried 3-1-8 Mg-hydroxychloride phase.

The Raman spectra for $MgCl_2$ solutions collected during cathodic polarization scans with a flow rate of 5 mL/min are show in Figure 60 as a function of concentration. As expected from thermodynamic calculations, brucite is the precipitating phase when the [$MgCl_2$] is < 2 M. This is evidenced by the large $O\text{-}H_{brucite}$ peak that grows in as the system becomes cathodically polarized. When the [$MgCl_2$] = 0.5 and 1 M, the $O\text{-}H_{brucite}$ peak is far more intense than the $O\text{-}H_{water}$ peak, suggesting that a significant amount of brucite had precipitated. While Raman is not a quantitative technique, peak areas can provide a qualitative estimate of the amount of the contributing species present. Only small $O\text{-}H_{brucite}$ peaks were observed when [$MgCl_2$] = 2 M, and no peaks were identified when the [$MgCl_2$] = 3.3 M. Additional experiments were run with [$MgCl_2$] > 3.3 M, and no peaks were observed in any of those Raman spectra. The absence of Raman peaks associated with any Mg precipitating phase when [$MgCl_2$] ≥ 3.3 M was

unexpected because the cathodic polarization scan behavior suggested that a phase precipitated, and based on geochemical modeling (Figure 55-a), the expected precipitating assemblage is the 3-1-8 phase.

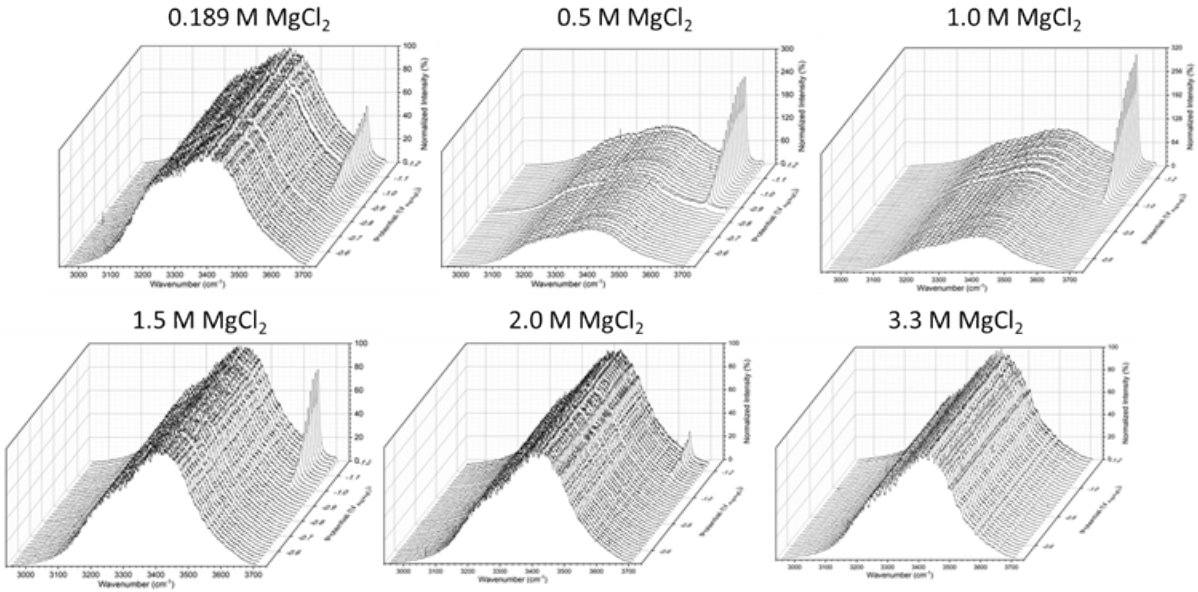

Figure 60. *In situ* Raman spectroscopy of SS304L surface as a function of potential (z axis) in $MgCl_2$ brine at concentrations from 0.189 M to 3.3 M at a flow rate of 5 mL/min.

The intensity of the O-$H_{brucite}$ peak (3645 cm^{-1}) normalized to the O-H_{water} peak (3411 cm^{-1}) versus polarization potential is shown in Figure 61 as a function of [$MgCl_2$]. This plot shows that, at as [$MgCl_2$] increases, the potential at which brucite forms becomes more negative and the system is more cathodically polarized. Also, the intensity of the O-$H_{brucite}$ peak is a function of [$MgCl_2$]; the peak intensity increases from 0.189 M to a maximum value around 0.5 or 1 M $MgCl_2$, then rapidly decreases in intensity until the peak disappears between2.0 M and 3.3 M $MgCl_2$.

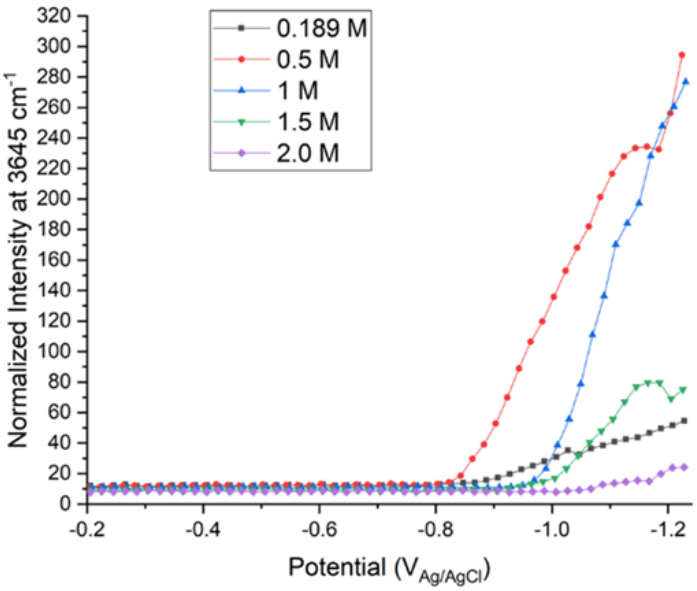

Figure 61. Normalized intensity at 3645 cm^{-1} vs cathodic potential showing influence of $MgCl_2$ concentration

The Raman spectra for the 76 % RH and 40 % RH equivalent sea-salt brines collected during cathodic polarization with a flow rate of 5 mL/min are shown in Figure 62. Peaks are observed in the 76 % RH brine and correspond to brucite. This is expected as the [$MgCl_2$] ~ 0.189 M, and from geochemical modeling, brucite is the expected precipitating Mg-phase. In the 40% RH brine, no peaks were observed. As with higher concentrations of pure $MgCl_2$, it was expected that some phase would precipitate. The cathodic polarization scan (Figure 57) shows the absence of a mass transport controlled region, an absence which has previously been closely associated with the formation of a precipitating phase; however, none were detected in the Raman. *Ex situ* inspection revealed a film was present (though inconsistently), however its identification could not be determined.

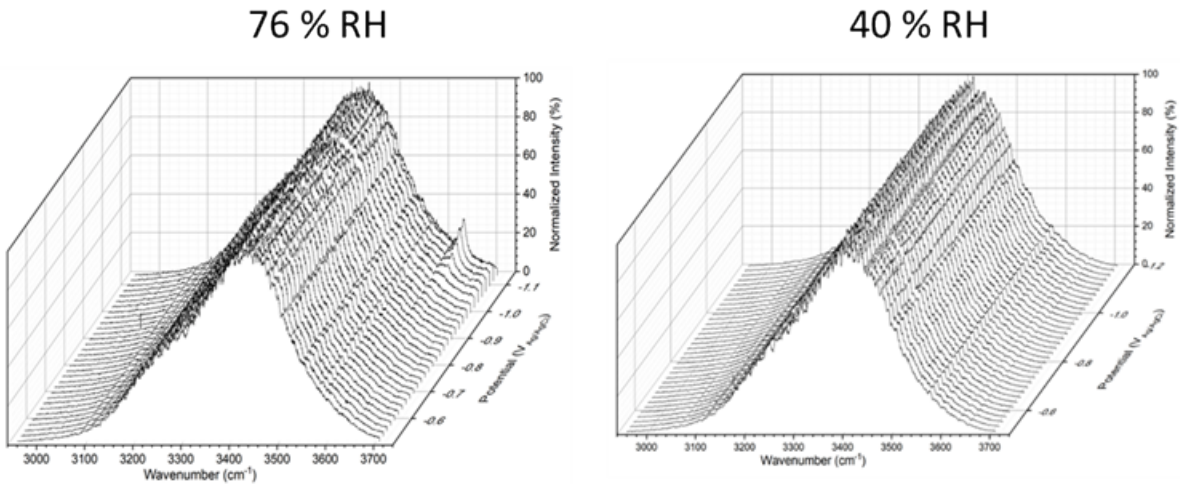

Figure 62. *In situ* Raman spectroscopy of SS304L surface as a function of potential in 76% RH and 40% RH equivalent sea-salt brine at a flow rate of 5 mL/min

Since the i_{lim} in the 76 % RH brine may be flow rate dependent, Raman spectra were collected at flow rates of 2.5 mL/min to 20 mL/min (Figure 63). As the flow rate increased, there was as slight shift to more negative potentials at which brucite precipitates (Figure 63a). This result was unexpected; RDE experiments showed that a higher rotation speed resulted in a higher current density and increased OH^- production, suggesting that the potential would increase with flow rate [71]. However, due to the Raman collection times (every 120 seconds), the uncertainty in the potential is ~ +/- 0.02 V. The differences in the potential of brucite formation may be changing with flow rate, but it is a very small change. One way to mitigate this issue would be to hold the surface at a defined cathodic current density and observe the in-growth of the $O\text{-}H_{brucite}$ peak at different potentials. Also, when comparing 0.189 M $MgCl_2$ and 76 % RH sea-salt brine, which have equivalent $MgCl_2$ concentrations, there is a significant shift in the potential when brucite is first detected. Brucite begins to form around -0.88 $V_{Ag/AgCl}$ in 0.189 M $MgCl_2$ and around -1.0 $V_{Ag/AgCl}$ in 76 % RH sea-salt brine (Figure 63-b). This shift may be caused by the differences in the electrochemical behavior of the two solutions. In 76 % RH sea-salt brine, there is a larger potential region over which the current is limited by mass transport ORR, whereas in 0.189 M $MgCl_2$, the system more rapidly transitions to HER. Previous work has shown that initial detection of brucite occurs near the transition from ORR to HER [79].

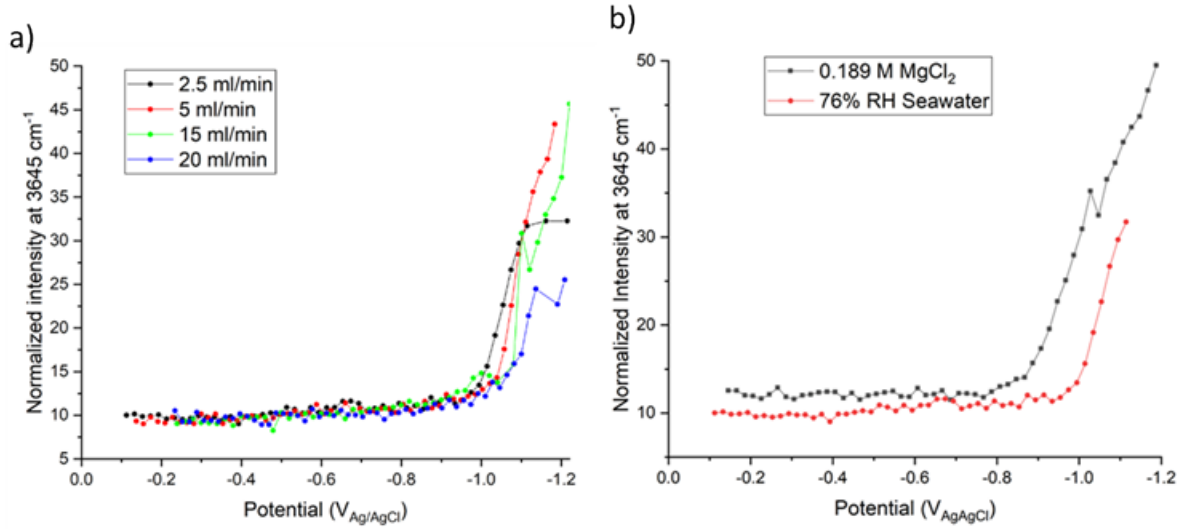

Figure 63. Normalized intensity at 3645 cm^{-1} vs cathodic potential showing influence of 76% RH equivalent sea-salt brine.

Figure 64 compares the electrochemical and precipitation behavior of $MgCl_2$ solutions as a function of concentration (up to 2.0 M $MgCl_2$ for precipitation reactions and up to 3.3 M for i_{lim}) and of 76 % RH sea-salt brine (40% RH was not included as no precipitates were detected in the Raman). The potential of brucite precipitation decreased as the $MgCl_2$ concentration increased. The i_{lim} follows a similar trend as the potential of brucite precipitation. The current density at brucite precipitation increases as the concentration of $MgCl_2$ increases. One possible explanation for this observation is that as the [$MgCl_2$] increases the solubility of O_2 decreases, which results in a decrease in i_{lim}. A decrease in i_{lim} results in less OH^- production, as OH^- is related to current density, and subsequently a decrease in the rise in pH. Since the brucite precipitation does not occur (or is not detected) in the i_{lim} region, the system has to be further cathodically polarized (more negatively) (Figure 64-a) to reach a current density, or rather a pH, where the brucite will precipitate. The current density required for brucite to precipitate increased as the [$MgCl_2$] increases (Figure 64-c). This could be caused by the fact that the initial solution pH decreases as the [$MgCl_2$] increases (Figure 65), which would require more current to generate more OH^- in order for the pH to increase high enough to saturate the solution with respect to brucite.

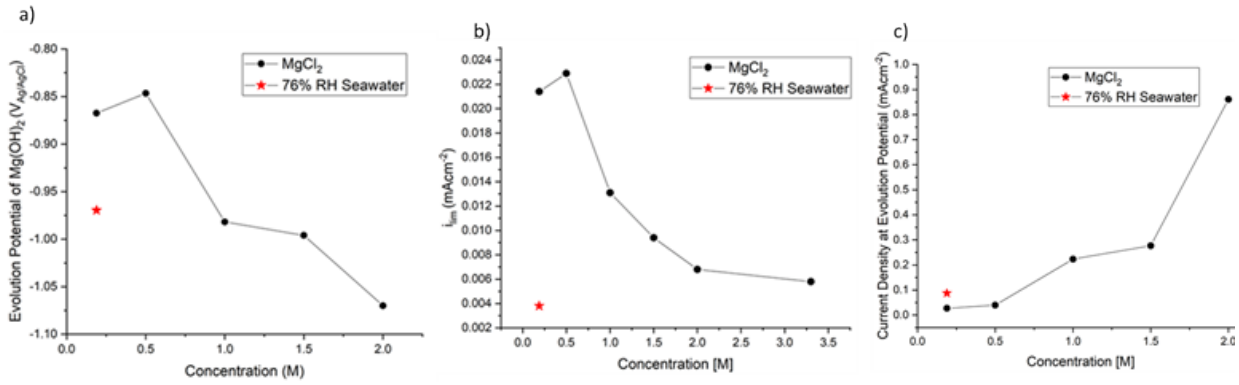

Figure 64. Influence of $MgCl_2$ concentration and 76% RH sea-salt brine on a) evolution potential of $Mg(OH)_2$, b) limiting current, and c) current density during cathodic polarization.

While the polarization scan and *ex situ* interrogation [16, 70] indicate that something precipitated, and geochemical modeling suggests that it should be the 3-1-8 phase (Figure 65), no precipitate was observed in the Raman when $[MgCl_2] \geq 3.3$ M. The 3-1-8 phase does contain Raman active vibrational frequencies (Figure 59), so it is detectible by Raman. Previous methods to precipitate the 3-1-8 phase required several hours to several years of incubation and equilibration prior to precipitation [21, 23, 47, 49, 53, 77]. Experiments in FY20, in which NaOH was added to $MgCl_2$ brines (at a concentration where the 3-1-8 phase is expected), showed that a gel would form immediately in solution. When the gel was analyzed by SEM/XRD, halite and brucite were the primary phases detected; however, if the gel was analyzed after several hours, only the 3-1-8 Mg-hydroxychloride phase was detected. This suggested that kinetic factors may determine whether the 3-1-8 phase precipitates. The cathodic polarization experiments last ~2 hours, however the 3-1-8 phase will only be oversaturated in solution for 30 mins or so (resulting from a rise in pH from OH^- production), which may not be sufficient time for the 3-1-8 phase to precipitate. When $[MgCl_2] = 2$ M, $O\text{-}H_{brucite}$ peaks are detected in the Raman spectra; this result is consistent with the NaOH method for precipitating the 3-1-8 phase, as a meta-stable brucite intermediate formed prior to the 3-1-8 phase [21]. However, when $[MgCl_2] \geq 3$ M (including 40 % RH sea-salt brine), $O\text{-}H_{brucite}$ peaks were not observed by Raman to form *in situ*. At this point, it remains unclear what is causing HER to be the primary cathodic reaction of SS304 in $MgCl_2$ when $[MgCl_2] \geq 3$ M, and what the identity of the gels or precipitating phases may be.

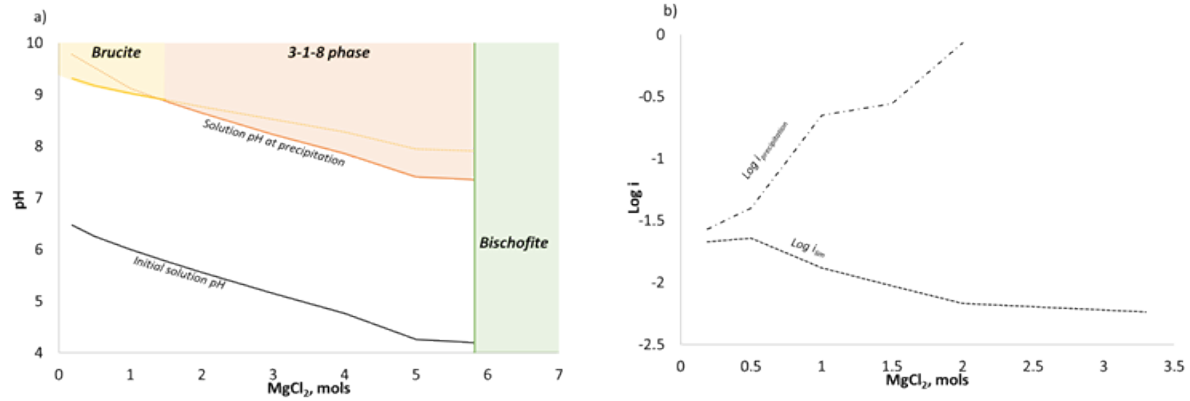

Figure 65. a) Diagram showing the initial solution pH and the pH at precipitation for brucite and the 3-1-8 Mg-hydroxychloride phase, and b) Log i_{lim} and Log $i_{precipitation}$ as a function of the $MgCl_2$ concentration.

The implications of this work for SNF canister corrosion are related to the $MgCl_2$ brine stability during corrosion processes. These results suggest that under some conditions on an actively corroding SS surface, the brine pH in the cathode, would lead to precipitation, and result in brine dry out. When [$MgCl_2$] values are higher, (for example, in 40 % RH sea-salt brine environments), HER is the dominant electrochemical reaction and there is evidence of precipitation of an Mg phase that could lead to brine dry-out; however, this is not yet fully understood, as no such phase was observed. Additional work to address this knowledge gap is to perform cathodic hold experiments extended over several hours. Over these time intervals, it would be expected that the 3-1-8 phase would eventually crystallize, however, the electrochemical potential and the equilibrium time required for its formation will need to be determined. Additional experiments will be performed at elevated temperatures, since the calculated phase diagram of the $Mg(OH)_2$-$MgCl_2$ – H_2O system is temperature dependent (See Section 2.2.1). Performing these experiments at different temperatures will lead to a better understanding of the conditions at which Mg-precipitates form as the SNF canister cools over time. For example, at 80 °C, the 2-1-4 Mg-hydroxychloride phase was experimentally observed [14] and is predicted as the phase that should precipitate (See Section 2.2.1). High temperature cathodic polarization measurements using the electrochemical Raman cell could provide a better understanding of the conditions of the precipitation of this phase and its impact on the electrochemical behavior of the system. Lastly, the contribution of other species (e.g. carbonate) in seawater brines may have an impact on brine stability and electrochemical behavior. This is demonstrated in section 3.1.1 and elucidated by the differences in electrochemical behavior between 0.189 M $MgCl_2$ and 76 % RH equivalent sea-salt brine (which is a NaCl dominated brine, but contains ~ 0.189 M $MgCl_2$). Development of an enhanced understanding of the brine evolution over time, at differing environmental conditions (i.e. T, RH, etc.) and with and without concurrent corrosion, will enable a more complete understanding of the canister surface conditions and enhance predictions of pitting and SCC damage and susceptibility.

3.1.5 Effect of Brine Thickness and Natural Convection Boundary Layer on Corrosion

In addition to brine composition and chemical evolution over time, the morphology, specifically the water layer thickness, can also play a large role in governing the subsequent corrosion damage. A manuscript published (as Editor's Choice) in the Journal of Electrochemistry in FY21 measured cathodic kinetics on platinum (Pt) and SS 304L (SS304L) under varying electrolyte layers using a rotating disk electrode, and quantitatively determined the natural convection boundary layer thickness (δ_{nc}) as a function NaCl concentration and temperature. The "Natural Convection Boundary Layer Thickness at Elevated Chloride Concentrations and Temperatures and the Effects on a Galvanic Couple" is presented in Appendix D and is summarized herein [71]. Cathodic kinetics in NaCl and $MgCl_2$ brines were combined with calculated δ_{nc} values to estimate cathodic currents in a galvanic couple system under thin film and bulk conditions. While a galvanic system was employed in the manuscript, the general conclusions of the study are applicable to understanding pits in SS, as the effects on pits that exhibit anode-cathode separation can be interpreted somewhat similarly. The results of this study identified not only trends in δ_{nc} that can be described by mass transport phenomena, but also discussed controlling mechanisms for corrosion under varying environmental conditions.

Calculated natural convection boundary layer thickness (δ_{nc}) values are presented for NaCl solutions as a function of chloride concentration and temperature in Figure 66. Overall, with increasing chloride concentration, δ_{nc} decreases. Additionally, with increasing temperature, δ_{nc} decreases. Generally, SS304L had a higher δ_{nc} due to a lower i_{lim} than the Pt. Figure 66-b compares δ_{nc} for NaCl to $MgCl_2$ as a function of chloride concentration at 25 ^{O}C. Below 5 M chloride, δ_{nc} is similar for both salts. As seen in Figure 67, δ_{nc} decreases with increased calculated Sherwood number (Sh). The fit present in Figure 67

utilized data only from SNL experiments, but values of δ_{nc} from literature show good agreement with the fit.

This manuscript showed for the first time that the dependence of the natural convection boundary layer can be described by the *Sh*, enabling the prediction of the natural convection boundary layer with an electrochemical polarization scan and readily available solution parameters. Additionally, the total cathodic current capacity of an aluminum/SS galvanic couple was evaluated as a function of electrolyte film thickness, electrolyte composition, and cathode size. The water layer ranged from full immersion conditions where mass-transport kinetics dominated, to the thin film regime where ohmic drop dominated. Also, the natural convection boundary layer defined the upper limit for thin film atmospheric corrosion; for water layers above this limit, the total cathodic current scaled with cathode size. The results of this study have important implications for sample sizing and corrosion prediction as a function of environment.

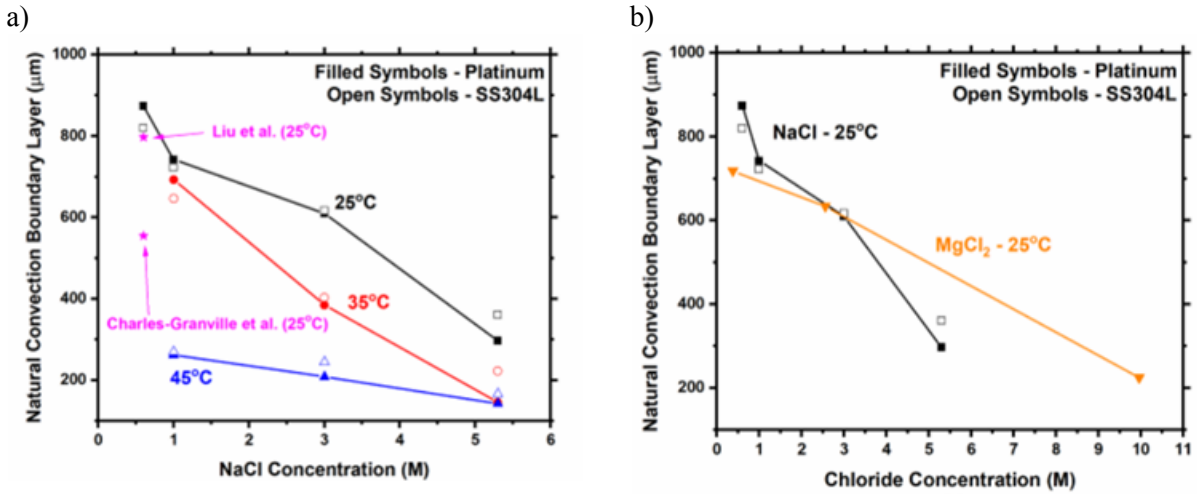

Figure 66. Experimentally calculated natural convection boundary layer thickness as a function of (a) NaCl concentration and temperature and (b) solution composition (NaCl and $MgCl_2$) at 25 ˚C. It is noted that the x-axis of (b) is total chloride concentration.[71]

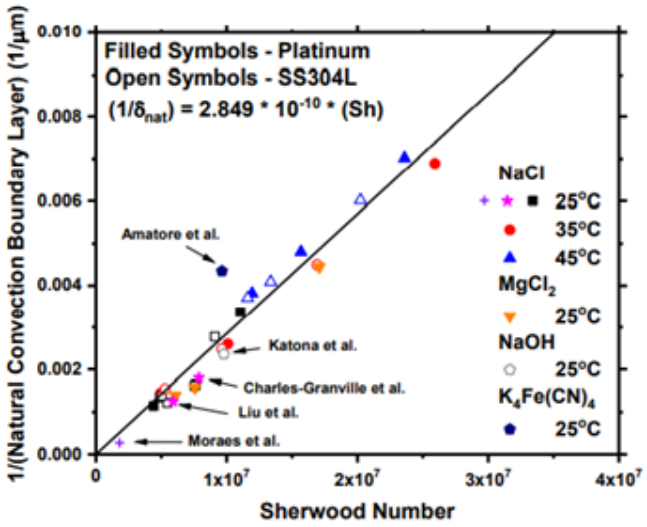

Figure 67. Inverse of natural convection boundary layer as a function of calculated Sherwood number (*Sh*). Values also plotted were obtained from Liu et al. [84], Charles-Granville et al. [85], Katona et al.[75] , Amatore et al. [86], and Moraes et al. [87].[71]

For atmospheric environments, the value of δ_{nc} and the length of the cathode, determine if a decrease in total current is experienced with increased water layer (WL) thickness. For example, in saturated NaCl solutions, at 25 °C, and WLs above δ_{nc} (~300μm), any cathode length shorter than 0.32 m (32 cm) experiences decreases in the total cathodic current per cathode width (I_C/W) in comparison to 100μm WL due to mass transport limitations. These limitations may play a role when selecting sample sizes for accelerated chamber testing and understanding field atmospheric exposure scenarios. The potential for corrosion damage reduction due to mass transport limitations may either not provide for an accurate representation of thin films or in-service atmospheric environments, or, due to mass transport controlling kinetics, may limit the damage that is observed on atmospheric exposure samples.

Another important point raised in this study is that under atmospheric conditions, as WL formation through salt deliquescence is possible, the cathodic current in a galvanic couple can be predicted as a function of environment. The WL=(LD. ρ_{sp})/(MW.C_{eq}), is dictated by the loading density (LD, grams of salt per unit surface area, g/m^2), the specific gravity of the solution (ρ_{sp}), the molecular weight (MW), and the equilibrium concentration of the salt (C_{eq}). The C_{eq} is controlled by the relative humidity (RH) and therefore, I_C/W for the galvanic couple could be calculated as a function of RH and LD. With increased RH, LD, and cathode length, I_C/W increased (Figure 68). This highlights the important, controlling behavior of cathodic kinetics under atmospheric corrosion, and the need for understanding the controlling factors on these kinetics to better determine potential corrosion damage.

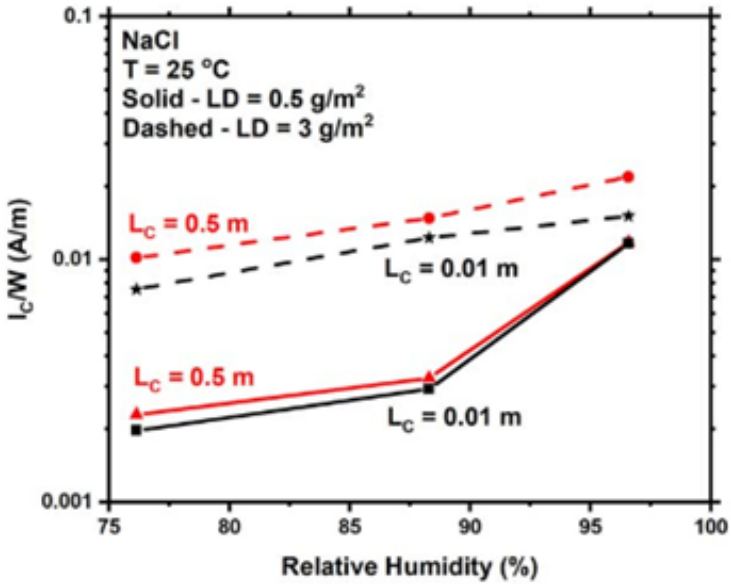

Figure 68. Comparison of the modeled total cathodic current per width (I_c/W) vs relative humidity (RH) as a function loading density (LD) and cathode length (L_c) [71].

3.1.6 Implications for the Maximum Pit Size Model and Relation to SCC Prediction

As has been shown throughout the corrosion work carried out in FY21, brine composition, brine evolution with corrosion, and material influences can significantly affect the corrosion damage across SS under canister relevant conditions. Accounting for these real-world effects in modeling can greatly enhance predictions for maximum pit sizes which, in-turn, will result in better overall SCC predictions.

Earlier this year, SNL produced a SFWST report, "FY21 Status Report: Probabilistic SCC Model for SNF Dry Storage Canisters" [88]. This report includes new experimentally informed maximum pit size models that will significantly impact the probabilistic SCC model because pit depth is a determining factor in crack initiation. The integral effect that changes in i_{eq} (equivalent current density), ΔE_{max} (maximum difference in the E_{OCP} and E_{RP}), and I_{pit}/r_{pit} (cathode current to pit radius ratio) have on the maximum pit size are shown throughout. A summary of this effect, for each of these parameters and the overall effect on pit size is shown below.

The effect of the changes on the i_{eq}, ΔE_{max}, and I_{pit}/r_{pit} on the maximum pit size are shown in Figure 69. This is compared across different fixed values of deposition density (with the inclusion of high

deposition values to show exaggerated effects). This new modeling approach results in larger predicted maximum pit sizes by about an order of magnitude. There results have significant implications for the overall SCC model, because as deeper pits correspond to larger stress concentrations, thus increasing the potential for crack initiation.

Finally, note that the new model is not probabilistic; the parameters have not been assigned distributions. However, uncertainty could easily be incorporated into the new model by calibrating the model to the actual experimental data.

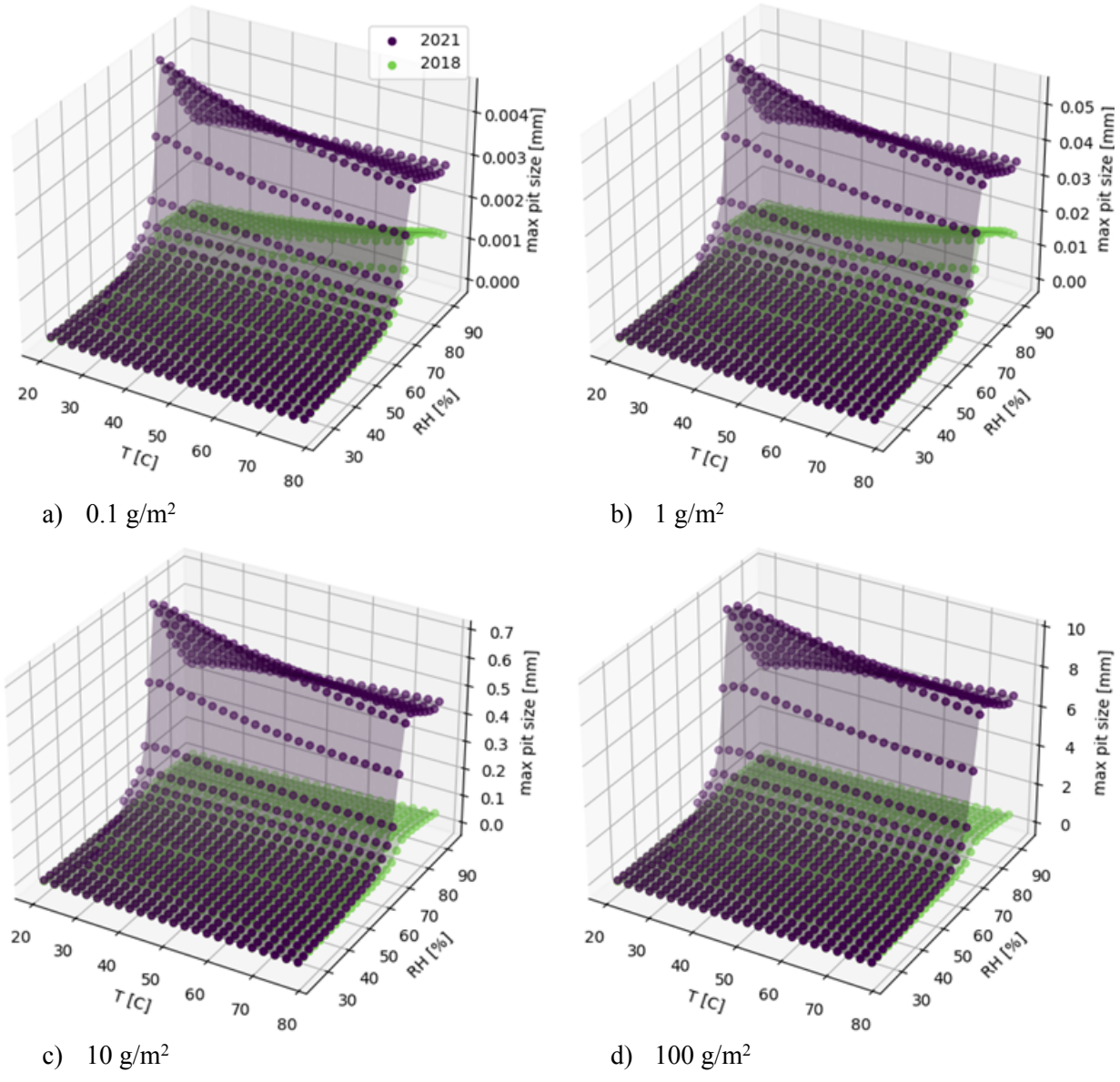

Figure 69. Effect of model changes on calculated maximum pit size for different deposited salt loads [88]. Purple—new model; Green—previous model.

3.2 Atmospheric Environmental Exposures

In the FY20 status report [3], three modified environments were developed and discussed for corrosion testing. These environments are intended to more realistically capture aspects of the natural environment that may have significant effects on corrosion damage and potentially SCC on canister surfaces. The first of these environments implements a diurnal cycle—a 24-hour cycle in temperature and RH—that was chosen to be representative of conditions that would eventually occur on a canister surface as the canister cooled. In such an environment, brine chemistry and volume may vary greatly as a function of RH, affecting the electrochemistry and corrosivity of the brine. The second addresses the potential effects of inert mineral grains on the metal surface. At all sites that have been evaluated to date, detrital mineral grains—largely quartz and aluminosilicates—are the most abundant particles present in the dust. Although not chemically reactive, such grains may affect corrosion processes in a few different ways. First, mineral grains may affect the distribution of brine on the metal surface, facilitating brine spreading via capillary processes; changes in the continuity of the brine layer could affect the available cathodic current for corrosion. Second, larger mineral grains may act as crevice formers, promoting corrosion relative to a surface without dust particles[89]. Finally, most of the experimental work to date has focused on near-marine sites, and has assumed that the corrosive salts on the surface of the canisters are sea-salts. However, the actual soluble salt compositions that have been measured from field samples [3] show that continental salts, high in calcium, potassium, nitrate, and sulfate, were present as well as sea salts; moreover, there was evidence of interactions atmospheric gases that convert chloride salts to nitrates and sulfates. The measured salts at most sites contained significant levels of nitrate and sulfate—frequently, at concentrations higher than that of chloride. As nitrate has been observed to inhibit corrosion in experimental studies [90], corrosion testing with relevant salt compositions that include nitrate and sulfate have been planned, and some initial electrochemical experiments have been carried out.

3.2.1 Cyclic Diurnal Influences on Corrosion

As stated above, in FY20, a profile for a diurnal cycle based on Arkansas Nuclear 1 weather data was developed for laboratory accelerated exposure testing [3]. This specific site and developed exposure was selected as the RH and T cycle passes through the $MgCl_2$ deliquescence point, thus sea-salt brines on the surface can concentrate, potentially dry out, and re-wet over the course of this exposure cycle. As the solution chloride concentrations increase during dry-out (due to equilibration of the brine with the surrounding atmosphere), an enhancement of the corrosion rate may occur [91]. However, this may compete with periods of dry-out (lower RH) or less concentrated brines on the surface (higher RH). The purpose of these long-term cyclic exposures is to determine the influence of the cyclic environment, material surface finishes, and alloy composition on the resultant corrosion damage across exposed coupons, and evaluate the maximum pit size possible under canister relevant cyclic diurnal conditions to further parameterize the maximum pit size model. This will provide better pitting predictions, as these environments more closely mimic those actually observed at ISFSI locations, and will also better inform overall CISCC predictions across these canisters.

3.2.1.1 Experimental Setup and Cyclic Exposure

A modified LogoJet Pro H4-2400 industrial inkjet printer was used to print artificial seawater (ASTM D1141) onto stainless steel coupons at an ambient RH of 80% and temperature of 21 ºC. This procedure follows the same procedure that was performed by Weirich et. al. [60, 68]. The purpose of using an inkjet printer is to produce uniform fields of picoliter-sized droplets with a salt load density of 300 µg/cm^2 over the entire surface of the coupons [68]. Salt was printed on coupons of 316L, 304, and 304H with both a mechanically ground #4 (equivalent to a 60 - 120 grit finish), hand ground 600 grit surface finish, and a subset of #8 (mirror polish finish) coupons. All salt printed coupons were then placed in humidity chambers following a 24-hour diurnal cycle repeated over the exposure that is demonstrated in Table 10. Since the RH fluctuates from roughly 27% to 50%, NaCl remains primarily precipitated out of solution (the conditions are below the NaCl deliquescence RH), leaving an Mg-Cl-rich brine present on the surface

[89, 92-94]. The temperature and RH cycles can lead to further brine dry-out followed by re-wetting [95]. The sample exposure matrix is presented in Table 11 with a subset of exposures for mirror polished coupons in Table 12. Samples will be removed after exposure times of 1, 2, 4, 26, 52, and 78 weeks (or 104 weeks dependent on extent of corrosion damage). A smaller matrix of mirror polished coupons (fewer coupons and time pulls) was exposed as results under static conditions revealed no corrosion damage across mirror polished surfaces [95]. Therefore, only a smaller mirror polished subset was exposed under cyclic conditions for comparison.

Table 10. Calculated cyclic atmospheric parameters modeled after Arkansas nuclear 1 weather data.

Hour	Temperature, ºC	RH, %
2	41.68	30.33
4	36.45	41.68
6	35.27	43.92
8	34.35	46.69
10	33.69	48.68
12	32.74	49.54
14	33.44	49.57
16	38.24	40.98
18	40.55	34.62
20	42.69	30.62
22	43.51	27.82
24	42.97	29.15

**Note: Cyclic chamber can only be programmed out to 0.1 decimal place, thus conditions here were rounded for exposure inputs.*

Table 11. Cyclic sample exposure matrix.

Sample	Artificial Seawater Deposition	Surface Finish	Cycle		Exposure Time (weeks)						Total
	μg/cm²	*Grit/polish*	*Site*	*0*	*1*	*2*	*4*	*26*	*52*	*78 / 104*	
304H	300	120	Arkansas Nuclear 1	2	3	3	3	3	3	3	20
304H	300	600	"	2	3	3	3	3	3	3	20
304	300	120	"	2	3	3	3	3	3	3	20
304	300	600	"	2	3	3	3	3	3	3	20
316L	300	120	"	2	3	3	3	3	3	3	20
316L	300	600	"	2	3	3	3	3	3	3	20
Total:				12	18	18	18	18	18	18	120

Table 12. Subset of cyclic sample exposure matrix for mirror polished coupons.

Sample	Artificial Seawater Deposition	Surface Finish	Cycle		Exposure Time (weeks)						Total
	μg/cm²	*Grit/polish*	*Site*	*0*	*1*	*2*	*4*	*26*	*52*	*78 / 104*	
304H	300	Mirror	Arkansas Nuclear 1	2	2	-	2	2	2	-	10

3.2.1.2 Post exposure analysis

Post exposure corrosion damage analysis was carried out with optical and SEM imaging both pre-corrosion product removal, as well as imaging post corrosion product removal. Additionally, profilometry was applied to analyze pitting statistics across the samples. Comparisons will be made to previous static exposures of similar coupons [69]. For optical imaging, a Keyence VHX-5000 Digital Microscope was used to examine coupons post-exposure but prior to removal of corrosion product. For further examination of corrosion damage, corrosion products and excess salts were removed by scrubbing the sample surfaces with a Nylon bristle brush in deionized (DI) water and then sonicating in 10 vol. % HNO_3 for 60 minutes, followed by a rinse in DI water, and drying with compressed air [68]. Once cleaned, all corrosion damage was imaged using a Zeiss Gemini 500 Field Emission Scanning Electron Microscope (SEM) at 20 kV accelerating voltage with secondary electron as well as back scattered scans.

A Zygo Nexview 3D optical profilometer was used to measure pitting damage and statistics on all coupons post-exposure and post corrosion product removal. The profilometer was set to measure with green light, a 5X objective, a lateral resolution of 1.46 μm, and a vertical resolution of <1 nm. Three 12 x 12 mm areas were measured on each coupon with each measurement taken at least 5 mm away from the edge of the sample, similar to previous studies performed by Weirich et al. [68].

Corrosion damage was quantified by pitting density (number of pits per square cm), pit volume (total volume loss per square cm), and pit depth (ten deepest pits per sample). All pitting data was analyzed using Digital Surf Mountain Maps 8 profilometer software. To identify pits outside of the sample surface roughness, thresholding was applied within the Mountain Maps profilometry analysis software as follows. The threshold for all pits and defects was set at greater than 10.4 μm below the zero-plane to account for

surface roughness, similar to Weirich [68]. The pit volume was manually filtered based on the radii of the largest predicted pits with the assumption of a hemispherical pit (modeled for static conditions of an equivalent brine) and smallest lateral resolution (minimum of two pixels). The average and standard deviation was calculated for all measurements from each sample.

3.2.1.3 Initial Cyclic Exposure Results

In FY21, samples exposed under cyclic conditions for and up to 26 weeks for #4 and 600 grit coupons and up to 4 weeks for mirror polished coupons have been removed from exposure chambers and have undergone initial analysis. The results of which will be presented here and discussed in the following pages.

Optical images show significant amounts of surface rust and corrosion products on the rough ground (#4) samples (Figure 70 and Figure 71), yet it appears corrosion damage was visibly lower across the 316L coupons. Also, the surface staining observed across all 600 grit polished samples and mirror polish finished samples is much less severe as compared to the rough ground samples (Figure 71). On all finishes, residual salt particles are clearly still visible across the surfaces, however, are distributed differently across the different surface finishes. Analysis in FY22 will address identification of corrosion products as well as residual salts across the sample surfaces. Additionally, the surface staining (visible corrosion) decreases with a finer surface finish. After samples were characterized through optical microscopy, excess salts and corrosion products were removed and samples were then imaged in SEM.

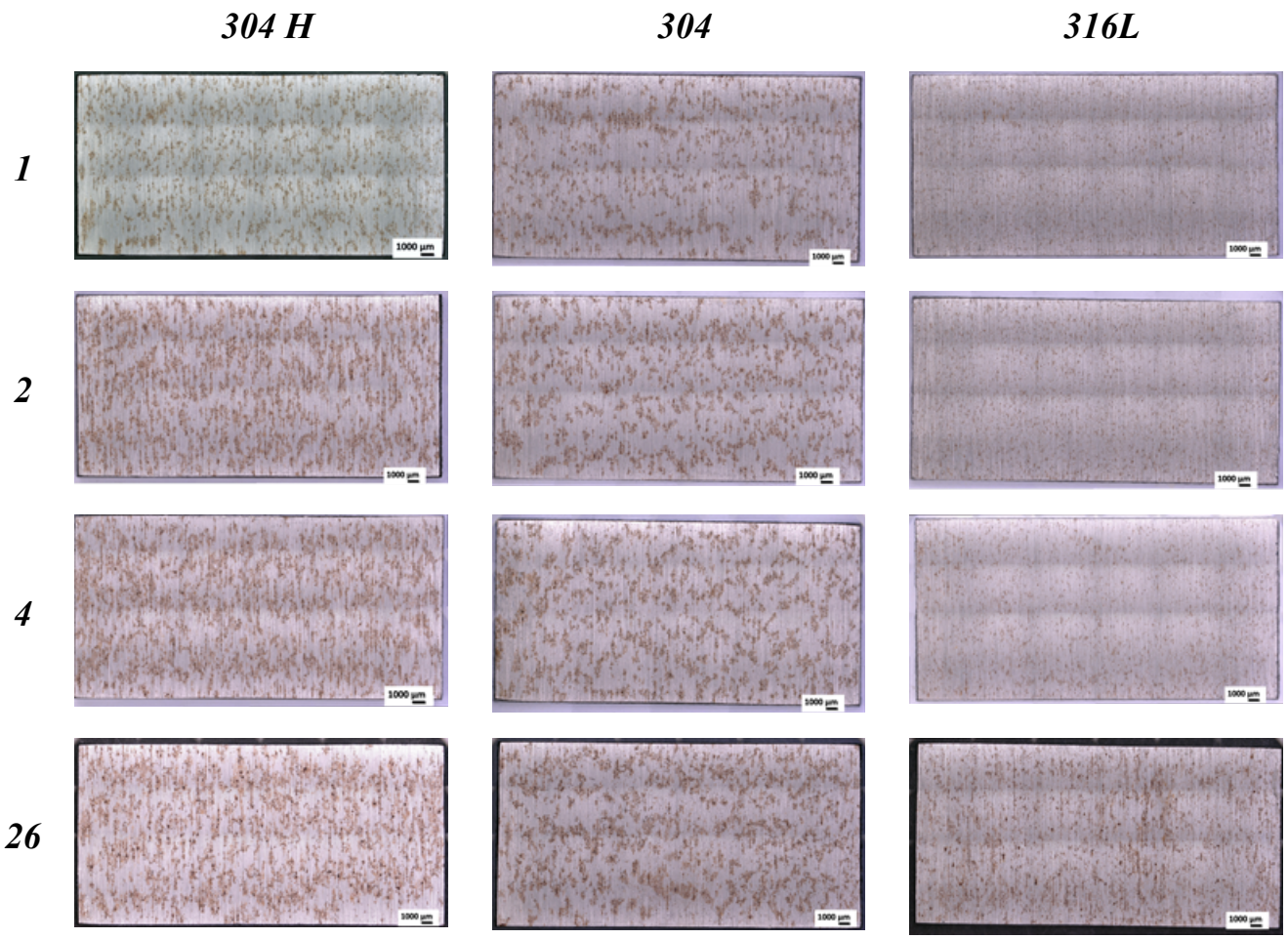

Figure 70. Optical imaging of post-exposure rough ground (#4 finish) 304H, 304, and 316 coupons versus exposure time in weeks.

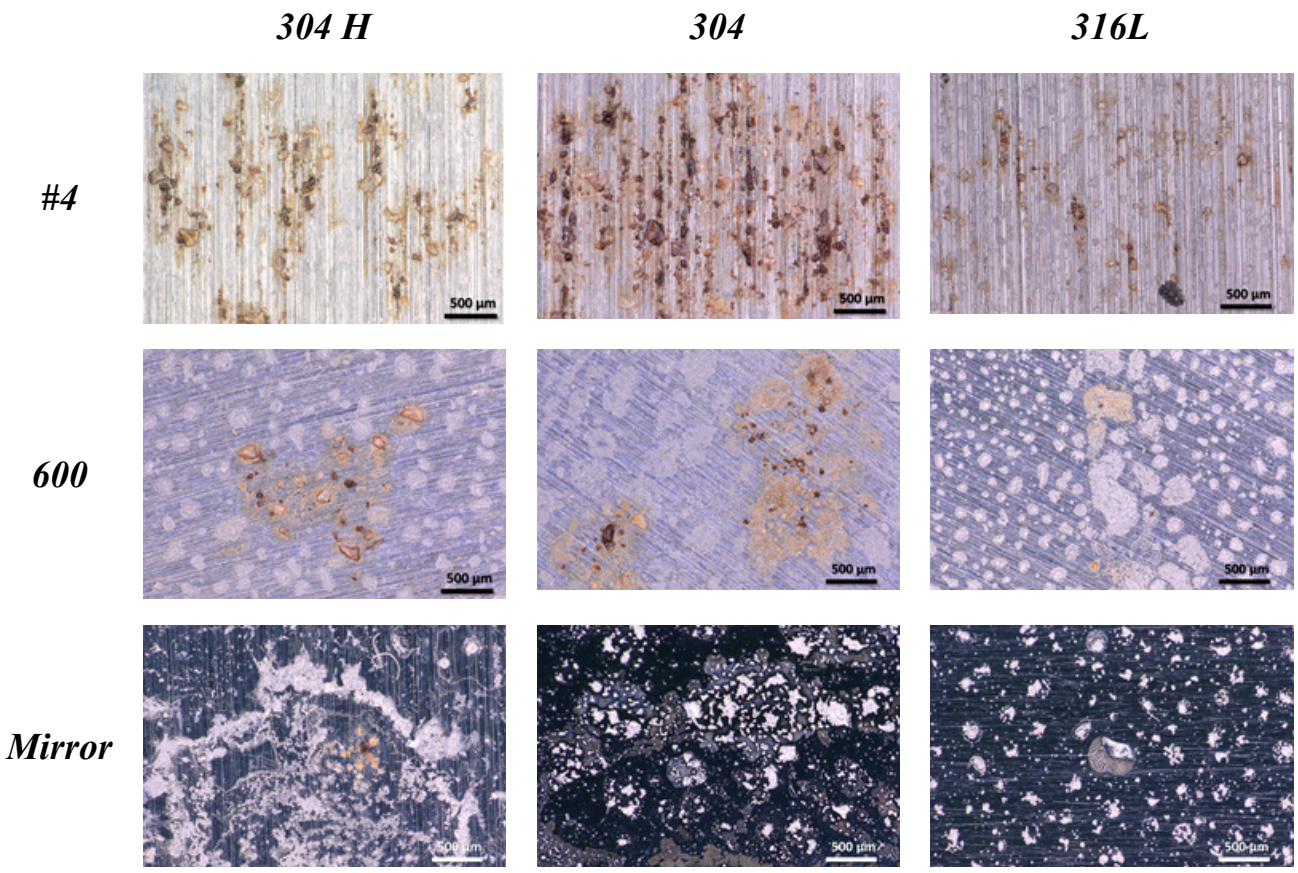

Figure 71. Optical image comparison of rough (#4 finish). 600 grit, and mirror finish for 1 week post-exposure 304H, 304, and 316L coupons.

Typical pit morphologies observed across the #4, 600 grit samples, and mirror polished samples are shown in Figure 72, Figure 74, and Figure 75 respectively. It is apparent from these images that pit morphology correlates both with surface finish and material composition. Across all rough ground, #4, exposures (Figure 72) pits are irregular in morphology, exhibit microstructural etching, and surface microcracking. These microcracks are further identified in higher resolution images in Figure 73, where yellow arrows point to example microcracks in each image. These microcracks are only observed on samples with a #4 rough grind finish, but are observed across all material types. In FY22, efforts will focus on quantification of near surface residual stress as well as potential further microstructural influences that may lead to these microcracks.

For the 600 grit samples, differences in pit morphology across material type are much more apparent (Figure 74). Only the 304H coupons display microstructural etching within the pits and have more irregular morphologies (Figure 74). The 304 and 316L coupons exhibit pits that are much more hemispherical in nature, with crystallographically faceted bases. However, both coupons do show signs of crevice corrosion around the mouths of the pits (shallow, wide areas of corrosion damage), likely due to enhanced corrosion at the surface under precipitated salts [89].

Finally, unlike previous static coupon exposures reported on in FY20, mirror polished coupons exposed under cyclic conditions did exhibit corrosion damage. Typical pits observed are shown in Figure 75, where again, only the 304H coupons displayed microstructural etching. The 304 and 316L coupons again have hemispherical, crystallographically faceted pits, however they do not show signs of crevice corrosion around the mouth of the pits.

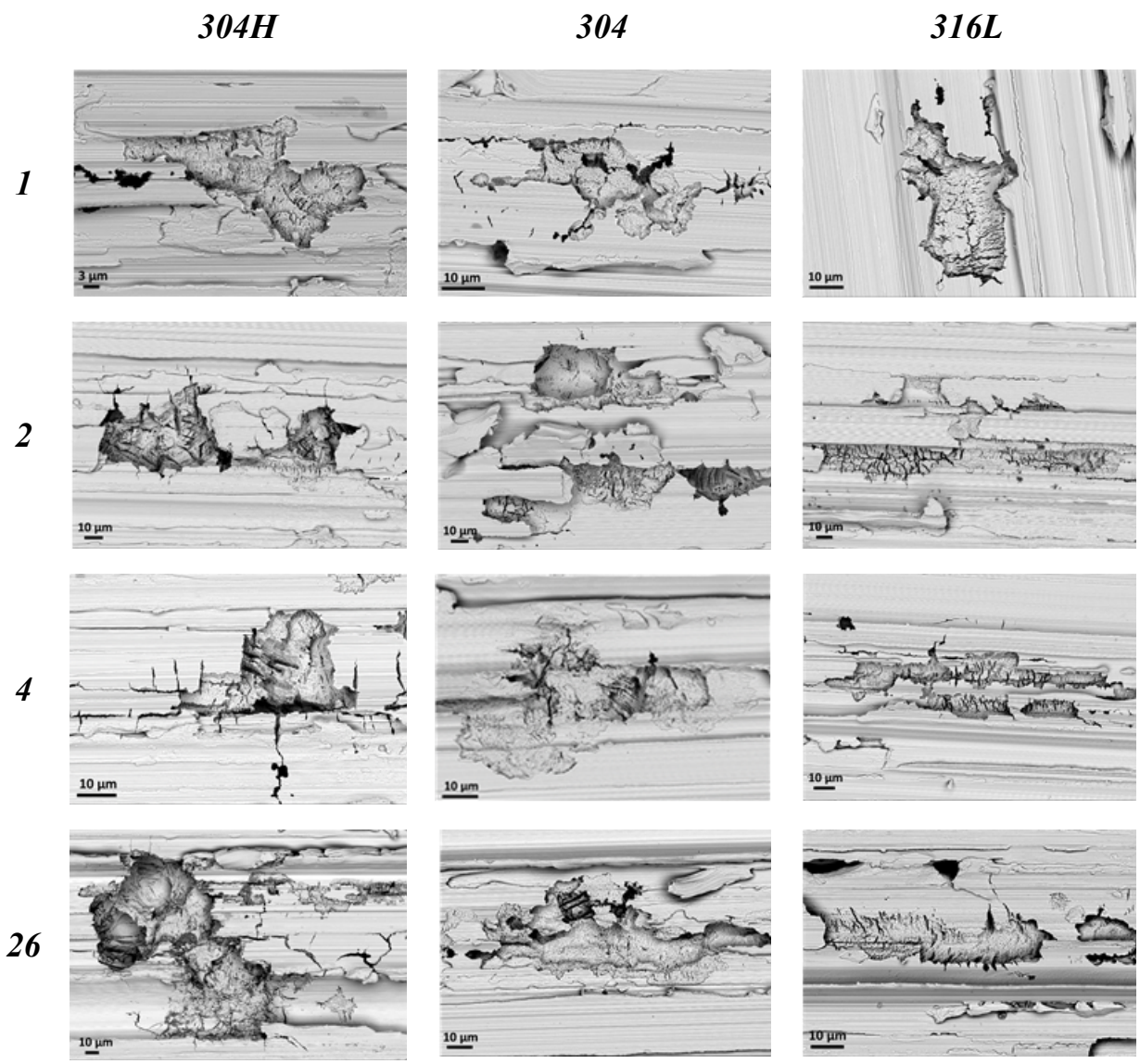

Figure 72. Representative SEM images of post-exposure rough ground (#4 finish) 304H, 304, and 316 coupons versus exposure time in weeks.

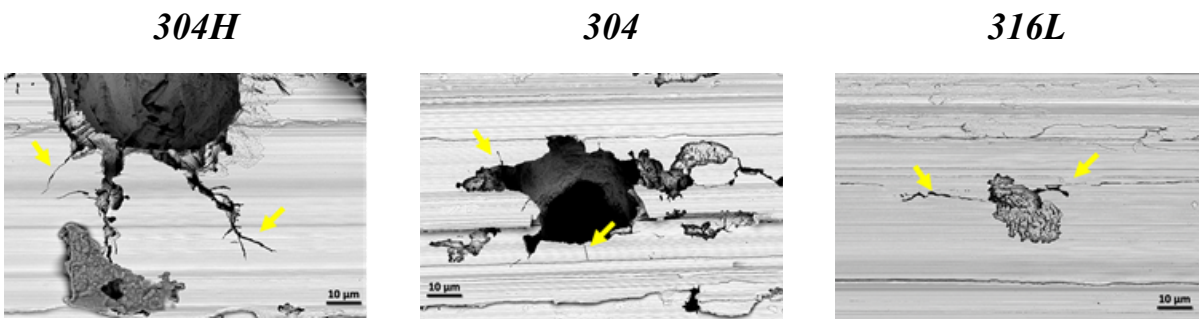

Figure 73. Representative SEM images of microcracks (identified by yellow arrows) in post-exposure rough ground (#4 finish) 304H, 304, and 316 coupons exposed for 26 weeks.

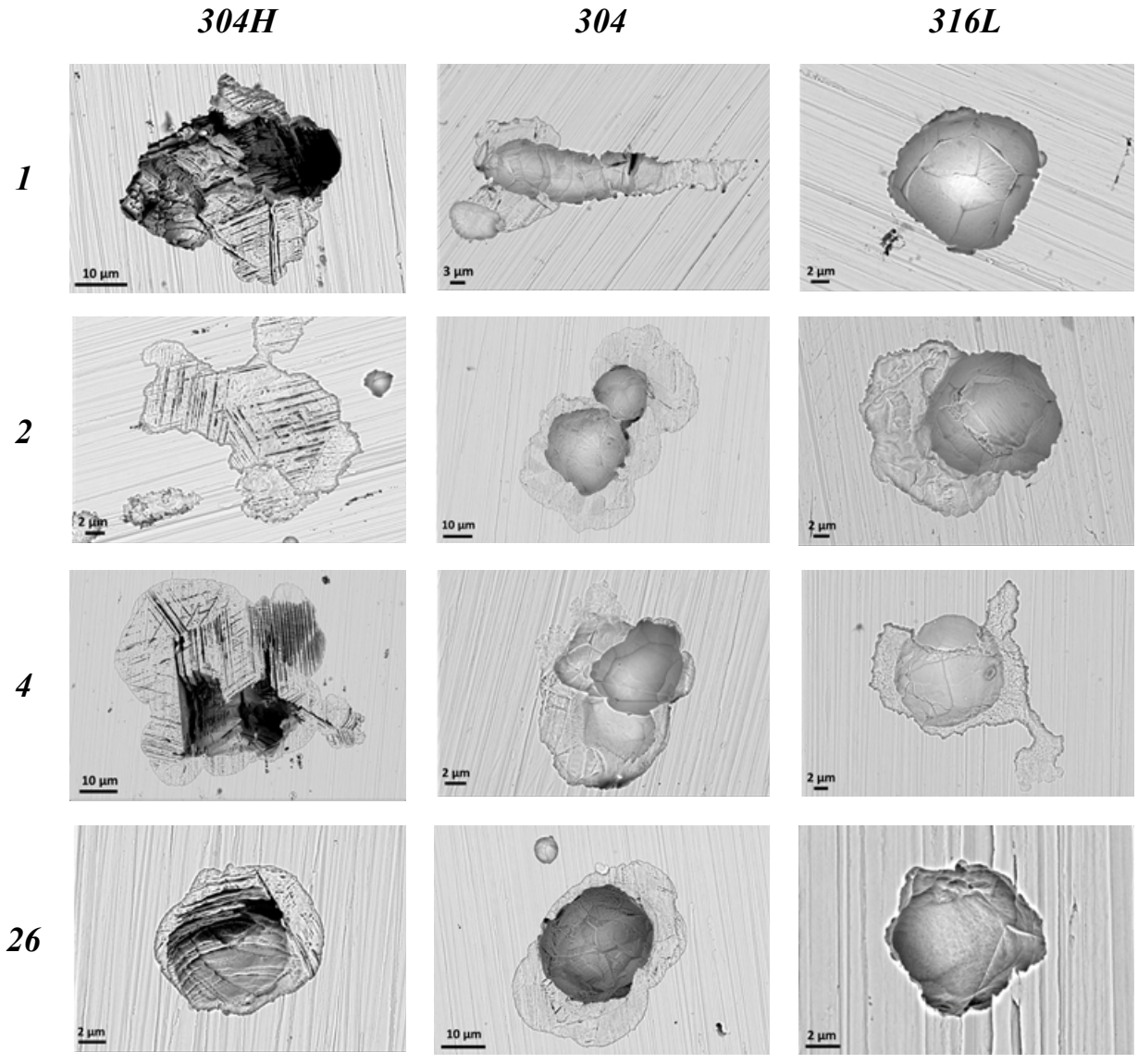

Figure 74. Representative SEM images of post-exposure 600 grit ground 304H, 304, and 316 coupons versus exposure time in weeks.

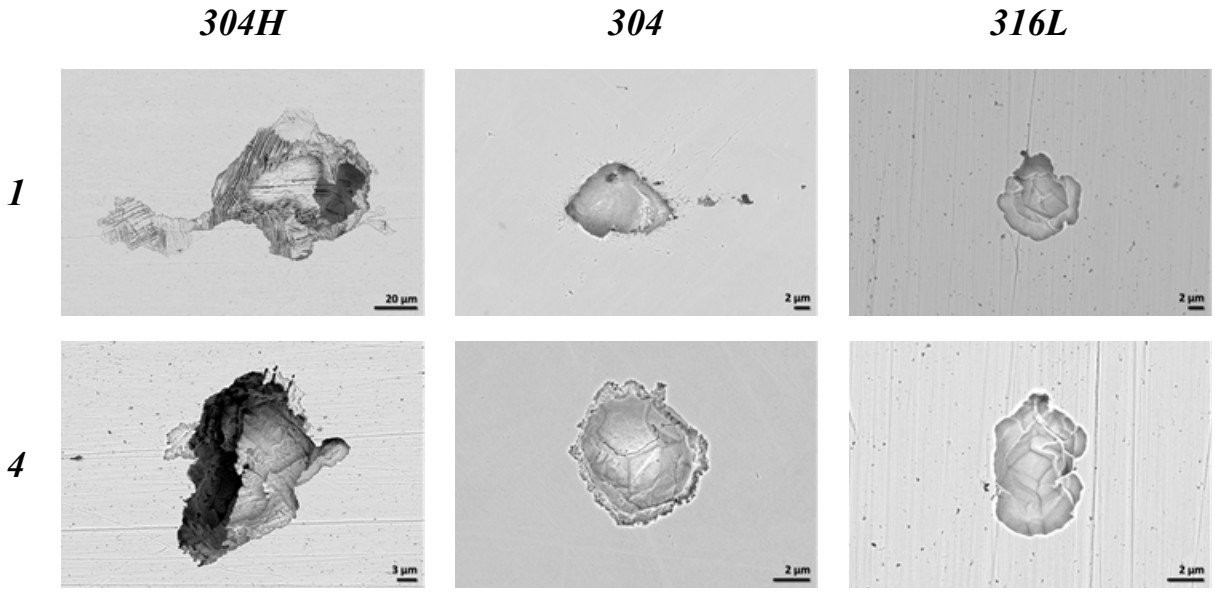

Figure 75. Representative SEM images of post-exposure mirror polished 304H, 304, and 316 coupons versus exposure time in weeks.

In an attempt to further explore the influence of surface roughness on the morphology and extent of corrosion damage, a short full immersion exposure was carried out in sea-salt equivalent brines of 40 and 76% RH at 35 ^{o}C for two weeks. Samples of a #4 surface finish were compared to a 120 grit hand ground surface finish (comparable roughness) in each condition. As can be seen in the post exposure SEM images in Figure 76, the micro-cracking is still only readily apparent on the #4 surface finish coupon under the $MgCl_2$ dominated brine (40% RH). The 120 grit ground coupon displays microstructural etching at 40% RH, but no microcracking. The samples exposed in 76% RH equivalent brine display neither.

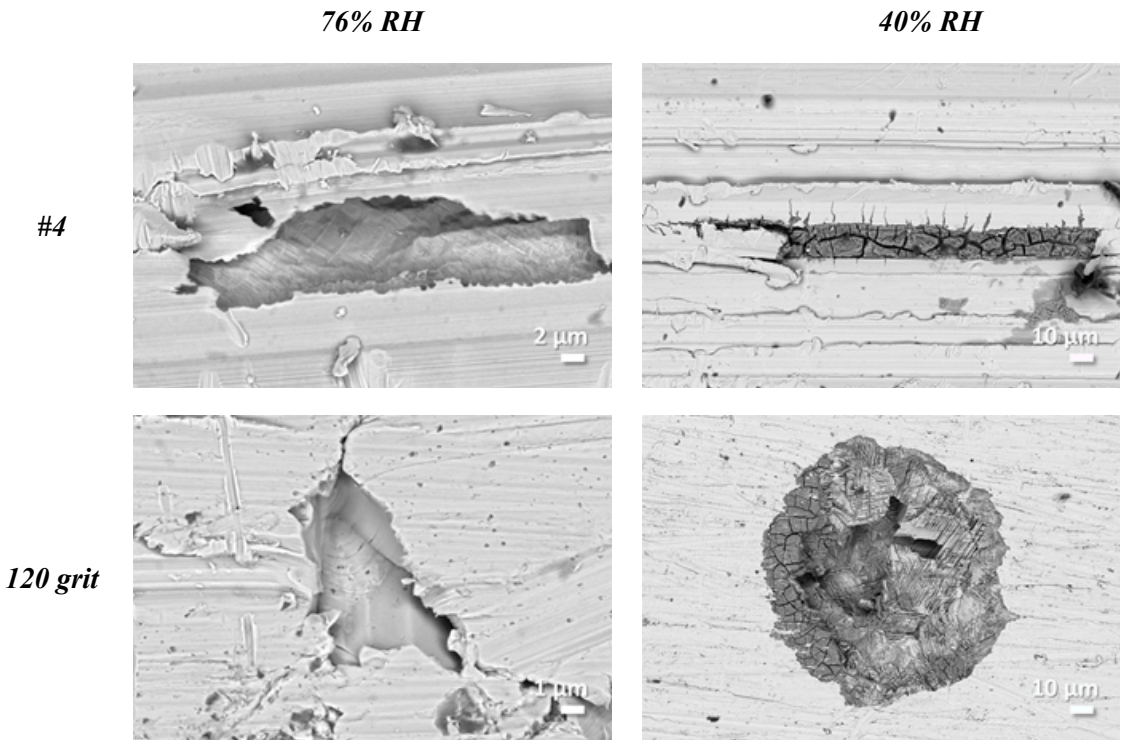

Figure 76. Representative SEM images of post-exposure full immersion in 76 and 40% sea-salt brines for 304H coupons versus surface finish. *Note not all corrosion product has been removed from the surfaces.

Post exposure and post corrosion product removal, initial profilometry measurements were collected for #4 finish 304H coupons and compared to two time-exposure intervals collected from previously exposed 304H coupons under static exposure [69]. These were printed with the same sea-salt deposition of 300 µg/cm^2 and exposed at 40% RH and 35^{o}C for 6 months and 1 year. While these are the same coupons exposed in [69] and [68], profilometry measurements were retaken at SNL and analyzed using the exact same procedure applied here to avoid differences or potential discrepancies across measurement formats. From the initial comparison of profilometry results, it is difficult to discern a difference in these two exposures (Figure 77). It appears that the cyclic results fall in line with those taken on the static coupons for all measurements taken (density, ten deepest pits, and volume loss), however the 6 month coupon for the cyclic exposures exhibits much lower values for density and volume loss. This may be an anomaly, but to confirm, further testing of additional 6 month cyclic exposure coupons will be carried out in FY22.

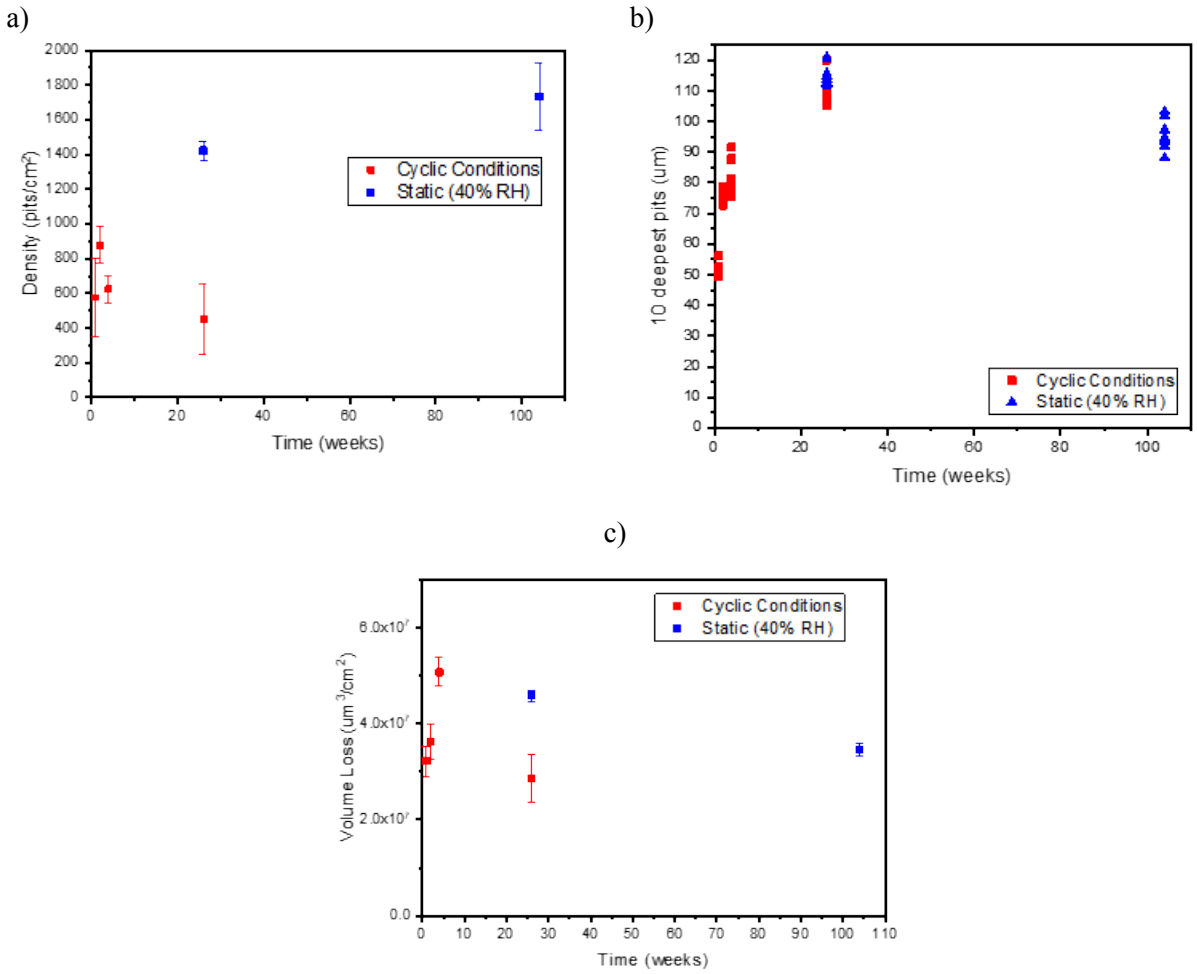

Figure 77. Initial profilometry results for 304H #4 finish coupons exposed under cyclic conditions for up to 4 months as compared to static (40% RH, 35°C, 300 µg/cm² seasalt) exposures for 6 months and 1 year for a) density, b) ten deepest pits, and c) volume loss.

Additionally, as the cyclic exposure coupon matrix is completed and removed from the exposure chambers, increased datasets will be collected. Coupons will be examined across all material types and surface roughness and general trends from profilometry will become more apparent. In FY22, further analysis with SEM combined with ImageJ software (for measurement of density and area of pits) and cross sectioning of coupons (for pit depths) will be performed. Initial profilometry measurements are difficult to obtain from the #4 finish samples as surfaces are extremely rough, and a potentially significant amount of pit information is lost due to thresholding techniques. FY22 will focus on development of improved procedures (including the aforementioned SEM and cross sectioning) to enhance quantitative measurements of pitting statistics across these exposure samples.

3.2.2 Impact of Inert Dust on Corrosion

As discussed in FY20, dust present on the SNF canisters may impact how the brine interacts with the canister surface as well as the form and severity of subsequent corrosion damage. In FY21, tests were performed co-depositing quartz dust with artificial seawater on SS coupons. MIN-U-SIL® 5 (~ 5 µm), a well-sorted, high-purity crushed quartz, was selected as an analog for the small size fraction of detrital grains on canister surfaces. SIL-CO-SIL® 75 (~ 75 µm) quartz dust was selected for testing to evaluate potential dust crevicing, representing larger dust sizes. The effects on corrosion of each size fraction will

be evaluated individually, and with a mix of both sizes, which will be used to examine coupled effects representing a wide distribution of dust present on the canister surface.

3.2.2.1 Experimental Setup and Dust Evaluation

In FY21, SNL continued to develop the test capabilities to deposit dust and ASW on SS coupons and began coating coupons for corrosion exposure testing. It was determined that coating the SS coupons with ASW first and then with dust would be the most straightforward method and would allow for the most accurate determination of the total mass of ASW and dust deposited onto the coupons. Several tests were performed to determine the deposition efficiency, dust sizes, and dust distribution for both SIL-CO-SIL® 75 and MIN-U-SIL® 5 dusts.

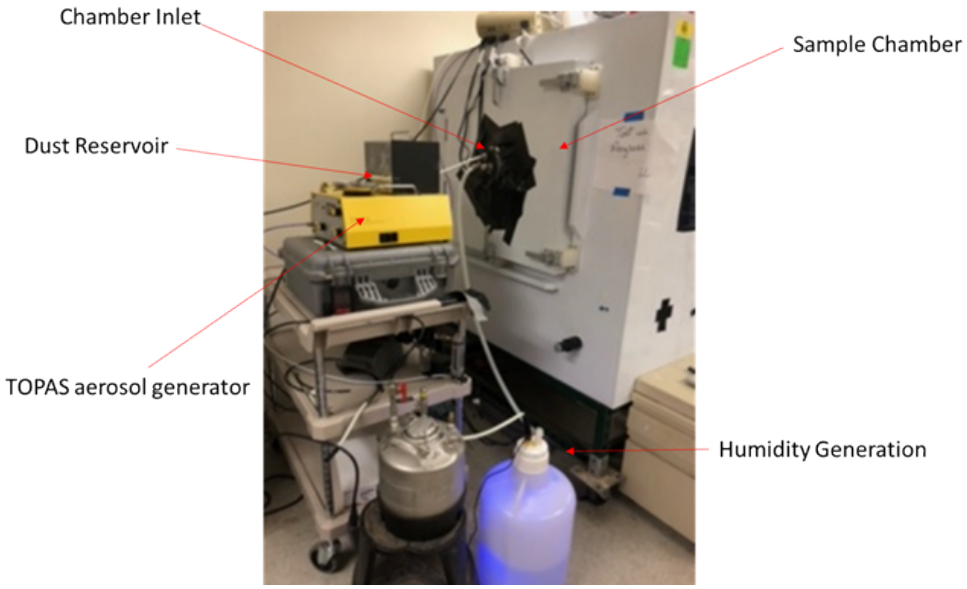

Figure 78. Experimental set up for the dust deposition using the TOPAS aerosol generator and SIL-CO-SIL® 75.

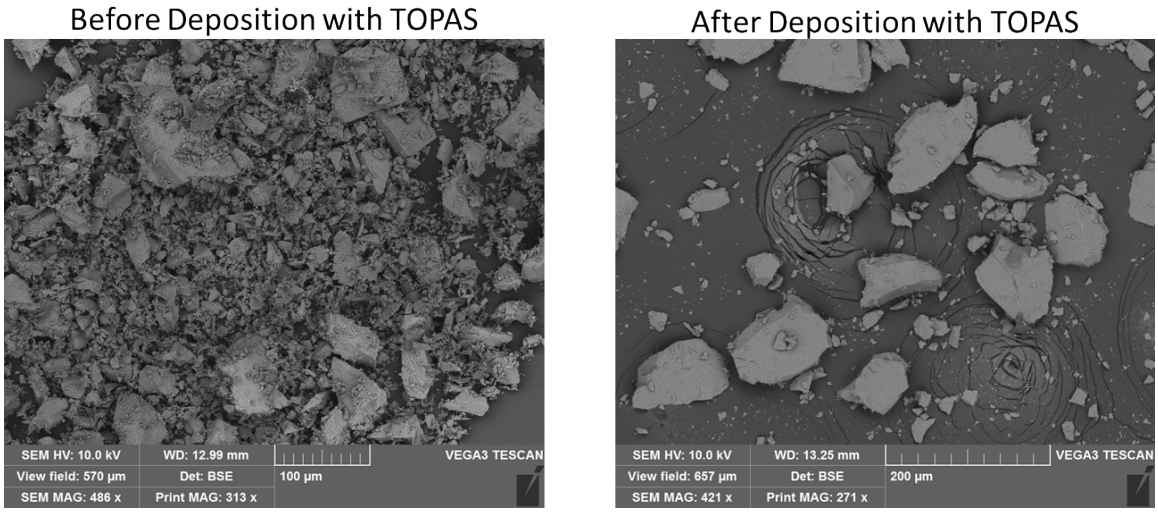

Figure 79. SEM image of SIL-CO-SIL® 75 dust analyzed as is (left) and after deposition using the TOPAS system (right)

Experimentally, the dust was deposited onto SS coupons that already had ~300 µg/cm^2 sea salt (deposited using an ink jet printer [60]). The SIL-CO-SIL® 75 was deposited using a TOPAS SAG 410, with the RH held at ~45-50 % during deposition. At this RH, the $MgCl_2$ in the salts was deliquesced (but not the NaCl), such that the surface of the SS coupons was slightly wetted at the time of dust deposition. This allowed for better adherence of the dust to the surface and reduced potential static issues. The surface was not fully wetted to avoid redistribution or pooling of the salts into larger droplets/deposits. Following injection of the dust, the humidity generation ceased (allowing slow equilibration to the ambient RH), and the dust was allowed to settle out of the air for several hours. The coupons were then weighed to determine the mass change resulting from the deposited dust. The experimental set up is shown in Figure 78. SEM images of the SIL-CO-SIL®75 were acquired prior to and following deposition to evaluate the distribution and particle sizes of the dust (Figure 79). As shown from this image, while there are large dust particles were present, there were also a significant amount of small dust particles in the SIL-CO-SIL® 75, and many of those small particles were deposited by the TOPAS. This is unacceptable, as the goal of the experiment with SIL-CO-SIL® 75 is to evaluate the potential for crevice corrosion to occur when only large dust particles are present. As there were smaller dust particles present in the SIL-CO-SIL® 75, it represented more of a mixed system than anticipated, and thus would convolute the two hypothesized potential factors influencing corrosion in the presence of dust. To mitigate this issue, SIL-CO-SIL® 75 was size fractionated using a column settling procedure based on Stokes Law, shown in Equation 5.

$$W_s = \frac{(P_s - P) * g}{18\mu} * d^2 \qquad \text{(Eq. 5)}$$

Where W_s is the settling velocity, $(P_s\text{-}P)$ is the difference in density between the particles and the liquid, μ is the viscosity of the liquid, d is the particle diameter, and g is the force of gravity. Using a graduated cylinder filled with 1 L of DI H_2O, 20-30 g of the SIL-CO-SIL® 75 was added and the column was inverted several times to suspend the solids. Then the suspended dust was allowed to settle for 1.5 – 2 hours to separate the larger particles from the smaller, unsettled ones. The supernatant (containing small dust particles) was decanted, and the solids at the bottom of the cylinder were dried in an oven at 60 °C. The resulting dust is shown in Figure 80 and shows that the bulk of the small dust has been removed and only larger quartz grains remain. The size fractionated dust was used for the dust deposition experiments with SIL-CO-SIL® 75.

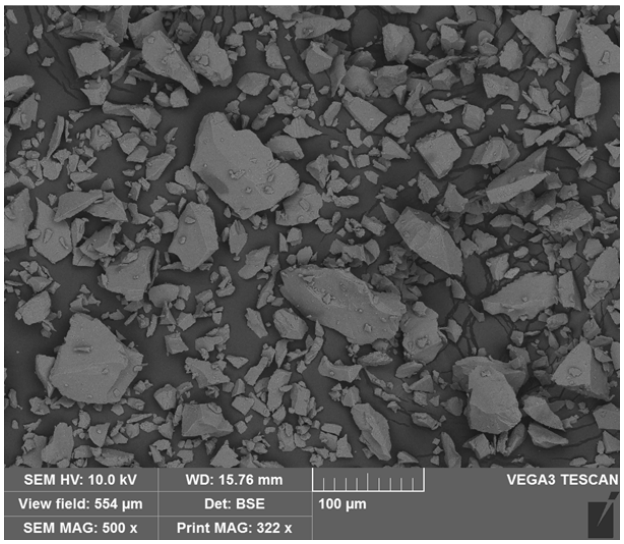

Figure 80. SEM image of SIL-CO-SIL® 75 quartz dust after a particle settling procedure.

Following dust deposition, a SS coupon containing pre-printed sea salt and dust was analyzed by SEM/EDS to assess the uniformity of the dust deposition across the sample and the size distribution of dust. Figure 81 shows large NaCl crystals aproned by crystals of other seawater evaporites — including other chloride and sulfate bearing salts. The Si-elemental map, representing the quartz dust, is shown in pink. It is clear that the dust randomly distributes across the coupon surface and does not segregate around the sea salt. There is some unique cross-hatching of NaCl in the bottom and bottom-right side of the image; this may be an indication that some of the NaCl deliquesced. However, the bulk of the NaCl appears to be intact as large halite crystals. In FY21, all of the coupons for investigating the impact of large dust have been deposited with the size fractionated SIL-CO-SIL® 75 and placed in environmental chambers for either static or cyclic exposure (Table 14 and Table 13). Current work is evaluating the actual particle size distribution as the aerosols are generated from the TOPAS system and deposited on the coupons.

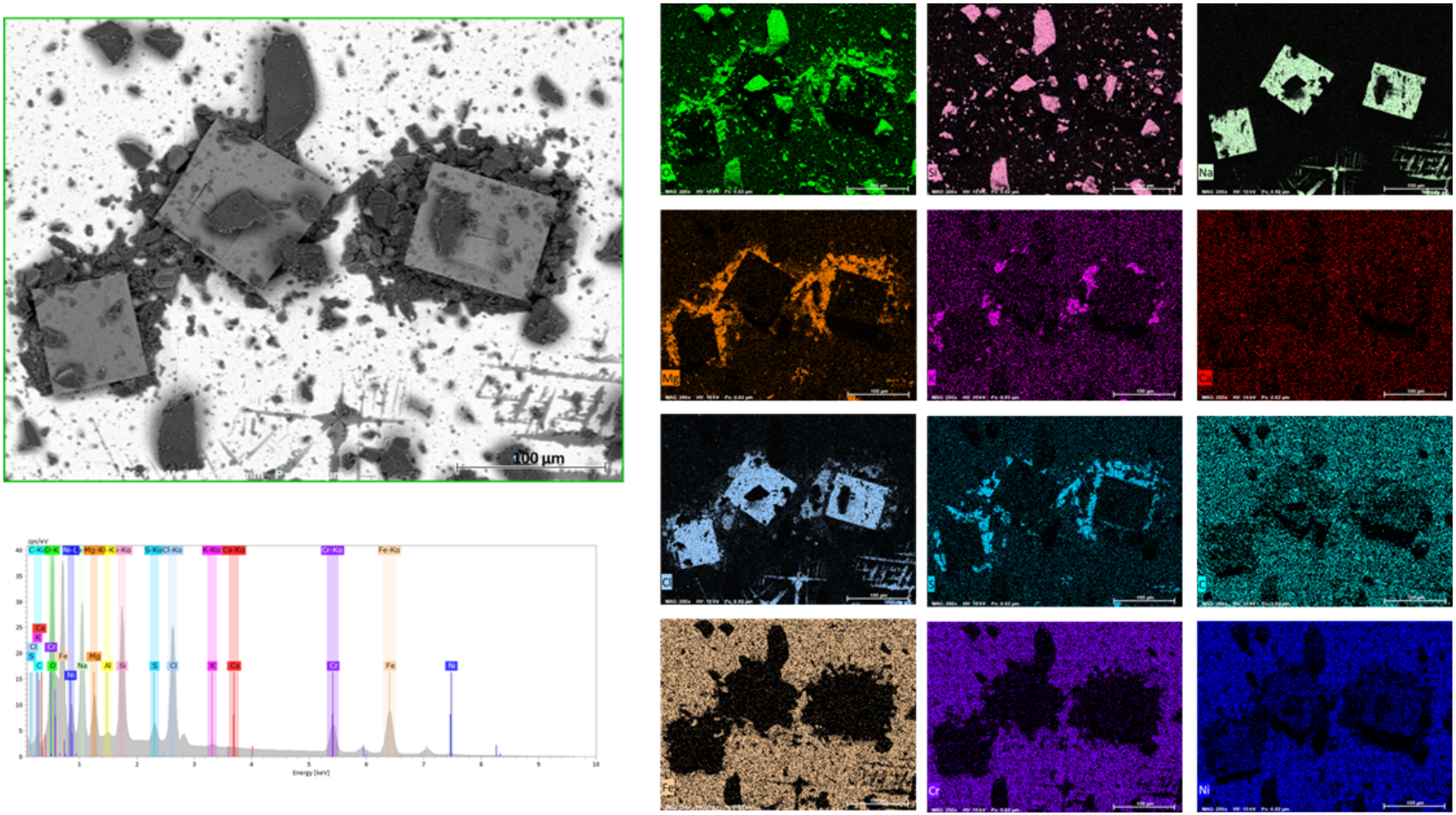

Figure 81. SEM/EDS analysis of SIL-CO-SIL® 75 dust deposited on a coupon previously coated with sea salt.

The MIN-U-SIL® 5 was characterized by SEM (Figure 82), and it was determined that no additional settling procedures were necessary prior to deposition, as the distribution of small dust seems appropriate to test the hypothesis that small dust particles will create a more uniform brine layer. However, it was not possible to deposit the MIN-U-SIL® 5 using the TOPAS in the same way as the SIL-CO-SIL® 75 because the smaller dust particles tend to clump together, likely due to static, and therefore did not deposit evenly. Additional work is ongoing to determine how to effectively deposit the MIN-U-SIL® 5 evenly on SS coupons coated with sea salt. Some characterization studies using a fluidized test bed for deposition have yielded predictable and consistent results, and therefore in FY22, final experimental characterization tests for MIN-U-SIL® 5 will be performed and deposition on exposure coupons will begin.

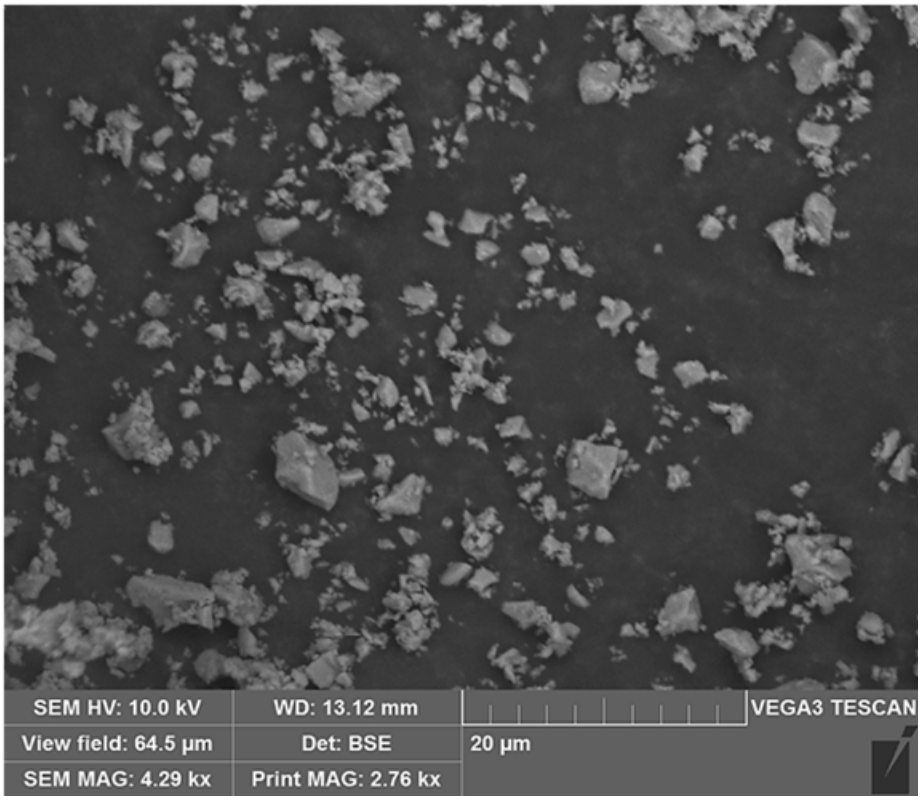

Figure 82. SEM images of the MIN-U-SIL® 5 quartz dust.

3.2.2.2 Environmental Exposure

Following deposition, coupons deposited with ~300 µg/cm^2 sea salt and ~300 µg/cm^2 of inert dust will be exposed to atmospheric corrosion conditions similar to those of samples without dust, to evaluate the role of dust on corrosion morphology and severity. These corrosion studies will involve exposures for up to 2 years with periodic sampling at specific time intervals. The coupons used in this study are mirror polished, and previous testing under static exposure conditions resulted in minimal, if any, corrosion – this result is summarized in the SNL FY19 status report ([76; Section 4.2]. Comparing the previous results to those of the dust coupons will allow for direct evaluation of the role that inert dust may have on corrosion. In FY22, exposure testing will begin; one sample set will be exposed to static atmospheric conditions for 24 months at either 75% RH and 50°C, or 40% RH and 50°C, corresponding to the Na-rich and Mg-rich brines, respectively (Table 13). In the exposure at 75 % RH, NaCl will have deliquesced and therefore any visible crevice corrosion can be attributed to the presence of the large SIL-CO-SIL® 75 dust particles. In contrast, when coupons are exposed to 40% RH and 50°C, the brine volume will be smaller, and NaCl will still be present as a solid; the deliquesced brine will be much smaller volume, and will be $MgCl_2$-rich. Under these conditions, both the SIL-CO-SIL® 75 and the halite crystals may act as crevice

formers. The tests with MIN-U-SIL® 5 will allow for an evaluation of brine spreading and the cathode size.

Table 13. Test matrix for samples being analyzed for the impact of the presence of dust under static exposure conditions.

304 Coupon Size, in.	Condition	Dust Deposited	Count	1 mo.	6 mo.	12 mo.	24 mo.
8x8	75% RH 50ºC	SIL-CO-SIL® 75	2	0	0	1	1
		MIN-U-SIL® 5	2	0	0	1	1
		SIL-CO-SIL® 75/ MIN-U-SIL® 5 mix	1	0	0	0	1
		No Dust	1	0	0	0	1
4x4	75% RH 50ºC	SIL-CO-SIL® 75	5	0	1	2	2
		MIN-U-SIL® 5	5	0	1	2	2
		SIL-CO-SIL® 75/ MIN-U-SIL® 5 mix	5	0	1	2	2
		No Dust	3	0	1	1	1
2x2	75% RH 50ºC	SIL-CO-SIL® 75	10	2	2	3	3
		MIN-U-SIL® 5	9	2	2	2	3
		SIL-CO-SIL® 75/ MIN-U-SIL® 5 mix	9	2	2	2	3
		No Dust	4	1	1	1	1
	40% RH 50ºC	SIL-CO-SIL® 75	10	2	2	3	3
		MIN-U-SIL® 5	10	2	2	3	3
		SIL-CO-SIL® 75/ MIN-U-SIL® 5 mix	10	2	2	3	3
		No Dust	4	1	1	1	1
2x1	75% RH 50ºC	SIL-CO-SIL® 75	11	2	3	3	3
		MIN-U-SIL® 5	11	2	3	3	3
		SIL-CO-SIL® 75/ MIN-U-SIL® 5 mix	11	2	3	3	3
		No Dust	5	1	1	1	2

A subset of mirror polished samples will be exposed to cyclic conditions. No pitting was observed on mirror polished coupons with sea salt under static conditions, but as noted in Section 3.2.13.2.1.3, pitting was observed on mirror polished coupons in a cyclic environment, and the presence of dust may further enhance that. The specific cyclic conditions are described in detail in Section 3.2.1, and the test matrix is shown in Table 14. The results of these analyses will be compared to coupons coated with sea salts and exposed to cyclic conditions, as well as coupons with deposited sea salt and dust exposed to static exposure conditions.

Table 14. Test matrix for samples being analyzed for the impact of the presence of dust under cyclic exposure conditions.

304 Coupon Size, in.	Condition	Dust deposited	4 weeks	6 Month	12 Months
2x1	Cyclic	MIN-U-SIL® 5	1	2	2
		SIL-CO-SIL® 75	1	2	2
	75 % RH 35 ºC	MIN-U-SIL® 5	1	2	1
		SIL-CO-SIL® 75	1	2	1
	40 % RH 35 ºC	MIN-U-SIL® 5	1	2	2
		SIL-CO-SIL® 75	1	2	2

Post-exposure analysis for corrosion damage will include optical microscopy, profilometry, and SEM, similar to that described in Section 3.2.1.2 Additional detailed analysis including extraction and evaluation of pit cross sections or other detailed techniques may be carried out to further examine corrosion morphology and extent. The data gained from the dust exposures will be compared to previous sea-salt only exposures to help characterize and understand the influence of inert dust.

3.2.3 Effect of Nitrate and other Anionic Components

Realistic near-marine brine chemistries are not solely sea-salts brine. They contain significant amounts of nitrate and sulfate, both from particle/gas conversion reactions with atmospheric gases, and because of the presence of a significant component of continental salts, which are enriched in these species. In the FY20 report [3], realistic near-marine brine chemistries were calculated based on soluble salt analyses of dust samples from two east coast near-marine ISFSI sites. These brines contained significant levels of nitrate and sulfate, and a relatively dilute solution composition was described for deposition of these salts using an inkjet printer. Using this approach, test coupons for exposure testing will be prepared.

The actual brines that will be present on the metal surface will vary with the exposure RH. In order to evaluate the electrochemical properties (open circuit potential, repassivation potential) of the predicted brines at the planned exposure RH, an attempt was made to mix bulk solutions of the brines at the predicted RH. However, a mixed Na-K sulfate phase precipitated; this phase was not present in the thermodynamic database used to calculate the solution compositions. Hence, while the predicted salt solutions can be deposited using an inkjet printer for atmospheric testing, the low-RH versions cannot be mixed in bulk concentrated solutions for electrochemical testing (e.g. cyclic potentiodynamic polarization scans). One possible solution is to mix the brines, fully equilibrate them with atmospheric CO_2 at the temperature of interest, and then filter out the precipitated phases before testing. This is currently being investigated.

The effects of nitrate on SCC crack stability and crack growth rates are being evaluated at PNNL [96]. Initial results indicate that nitrate has an inhibitory effect on SCC propagation, at least in two-component, $NaCl/NaNO_3$ brines. In order to better understand the results and how to extrapolate them to field conditions, electrochemical testing in the same brines is being carried out at SNL. The electrochemical testing will evaluate changes in open circuit potential and in the cathodic current density as well as potential pitting susceptibility as a function of nitrate concentration. The initial brines that will be tested are provided in Table 15 and Table 16.

Table 15. Composition of the proposed brine simulant, based on Main Yankee salts.

Species	Conc., molal	To mix:	
		Salt	Wt, grams
Na^+	2.417E-01	NaCl	5.3590
K^+	8.499E-02	$NaNO_3$	3.5070
Ca^{2+}	9.416E-03	KNO_3	8.5929
Mg^{2+}	3.209E-03	$CaCl_2$	1.0450
Cl^-	1.169E-01	$MgCl_2{:}6H_2O$	0.6524
NO_3^-	1.263E-01	Na_2SO_4	7.6789
SO_4^{-2}	5.406E-02	$NaHCO_3$	0.0543
HCO_3^-	6.467E-04	**SUM**	26.8896

Table 16. Composition of PNNL NaCl/$NaNO_3$ brines, for electrochemical testing.

$NaNO_3$/NaCl molal ratio	NaCl conc., molal	$NaNO_3$ conc., molal
5.9 molal NaCl		
1:0	5.9	0.0000
1:24	5.9	0.2458
1:12	5.9	0.4917
1:9	5.9	0.6556
4.3 molal NaCl		
1:0	4.3	0.0000
1:24	4.3	0.1792
1:9	4.3	0.4778
1:4	4.3	1.0750
1:2	4.3	2.1500
1:1	4.3	4.3000

Initial Electrochemical Testing:

In FY21, initial electrochemical testing was carried out to evaluate both the SNL calculated brines as well as those used by PNNL in their CISCC testing [96]. Brines were mixed at room temperature prior to electrochemical testing. For electrochemical testing, a three-electrode jacketed cell was used. Temperature was controlled by circulating water from an external water bath through the jacketed cell. A Pt-Nb mesh was the counter electrode and an Ag/AgCl reference electrode was used. Prior to testing, SS304 coupons were hand ground to 1200 grit within 10 min of exposure to avoid large differences in air-formed oxide layers, rinsed with deionized water, and dried with lab air. The samples were clamped into the cells, brine was introduced at 40 ^oC, and maintained at this temperature for the duration of the electrochemical experiment. Initial testing underway in FY21 has been applied to explore the required time for the open circuit potential (E_{OCP}) to stabilize prior to potentiodynamic polarization. A time of

20 h was selected after multiple, multi-day E_{OCP} acquisitions. Potentiodynamic anodic polarizations were acquired immediately following the E_{OCP} measurements at a scan rate of 0.1667 mV/s from -0.2 V vs E_{OCP} to 1.5 $V_{Ag/AgCl}$ or a current cut off of 10^{-3} A. Results of initial electrochemical testing will be analyzed in FY22 and further applied to develop relevant atmospheric exposures for pitting and SCC testing.

3.3 Pit to Crack Transition

Experiments in FY20, and carried on into FY21, elucidated potentially significant influences of $MgCl_2$ dominated brines on corrosion damage morphology, which may play a role in governing crack initiation. Initial studies in FY21 further evaluated these conditions and their potential influences on crack initiation. Specifically, work in FY21 at SNL sought to address hierarchal identification of features controlling pit to crack transitions (environment, material, pit morphology, etc.). It is significant to not only understand canister-relevant material and environmental influences on crack growth rates (which are being heavily studied both by PNNL and SNL), but also on the potential for cracks to initiate. This was established through work both at SNL and in collaboration with the Ohio State University and is detailed in the following sections.

3.3.1 Understanding the Influence of Pit Morphology on Crack Initiation

Over FY21, it has been shown that both environment and material properties play a large role in the resultant corrosion damage on stainless steel coupons under canister relevant conditions (sections 3.1.1 and 3.2.1). Existing models relate pit depth to crack initiation through the calculated crack tip stress intensity factor; however, most assume corrosion damage in the form of hemispherical shaped pits [5, 97]. When the local stress intensity at the surface of a pit exceeds an empirically-determined SCC threshold stress (i.e., $K > K_{ISCC}$), a crack can initiate from that pit. The relevance of this relationship and accessible limits of these models, in general, are unknown for storage canister conditions. A few studies have begun to explore the influence of irregular pit geometries (i.e., aspect ratios, asperities, etc.) on changes to stress concentrations around a pit and how this might affect the potential for pit to crack initiation [98, 99]. It is essential to understand these influences, because non-hemispherical, irregularly shaped pits with microstructural etching and surface microcracking have been observed across many laboratory atmospheric exposures under canister-relevant conditions (Section 3.2.1), as well as being observed on field-exposed coupons.

3.3.1.1 Modeling the Influence of Pit Shape on Stress Concentration

Efforts in FY21 have included modeling to evaluate the influence of irregularly-shaped pits on the stress distribution around a pit and to inform upon the subsequent susceptibility to crack initiation. While previous studies have employed either hemispherical geometries or simulated irregularities for finite element modeling (FEM) of stress concentrations, the goal of the work initiated in FY21 was to analyze real, observed pit geometries and to determine their potential influence on stress distributions around the pit, as compared to previously examined idealized structures. Pit geometries for this modeling effort were determined by measurement of pits through X-ray tomography (XCT) to obtain the full three-dimensional morphologies. XCT was performed as described in [69] on 304H coupons that were exposed with 300 $\mu g/cm^2$ sea salt under static 40 %RH and 35 ^oC for 52 weeks. The 3-D data sets were extracted as voxel data (as shown in Figure 83) and converted using a Python script to Forge Viewer files to develop an inverted model. This allowed for insertion of the inverted pit model into a finite volume model that can be manipulated with an externally applied stress. From this model, stress concentrations around the irregularly shaped pits can be calculated and compared to hemispherical and other model pit geometries (this will be a primary research focus in FY22). Results of these models will provide insight into the role of potentially deleterious pit morphologies on the transition of pit to SCC cracks.

a)

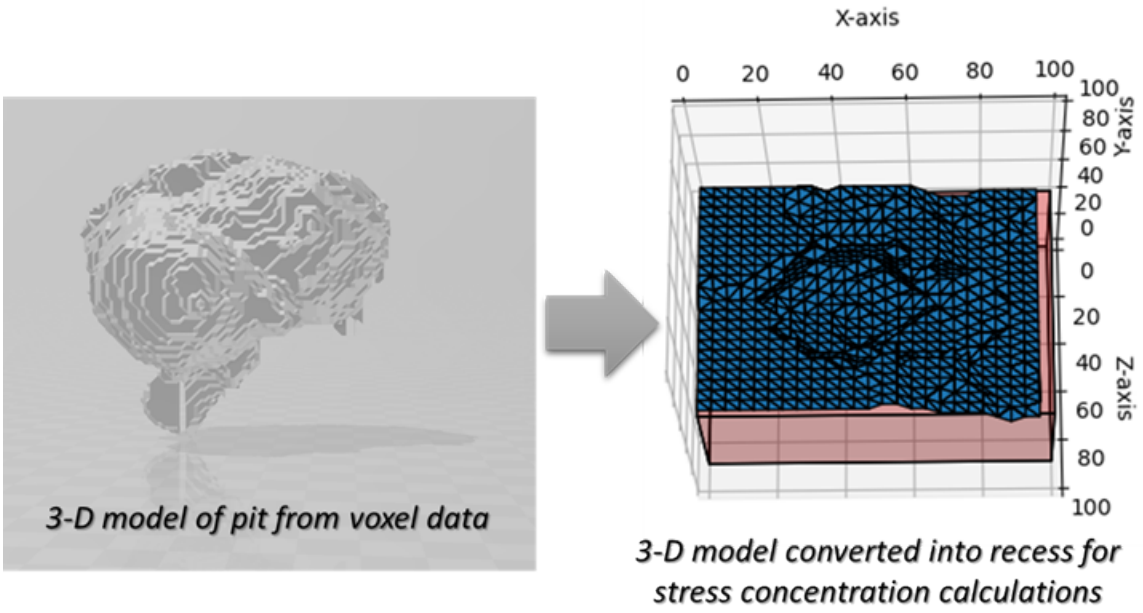

b)

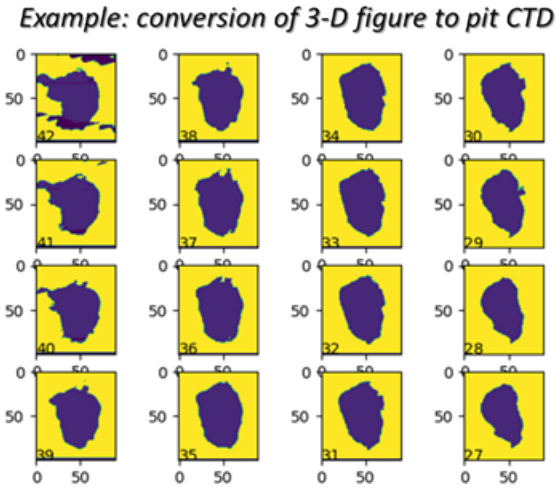

Figure 83. A) Example voxel dataset for a pit morphology in 304H stainless steel coupon exposed with 300 µg/cm² sea salt for 52 weeks at 40% RH and 35 °C with corresponding inverted 3-d model, and b) horizontal slices through the 3-D model.

3.3.1.2 Measurement of Brine Influence on Pit to Crack Transition

In addition to modeling efforts to better understand pit to crack transition, initial experiments were carried out in FY21 to evaluate the influence of brine composition on pit to crack transition. Specifically, samples were both evaluated under full immersion in equivalent 40% RH sea-salt brines and under atmospheric conditions exposed at 40% RH with sea salt printed on the exposed surface. The 40% RH conditions were selected as these were shown previously to produce large, irregularly-shaped pits on

stainless-steel surfaces[68, 69], which are suspected to be more deleterious for crack initiation. Additionally, these lower RH conditions are of particular interest as they are similar to those predicted to establish initially on canister surfaces[3].

The approach to understanding the controlling features for pit to crack transition, and their prevalence under ISFSI-relevant conditions, is to examine the cracking initiation behavior of 304L tensile test specimens exposed to relevant environmental conditions while under a tensile load. During the period of exposure, the specimens are held at a constant load with periodically introduced high R ripple fatigue load cycles, that are intended to introduce marker bands on the fracture surface along the crack front as it grows. These bands can be followed back to the point of crack initiation upon post-test SEM fractography examination [100]. As mentioned above, in FY21, initial tests were carried out via immersion in equivalent 40% RH sea-salt brines or in atmospheric conditions at 40%.

Tensile bars were pre-exposed (unloaded) to full immersion equivalent 40% RH sea-salt brine for 2 weeks to 5 months, followed by tensile loading with interruptions by ripple loading to insert marker bands. Post-mortem SEM analysis for one sample bar, pre-exposed while unloaded for 5 months in full immersion, followed by loading and the marker band ripple loading procedure, are shown in Figure 84. The loading and marker band testing on this sample were carried out for 2.5 weeks with a 6 hour hold at a maximum load of 612 MPa, then at 20 min cycles each at 1 Hz (1200 cycles), 0.1 Hz (120 cycles), and 0.01 Hz (12 cycles) between the maximum load and a minimum load of 421.3 MPa. Following this, the maximum load was increased to 630 MPa, with the same cycling procedure for 24 hours, at which point the tensile bar failed. Post-mortem SEM analysis was carried out on the crack face of the cracked open tensile bar after residual salt and corrosion product were removed (procedure in [68]). Images indicate that crack initiation likely occurred at a corrosion defect with microstructural etching (Figure 84-b). However, further analysis and testing is necessary to determine if these irregular shaped features were the likely cause of the crack initiation, and if so, if they have a greater influence or tendency to initiate cracking than hemispherical, smooth pits.

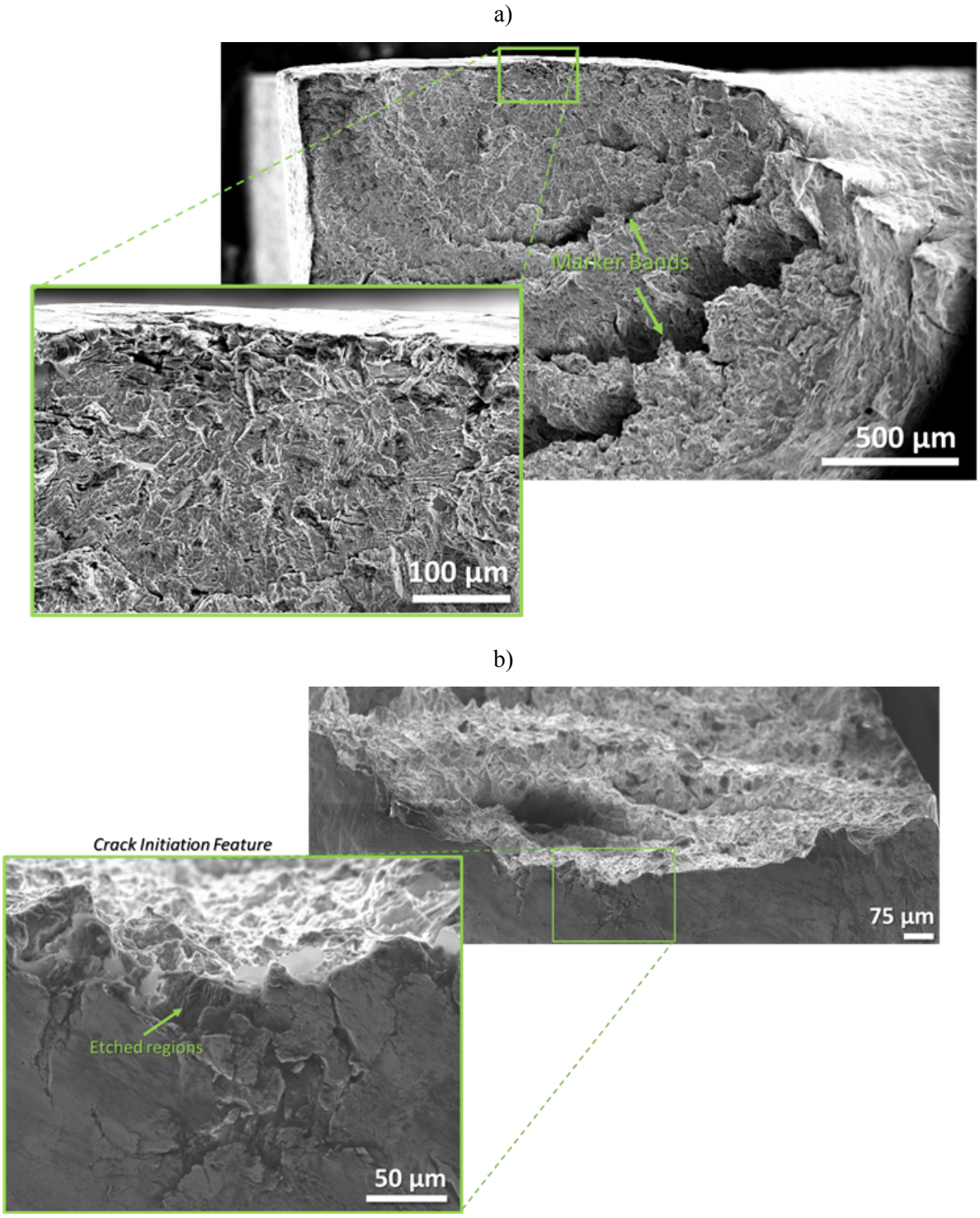

Figure 84. Full Immersion pit to crack post-exposure SEM analysis of a) marker bands centered around the defect region where cracking initiated and b) higher resolution of the crack initiation feature with evidence of microstructurally etched regions (similar to those previously observed in pits).

Atmospheric exposure testing was also examined in FY21, with example post-mortem analysis shown in Figure 85. This sample was pre-exposed for 6 months with 300 ug/cm^2 sea-salt printed on the narrow faces of the tensile bar and exposed at 35 ^{o}C and 40% RH, then printed again with 300 µg/cm^2 sea-salt on the broad faces. It was then placed under a load at the nominal yield strength of the metal in the same environmental conditions. The sample was exposed under load for 6 months. Marker band testing was then carried out in a similar manner as described for the full immersion sample, except the maximum load applied was 620 MPa. In Figure 85, marker bands can be observed centered around a defect region; however, further analysis is necessary to fully understand the crack initiation that occurred.

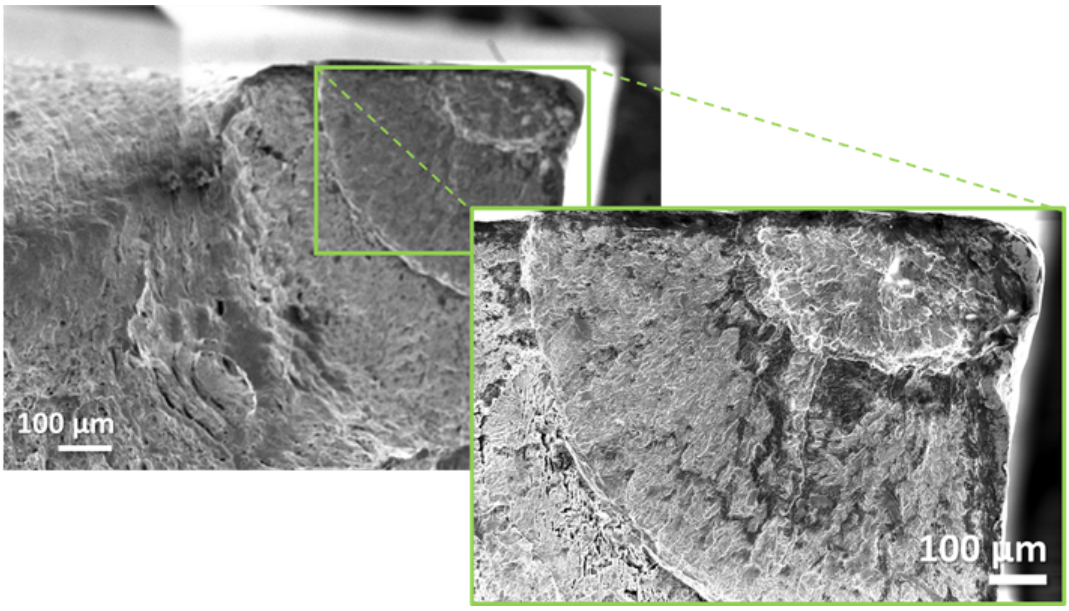

Figure 85. Atmospheric pit to crack post-exposure SEM analysis of marker bands centered around the defect region where cracking initiated.

Future tensile testing in FY22 will focus on chemistries that promote development of key pitting morphologies on the tensile bar surface. Equivalent 76% RH sea-salt brines will be used to produce small hemispherical pits, while 40% RH sea-salt brines will create larger, more irregular pits with cross-hatching and potentially microcracks (likely surface finish dependent). A 4.47 M MgCl2 brine will be used to produce large, asymmetrical pits that feature cross-hatching but not microcracking (as developed in Section 3.1.1). The first step in testing will be to pre-expose samples under full immersion to generate the representative corrosion morphology prior to testing. Based on FY21 experience, samples will be pre-exposed for 4 weeks. These pre-exposed bars will then be loaded under full immersion in the same electrolyte. Testing will be conducted at least twice on each chemistry and possibly more if there are considerable differences. Full immersion SCC testing will be performed to ensure electrolyte delivery to the pits and growing crack. As this first round of testing will cause pitting and crack initiation at a location that cannot be predicted in advance, a second round of testing will be carried out on samples where one single pit or defect is located on the surface. This location can then have DCPD wires placed alongside it for monitoring large crack initiation and growth. In FY22, testing will be done to determine the proper electrochemical procedures necessary to develop one single pit on a tensile bar, and pits that can represent the different morphologies of interest. After this is determined, SCC testing will occur on samples with a pit of a distinct morphology and loaded under full immersion in the associated chemistry. Again, full immersion will be used to guarantee delivery of electrolyte to the pit. A proposed matrix for testing both electrolyte and pit geometry is presented in Table 17.

Table 17. Proposed test matrix for pit to crack initiation tensile testing.

Test Number	Chemistry	Pre-Exposure Method	Test Environment	Other Parameters	Replications
1	40% RH sea-salt brine	Full Immersion	Full Immersion		2
2	4.47 M $MgCl_2$	Full Immersion	Full Immersion		2
5	76% RH sea-salt brine	Full Immersion	Full Immersion		2
6	40% RH sea-salt brine	Single Droplet	Full Immersion	Polarized During Pre-Exposure	3
7	4.47 M $MgCl_2$	Single Droplet	Full Immersion	Polarized During Pre-Exposure	3
8	76% RH sea-salt brine	Single Droplet	Full Immersion	Polarized During Pre-Exposure	3

3.3.1.3 Surface Finish and Applied Stress Effect on Pit to Crack Transition

Simultaneously, along with the modeling and tensile testing efforts, in FY21, development of a U-bend exposure matrix for pit to crack analysis has been underway. The primary goal of this exposure set will be to evaluate, across a large set of samples, the effects of surface roughness, residual stress, and applied stress on SCC initiation for 304 stainless steel. U-bend samples will be exposed and compared to test coupons of the same materials and similar surface finishes under accelerated atmospheric exposure environments relevant to canister conditions (similar to those described in Section 3 for pitting exposures). The details of this planned matrix are described herein, sample procurement is underway, and exposures will begin early in FY22.

Exposure samples will be comprised of 304 stainless steel coupons. A total of 52 samples, 0.6” x 0.6” x .06”, for hole-drilling (residual stress), witness coupons, and boiling $MgCl_2$ (for comparison to atmospheric exposures) will be prepared following the matrix in Table 18.

Table 18. Sample preparation for comparative coupons.

	#4 finish/60 grit	#6 finish/600 grit	#8 finish/1200 grit	Total
Machine	8	8	8	24
Hand	8	8	8	24

For U-bend analysis, 60 samples, 1” x 5” x .06”, of the same 304 stainless steel material will be procured and prepared following the matrix in Table 19.

Table 19. Sample preparation for U-bend coupons.

	#4 finish/60 grit	#6 finish/600 grit	#8 finish/1200 grit	Total
Machine	10	10	10	30
Hand	10	10	10	30

Pre-exposure, all samples will be numbered and characterized using optical profilometry before hole-drilling, salt deposition, or immersion in order to later assess effects of surface roughness. The four sample types will be evenly divided between immersion, atmospheric, and boiling $MgCl_2$ tests (Table 20).

Table 20. Initial sample exposure plan.

	Machine, #4 finish	Machine, #6 finish	Machine, #8 finish	Hand, 60 grit	Hand, 600 grit	Hand, 1200 grit
Immersion	4	4	4	4	4	4
Immersion, witness	2	2	2	2	2	2
Atmospheric	6	6	6	6	6	6
Atmospheric, witness	2	2	2	2	2	2
Boiling $MgCl_2$	2	2	2	2	2	2
Hole Drilling	2	2	2	2	2	2

The tests mentioned in Table 20 for sample exposure will be carried out as follows:

Immersion Testing: Samples will be bent in a U-bend fixture to a radius of 25 mm (following the ASTM G-30). Two of each type (i.e. two machine #4, two machine #6, etc.) will be submerged in equivalent sea-salt brines of 40% RH at 35 °C and another two of each type will be submerged in equivalent sea-salt brines of 75% RH at 35 °C. Samples will be observed (with optical microscopy) in one-week intervals for evidence of SCC. For each type of brine, a witness coupon of each sample surface finish will be simultaneously immersed.

Atmospheric Testing: Deposition of 300 μg/cm^2 of chloride as artificial seawater will be done on samples for atmospheric testing (36 total) including: one 1" x 5" face (to be put in tension in a U-bend fixture) and 3 witness coupons of each type. Samples will be weighed after deposition to verify chloride deposition density. Deposition will occur on pre-bent fixtures (i.e. coupons will already be in U-bend fixtures). Two U-bends and one witness coupon of each type (i.e. two machine #4, two machine #6, etc.) will then be placed into a humidity chamber at 40% RH and 35 °C, another two u-bends and a witness coupon (1) of each type will be put into a humidity chamber at 75% RH at 35 °C, and the last two U-bends of each type and a witness coupon (1) will be put into a humidity chamber with cyclic conditions (same as those described in Section 3.2.1).

Boiling $MgCl_2$ Test: Samples will be coated on sides that are not ground (the top surface of interest) with epoxy prior to immersion in saturated boiling $MgCl_2$ at 155 °C, following ASTM G36-94. Samples will be examined every 24 hours for evidence of SCC. This will be used as a benchmark test to assess differences in surface roughness and grinding type on SCC susceptibility.

Hole-Drilling: Hole drilling will be used to assess the residual stresses imparted from the surface finishing method and the level of surface finish. Five holes will be drilled per sample on the 0.6" x 0.6" face, one in each corner and one in the center. Electronic Speckle Pattern Interferometry will give residual stress measurements as holes are drilled, incrementally, to a 0.6 mm depth.

Post Test Analysis: Post atmospheric and full immersion exposure, corrosion product will be removed from samples by sonicating in 10% nitric acid for 1 hour. Samples will be examined using profilometry and SEM. Select pits may be cross-sectioned in FIB (focused ion beam) and examined using SEM to determine shape and depth as well as where possible cracks originate; whether they are associated with pit formation, and if so, if they occur on the pit (on the sides near the mouth of the pit or from the bottom of

the pit). High-resolution EBSD will also be performed on some cross-sectioned pits to examine potential microstructural influences on pitting.

Through this large-scale exposure testing, we plan to characterize potential differences in pit size, shape, location, and density that may occur across the various roughness and grind methods examined. Additionally, we plan to document any differences in cracking density, location on the sample, and location on a pit (bottom vs mouth). This will allow for establishment of statistics related to pit size across all samples and the susceptibility to crack initiation. Attention will also focus on pit morphology, whether this is governed by environment and/or material processing, and how this plays a potential role in crack initiation.

3.4 Crack Tip Modeling

In FY21, development of a crack tip model to determine pertinent electrochemical parameters was carried out. Further enhancement of such a model will aid in determination of similitude between laboratory accelerated testing and real-world cracks to enhance overall CISCC prediction. Crack tip electrochemical conditions were explored utilizing a reactive transport FEM. The FEM utilized the Laplace equation coupled with the transport of dilute species (with concentration dependent diffusivities) to inform upon equilibrium crack tip conditions under various conditions. Electrochemical boundary conditions (ORR, HER, and anodic dissolution) are dependent upon the chemistry of the solution and were evolved over time. Metal salt formation ($Me^{n+} + zCl^{-} \rightarrow MeCl^{n-z}$) and hydrolysis ($Me^{n+} + H_2O \rightarrow Me(OH)_{n-1} + H^{+}$) reactions were incorporated for Fe, Ni, and Cr. The reactions were assumed to be at equilibrium. The consumption and production of solution species (as a byproduct of electrochemical reactions) were dictated by the respective current densities. The simulation was performed in a 2D scenario representative of the centerline of the crack where the shortest diffusion distance was through the crack mouth; the model is shown schematically in Figure 86. Such a geometry is representative of a transgranular crack. The surface of the crack and the crack walls were considered homogenous and did not account for influences from chemical or structural differences. Additionally, roughness of the crack walls was not considered.

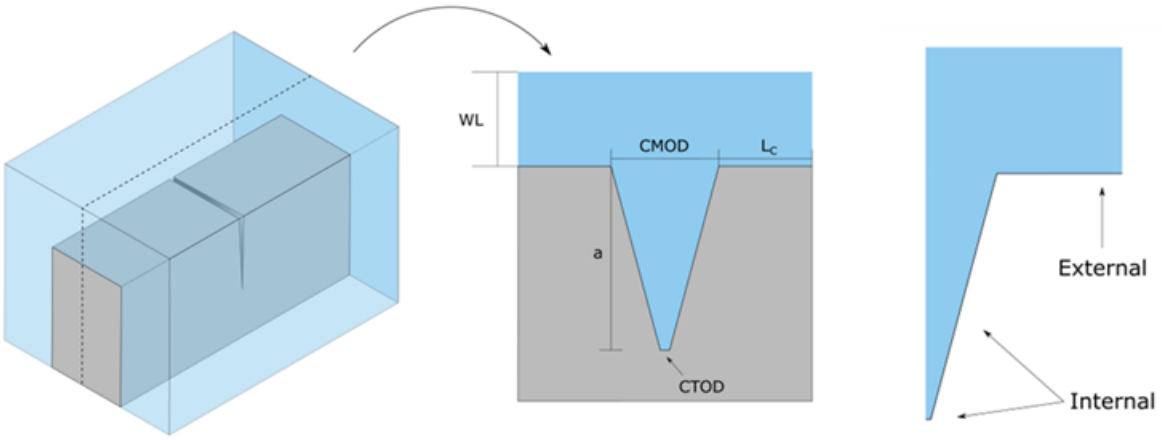

Figure 86. Schematic representation of SCC modeling.

Total anodic and cathodic current per width (I_C/W) are presented in Figure 87-a and b respectively. It is noted that cathodic currents are presented on a logarithmic scale and are positive. In reality, the

magnitude of the total cathodic current is equal to that of the total anodic current, with its sign indicating its direction. Overall, with increasing time, both anodic and cathodic currents generally increase with time before reaching a steady state value. It is noted that there is a temporary maximum near 1.5 hours in both the anodic and external ORR currents before decreasing to their respective steady state values.

Further analysis was performed on the full immersion conditions in which the total cathodic current was evaluated both internal and external to the crack as displayed in Figure 87-c. A greater portion of the cathodic current is external to the crack at all times. Of the current that is external to the crack, a majority of this current is due to the ORR reaction as displayed in Figure 87-d. Internal to the crack, a majority of the cathodic current is due to HER after roughly 0.75 hours (Figure 87-e).

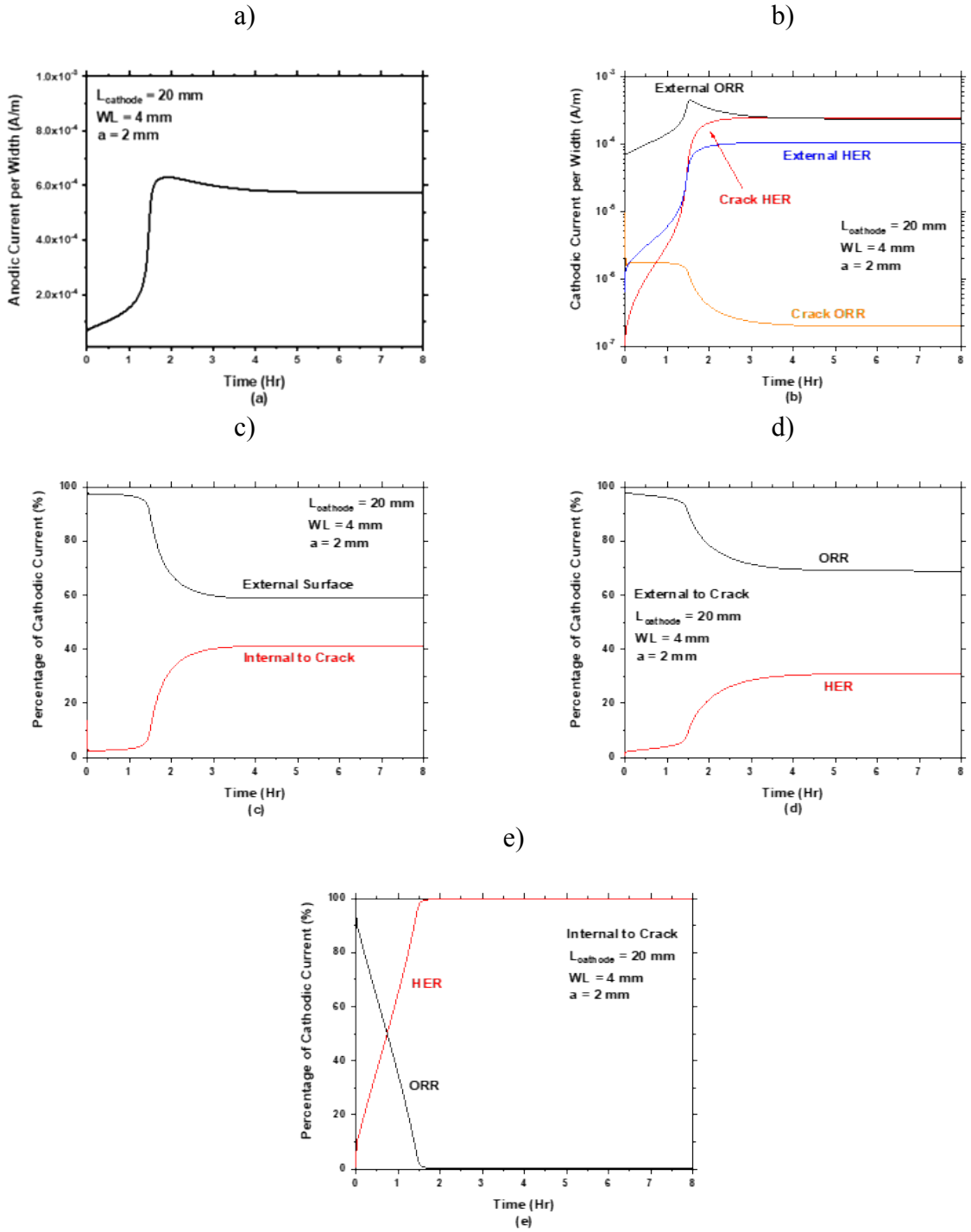

Figure 87. Electrochemical conditions for a crack under full immersion conditions showing (a) total current per width and (b) cathodic currents per width separated into HER and ORR contributions on the internal and external of the crack. It is noted that cathodic currents are opposite signs that of anodic currents; however, in (b) the cathodic currents are presented as positive for easier interpretation. (c) Percentage of cathodic current on the external and internal surface, (d) percentage of cathodic current due to HER and ORR external to the crack, and (e) percentage of cathodic current due to HER and ORR on the internal surfaces.

The potential, presented in Figure 88-a and b, is lowest at the crack tip, followed by the crack mouth and cathode edge. The potential drop that exists at steady state between the crack tip and crack mouth is roughly 7 mV and results in a potential drop of 3.5 V/m. Additionally, the highest metal concentration is at the crack tip, followed by the crack mouth and cathode edge as presented in Figure 88-c. The equilibrium concentration of metal at the crack tip is roughly 2.4 M while the cathode edge does not get above 10^{-7} M. Finally, the crack tip experiences the lowest pH (1.9 at steady state) and the cathode edge has the highest pH (Figure 88-d).

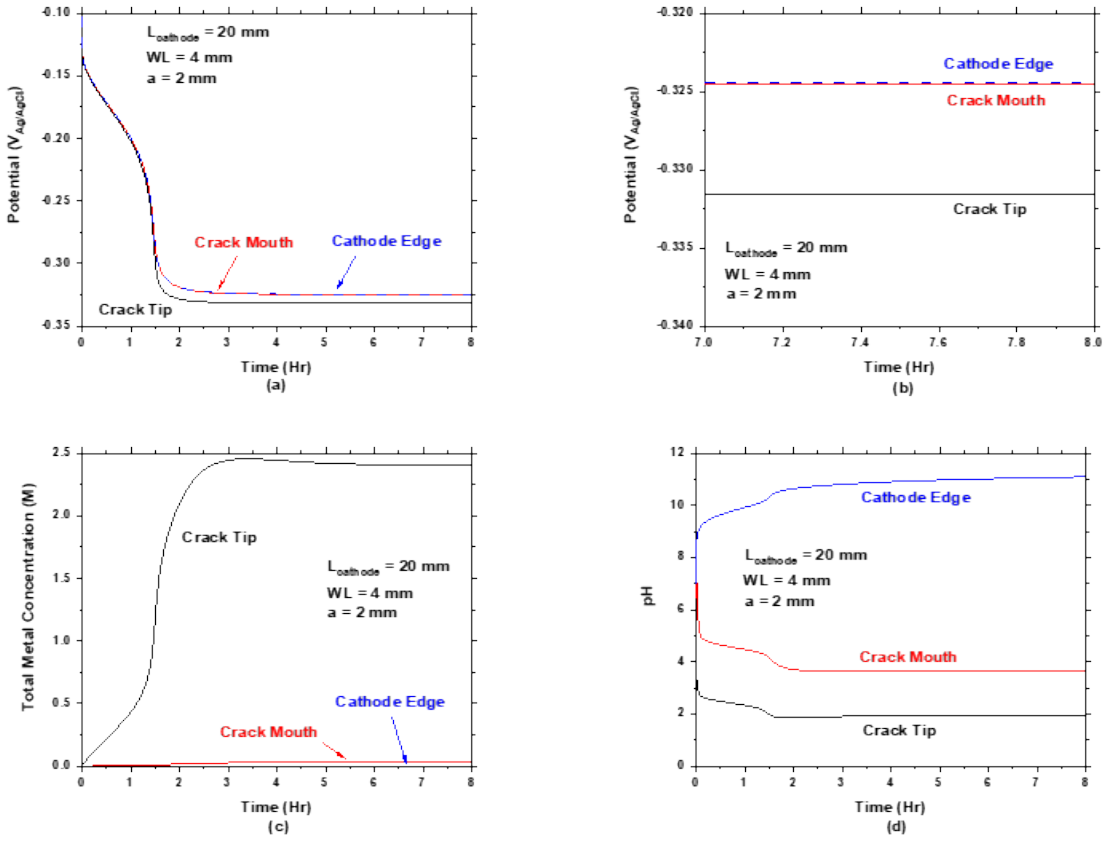

Figure 88. Influence of full immersion on the (a) potential of the crack tip, crack mouth and cathode edge, (b) potential at long time, (c) total metal concentration, and (d) pH.

As presented in Figure 89-a, increasing L_C from 20 mm to 100 mm under full immersion conditions (WL = 4000 µm = 4 mm), increases the I_C/W by roughly a factor of 4 under steady state conditions. Additionally, the crack tip total chloride concentration, Figure 89-c, increases with increasing L_C causing for a decrease in crack tip pH (Figure 89-d). It is also interesting to note that the cathode pH is decreased with increased L_C. These results potentially indicate that there could be an influence of sample size (especially available cathode area) on measured crack growth rates.

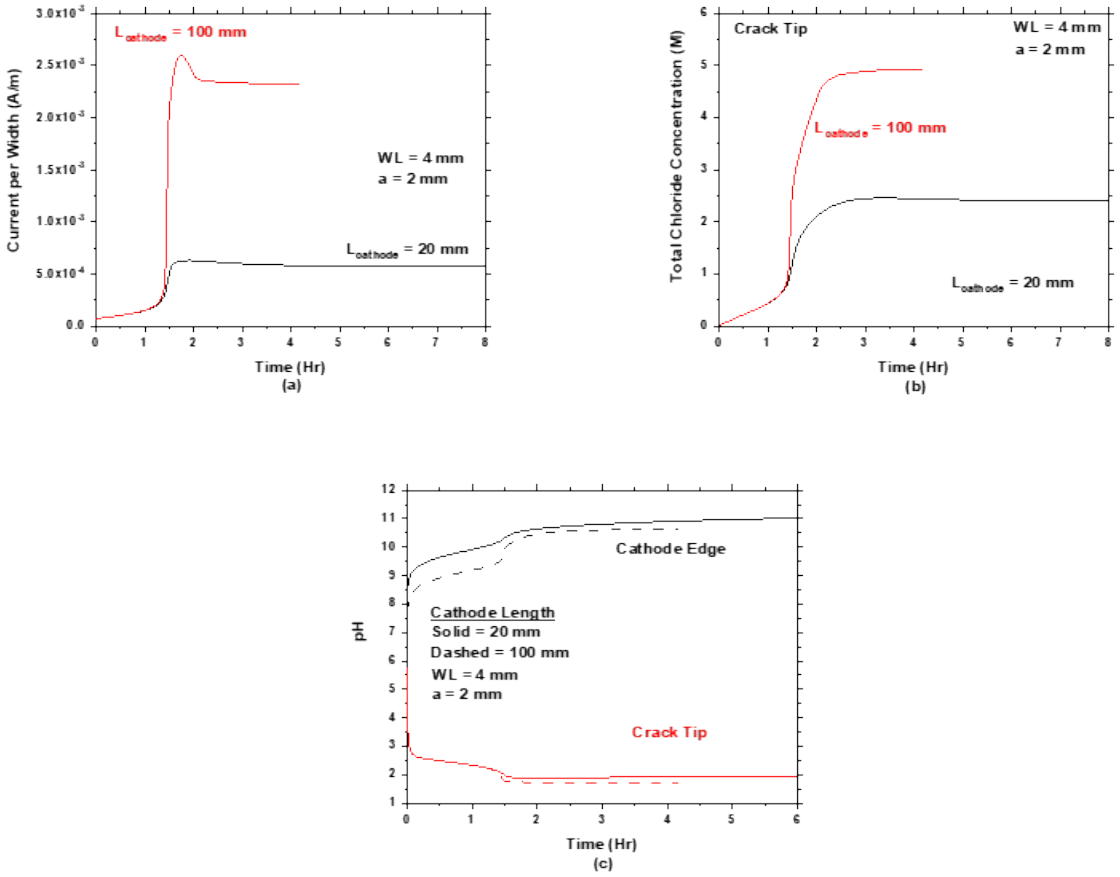

Figure 89. Influence of cathode length on (a) the total current per width, (b) metal concentration at the crack tip, and (c) pH at the crack tip and cathode edge. It is noted that the stress intensity (10 MPa*m$^{1/2}$), crack length (2 mm), and WL thickness (4 mm) are held constant.

Decreasing the *WL* thickness from 4 to 0.1 mm (bulk to thin film respectively) increases the I_C/W by roughly a factor of 2 as shown for steady state conditions in Figure 90-a. Decreasing the *WL* thickness to 0.1 mm increases the crack tip chloride concentration (Figure 90-b) in comparison to a crack exposed to a 4 mm *WL* thickness. Figure 90-c displays that the pH at the crack tip is decreased and at the cathode edge it is increased for a decrease in the *WL*. These results potentially indicate the influence of *WL* thickness on measured crack growth rates, possibly increasing with a decreased WL in this range.

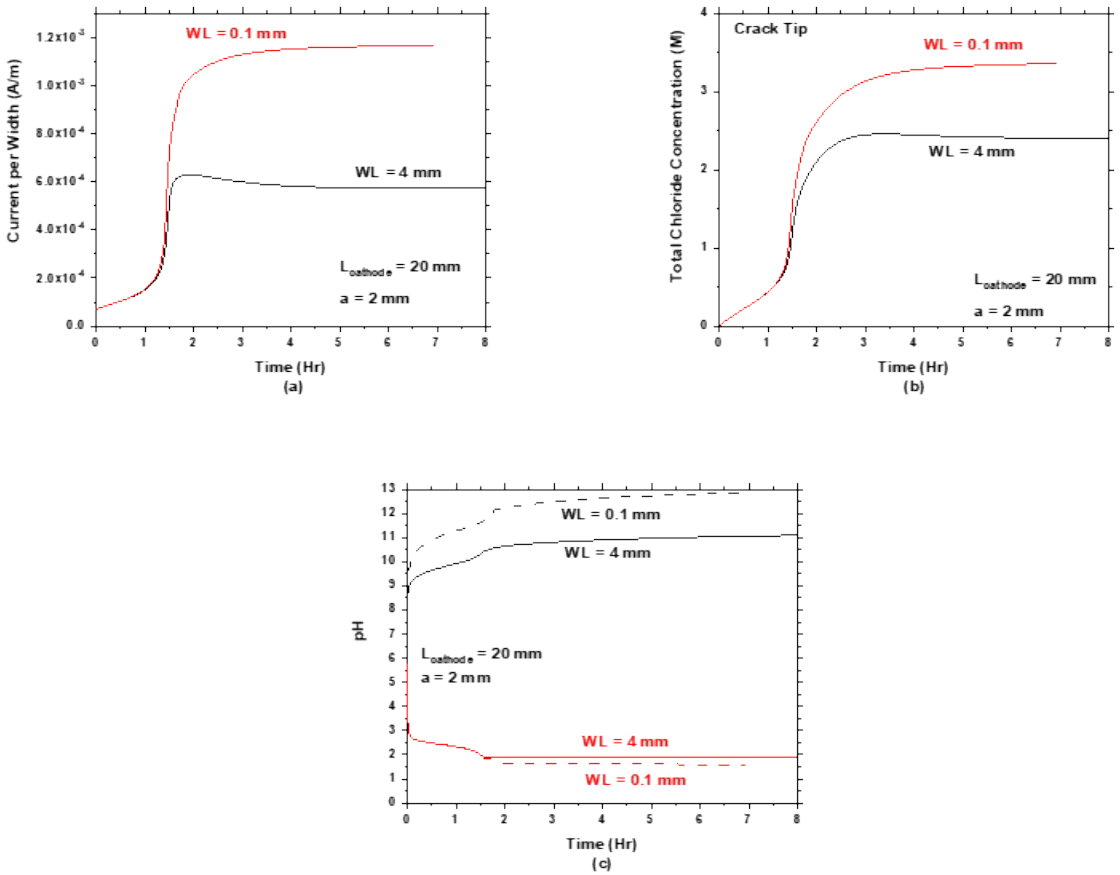

Figure 90. Influence of WL thickness on (a) the total current per width, (b) crack tip chloride concentration, and (c) pH at the crack tip and chloride concentration. It is noted that the stress intensity (10 MPa*m$^{1/2}$), crack length (2 mm), and cathode length (20 mm) are held constant.

Further explorations of crack tip modeling as well as experimental validation are necessary to fully understand the implications of the exercises presented herein. Additionally, assumptions taken in modeling need validation prior to full application. In FY22, increased datasets (both in sample geometry and electrolyte of exposure) will be modeled as well as 3-D geometries for verification of the 2-D model. These will be compared to experimental measurements to initiate model validation.

4. Crack Growth Rate Analysis

The results presented herein are a summary of the frame setup, reduction of noise, establishment of measurement techniques, and development of methods to ensure repeatable and measurable crack growth rates over FY21. These are preliminary datasets to show proof of concept, however crack growth rates reported herein should not be taken as quantifiable values as they have not been fully calibrated. FY22 will employ lessons learned over FY21, and begin the development of a quantifiable CGR database across canister relevant environmental exposures.

In FY21, the four servomechanical load frames acquired in FY20 were installed in a recently remodeled lab. These load frames enable the *in situ* measurement of crack length over long periods of times (weeks to months). Three frames were oriented vertically (Figure 91) to enable the use of full-immersion exposure cells and one was oriented horizontally (Figure 92) to enable the development and study of atmospheric exposure methods such as wicking and spraying. Later, a circulating heating and oxygenation system was installed on one vertical frame and a second oxygenating only system on another vertical frame. The frames were spaced three feet apart to reduce electrical crosstalk between the measurement systems. The Direct Current Potential Drop (DCPD) system features a precision power supply, a nanovoltmeter, a solid-state relay and a computer-controlled multi-channel relay card which are together used to measure the change in crack length in a test specimen. The precision power supply is used to source a constant current flow through the test specimen. The nanovolt meter is used to measure the voltage drop across the mouth of crack tip and from a reference attached on the rear surface of the specimen. The computer-controlled relay card switches between signals measured by the nanovoltmeter, which can only make measurements on one channel at a time. The open-circuit potential, temperature, reference voltage, and DCPD voltage are the four signals which are switched between with the multichannel relay and measured with the nanovoltmeter. Further details on the function, layout and accuracy/precision of this equipment can be found in the FY20 final report [3].

Figure 91. Three vertical SCC test frames and horizontal frame.

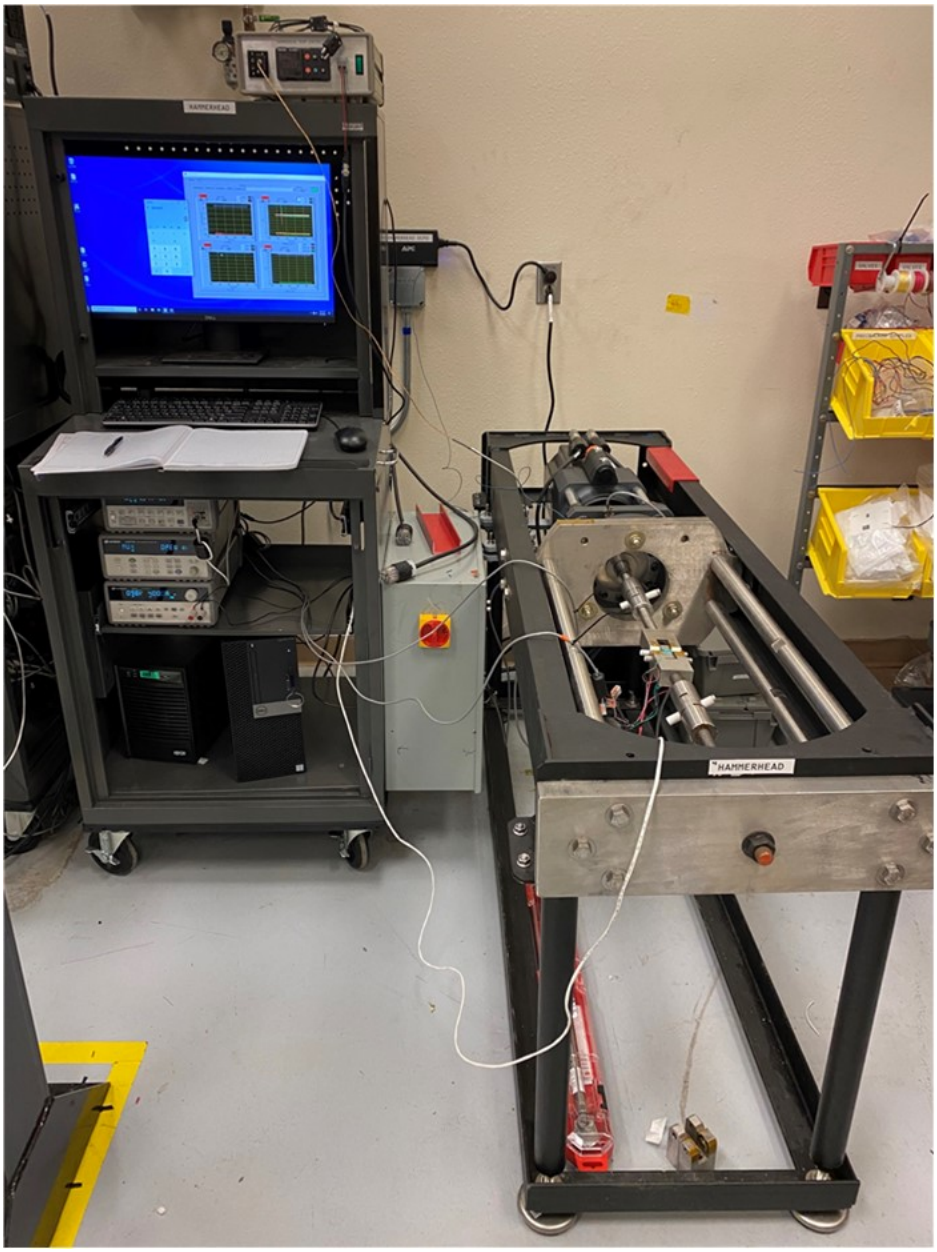

Figure 92. Horizontal test frame.

In January 2021, CISCC corrosion testing equipment was moved into the new lab which featured increased space, improved access to chemicals and sample preparation equipment as well as improved proximity to staff offices. As this was a somewhat dated facility, improvements to the electrical outlets in the room were necessary and a series of noise and drift measurements were performed prior to usage of the frames to ensure relevant and reliable resolution necessary for SCC testing. After the first series of noise measurements, wire routing and the location of uninterruptible power supplies were optimized to further reduce noise and drift in the measurements. No load was applied to the samples, nor was the temperature controlled. The noise was again tracked for several days after the changes were made. Various metrics were used to track the changes made to the infrastructure and power quality in the lab. Daily drift was used to determine the short-term influence of changes that were made to the setups.

Figure 93 shows an example of the daily drift for each of the four test frames. On 5/25/21, the wire routing was changed, resulting in improved daily drift performance in frames 1 and 3, but increased drift on frame 2. Frame 4 already had high daily drift and did not experience any improvement after better wire routing. Further changes were made to the behavior of the software (such as the number of averages per measurement) that did not seem to have as large of an impact on drift.

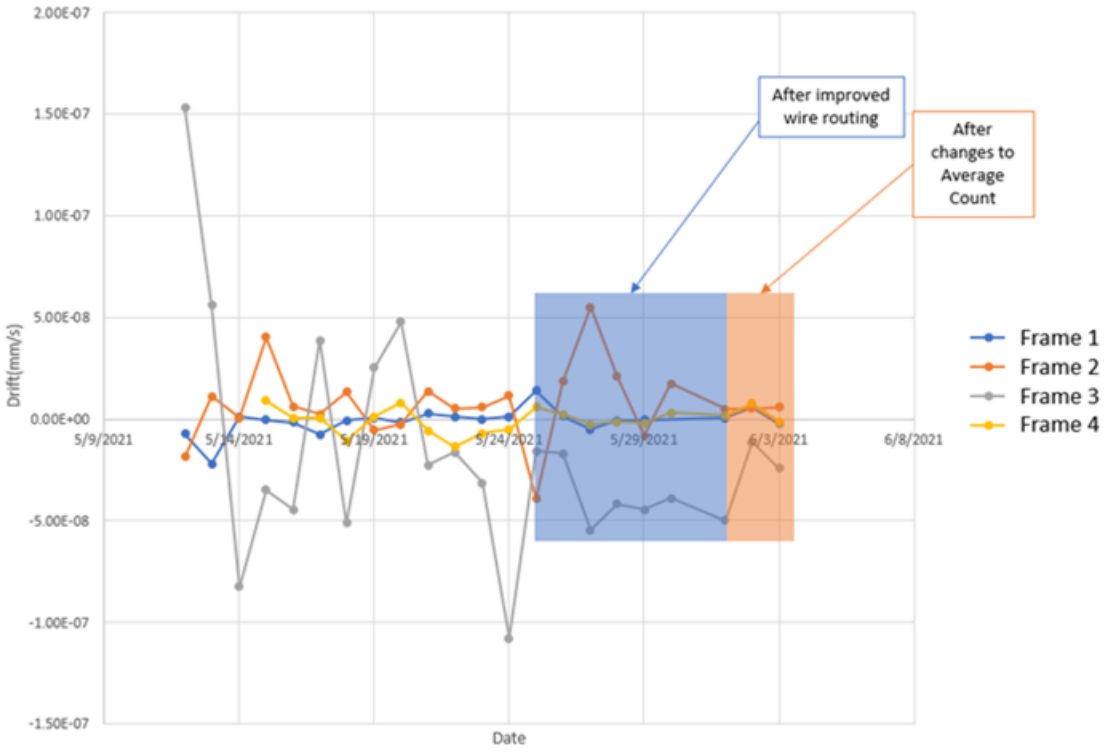

Figure 93. Daily drift for each CISCC test frame.

Long term drift was measured over the course of several weeks. Since CGR measurements usually occur over many weeks, it was necessary to characterize drift in the measurements over similar time periods. The long-term drift is a better measure of the system behavior when measuring very low crack growth rates (10^{-8} mm/s or less). Long-term drift was measured by loading a pre-cracked specimen in ambient conditions to 50 pounds (0.42 MPa$\sqrt{m}$). The load was maintained for many days or weeks at a time while measuring the crack length. It is assumed that the crack would not grow under these low-load, ambient conditions so any change in crack length can be attributed to drift in the measurement. Figure 94, Figure 95, and Figure 96 display long-term drift measurements for frames 1, 2 and 4. The drift rate for these frames varied between 10^{-8} and 10^{-10} mm/s. CGR measured above these rates can be attributed to real crack growth, while rates below are assumed to be caused by measurement drift. The amount of noise in the crack length measurement was ±1-10 µm for all frames.

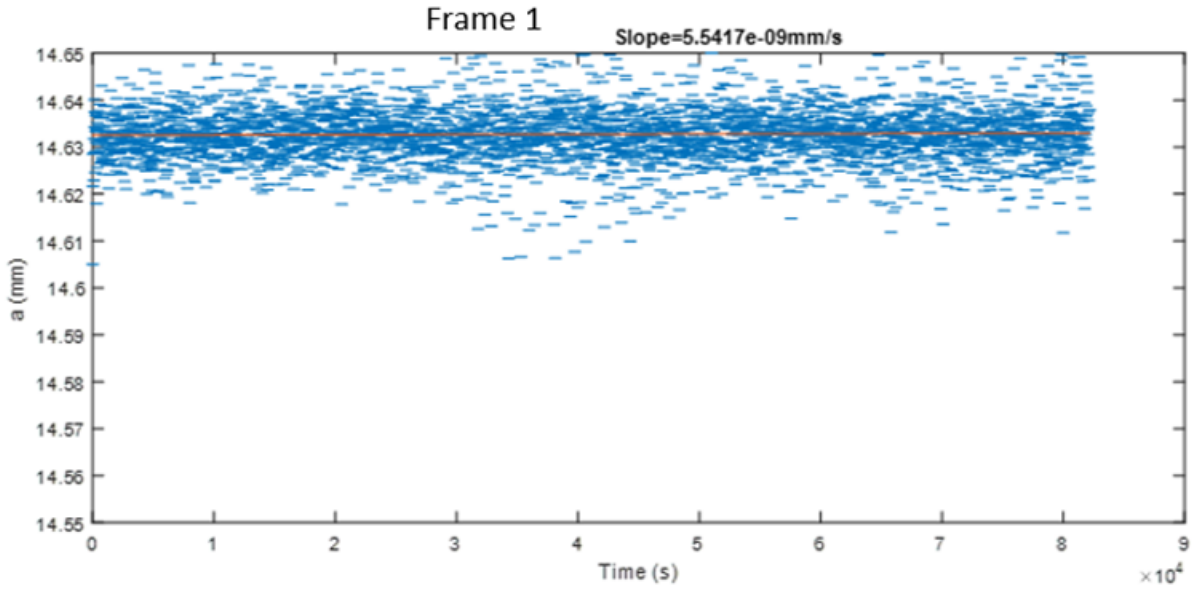

Figure 94. Long-term, reference-corrected crack length measurement drift for frame 1. The slope of the red line represents drift in mm/s.

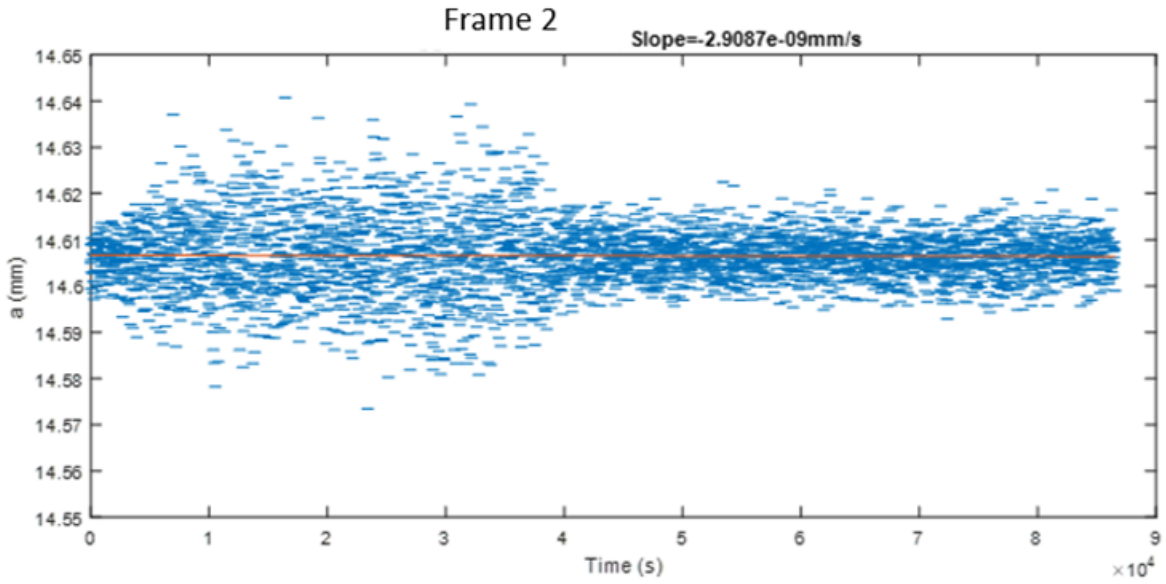

Figure 95. Long-term, reference-corrected crack length measurement drift for frame 2. The slope of the red line represents drift in mm/s.

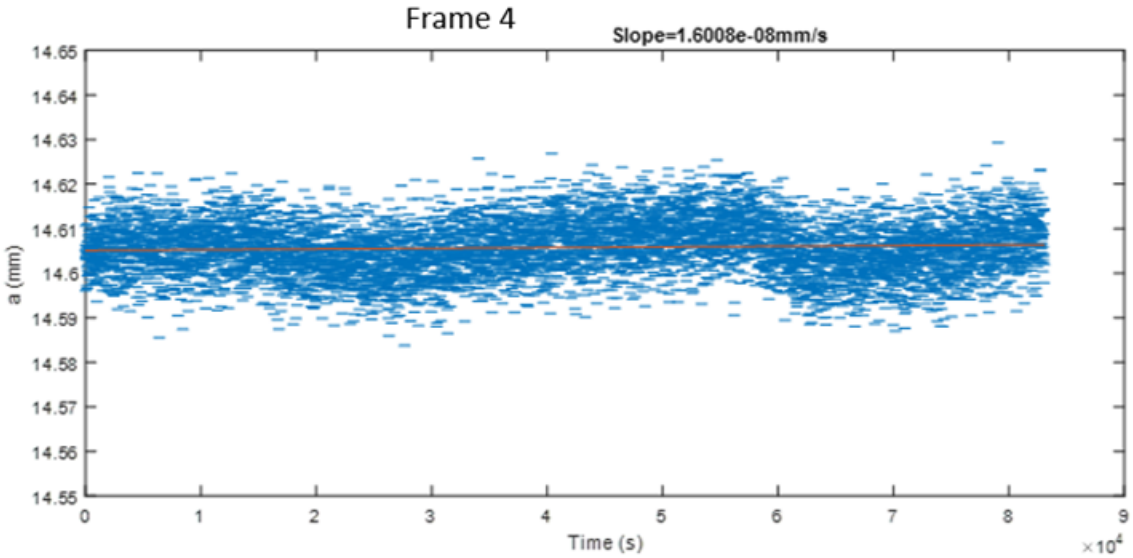

Figure 96. Long-term, reference-corrected crack length measurement drift for frame 4. The slope of the red line represents drift in mm/s.

4.1 SCC Materials and Test Methods

4.1.1 Alloy Lots

Table 21 shows all alloy lots currently in possession at SNL. Alloy lots 1 and 3 were used for all experiments in this report. Lot 1 has a higher ultimate tensile strength and higher hardness, but lower elongation than Lot 3 as seen in Table 22. Lot 3 has a higher molybdenum and copper content but lower amounts of sulfur than Lot 1 (see Table 23). Sulfur is known to increase stress corrosion cracking susceptibility of steels due to the formation of manganese sulfide inclusions which dissolve upon contact with aqueous solutions [101, 102]. Lots 1 and 3 were chosen due to their higher UTS, yield strength and hardness when compared to the other lots. Lot 5 is a 316 stainless steel alloy that has not yet been used.

Table 21. Basic lot identification information.

Lot ID	Plate #	Heat #	PNNL Reference #	Form	Nominal Alloy
1	206972	SD23822	n/a	Plate, 12" x 12" x 1"	SS304
2	208866	863831	n/a	Plate, 12" x 12" x 1"	SS304- EZ
3	213104	04E28VAA	P304L1	Plate, 12" x 12" x 1.5"	SS304
4	213156	SD41059	P304L2	Plate, 12" x 12" x 1.5"	SS304
5	212828	02D84WAB	P316L1	Plate, 12" x 12" x 1"	SS316

Table 22. Lot mechanical properties from manufacturer certificates (UTS – ultimate tensile strength, YS – yield strength, Elongation - % strain at failure, HRB – Rockwell Hardness B).

Lot ID	UTS (Mpa)	YS 0.2% (Mpa)	Elongation(%)	HRB
1	647	267	57.6	82.2
2	562	251	51.7	75
3	623	292	62.9	81
4	593	242	61.3	78
5		270		81

Table 23. Nominal lot composition from manufacturer certification.

Lot ID	C	Co	Cr	Cu	Mn	Mo	N	Nb	Ni	P	S	Si	Ti
1	0.02	0.2	18.14	0.25	1.7	0.08	0.07	-	8.04	0.031	0.004	0.4	0.001
2	0.01	0.14	18.28	0.34	1.4	0.27	0.07	-	8.16	0.025	0.023	0.4	0.003
3	0.017	0.234	18.1	0.412	1.782	0.414	0.08	0.014	8.03	0.037	0.001	0.236	0.002
4	0.019	0.21	18.2	0.335	1.63	0.1	0.073	0.01	8.155	0.028	0.008	0.385	0.003
5	0.017	0.36	16.7	0.477	1.178	2.002	0.062	0.023	10.085	0.037	0.001	0.282	0.004

4.1.2 Tensile Specimens

Round bar tensile specimens were manufactured from Lots 1, 4, and 5 according to ASTM E8 [103] with dimensions shown in Figure 97. Tensile tests on Lots 1 & 2 were performed by Westmoreland Mechanical Testing and Research Inc. and were reported in the FY20 report [3]. Lot 3 tensile results were not completed as of the writing of this report.

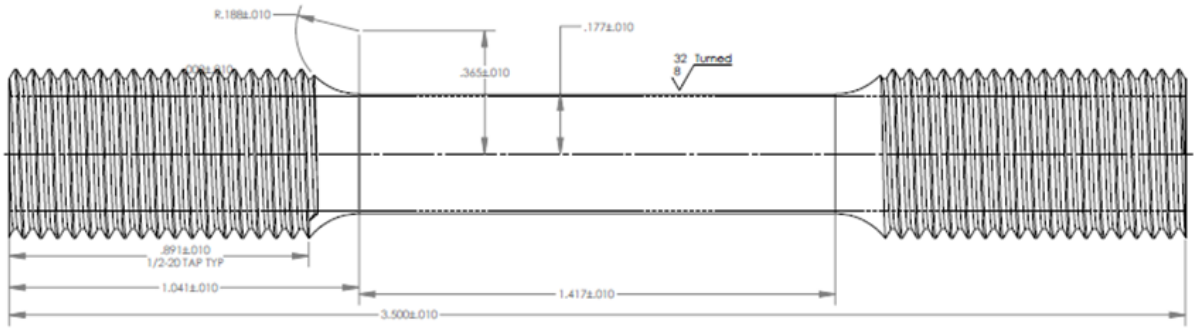

Figure 97. Round tensile specimen used for all tensile tests per ASTM E8 [103].

4.1.3 Compact Tensile Specimens

Compact Tensile (CT) specimens, commonly used for CGR measurements, were selected as the sample geometry for CISCC tests at Sandia. CT specimens are rectangular in cross-section and feature a series of notches designed to focus stress and ensure that planar crack propagation occurs through the ligament of the sample [104-106]. A wire-EDM is used to create a large medial notch with a sharp tip through the cross-section of the sample. Small, lateral grooves are machined on either side of the ligament to ensure cracking is planar through the middle of the ligament. This design is seen schematically in Figure 98 and Figure 99. Several ¾ CT and ½ CT specimens were cut from Lot 3. Lot 1 specimens were ¾ CT geometry exclusively. Lot 3 was chosen to enable comparison of results with results from PNNL.

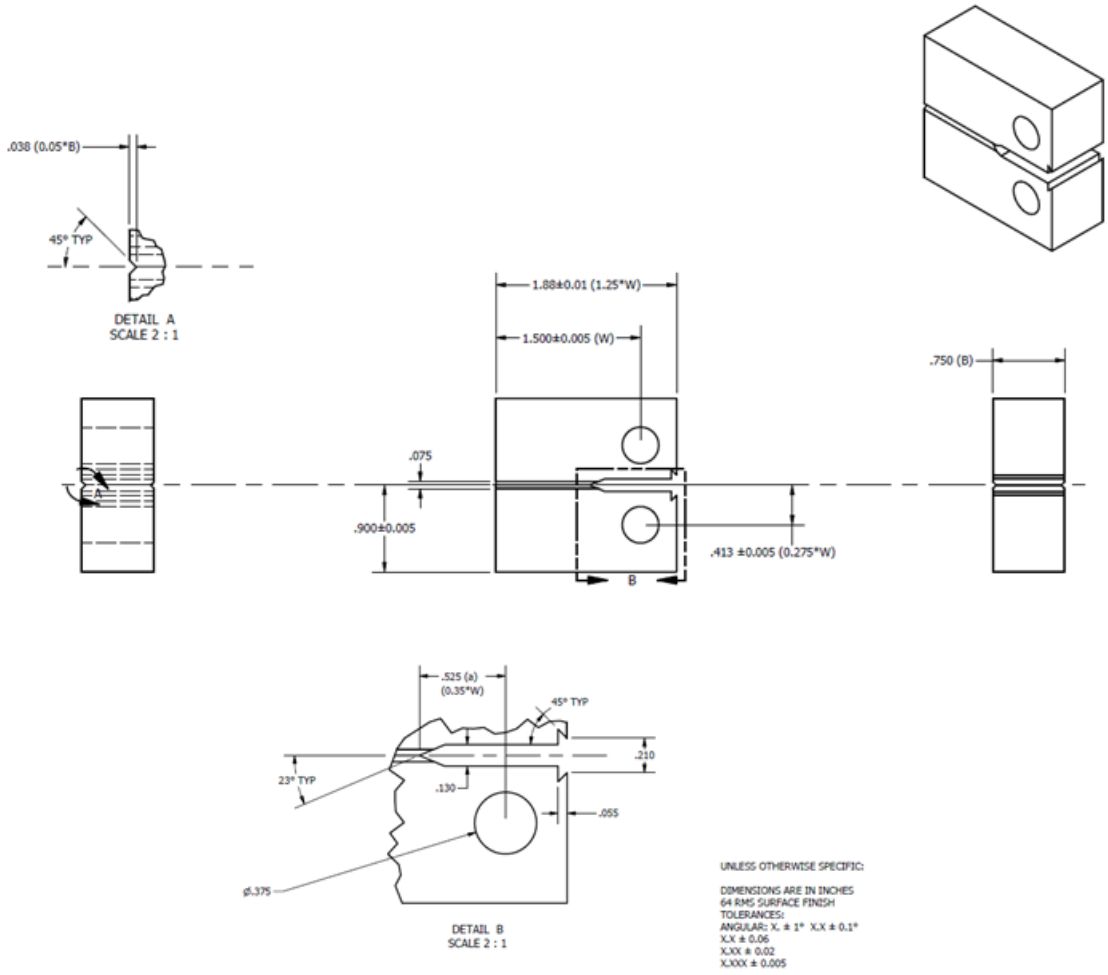

Figure 98. Schematic of ¾ CT specimen geometry (ASTM E1681-03 [104] and ASTM E647 [106]).

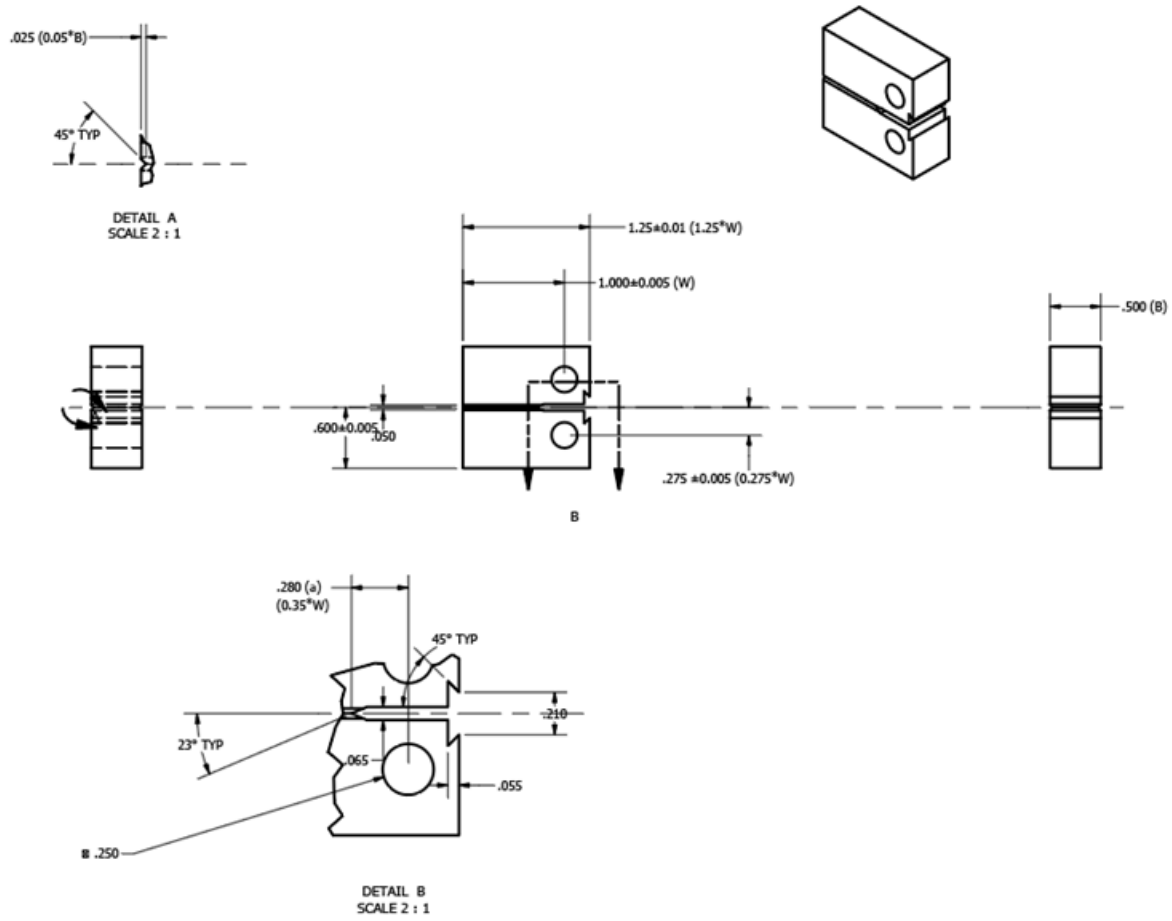

Figure 99. Schematic of ½ CT specimen geometry (ASTM E1681-03 [104] and ASTM E647 [106]).

The Johnson equation [107, 108] is used to calculate the crack length in a CT specimen based on the real-time voltage drop across the crack mouth as measured using DCPD. The voltage is produced when current flows through the gauge span of the CT specimen. When the initial crack length a_o is known (initially assumed as the notch length), a baseline voltage U_o can be measured and used as reference condition for calculating the crack length based on the potential drop measurement, *U*. In the Johnson equation, a, the crack length, is given by:

$$a = \frac{2W}{\pi} cos^{-1}\left[\frac{\cosh\left(\frac{\pi y}{2W}\right)}{\cosh\left[\left(\frac{U}{U_0}\right) cosh^{-1}\left[\frac{\cosh\left(\frac{\pi y}{2W}\right)}{\cos\left(\frac{\pi a_0}{2W}\right)}\right]\right]}\right] \quad \text{(Eq. 6)}$$

where *U* is the potential drop measurement, *y* is half of the potential gauge span (4.445mm for 3/4 CT specimens), *W* is the specimen width, a_0 is the initial crack length and U_0 is the initial potential drop measurement. The potential drop measurement can also be corrected using a secondary reference voltage, U_r, which is measured over a small area on the rear surface on the sample. It is assumed that this

reference location will vary with temperature changes in the sample, but not with stress or crack length changes.

The stress intensity factor at the crack tip for CT specimens can be calculated using Equation 7 [108, 109]

$$K_{i,CT} = \frac{P_i S}{(BB_N)^{1/2} W^{3/2}} \times \frac{\left(2+\frac{a_i}{W}\right)\left[0.886 + 4.64\left(\frac{a_i}{W}\right) - 13.32\left(\frac{a_i}{W}\right)^2 + 14.72\left(\frac{a_i}{W}\right)^3 - 5.6\left(\frac{a_i}{W}\right)^4\right]}{\left(1-\frac{a_i}{W}\right)^{3/2}} \quad \text{(Eq. 7)}$$

Where P_i is the load at the ith data point, S is the specimen span dimension, B is the specimen thickness, B_n is the specimen net thickness, a_i is the crack length at the ith data point, and W is the specimen width (effective from the holes for pins). All analyses of stress intensity factor in this report assume that the plastic limit is not exceeded at the crack tip.

Stress intensity factor depends heavily on the length of the crack and the geometry of the specimen. For example, if a load of 8900 N is applied to a ¾ CT specimen with a crack length of 13.3 mm the stress intensity is 14 MPa$\sqrt{m}$. The same load applied to the same specimen but with a crack length of 15.4 mm imparts a stress intensity of 16 MPa$\sqrt{m}$. Thus, any uncertainty or noise in crack length measurements is compounded into the calculated stress intensity factor. Any compounded error in stress intensity may cause stress intensities in excess of the plastic limit.

4.1.4 Tensile Test Methodology

Tensile tests were performed on a servo-hydraulic load frame at a constant strain rate of 10^{-3} inch/inch while measuring strain with digital image correlation (DIC). DIC is an optical strain measurement that uses digital cameras to track unique features as the sample is deformed. DIC is known to be both highly accurate and easy to perform for standard test specimens [110]. Sample stress and strain were measured until complete plastic rupture of the sample occurred.

Lots 1 and 2 were tested at Westmoreland and were reported in the FY20 report [3] and are reported here for comparison. Results from Westmoreland are marked with "W".

4.1.5 Crack Growth Rate Measurements

Crack growth rate measurements are performed in a series of steps that must be performed in order. First, a pre-cracking procedure was performed to form an atomically sharp crack at the tip of the notch in the sample. A sharp crack tip is most easily developed by high-frequency cyclic fatigue. Samples were fatigued at a frequency of 0.33-0.5 Hz with a minimum stress intensity (K_{min}) of 4 MPa$\sqrt{m}$ and maximum stress intensity (K_{max}) of 20 MPa$\sqrt{m}$ until an a/W ratio of 0.383 was achieved. Typical pre-crack times were 30-50 hours.

After pre-cracking, the test environment (ambient air or solution immersed) was introduced to the sample. If the sample was immersed in brine, the brine was heated to the target temperature before the transitioning procedure was started to reduce the impact of temperature changes on the calculated crack length using DCPD. The transitioning procedure is a tapered-frequency fatigue stress profile which transitions the crack tip from environmentally-assisted fatigue cracking to full stress corrosion cracking. Figure 100 shows load and crack length vs. time from a crack transition profile performed on a ¾ CT specimen in 55°C saturated $MgCl_2$. Starting from the most representative crack tip morphology is important to the accuracy of the crack growth rate measurements. The transitioning procedure began with a trapezoidal stress waveform imparted on the sample at low frequency (typically 0.1 Hz, see Table 24). The amplitude of the trapezoidal waveform was controlled between K_{min} and K_{max}. As the transitioning

procedure progressed, the frequency was decreased by decades (e.g. 0.01, 0.001, $1x10^{-4}$ Hz). Each frequency was used until the crack length increased by at least two grain widths (for Lot 3 ~100 micrometers). As the frequency was decreased the resulting corrosion fatigue crack growth rate decreased (as seen in Figure 100). Table 24 outlines the corrosion fatigue transitioning procedures of labs at PNNL, DNV-GL (SNL Collaborators), and SNL. The main difference between these two transitioning procedures is that DNV-GL/SNL perform an additional step prior to the end of the procedure by holding the sample at constant stress for 1 day prior to the next unload cycle. The final step (not shown in Table 24) was to maintain constant stress indefinitely until the test was stopped by the operator.

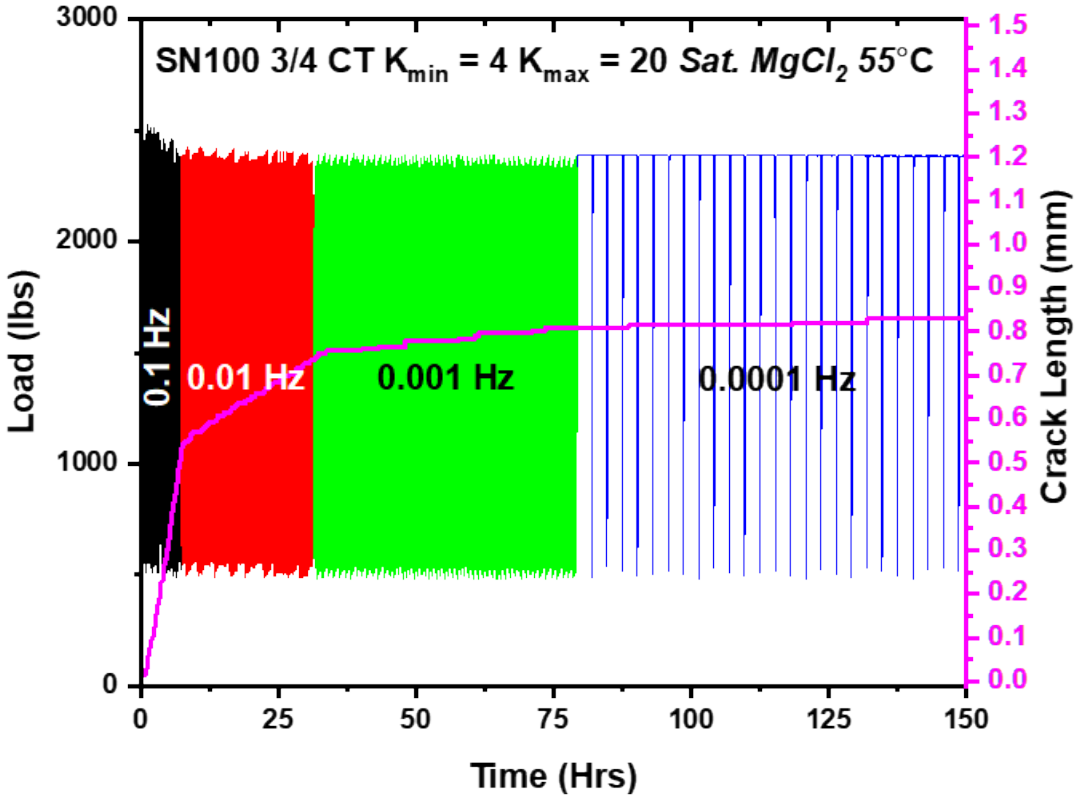

Figure 100. Example crack transitioning dataset spanning 4 decades of decreasing fatigue frequency and resulting crack length.

Table 24. Comparison of PNNL and DNV-GL/SNL transitioning procedures.

Name in Report	PNNL Hold Time (s)	PNNL Rise Time (s)	DNV-GL/SNL Hold Time (s)	DNV-GL/SNL Rise Time (s)	Equivalent Fatigue Frequency (Hz)
9/1	9	1	9	1	0.1
90/10	90	10	90	10	0.01
900/100	900	100	900	100	0.001
9000/1000	9,000	1,000	9,000	1,000	10^{-4}
1 day holds	N/A	N/A	86,400	1,000	10^{-5}

Once the transition procedure reached a fatigue frequency of 1x10-4Hz or less (9000/1000 or 1 day holds), the next step was to stop imparting a fatigue stress profile. Stress corrosion cracking was measured after fatigue transitioning is complete using constant K testing. In Constant K tests, stress intensity is held constant until the DCPD indicated crack length has increased enough (at least 100 microns). Constant K tests are representative of the natural conditions in which stress corrosion cracks can form and grow. Additionally, multiple constant K tests can be performed on a single sample (at different K levels or exploring different environmental conditions).

A good understanding of the plastic zone size is required to determine how far the crack must grow between tests to get an accurate CGR measurement. Further detail on the plastic zone size and other considerations can be found in the FY20 final report [3]. All CGR data presented in this report has been reference corrected but has not been fully verified through fractography or post-test inspection of the sample.

For sample removal from the test environment, a fractography preparation procedure was followed. First, the test solution was drained, and the sample was rinsed multiple times with deionized water. If metallography or other analysis was to be performed at the crack tip, the entire specimen was removed and rinsed with methanol and dried. The specimen was heat tinted in an oxygen rich environment to highlight the tip of the crack for fractography. Next, the specimen was sectioned into 1/3 and 2/3 width pieces using a wire EDM. For example, the ¾ CT specimen shown in Figure 98 the “B” dimension would have a dimension of 0.25” for the 1/3 section, and the 2/3 section would be 0.5” thick. Figure 101 illustrates the method used to prepare a fractographic cross-section specimen for SEM/EBSD analysis. The 2/3 section was re-mounted in the load frame and fatigued at a high frequency (0.1-0.5 Hz) until the specimen failed. If crack-tip analysis was not performed, the sample was fatigued to failure immediately. The sample was then removed, rinsed thoroughly with methanol, dried, and stored in a desiccator until fractography analysis was performed.

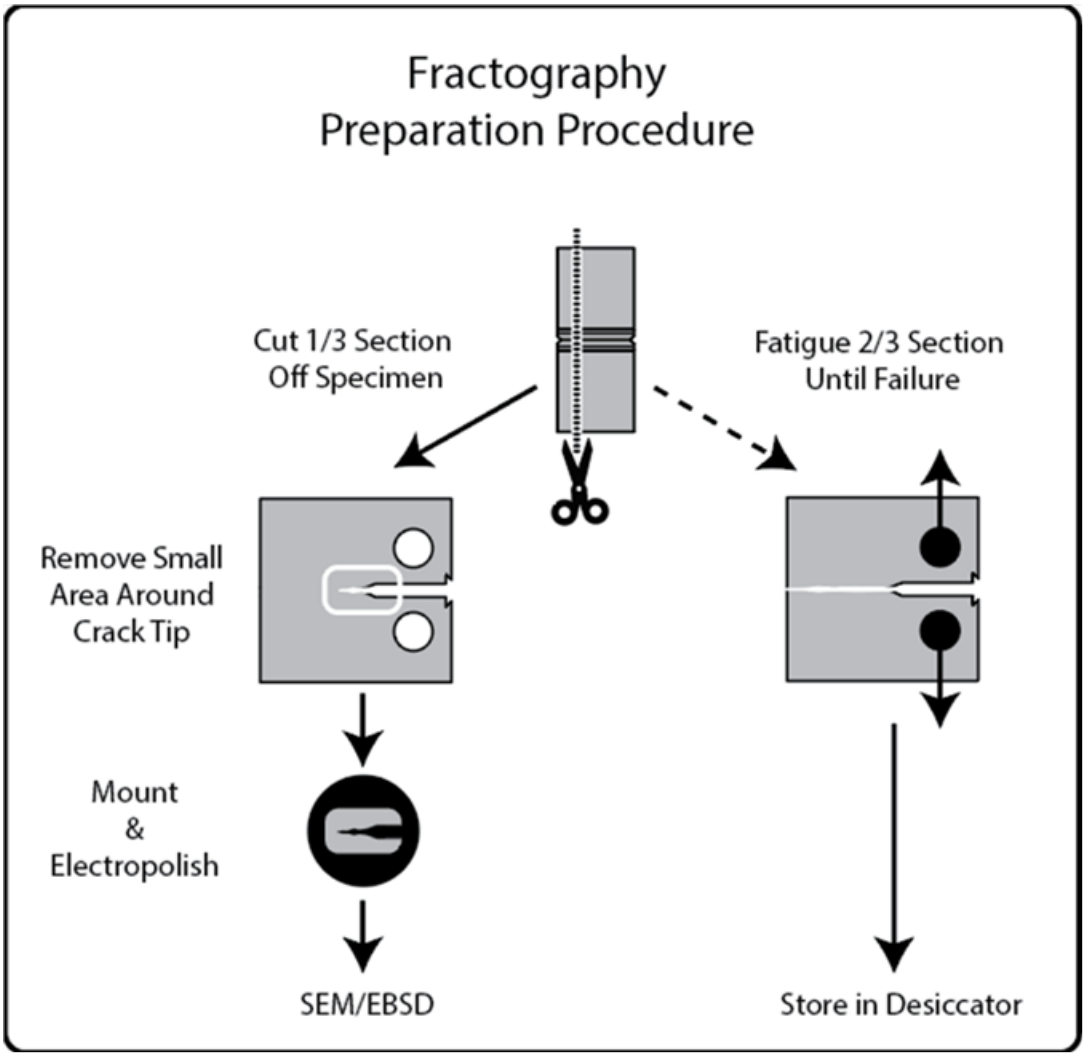

Figure 101. Method for preparing CT specimens for imaging using SEM/EBSD.

4.2 Fractography

Three CT samples tested by DNV in FY20 were sectioned by wire EDM into two sections, 2/3 and 1/3 thick respectively as shown in Figure 101. A example sectioned sample can be seen in Figure 102. The region around the notch tip and crack were wire electrical discharge machined (EDM) from the 1/3 portion as seen in Figure 102 (A). The 2/3 portion was fatigued open in air to make the fracture surface more accessible. A side view of the 2/3 portion of the specimen broken by fatigue can be seen in Figure 102 (B). In Figure 102 (C), a top down view of the 2/3 portion after being fatigued open is seen. The greenish color on the notch and fracture surface is a result of heat-tinting after the test. The samples were fatigued open after heat-tinting, so the ductile surface still appears silver/grey in optical images. The fracture surfaces were examined in SEM. The crack tip was examined with EBSD.

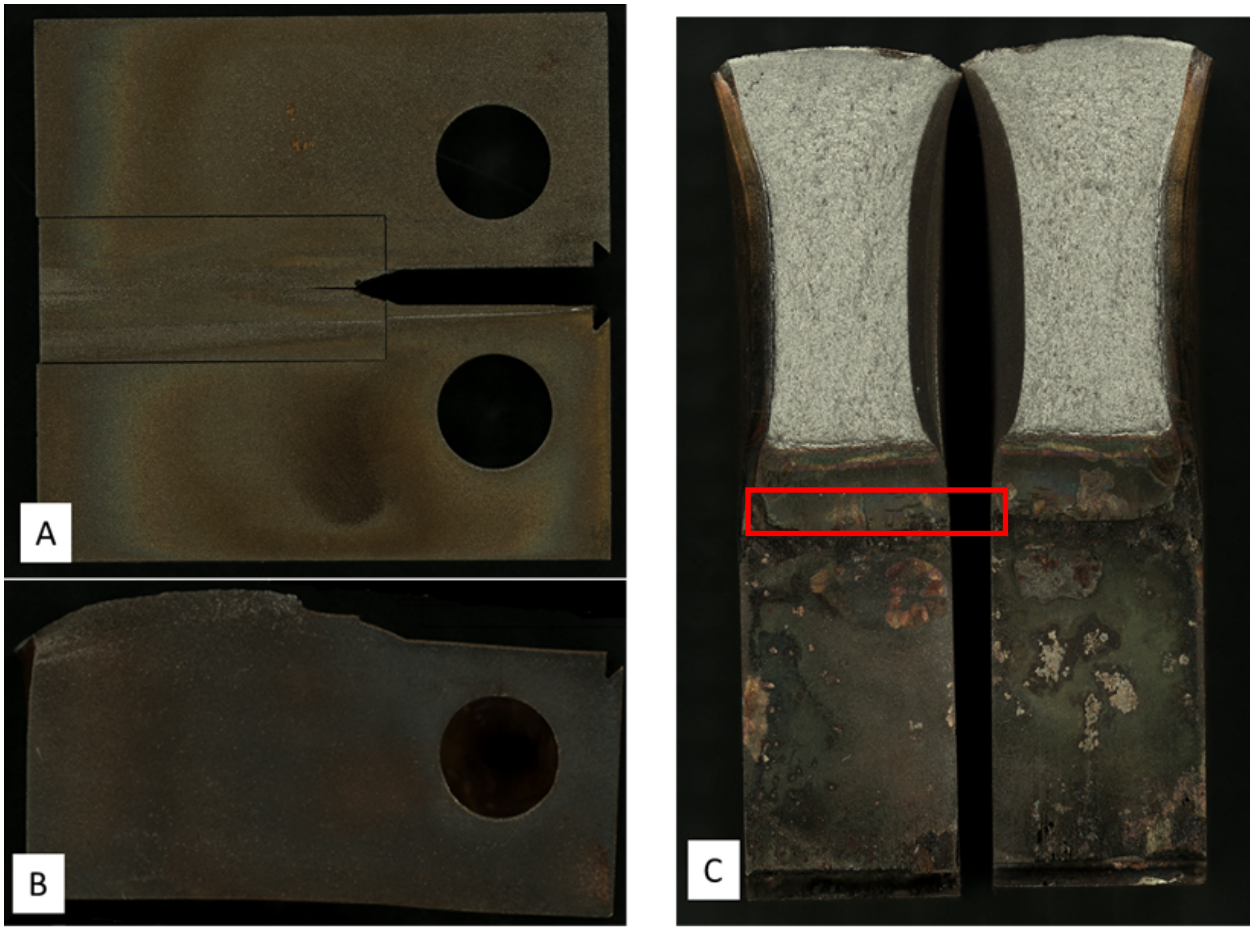

Figure 102. Optical (Keyence VHX-7000) images of the CT specimen tested in saturated NaCl. (A) 1/3 slice showing where the crack tip region was cut out. (B) One side of the 2/3 slice after being fatigued open. (C) Top down images of the 2/3 slice after being fatigued open. The notch is in the lower portion of the image and the ductile fatigue post-test is at the top of the image. The red box shows the approximate region of interest.

4.3 SCC Testing Environments

4.3.1 Ambient Air

A ¾ CT specimen manufactured from Lot 3 was tested using the same protocol as performed on full immersion experiments to determine the natural fatigue crack growth response and the drift of the crack length measurement of the specimen under constant stress conditions. This measurement of drift is more representative of drift seen in actual immersed tests since the sample was stressed to the same stress intensity and the measurement was conducted at the same time (same thermal drift, etc.). The ambient air tests were performed in the horizontal load frame at ambient temperature (~25°C), Figure 103.

a) b)

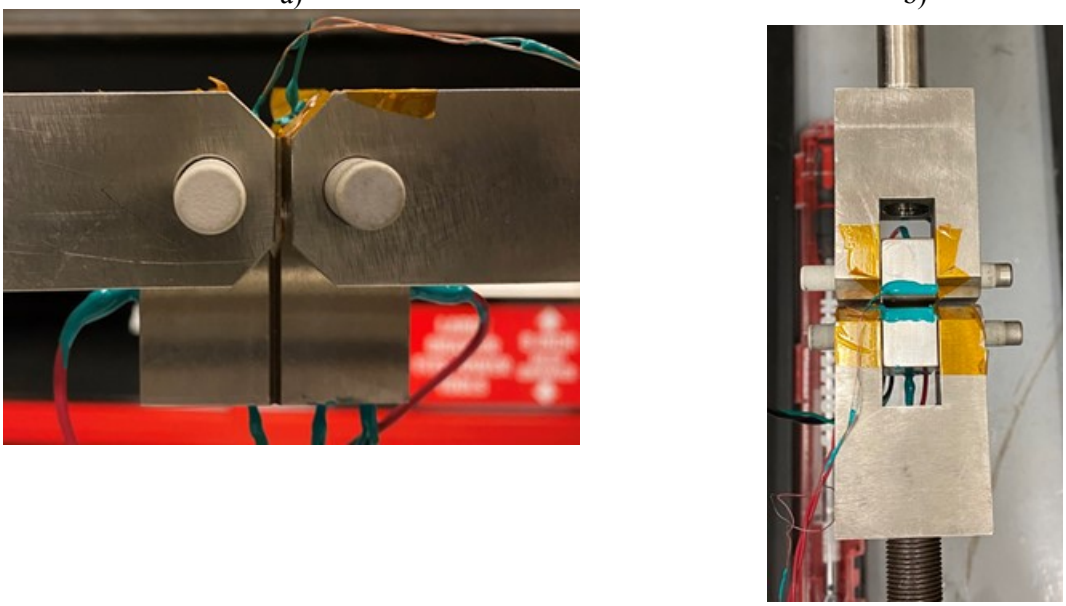

Figure 103. 3/4 Compact tensile specimen mounted in horizontal frame for ambient air CGR test, a) side and b) top.

4.3.2 Immersed Tests

Full immersion tests were performed on the three vertical frames. An immersion chamber was constructed around the sample (after pre-cracking was complete) and filled with the test solution. The solution was heated using a flexible heater adhered to the outer wall of the chamber. A thermocouple was inserted into the test solution and placed in close proximity to the crack area to ensure that the target temperature was achieved near the tip of the crack. The thermocouple was used as a feedback sensor for a PID controller which controlled heating of the brine when the flexible heater was used. Figure 104 shows a CT specimen mounted in an immersion chamber. The test leads, which were welded to the sample and insulated using 2-part epoxy, are routed out of the top flange of the immersion chamber. The specimen was electrically isolated from the frame by the use of ceramic loading pins and polyimide tape in the grip area (similar to Figure 103-b). This prevented current from flowing through the loading components which would change the magnitude of the current flowing through the sample. The small gauge wires in were welded across the notch opening and enable the primary DCPD voltage measurement, Figure 104-b. This same test setup was utilized for ½ and ¾ CT specimens.

a) b)

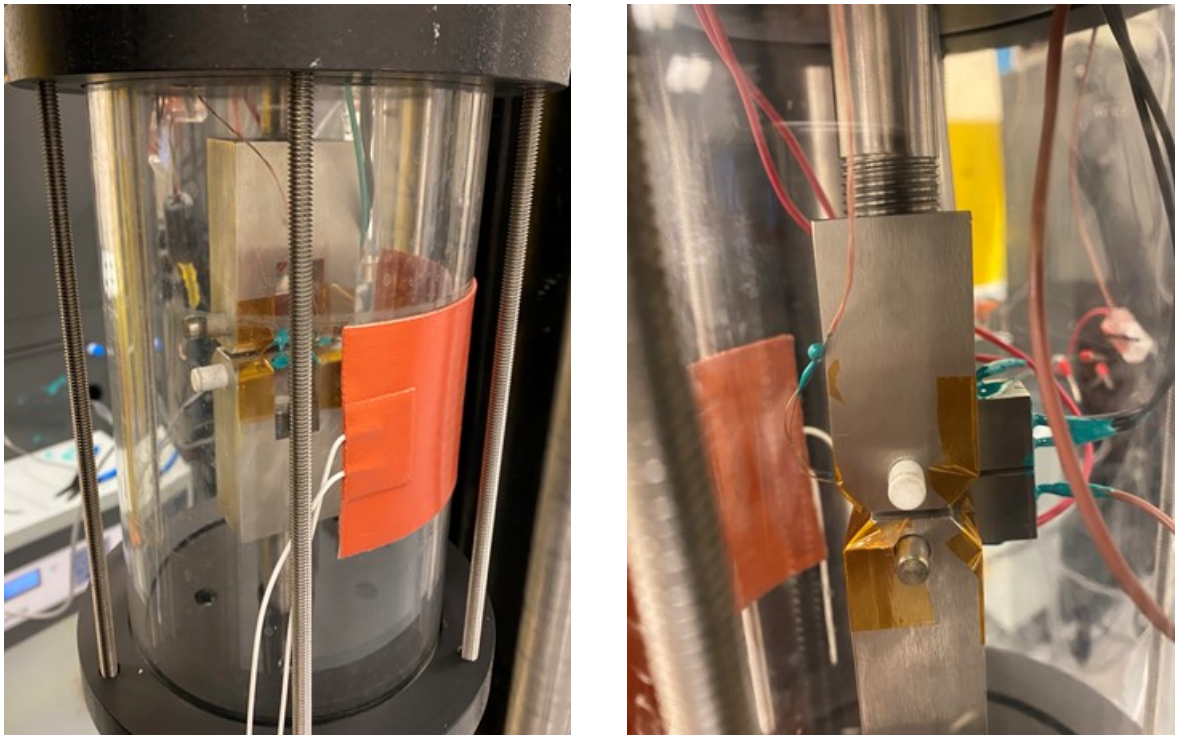

Figure 104. Compact tensile specimen mounted inside immersion chamber on vertical test frame. a) front view with flexible silicone heater is shown attached (orange) and b) side view with leads visible.

4.3.2.1 Circulation & Oxygenation

Quiescent brine conditions displayed no crack growth during initial testing in saturated magnesium chloride at 55°C (rates observed were below the established noise and drift levels). To enhance oxygen in solution, and avoid concerns of O_2 depletion as shown to be a potential issue by PNNL [111], circulation and oxygenation methods were installed on two load frames to determine the impact of circulation and oxygen on CGR.

Figure 105-a shows a simple schematic of the oxygenation method in which a bubbler was installed inside the immersion chamber. CGR was measured at constant K conditions before the addition of the bubbler. Other than fluid circulation caused by the percolation of bubbles, no other sources of circulation were added. A flow of 100 mL per minute of ambient air was bubbled to oxygenate the solution. The solution was heated using the same methods described in section 4.3.2. The sample was re-transitioned and CGR was measured at constant K conditions after the bubbler was installed.

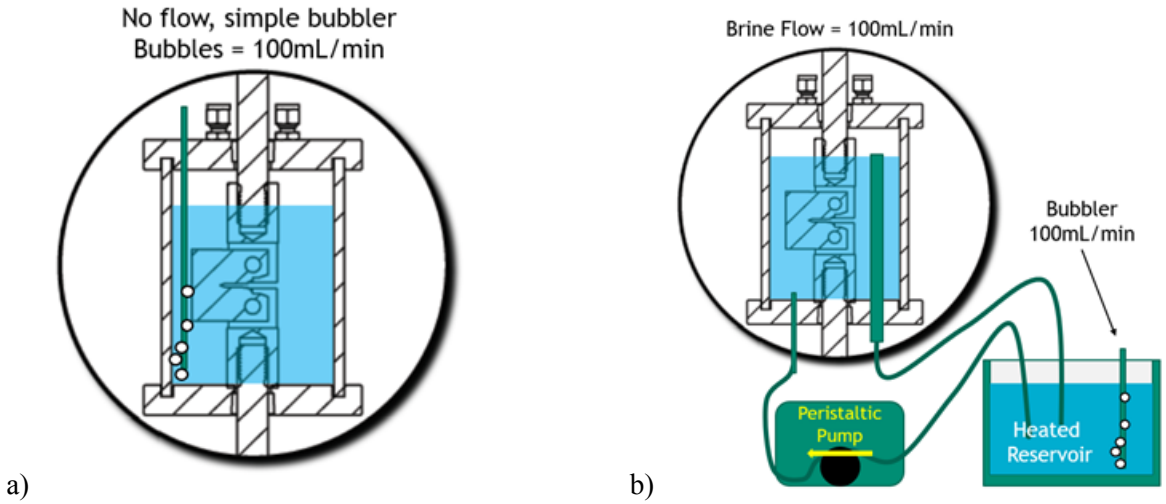

Figure 105. a) Schematic of simple bubbler system used to oxygenate brine during immersion tests and b) with the addition of the heated brine circulation system.

A second oxygenation and circulation method was installed on a second vertical frame which contained a ½ CT specimen. As described above, the CGR of the specimen was measured prior to installation of the oxygenation and circulation method shown in Figure 105-b. A heated reservoir was used to store, oxygenate, and heat a large volume (~10 liters) of test solution. A simple bubbler as shown in Figure 105-a was installed in the reservoir and 100mL per minute of ambient air was pumped into the solution. The solution was circulated through the cell at 100mL per minute. Fresh solution was pumped into the immersion chamber through a fitting in the bottom flange, while older solution was expelled through a large-diameter, gravity-fed drain tube which limited the level of the brine in the chamber. Further implementation around the cell, tubing, and external reservoir was applied to maintain a constant temperature.

4.4 SCC Results & Discussion

4.4.1 Initial Tensile Testing

Figure 106 features example images of a tensile test as it progressed from start to finish.

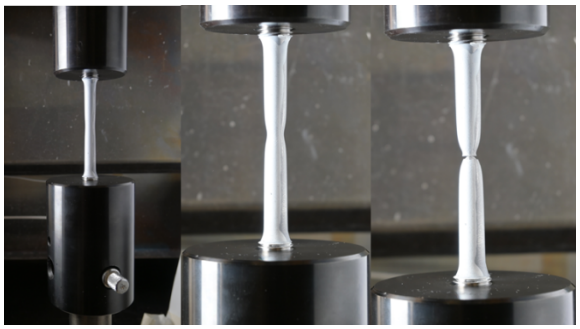

Figure 106. Example progression of tensile tests on round tensile specimens. The white coating is a random speckle pattern for Digital Image Correlation strain measurement.

a) b)

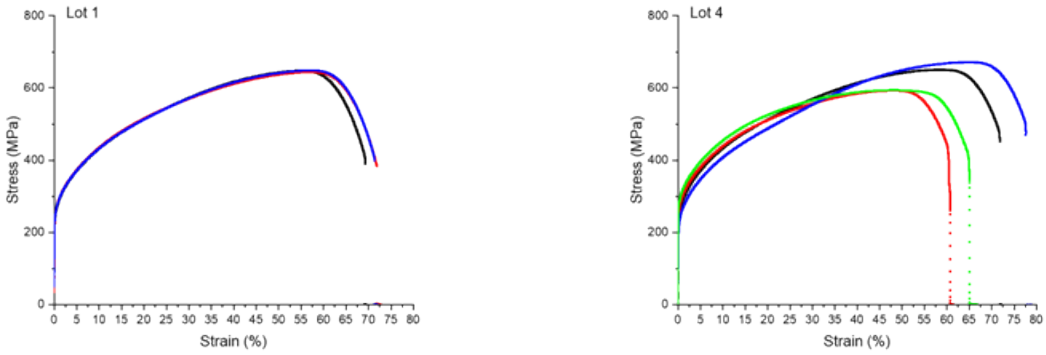

c)

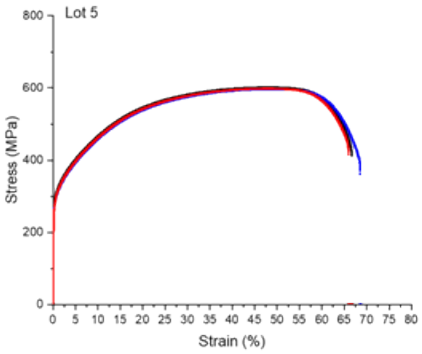

Figure 107. Stress vs. strain raw data for a) Lot 1, b) Lot 4, and c) Lot 5 (SS316L) tensile specimens. Note: Lot 4 tested with varied strain rates.

Lot 4 specimens, Figure 107-b, exhibited a large variability in UTS and strain-to-failure when compared to Lot 1 specimens, Figure 107-a. It was later determined that strain rates were varied during testing of Lot 4, therefore causing variability. Work in FY22 will include a re-run of this sample set. Lot 5 specimens (Figure 107-c) exhibited minimal variability between specimens and had remarkable agreement on strain-to-failure. Lot 5 specimens exhibited the least amount of specimen-to-specimen property variability of the lots measured.

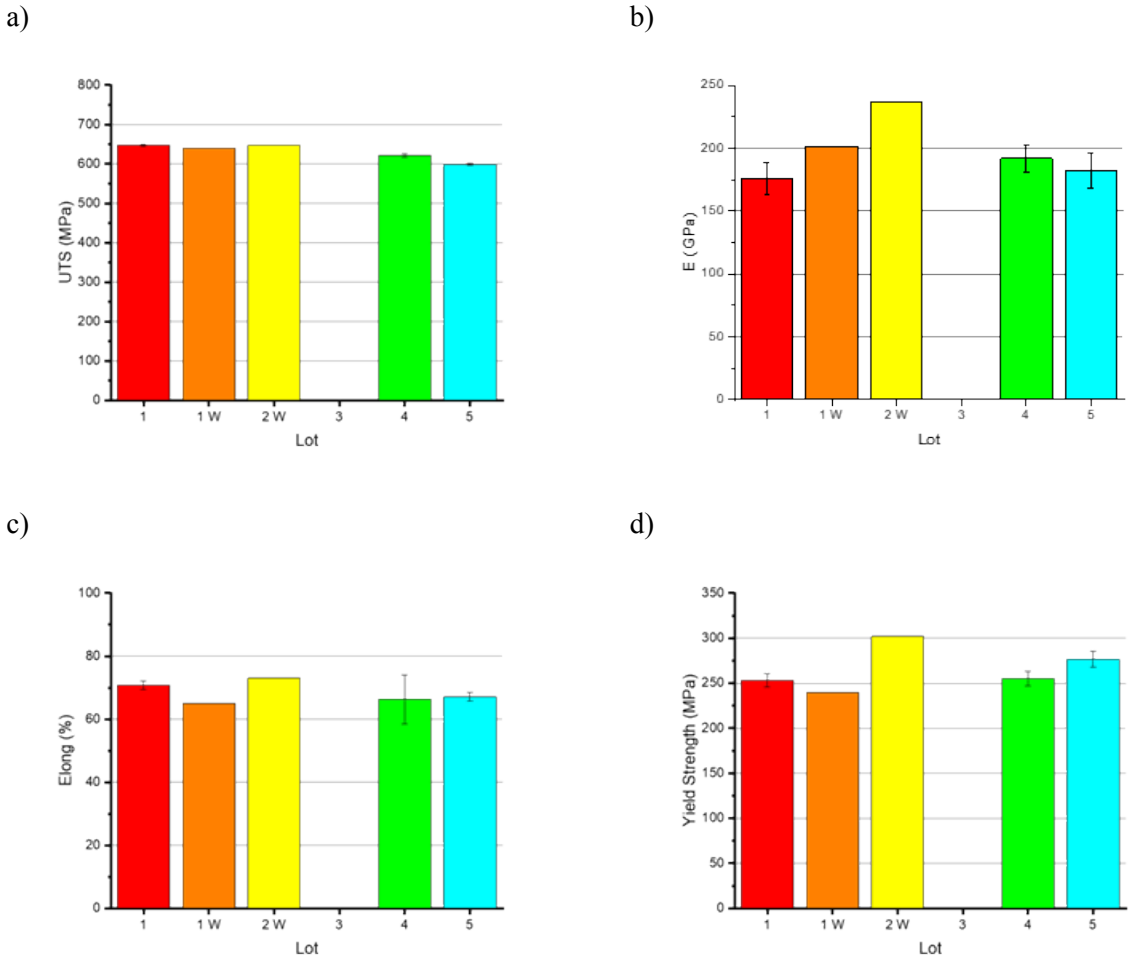

Figure 108. a) Ultimate Tensile Strength (UTS) in megapascals, b) Elastic Modulus (E) in Gigapascals, c) Elongation, and d) Yield strength in megapascals for all material lots. Lots marked with "W" were tested by Westmoreland Mechanical Testing and Research Inc. Lot 5 is a 316 SS alloy. Note: Lot 4 was tested with varied strain rates.

Ultimate tensile strength (Figure 108-a) did not vary much across material lots despite significantly increased sulfur concentration in Lot 4 when compared to Lots 1, 2, 3, and 5. All lots had a UTS of approximately 600-650 MPa. Further, the sample-to-sample variability of Lots 1, 4, and 5 (indicated as error bars in all figures in this section) was minimal. Error bars are not indicated on data from Westmoreland as only one specimen was tested for each lot. The largest property variability was observed in elastic modulus (E, Figure 108-b). Specimens tested at Westmoreland Mechanical Testing and Research Inc. in 2019 exhibited ~110-125% higher elastic modulus values than those measured at SNL. Elongation to failure shown in Figure 108-c varied between 60 - 70% for all lots. The highest sample variability was seen in Lot 4. This could be explained by the difficulty experienced while measuring large elongations with DIC and potential issues with optimization. Yield strength was highest in Lot 2 samples tested at Westmoreland, but Lot 5 exhibited the highest yield strength of lots tested at SNL, however it is also a SS316L alloy as compared to SS304.

4.4.2 Initial constant K SCC testing

As mentioned previously, CGR measurements presented herein are shown as an example of system enhancement and reliability. While some measurements are consistent with literature data trends, these are initial tests and should not be assessed as quantitative measurements of CGR. Work in FY22 will apply lessons learned and methods developed in FY21 to establish testing protocol that can be used to produce a quantitative assessment of CGR across canister relevant environmental conditions.

4.4.2.1 Ambient/Open Air Conditions

Measurements of CGR in ambient conditions provide the fatigue crack growth rate of a material (without the influence of corrosion). In air, when constant K is achieved, the crack should not grow unless the applied stress intensity is higher than the fracture toughness of the material. A stress intensity of 20 MPa√m is well below the fracture toughness of 304L which is ~375 MPa√m (this value is highly dependent on the composition of the alloy, level of cold-working, and testing conditions [112]). The fatigue transition and constant K test segments for a Lot 3, ¾ CT specimen in ambient air and at ambient temperature (25°C) are shown in Figure 109. A "CGR" of 1.9×10^{-9} was measured when the sample was at constant K. This can be attributed to the electrical drift of the DCPD measurement. Thus, for the remainder of this report CGR values less than this value will be reported as "No Crack Growth". The point of these measurements was to determine the "drift" in the DCPD below which a CGR could not be detected, additional measures were taken to reduce the overall noise observed in the system as well.

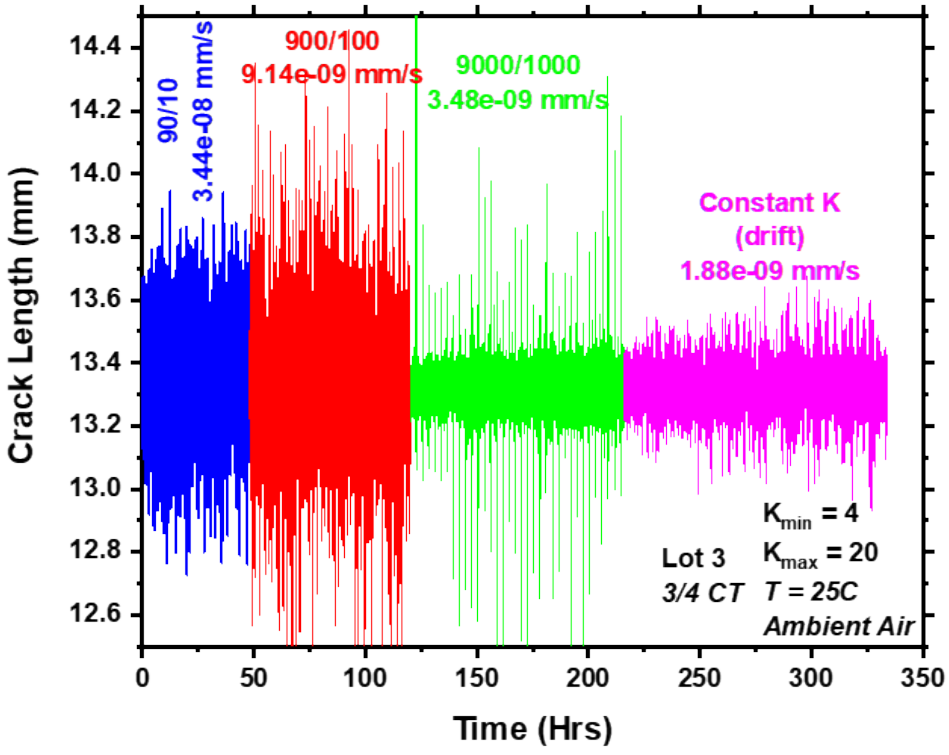

Figure 109. Transition procedure and constant K data for SN099 3/4 CT in ambient air and at ambient temperature. Note: Constant K growth rate is representative of *system drift* since crack should not grow at these stress levels.

4.4.2.2 Quiescent versus actively aerated conditions

Figure 110 and Figure 112 show data from CGR tests performed in quiescent saturated $MgCl_2$. After a significant measurement period of over 150 hours at constant K, both samples exhibited no measurable crack growth. Several factors may have caused this but one factor that was tested was dissolved oxygen content in the brine. Tests were re-run while oxygenating the brine with air (denoted as "bubbled", see Figure 111) and while circulating heated/oxygenated brine through the test chamber (denoted as "bubbled/circulated", see Figure 113), to determine whether dissolved oxygen content in the brine had an impact on the crack growth rate in these specimens. Constant K conditions were maintained on these samples for 200-300 hours before significant crack growth was observed. For this reason, the initial period and the region of significant crack growth are reported as separate CGR values. In FY22, fractography will be performed on these samples to better understand the changes observed in CGR, the influences of aeration, and for DCPD calibration.

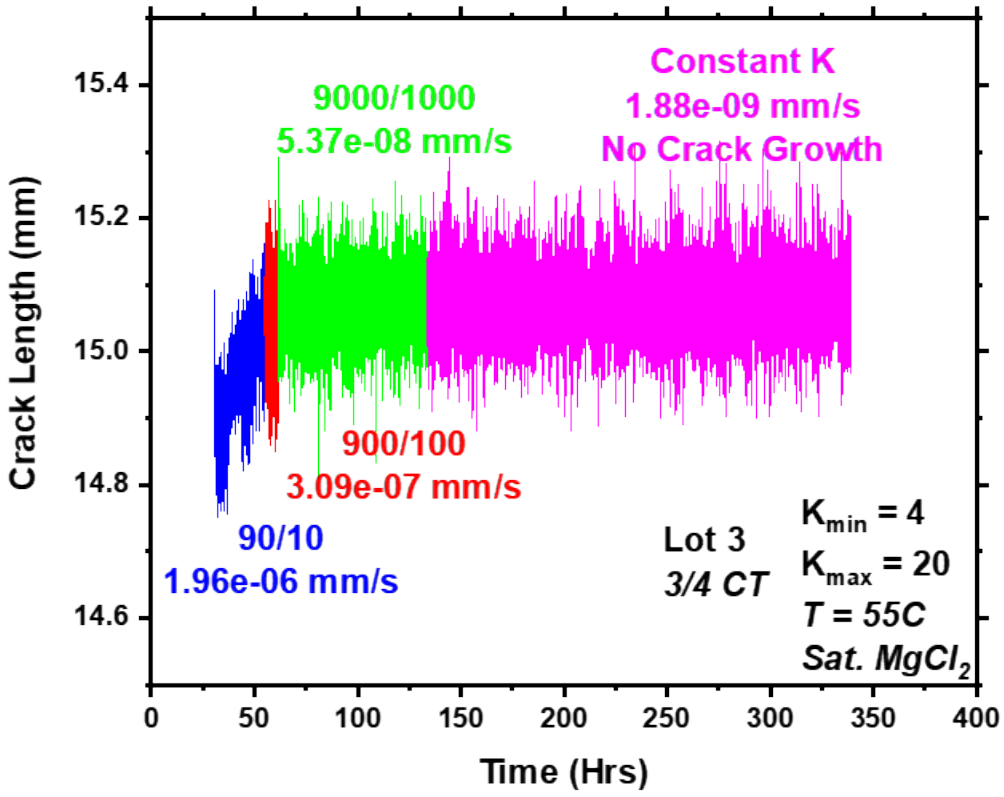

Figure 110. Transition procedure and constant K data for Lot 3 ¾ CT in quiescent saturated $MgCl_2$ at 55°C. Note: CGR at constant K is equal to system drift and is considered "*No Crack Growth*".

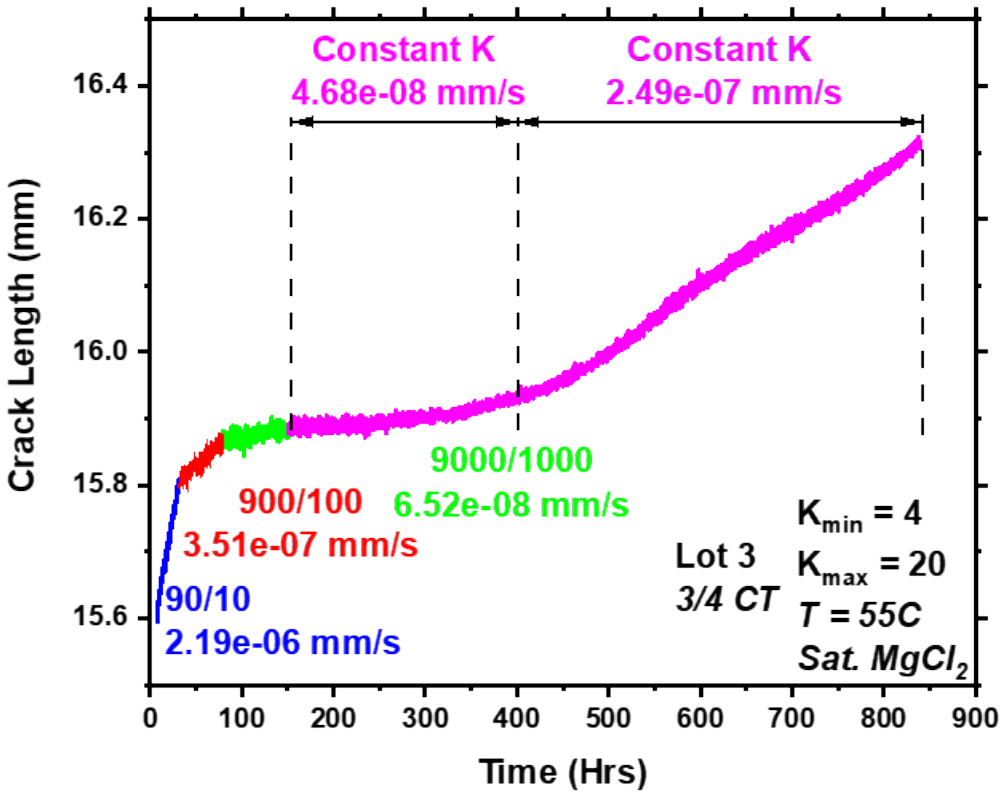

Figure 111. Transition procedure and constant K data for Lot 3 ¾ CT in bubbled saturated $MgCl_2$ at 55°C. Note bi-modal distribution of CGR at constant K.

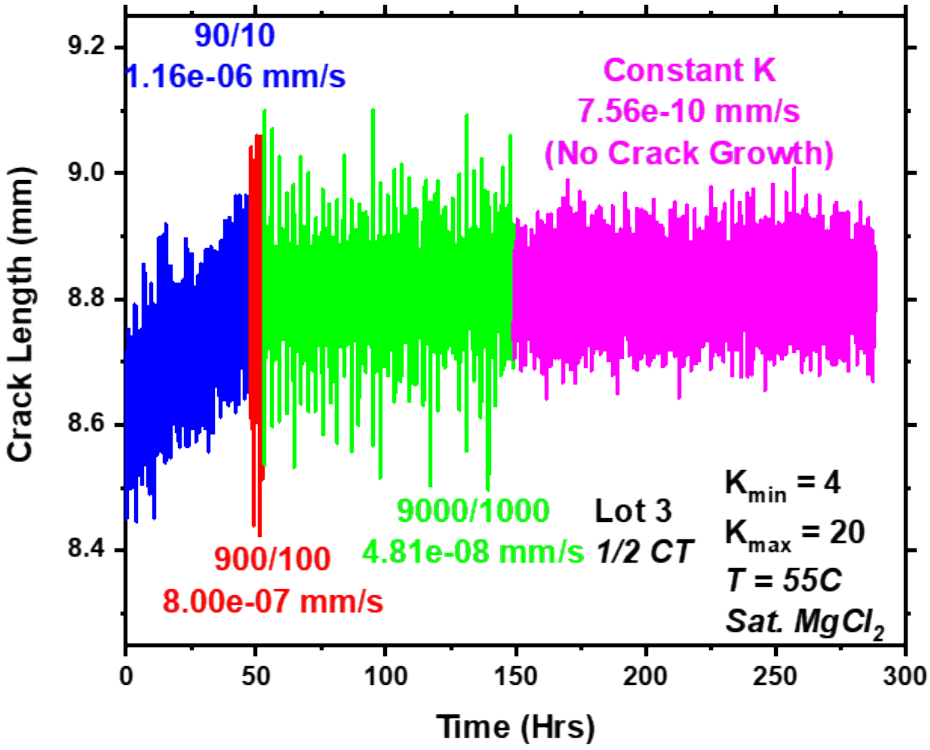

Figure 112. Transition procedure and constant K data for Lot 3 ½ CT in quiescent saturated $MgCl_2$ at 55°C. Note: CGR at constant K is equal to system drift and is considered "*No Crack Growth*".

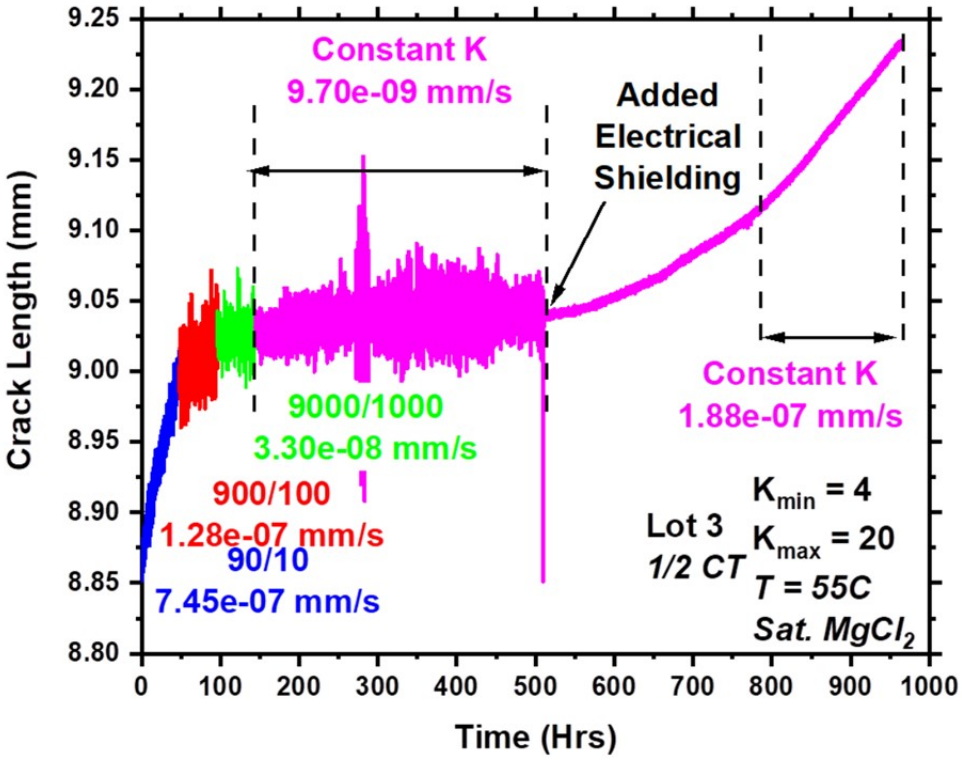

Figure 113. Transition procedure and constant K data for Lot 3 ½ CT in bubbled saturated $MgCl_2$ at 55°C. Note bi-modal distribution of CGR at constant K. Noise was significantly improved after adding high-quality electrical shielding.

Figure 114 illustrates the impact of bubbling and bubbling/circulation on the corrosion fatigue crack growth rate measured during the corrosion fatigue transition period for all Lot 3 specimens. While crack growth rates are significantly increased between ambient tested and brine immersed samples, the differences between quiescent and perturbed (circulating or bubbling) conditions are minimal.

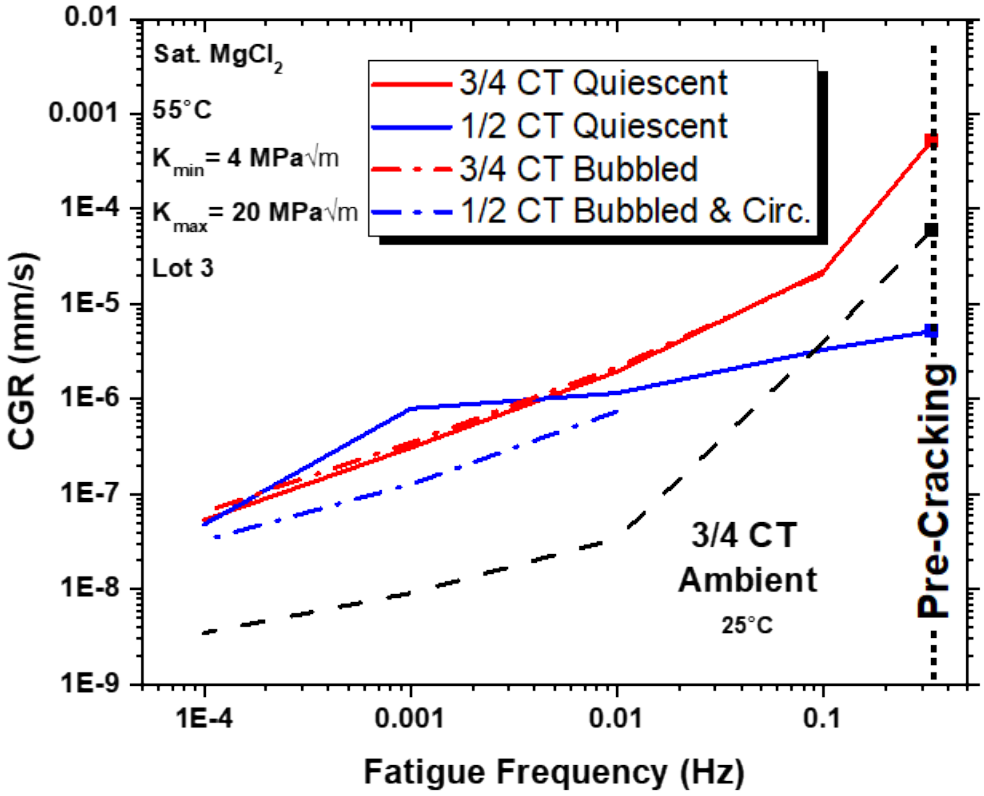

Figure 114. Corrosion fatigue crack growth rate as a function of fatigue frequency. Points at 0.33 Hz were pre-cracks performed in ambient air and at ambient temperature.

4.4.2.3 FY21 results from CGR collaborators

In collaboration with SNL, DNV-GL performed constant K CGR measurements on Lot 3, ¾ Ct specimens in 55 °C saturated $MgCl_2$ purged with zero air. Zero air is processed, compressed air that has very low or undetectable concentrations of CO_2. DNV-GL used the same transitioning procedure described previously. Figure 115 shows the transitioning and constant K behavior over a period of nearly 1,800 hours at a stress intensity of 16 MPa√m. Again, an initial region of no CGR is observed, spanning nearly 750 hours with no crack growth. After the incubation period, the CGR increased by three orders of magnitude to 4.07×10^{-7} mm/s.

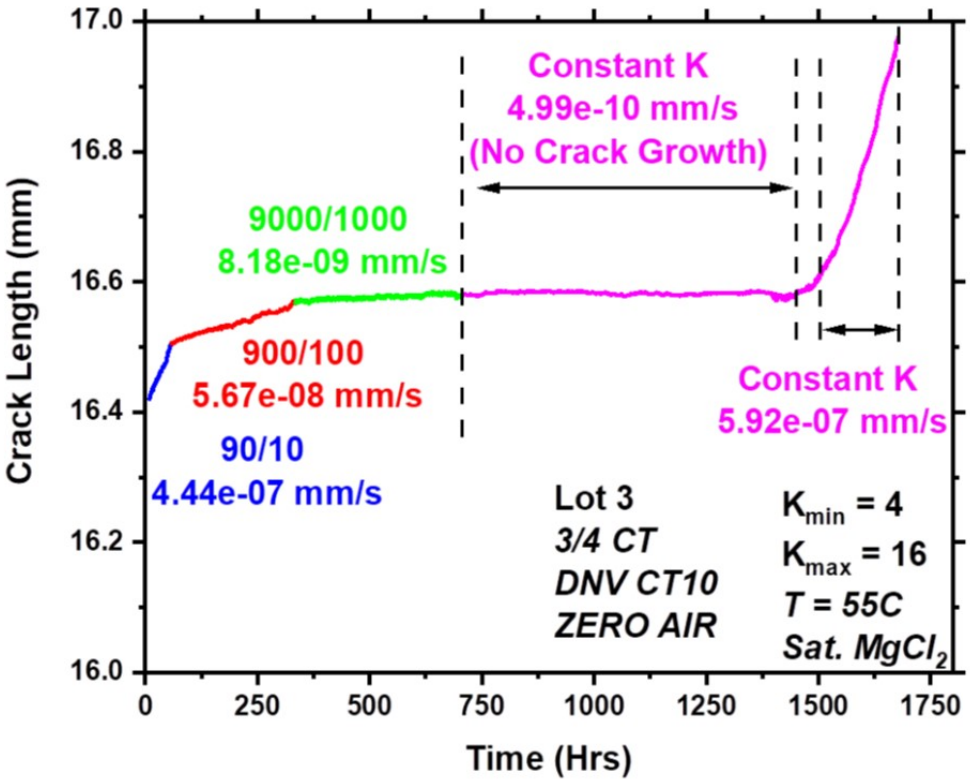

Figure 115. Transition procedure and constant K data for Lot 3 ¾ CT in saturated $MgCl_2$ at 55°C purged with Zero Air. Note bi-modal distribution of CGR at constant K.

When comparing initial results from different sample geometries, brine oxygenation method, and test lab it becomes clear that quiescent conditions results in CGR values well below the "No Crack Growth" threshold. Circulation and oxygenation (bubbling) of the brine produces CGR values at least one order of magnitude higher than quiescent conditions. Further development and optimization of a circulation and aeration system appropriate for relevant replication of SCC environments, that also produces reliable conditions and detectable CGRs will be carried out in FY22. This system will then be implemented across all SNL load frames and measurements.

4.4.3 Fractography of FY20 SCC Specimens

SEM image maps were taken of the fracture surfaces as seen in Figure 116 for the test specimens reported upon in the FY20 year-end report [3]. These images are oriented with the ductile, fatigued-open surface toward the top of the image and the initial notch in the lower portion of the image. Some regions appear clearly delineated on the fracture surface. High magnification images were acquired across the different distinct regions; regions were defined by those areas with visible differences in the SEM images and/or determined by DCPD data.

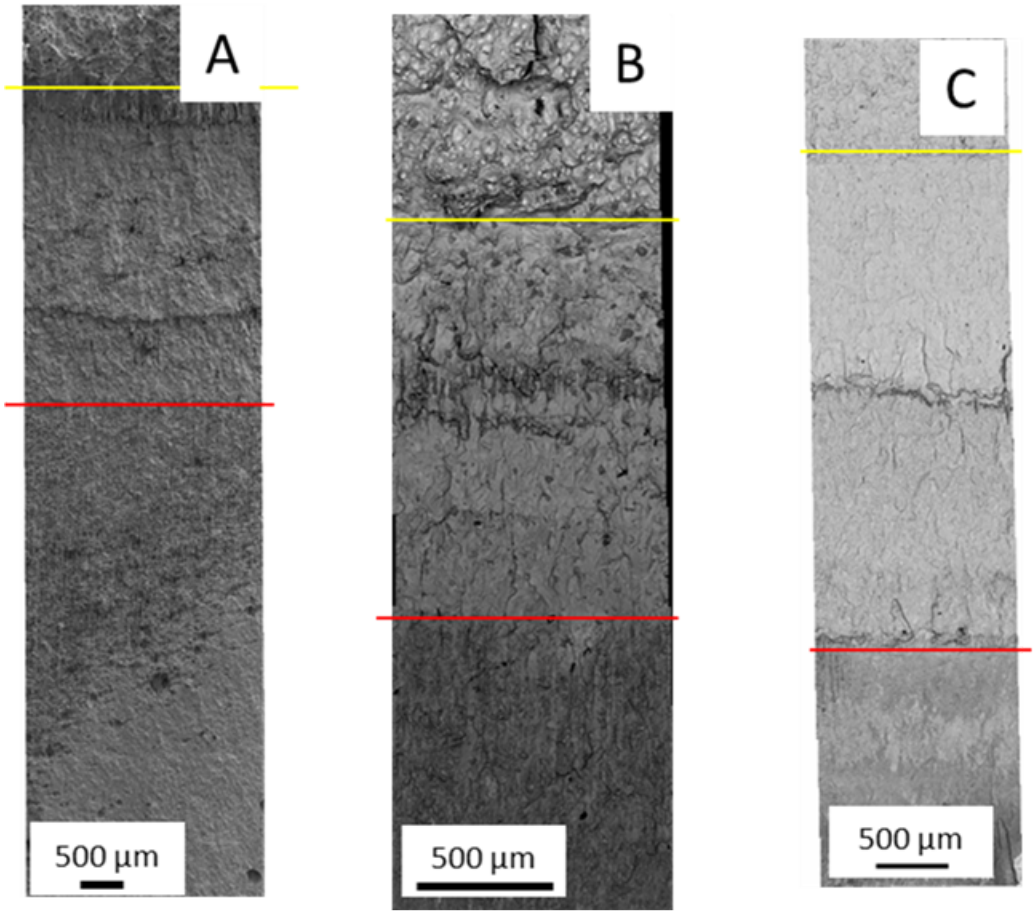

Figure 116. SEM micrographs of fracture surface for samples tested in (A) 76% RH, (B) saturated NaCl, and (C) saturated $MgCl_2$. Oriented with the ductile region (above the yellow, upper line) at the top of the image and the pre-crack at the bottom (below the red, lower line). These correspond to specimens reported on in the FY20 year-end report.

Figure 117 indicates the different regions of interest on the saturated $MgCl_2$ sample as determined by DCPD. DCPD indicated crack lengths for each test segment and these were used to calculate the expected positions of the resultant crack fracture surface in the image. This method helped narrow down regions of interest that feature fracture surfaces caused by stress corrosion cracking.

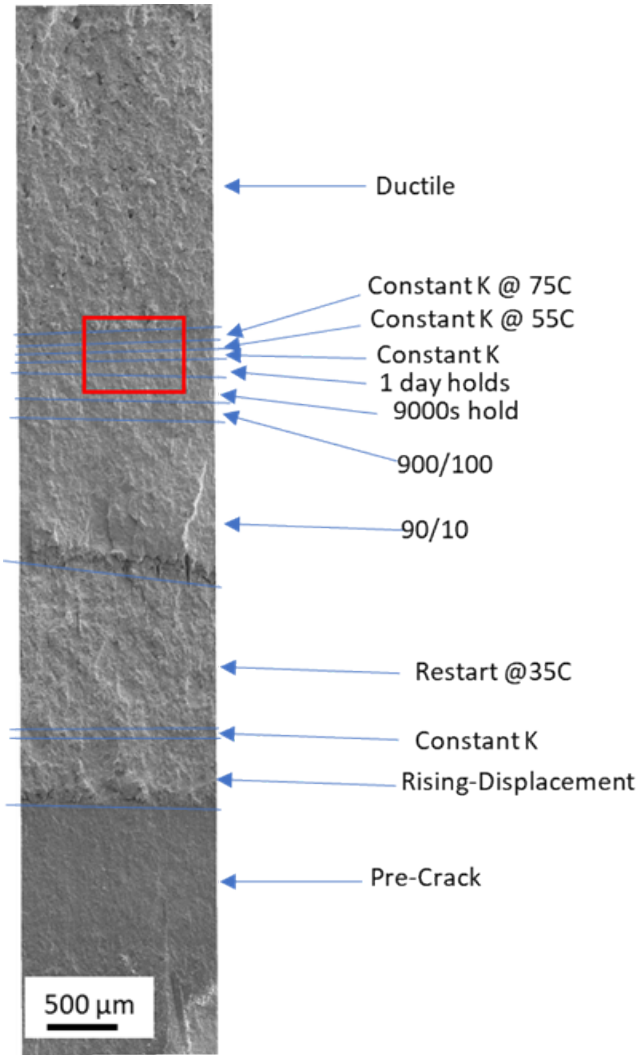

Figure 117. SEM micrographs of fracture surface for sample tested in saturated $MgCl_2$. Oriented with the ductile region at the top of the image and the notch at the bottom. Regions are labeled based on DCPD. Red box shows location of higher magnification images. This corresponds to the saturated $MgCl_2$ sample in the FY20 report.

For the sample tested in saturated $MgCl_2$, high magnification images were taken in various sections of the test, an example of the crack near the ductile region is presented in Figure 118. In the presented images, fatigue striations appear in all cases. These striations exist on the fracture surface all the way up until the ductile region, where the sample was fractured opened, post-mortem. In the constant K regions where the DCPD indicated a rate of 1.88×10^{-9} mm/sec, the sample did not exhibit crack growth that could be identified with SEM, further confirming that this is a no crack growth rate condition.

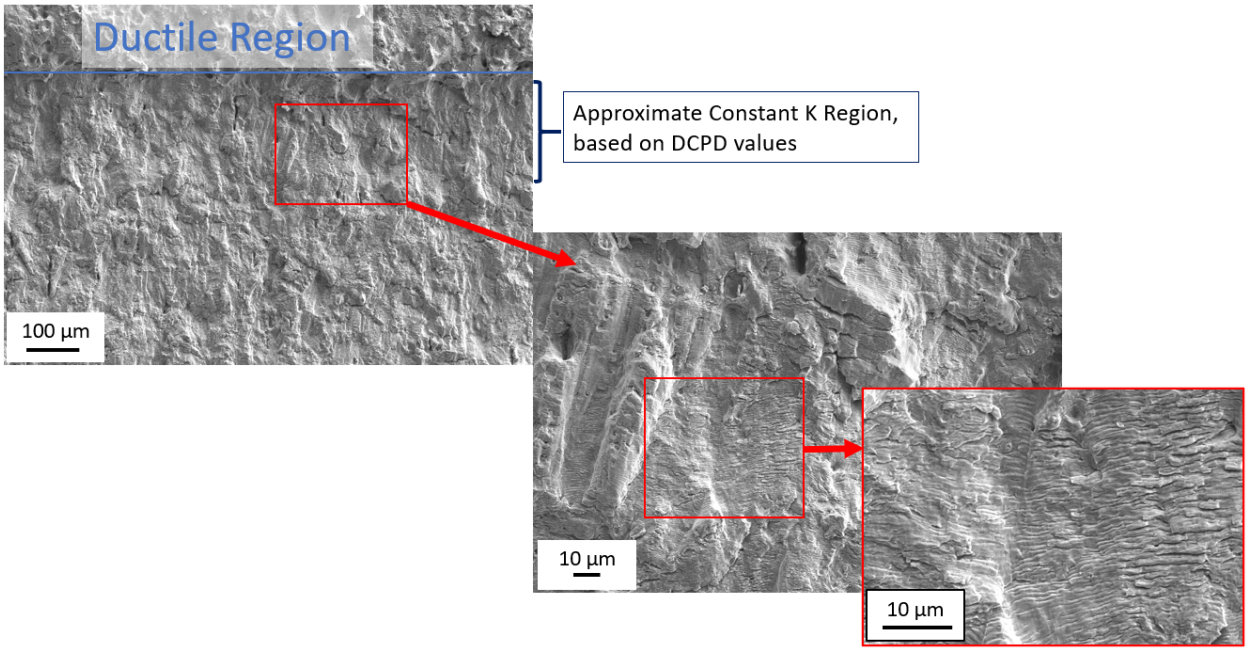

Figure 118. SEM micrographs of the fracture surface at/near the ductile region for the sample tested in saturated $MgCl_2$ at increasing magnifications. Oriented with the ductile region at the top of the image.

Further analysis was performed on the crack-tip portions of the 1/3 slices which were mounted in epoxy, polished to a mirror finish, and followed by a vibratory polish. Electron backscatter diffraction (EBSD) was performed near the crack front and can be seen in Figure 119. The behavior of the crack in all three cases is different. The sample tested in 76% RH equivalent sea-salt brine, in Figure 119-a, shows a wider crack with a narrower crack front extending further. The sample tested in saturated NaCl solution, in Figure 119-b, shows bifurcation and the crack stays much narrower. This bifurcation raises concerns about the ability to monitor crack growth with methods such as DCPD. Having multiple crack fronts will likely create noise in the data as Johnson's Equation is only valid for a single crack. If the cracks are continually overtaking one another, deconvolution of the data to extract a crack growth rate is complicated. In addition to this, the external stresses are also distributed across the bifurcated cracks further convoluting analysis. In Figure 119-c, the sample tested in saturated $MgCl_2$ solution, the crack front is very blunt. None of these cracks are very sharp, a feature anticipated in SCC. The sharpness of the crack could have potentially been degraded by atmospheric corrosion occurring during or after testing. Additionally, as these tests are all considered to be no crack growth conditions, it is likely that the morphology is due to corrosion at the pre-crack, rather than crack growth. Future experiments will include a more rigorous cleaning post-test. Additionally, the appearance of the sharpness in the EBSD is restricted by the step size, 400 nm in this case.

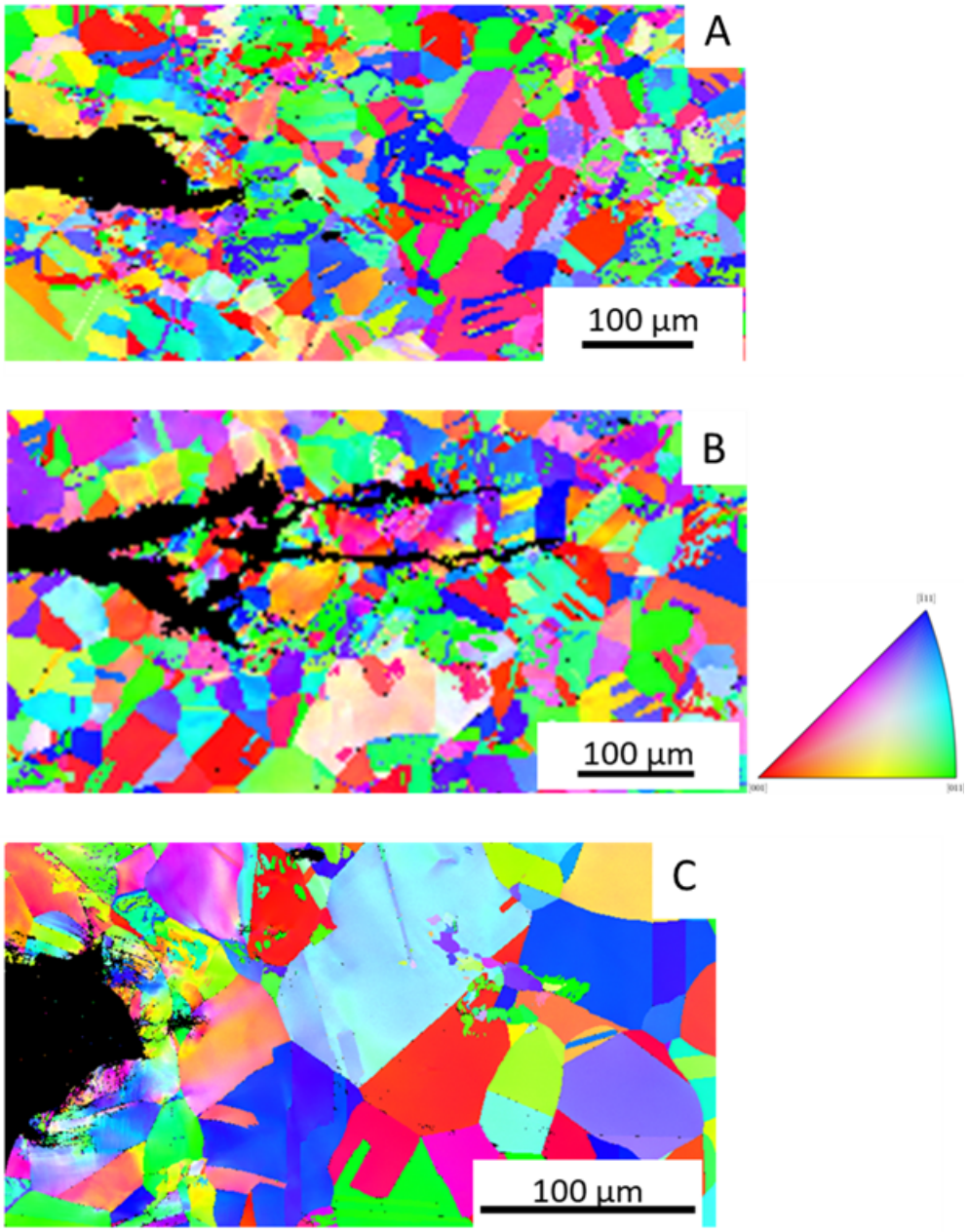

Figure 119. EBSD of crack tip region for DNV specimens from FY20 (A) 76% RH , (B) saturated NaCl, and (C) Saturated $MgCl_2$.

From the fractography results, there are multiple aspects of SCC testing and analysis that have to be considered. First, the blunted crack tips in Figure 119 indicates that corrosion reactions can have a significant influence not only on the stresses distributed at the crack tip but potential influences on the measured DCPD potential. Second, the bifurcating crack tips pose a potential problem both in DCPD signal and the ability to utilize a sample for multiple different environments (i.e. changing temperature). Finally, it is important to remember that the EBSD results are from a portion of the crack front. It is possible that the behaviors seen in the section taken at 1/3 through sample are not representative of the entire crack front, complicating analysis further.

4.5 SCC Future Test Plan

The primary goals of FY22 will be to apply lessons learned during the initial CGR setup with regards to test-setup (aeration, solution cycling), data acquisition, noise reduction, and post-mortem analysis to future data collection in more uniform and carefully controlled environments. From an instrumentation standpoint, efforts are underway to standardize the methods with which the test brine is heated, oxygenated, and circulated through the test chambers for all load frames and to establish relevant conditions for canister environments. Additionally, development of realistic exposure methods (such as spraying or salt printing) and under atmospheric conditions will be carried out. Alternate sample geometries may be explored to enhance results obtained from realistic exposure methods.

4.5.1 Exposure Conditions

The physical methods used to expose the samples to the test environment are of extreme importance in measuring crack growth rates accurately with respect to real-world conditions. The full immersion tests currently applied for SCC may not fully represent the canister relevant environments. Additionally, canisters exhibit many inhomogeneities which impact the severity of the exposure conditions. These inhomogeneities may include surface temperature [113], surface finish, metallurgical conditions (like weld zones [114]) and orientation with respect to the passive cooling vents. These inhomogeneities impact the deliquescence of salts from the environment, how easily particles and salts cling to the surface of the canister, and the SCC susceptibility of the material where salts and particles are deposited. Efforts are already underway to understand more canister relevant corrosion environments, as discussed in Section 3.2, and the results of these studies will be used to inform brine chemistries and concentrations in future CGR tests. Surface finish has also been observed to impact the severity of pitting when brines are present, Section 3.2.1.3.

Thus, the methods used to expose CGR specimens to a test environment eventually need to take these factors into account. Some methods relevant to atmospheric testing are described in previous reports [3] and include wicking, spraying, and printing of brines near the notch tip in CT or Single-Edge Notched Tensile (SENT, see Figure 120) specimens. SENT specimens have a smaller cross-section and allow easier transport to the tip of the crack. FY22 research will further investigate the impact of circulation/bubbling, more accurate brine delivery methods (such as controlled-humidity tests), and testing in more representative brine chemistries such as those seen at coastal storage sites.

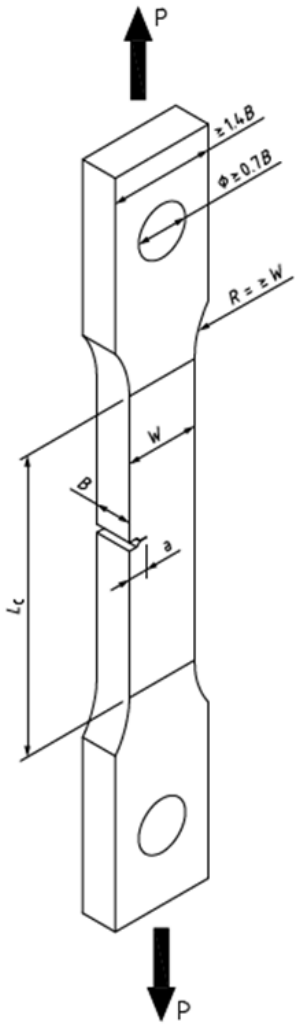

Figure 120. Schematic of Single Edge Notched Tensile (SENT) specimen from BS 8571:2014 [115].

4.5.2 Fractography

Future work will include validation of crack growth, both in air and in solution, with DCPD and fractography for SNL-tested specimens. Furthermore, longer crack lengths (across multiple grains) will facilitate correlation between the DCPD data and the microscopy of the fracture surface and the crack tip section. Further characterization of the crack tip portion will also examine potential microstructural influences, such as strain-induced martensite, on the CGR and crack morphology.

4.5.3 Lot-to-Lot Variation

Lot-to-lot variation in CGR measurements will be further investigated in FY22. More tests are planned to investigate the differences between Lot 1, which was reported in FY20 [3], and Lot 3 which was reported here, and is the same as material tested at PNNL.[96] More studies are also planned on Lot 2, which features an elevated concentration of sulfur. Sulfur content is known to increase susceptibility to stress corrosion cracking. Lot-to-lot variation will be evaluated across laboratories as well, including collaborations with PNNL.

This page is intentionally left blank.

5. Cold Spray Collaboration

In collaboration with Pacific Northwest National Laboratories (PNNL), work over FY21 has been carried out to assess initial corrosion resistance of cold spray coatings as a mitigation and repair strategy for SNF canisters. Efforts towards mitigation and repair strategies (other than cold spray) that are being carried out at SNL are detailed in the recently submitted Coatings FY21 milestone report [1]. The discussion here will focus on a summary of the corrosion work carried out only on cold spray samples with a further detailed analysis presented in PNNL's FY21 milestone report [9].

Cold spray is a solid phase metal spray process during which no melting occurs. Metal particles are carried by a heated gas stream that softens the metal and propels particles at supersonic velocities towards a substrate. The impact energy is high enough to bond metal particles to the surfaces they impact. Because it is a solid phase process, cold spray avoids oxidation, tensile residual stresses, and other detrimental effects typical of the high heat input and melting associated with thermal spray. Cold spray can produce infinitely thick coatings with beneficial compressive residual stresses. Cold spray process details and best practices are more fully in last year's cold spray report [116].

Cold spray samples were produced as per processing described in the PNNL Year-end report [9]. Three cold spray material types, Inconel, Super C, and CP Nickel were sent to SNL processed from the powder compositions provided in Table 23. All materials were deposited on SS304L base plates, as shown in Figure 121. As seen in Figure 121-b, the cold spray edge morphologies were tested in two configurations. Blended edges refer to those that are untreated and allowed to build up a tapered edge between the cold spray and base material due to overspray with successive cold spray passes. Masked edges refer to cold spray edges that were masked during application, thus the edge exhibits a sharp, 90° transition between the cold spray and base material. In addition to cold spray material differences and edge effects, samples provided by PNNL also employed two process gasses, He and N, which will be explored further in FY22. A summary of the samples used in corrosion testing is provided in the following section with a full detailed report in the PNNL FY21 Year End Report [9].

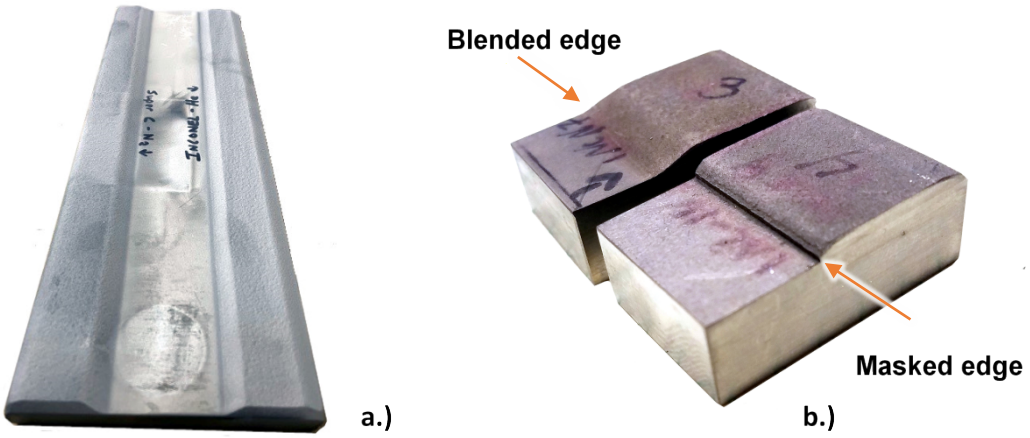

Figure 121. a) Cold spray plate and b) example edge geometries: Blended vs. masked.

Table 25. Elemental composition for the processing powders used.

	Inconel 625-2	Super C	CP Ni
C	0.01%	0.02%	-
Cr	21.19%	23%	-
Ni	Balance	Balance	>99.9%
Mo	9.1%	17.7%	-
Mn	0.04%	0.7%	-
Si	0.07%	0.5%	-
Cu	0.02%	-	-
Fe	3.94%	0.6%	-
Al	0.10%	-	-
Nb	3.68%	-	-
O	1.94%	-	-
V	-	0.30%	-
W	-	0.26%	-
V	-	0.30%	-

5.1 Initial corrosion evaluation of cold spray materials

Cold sprayed samples (example images in Figure 122) were analyzed through electrochemical (ASTM G5-14-e1) and full immersion $FeCl_3$ (ASTM G48) exposures to determine initial corrosion properties. Samples were tested in the "as-received" condition, as well as polished to 600 and 1200 grit. For full immersion testing (ASTM G48), sample surfaces other than the top cold spray to base material surface of interest, were painted (Figure 122-b) to minimize edge effects and other contributions during testing. The matrix of samples was supplied by PNNL and analyzed for corrosion susceptibility through accelerated testing methods as noted in Table 26.

a) b)

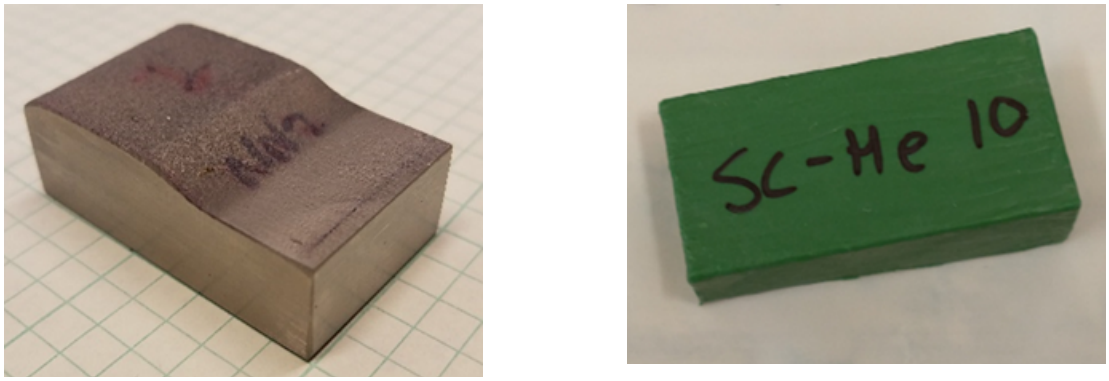

Figure 122. a) Top view of unpainted test coupon. b) Bottom view of painted test coupon. Bottom and sides of coupons were painted such that only the top surface will be exposed during pitting tests.

Table 26. Cold Spray sample corrosion testing matrix.

CS Material	Edge Process	Process Gas	Electrochemical Testing (ASTM G5)			$FeCl_3$ Testing (ASTM G48)
			As Sprayed	*600 grit*	*1200 grit*	
Inconel	Blended	He	X	X	X	X
Inconel	Blended	N	-	-	-	X
Inconel	Masked	N	X	X	X	X
Nickel	Blended	N	-	-	-	X
Nickel	Masked	N	X	X	X	X
Super C	Blended	N	X	X	X	X

Corrosion behavior of the cold-sprayed materials was evaluated by potentiodynamic polarization scans according to ASTM G5-14e1 (and detailed in the PNNL FY21 milestone report). Samples were tested in quiescent 0.6 M NaCl solution at room temperature (25 ºC) and measured a minimum of three repetitions (Figure 123) for each surface finish (As received and polished to 600 or 1200 grit). Only areas on the top cold spray surface were tested (no edges or interfaces). Electrochemical testing consisted of a one-hour open circuit potential (E_{OCP}) followed by an anodic potentiodynamic polarization (PP).

Accelerated full immersion pitting tests were performed in accordance with ASTM G48 Method A. This allowed for simultaneous evaluation of the base material, interface, and cold sprayed regions (depicted in Figure 123) of each sample. As-received (as-sprayed) cold spray samples were placed in 6% by mass ferric chloride solution in full immersion for a total of 72 hours at a constant temperature of 22 ºC. Following immersion, all samples were rinsed with DI water to remove corrosion product and dried with nitrogen. These immersed $FeCl_3$ tests do not force failure; instead, they accelerate failures that might occur over longer time periods in more benign environments, enabling us to understand, in short time frames, where failure is likely to occur and what failure is likely to be due to.

Pre and post exposure, samples were imaged using both optical and scanning electron microscopy (SEM) techniques to assess corrosion damage. Details of all techniques are provided in the PNNL Milestone report [9].

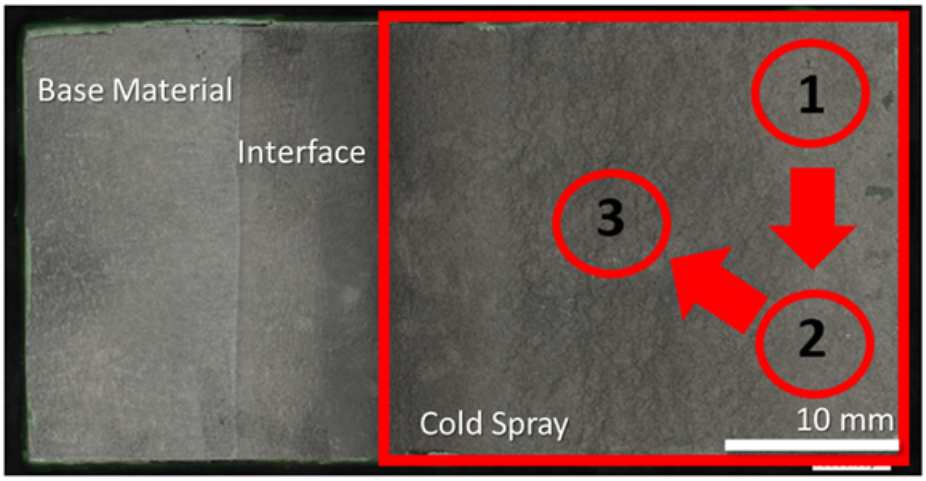

Figure 123. Representative CS sample with the red box indicating the CS area. The red numbered circles display the areas for corrosion testing.

A summary of the electrochemical tests is shown in Figure 124. As evidenced by the Inconel processed with nitrogen, and true for all cold spray cases, the as-sprayed conditions (solid lines) exhibit more unstable behavior in the E_{OCP} and evidence of metastable pitting incidents in the potentiodynamic polarization, seen as instability in the current measured over the passive region (Figure 124- a & b) . Also, to note, the E_{OCP}s decrease for the ground samples as the native oxides on the surface are removed, thus, as compared to the as sprayed state, the surface is slightly more active. However, during potentiodynamic polarization, the curves display smoother current responses, indicative of the reduction in metastable pitting. All scans that are presented are compared to measurements of the base material (black line) in 0.6 M NaCl.

A comparison summary of all cold spray samples examined is presented in Figure 124- c&d. All samples, in the as sprayed condition, exhibit a significantly higher E_{OCP} than the base material, roughly 200-350 mV higher. The passive current densities displayed in the potentiodynamic polarizations range from roughly 5 x 10^{-4} to 5 x 10^{-2} mA/cm^2 as compared to the base material which displays a passive current density of 1 x 10^{-3} mA/cm^2. However, more notable is the metastable pitting and bendover potentials observed. All samples except for the Nickel Nitrogen samples do not exhibit a bendover potential (Figure 124-d). However, the Nickel Nitrogen sample shows a bendover at a potential of 0.4 $V_{Ag/AgCl}$ indicative of the occurrence of sustained pitting or localized corrosion.

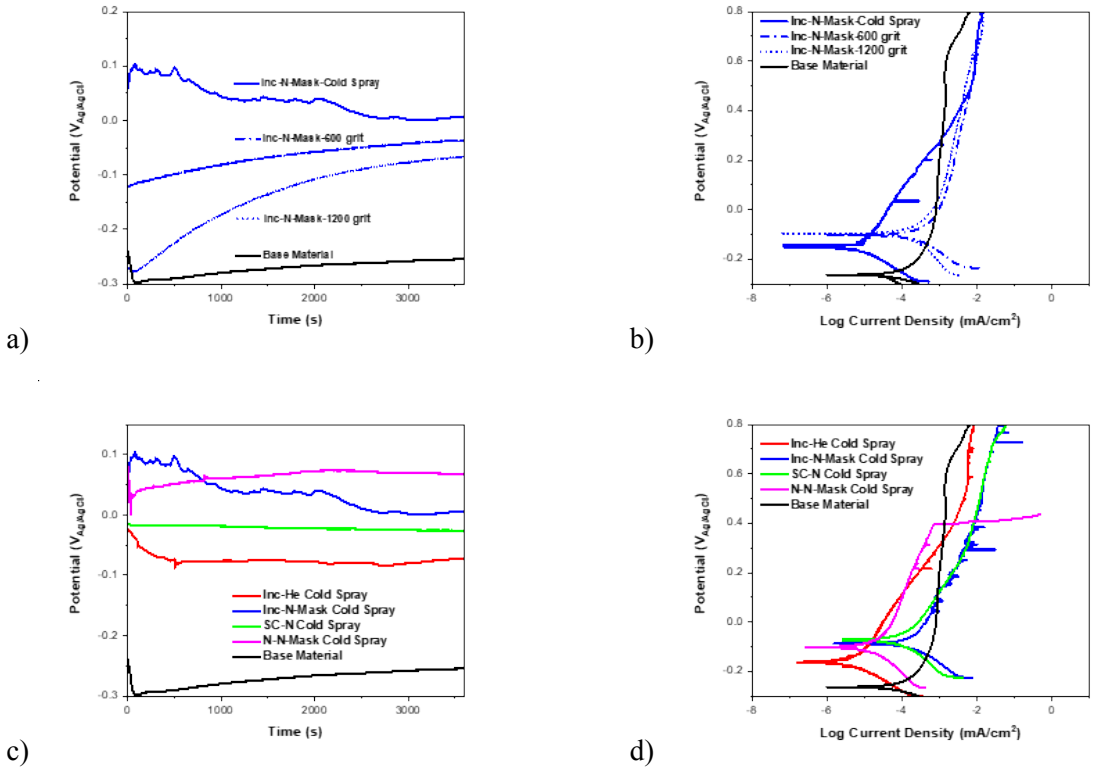

Figure 124. Example electrochemical testing of the as sprayed surfaces versus the 600 and 1200 ground samples as compared to the base material in 0.6 M NaCl. One-hour E_{OCP} followed by potentiodynamic polarization for a) & b) Inconel processed with N, and summary of all as sprayed CS samples; c) on hour E_{OCP} and d) potentiodynamic polarization.

Example images for the $FeCl_3$ full immersion exposures (ASTM G48) are presented in Figure 125. For all cold spray sample types and processing gasses, the interface region displayed the highest areas of attack (for both masked and blended samples). Additionally, notable differences are apparent between blended (Figure 125-b) and masked (Figure 125 – d) interfaces with regards to corrosion damage. In general, the cold sprayed regions presented relatively good corrosion resistance at the macroscale with the exception of the Nickel processed with N cold spray (not shown). Further analysis to examine local-scale corrosion damage was performed in SEM.

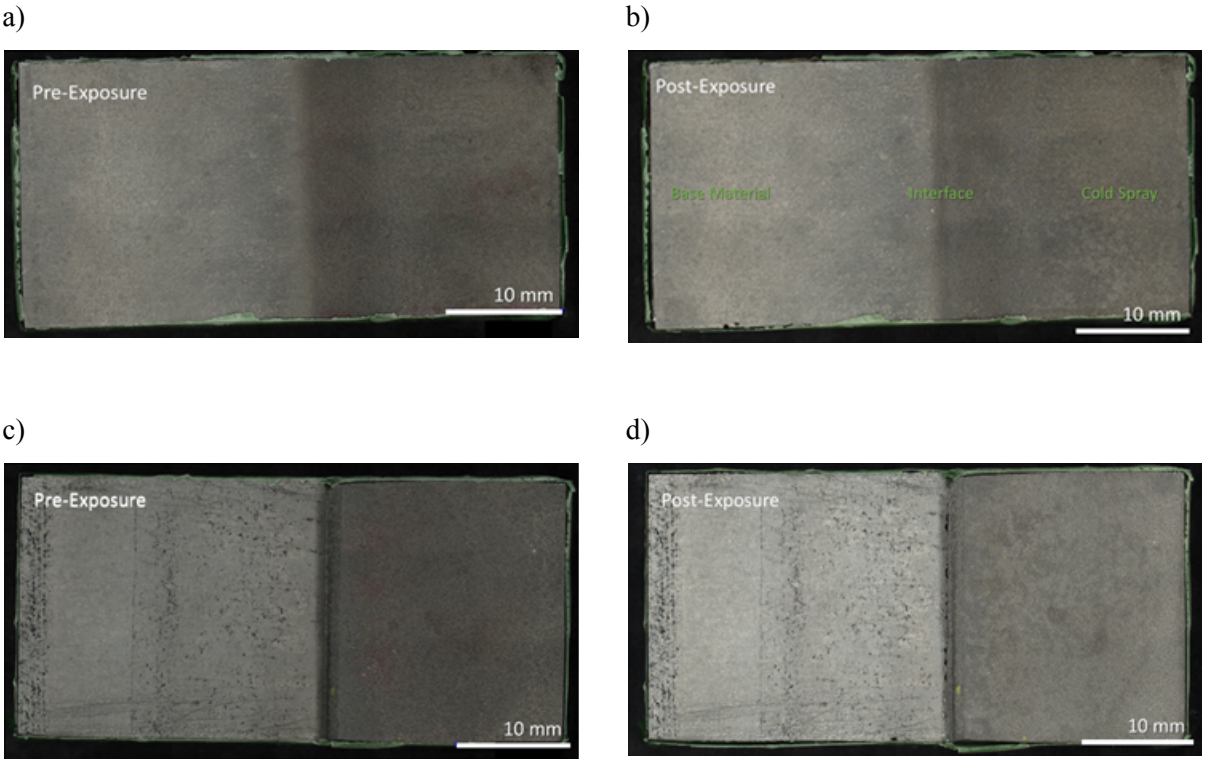

Figure 125. Optical images pre and post $FeCl_3$ 72 h exposure at 22 °C for a) & b) Inconel processed with N and c) & d) Inconel processed with N and masked. Samples are all oriented in the same direction as shown in b, with base material on the left and cold spray on the right of the image.

A representative micrograph of the base material, interface, and cold spray regions for Inconel cold spray samples processed with nitrogen can be seen in Figure 126. In general, the base material (SS304L) exhibited small, on the order of 10-40 μm in diameter, hemispherical pits that were widely dispersed in their distribution. Damage in the cold spray region is hard to discern as surface roughness and possible contamination remnants from processing limit the ability to identify pitting or localized corrosion. The interface regions, through SEM, were further observed to be the areas of largest concern. In general, for blended interfaces, higher densities of pitting occurred in the interface regions, often next to or underneath cold spray particles where the particles are present but do not form a fully dense layer (Figure 126-b). For the masked interfaces, a dual mode of corrosion appears to be present. Crevicing occurs at the base of the mask, potentially undercutting underneath the CS coating (Figure 126 – e). Additionally, an enhanced band of pitting corrosion occurs roughly 500 micrometers away from the masked interface. This band is likely present due to the establishment of a galvanic couple, but the distance to the interface may be influenced by the underlying residual stresses and/or potential changes in near surface microstructure. Additional evidence of crevice corrosion is presented in the example cross-section image

in Figure 127. Further analysis of the post-corrosion cross sections will be carried out in FY22 to determine material, microstructural, and potential residual stress influences on corrosion susceptibility.

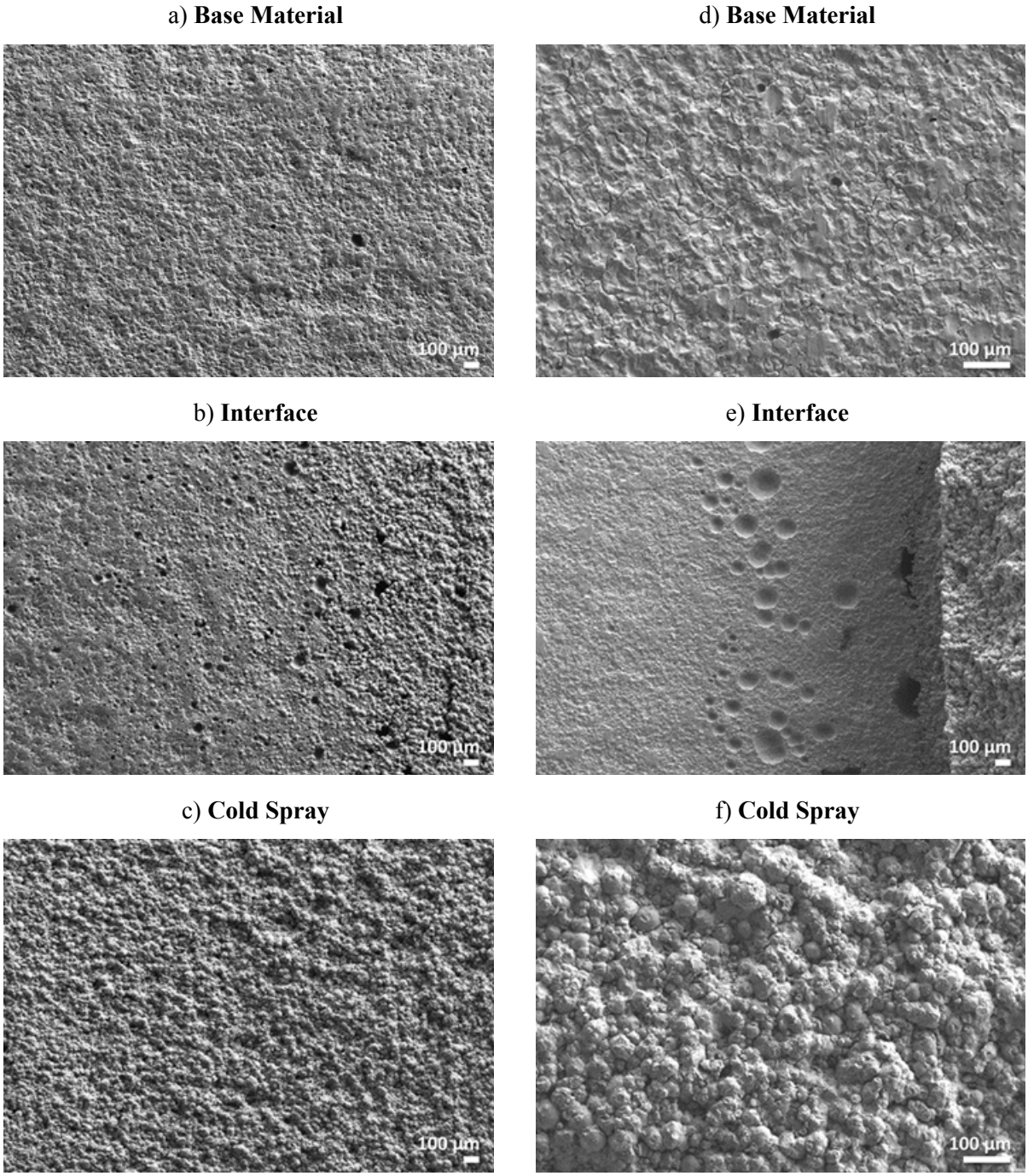

Figure 126. SEM secondary electron images of the base material, interface, and cold spray regions of the samples post 72 h exposure in $FeCl_3$ solution at 22 °C for a) - c) Inconel processed with N; and d) - f) Inconel processed with N and masked. Samples are all oriented in the same direction with base material on the left and cold spray on the right of the images.

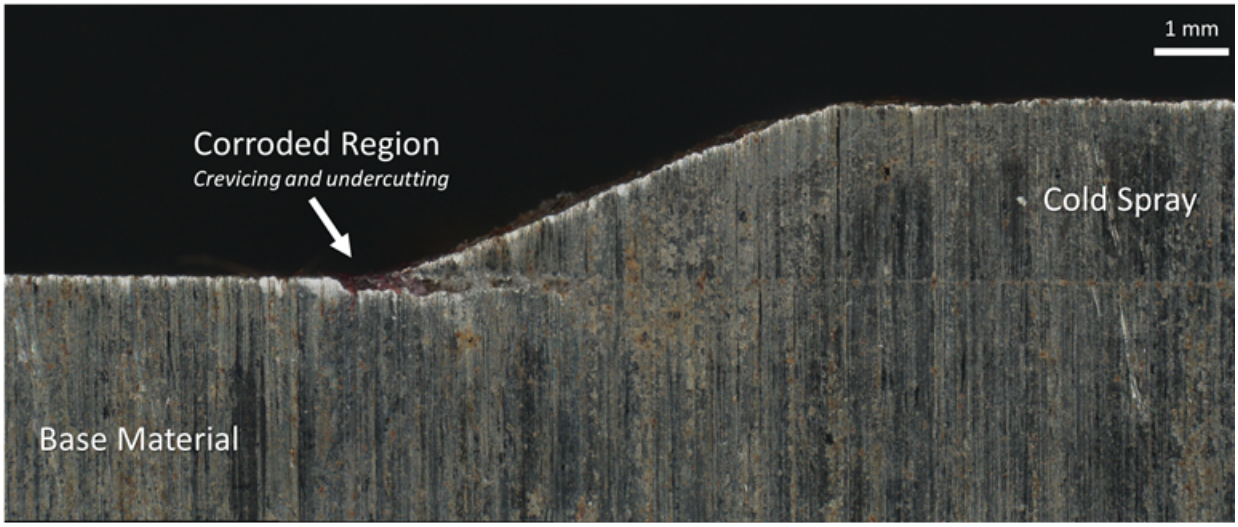

Figure 127. Example rough (unpolished) cross section of blended cold spray (Inconel processed with He) interface with base material (SS 304/304L), after accelerated testing in full immersion FeCl3 (ASTM G48 exposure).

In addition to SEM analysis, EDS was performed to identify any larger scale potential contamination due to processing that might have initiated the localized corrosion damage. Examples of EDS analysis for the Inconel CS processed with Nitrogen for the blended and masked sample interfaces are shown in Figure 128. No apparent contamination could be correlated with areas of enhanced corrosion damage and therefore corrosion is likely governed by the galvanic potential between the CS and base material, potential residual stresses, surface roughness, and/or microstructural changes due to the CS coatings.

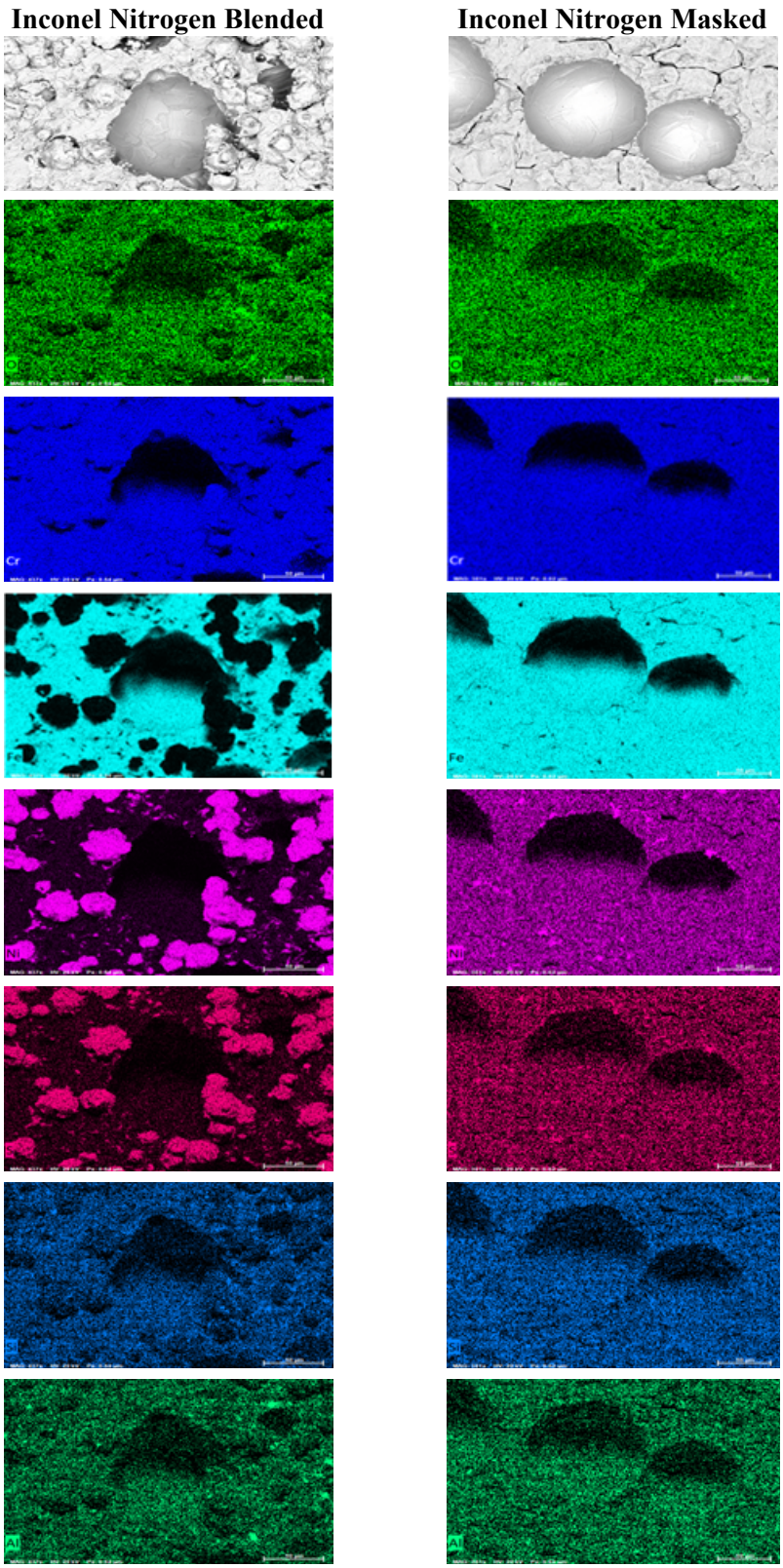

Figure 128. Example SEM and corresponding EDS of the interface regions of the Inconel cold spray processed with Nitrogen for the blended (left) and masked (right) interfaces.

From the full immersion accelerated electrochemical testing, it is evident that the surface roughness of the cold spray material plays a role in its susceptibility to metastable pitting; grinding the surface improved the resistance to metastable pitting. Additionally, even though CS materials were selected for compatibility with stainless steel, in comparison to the base material a difference in E_{OCP} was observed suggesting concern for galvanic corrosion at the interface. This was observed in $FeCl_3$ accelerated pitting testing where all interfaces of the samples examined presented the most deleterious regions for corrosion. In blended samples, pitting was exacerbated under regions of not fully dense particles of cold spray. In the masked samples, two modes of corrosion were observed; crevicing at the connection between the base material and cold spray, and enhanced pitting zones in the near interface regions. Further study is necessary to fully understand the mechanisms behind the enhanced corrosion attack. Future plans include cross-sectioning these exposed samples to determine the full extent of corrosion attack and potential relationship to microstructural changes and/or changes in residual stress. Additionally, full immersion $FeCl_3$ pitting testing will be carried out on ground CS coated samples (cut from the same plates/specimens as those tested here) to examine the influence of surface roughness on the corrosion occurring at the interface. Finally, an expanded set of CS materials and processing conditions will be examined in the coming year to identify enhancements to corrosion resistance.

While initial results displayed corrosion susceptibility, it is important to note that these are accelerated tests, designed to highlight areas of potential weakness. These results highlight the need to better understand the interface between the cold spray coating and the base material if used in a repair scenario (in which a patch might be applied). Further examination in more canister-relevant environments needs to be done to fully understand the impact of the galvanic effects apparent in these accelerated tests. Geometric effects and residual stresses are other factors of interest at the interface. Future testing will include more rigorous corrosion evaluation of optimized cold spray samples, in terms of both materials and geometries, in SNF canister-relevant environments.

This page is intentionally left blank.

6. Conclusions

This progress report describes work performed during FY21 at SNL to assess the localized corrosion performance of container/cask materials used in the interim storage of SNF. Of particular concern is SCC, by which a through-wall crack could potentially form in a canister outer wall over time intervals that are shorter than possible dry storage times. In FY21, modeling and experimental work was performed that further defined our understanding of the potential chemical and physical environment present on canister surfaces at both marine and inland sites. Research also evaluated the relationship between the environment and the rate, extent, and morphology of corrosion, as well as the corrosion processes that occur. Finally, in collaboration with PNNL, SNL is evaluating cold spray as a possible SCC mitigation and repair technique.

In FY21, work to define dry storage canister surface environments included several tasks. First, dust specimens were analyzed from the surface of in-service canisters at two inland ISFSI site locations. These samples represent the first that have been collected from inland sites and provide insights into the chemistry and mineralogy of dust and salts on canisters at those sites. The results showed that nitrates, sulfates, and carbonates dominated the soluble salts, but small amounts of chloride, mostly in the form of halite (NaCl), were present. The halite probably sources to cooling tower emissions (both sites have cooling towers), or to road salts used during winter months. Second, SNL continued to evaluate the stability of $MgCl_2$ brines on heated surfaces. $MgCl_2$-rich brines are the first to form when sea-salts deliquesce, and understanding their behavior is critical to prediction of canister corrosion and the potential occurrence of SCC. Work in FY21 focused on development of a consistent thermodynamic model for magnesium hydroxides, chlorides, and hydroxychlorides. This model is necessary for understanding and predicting when deliquescent $MgCl_2$ brines are stable on canister surfaces, and also in understanding corrosion processes in those brines. Additional work focused on experimental measurement of the stability of $MgCl_2$ brines as a function of temperature and RH. Finally, several support activities were initiated for the Canister Deposition Field Demonstration. These included developing a preliminary plan for sampling canister surface deposits; developing a method for measuring canister surface roughness on the macro-micro scale; evaluating techniques for marking sampling grids onto the canister surfaces; and developing specifications for site monitoring of atmospheric gases and aerosols at the CDFD site.

In FY21, the more canister-relevant environments developed in FY20 were implemented for corrosion testing. Large scale pitting exposures under cyclic diurnal conditions and inert dust conditions are underway. Initial analysis of coupons exposed under diurnal cyclic conditions was carried out and summarized in this report. These results show both the influence of a more relevant environment as well as material composition and surface finish on resultant corrosion damage. Data gained from these exposures will determine the potentially deleterious factors for corrosion and SCC initiation and help to further parameterize the maximum pit size model. In addition to implementing testing in more relevant environments, FY21 also continued modeling efforts for the maximum pit size model. Efforts focused on accounting for non-static brine/corrosion conditions to better predict pitting and SCC initiation; specifically influences of brine composition, evolution with corrosion, and brine morphology (thickness and coverage) were evaluated. Including evolving brine properties into the maximum pit size model greatly influenced the predicted maximum pit size and highlighted the necessity to both better understand canister-relevant conditions and to carry out work in canister-relevant brines. An understanding of the influence of environment on pitting was also expanded in FY21 to the influence on pit to crack transition. Both initial modeling and experimental efforts have been developed to explore pit to crack transition and these will be implemented over the course of FY22. Additionally, modeling efforts have expanded to include the development of a crack tip chemistry model in FY21. This model enables the prediction of electrochemical parameters that develop at a crack tip and will help to validate and understand laboratory versus field measurements of crack initiation and growth.

While FY21 saw major advancements with respect to understanding the relationship between canister-relevant brine conditions and corrosion, it is still unknown how cracks, once initiated, will behave under these conditions. To study this, SNL continued to establish SCC testing capabilities with the four load frames acquired in FY20. Laboratory setup, frame installation, and calibration (including noise reduction and development of environmental strategies for testing) have been completed in FY21. Lessons learned will be implemented in FY22 to develop quantitative testing of CGR under canister-relevant environments.

Finally, in collaboration with PNNL, SNL has helped to examine the corrosion properties of cold spray, a possible mitigation and repair strategy for SNF canisters. Initial results in FY21 have focused on accelerated corrosion testing to help optimize the cold spray coatings and determine potential deleterious features. In FY22, SNL will continue this collaboration to evaluate the performance of these coatings under canister-relevant conditions.

7. References

1. Knight, A.W.N., B.L.; Bryan, C.R.; Schaller, R.F., *FY21 Status Report: SNF Canister Coatings for Corrosion Prevention and Mitigation*, U.S.D.o. Energy, Editor. 2021.
2. Bryan, C.R. and A.W. Knight, *Analysis of Dust Samples Collected from an Inland ISFSI Site ("Site A")*. 2020, Sandia National Labroatories: Albuquerque, NM. p. 44.
3. Schaller, R.F., A.W. Knight, C.R. Bryan, B.L. Nation, T.J. Montoya, and R.M. Katona, *FY20 Status Report: SNF Interim Storage Canister Corrosion and Surface Environment Investigations*. 2020, Sandia National Laboratories: Albuquerque, NM. p. 209.
4. Lindgren, E.R., S.G. Durbin, S.R. Suffield, and J.A. Fort, *Status Update for the Canister Deposition Field Demonstration*. 2021, Sandia National Laboratories: Albuquerque, NM. p. 42.
5. Kondo, Y., *Prediction of fatigue crack initiation life based on pit growth.* Corrosion Journal, 1989. **45**(1): p. 7-11.
6. Turnbull, A., L. McCartney, and S. Zhou, *Modelling of the evolution of stress corrosion cracks from corrosion pits.* Scripta materialia, 2006. **54**(4): p. 575-578.
7. Newman, J. and I. Raju, *An empirical stress-intensity factor equation for the surface crack.* Engineering Fracture Mechanics, 1981. **15**(1): p. 185-192.
8. Newman, J.C. and I.S. Raju, *Analysis of Surface Cracks in Finite Plates Under Tension or Bending Loads*. 1979, NASA: Hampton, VA.
9. Ross, K.A., P. Mayur, T.J. Montoya, E. Karasz, and R.F. Schaller, *In Preparation: Cold Spray for Mitigation and Repair of Spent Nuclear Fuel Dry Storage Canisters* 2021, Pacific Northwest National Laboratories.
10. Bryan, C.R. and D.G. Enos, *SNF Interim Storage Canister Corrosion and Surface Environment Investigations.* 2015, Sandia National Laboratories: Albuquerque, NM.
11. Bryan, C.R. and D.G. Enos, *FY16 Status Report: SNF Interim Storage Canister Corrosion and Surface Environment Investigations.* 2017, Sandia National Laboratories: Albuquerque, NM. p. 86.
12. Enos, D.G. and C.R. Bryan, *Understanding the risk of chloride induced stress corrosion cracking of interim storage containers for the dy storage of Spent nuclear fuel: evolution of brine chemistry on the container surface.* , in *CORROSION 2016*, NACE, Editor. 2016: Vancouver, B.C.
13. Bryan, C. and E. Schindelholz, *FY18 Status Report: SNL Research into Stress Corrosion Cracking of SNF Interim Storage Canisters*. 2018, Sandia National Laboratories: Albuquerque, NM. p. 77.
14. Schaller, R., A. Knight, C. Bryan, and E. Schindelholz, *FY19 Status Report: SNL Research into Stress Corrosion Cracking of SNF Dry Storage Canisters*. 2019, Sandia National Laboratories: Albuquerque,NM. p. 98.
15. Schindelholz, E., C. Bryan, and C. Alexander, *FY17 Status Report: Research on Stress Corrosion Cracking of SNF Interim Storage Canisters*. 2017, Sandia National Laboratories: Albuquerque, NM. p. 59.
16. Katona, R.M., R.G. Kelly, C.R. Bryan, R. Schaller, and A.W. Knight, *Use of in situ Raman spectroelectrochemical technique to explore atmospheric corrosion in marine-relevant environments.* Electrochemistry Communications, 2020. **118**: p. 106768.
17. SNL, *In-drift precipitates/salts model*. 2007, Sandia National Laboratories: Las Vegas, NV. p. 358.
18. Miron, G.D., T. Wagner, D.A. Kulik, and B. Lothenbach, *An internally consistent thermodynamic dataset for aqueous species in the system Ca-Mg-Na-K-Al-Si-O-H-C-Cl to 800 C and 5 KBar.* American Journal of Science, 2017. **317**: p. 755-806.
19. Cox, J.D., D.D. Wagman, and V.A. Medvedev, *CODATA Key Values for Thermodynamics*. 1989, New York: Hemisphere Publishing Corp. .
20. Palmer, D.A. and D.J. Wesolowski, *Potentiometric measurements of the first hydrolysis quotient of magnesium(II) to 250 degrees C and 5 molal ionic strength (NaCl).* Journal of Solution Chemistry, 1997. **26**(2): p. 217-232.
21. Pannach, M., S. Bette, and D. Freyer, *Solubility equilibria in the system $Mg(OH)_2$-$MgCl_2$-H_2O from 298 to 393 K.* Journal of Chemical and Engineering Data, 2017. **62**(4): p. 1384-1396.

22. Johnson, J.W., E.H. Oelkers, and H.C. Helgeson, *SUPCRT92: A software package for calculating the standard molal thermodynamic properties of minerals, gases, aqueous species, and reactions from 1 to 5000 bar and 0 to 1000°C.* Computers & Geosciences, 1992. **18**(7): p. 899-947.

23. Altmaier, M., V. Metz, V. Neck, R. Muller, and T. Fanghanel, *Solid-liquid equilibria of $Mg(OH)_2$(cr) and $Mg_2(OH)_3Cl:4H_2O$(cr) in the system Mg-Na-H-OH-O-Cl-H2O at 25 degrees C.* Geochimica Et Cosmochimica Acta, 2003. **67**(19): p. 3595-3601.

24. Xiong, Y.L., H.R. Deng, M. Nemer, and S. Johnsen, *Experimental determination of the solubility constant for magnesium chloride hydroxide hydrate (Mg3Cl(OH)(5)center dot 4H(2)O, phase 5) at room temperature, and its importance to nuclear waste isolation in geological repositories in salt formations.* Geochimica et Cosmochimica Acta, 2010. **74**(16): p. 4605-4611.

25. Mcgee, K.A. and P.B. Hostetler, *Studies in the system $MgO-SiO_2-CO_2-H_2O$ (IV); Stability of $MgOH^+$ from 10 degrees C to 90 degrees C.* American Journal of Science, 1975. **275**(3): p. 304-317.

26. Brown, P.L., S.E. Drummond, and D.A. Palmer, *Hydrolysis of magnesium(II) at elevated temperatures.* Journal of the Chemical Society-Dalton Transactions, 1996(14): p. 3071-3075.

27. Travers, A. and C.R. Nouvel, *On the solubility of magnesium hydroxide at high temperatures.* Comptes rendus de l'Académie des Sciences, 1929. **188**: p. 499-501.

28. Robie, R.A. and B.S. Hemingway, *Thermodynamic Properties of Minerals and Related Substances 298.15 K and 1 Bar (10^5 Pascals) Pressure and at Higher Temperatures.* . 1995, U.S. Geological Survey.

29. Helgeson, H.C., J.M. Delany, H.W. Nesbitt, and D.K. Bird, *Summary and critique of the thermodyanmic properties of rock-forming minerals.* American Journal of Science, 1978. **278-A**: p. 1-229.

30. Giauque, W.F. and R.C. Archibald, *The entropy of water from the third law of thermodynamics - The dissociation pressure and calorimetric heat of the reaction $Mg(OH)_2 = MgO+H_2O$ - The heat capacities of $Mg(OH)_2$ and MgO from 20 to 300 K.* Journal of the American Chemical Society, 1937. **59**: p. 561-569.

31. Robie, R.A. and B.S. Waldbaum, *Thermodynamic Properties of Minerals and Related Substances at 298.15 K (25 C) and One Atmosphere (1.013 bars) Pressure and at Higher Temperatures*. 1968, U.S. Geological Survey. p. 256.

32. Kelley, K.K. and E.G. King, *Contributions to the data on theoretical metallurgy. XIV: Entropies of the elements and inorganic compounds.* U. S. Bureau of Mines Bulletin 1961. **592**.

33. Mostafa, A.T.M.G., J.M. Eakman, M.M. Montoya, and S.L. Yarbro, *Prediction of Heat Capacities of Solid Inorganic Salts from Group Contributions* Industrial & Enginnering Chemistry Research, 1996. **35**: p. 343-348.

34. Wagman, D.D., W.H. Evans, V.B. Parker, R.H. Schumm, I. Halow, S.M. Bailey, K.L. Churney, and R.L. Nuttall, *The NBS Tables of chemical thermodynamic properties - Selected Values for Inorganic and C-1 and C-2 Organic-Substances in Si Units.* Journal of physical and chemical reference data, 1982. **11**: p. 1-&.

35. Lambert, I. and H.L. Clever, *Solubilty Data Series*, in *Alkaline Earth Hydroxides in Water and Aqueous Solutions* 1992, Pergamon Press LTD: Headington Hill Hall, Oxford, England.

36. Li, D.D., D.D. Gao, Y.P. Dong, and W. Li, *Modeling of phase relations and thermodynamics in the $Mg(OH)_2 + MgSO_4 + H_2O$ system with implications on magnesium hydroxide sulfate cement.* Calphad-Computer Coupling of Phase Diagrams and Thermochemistry, 2019. **67**.

37. Harvie, C.E., N. Moller, and J.H. Weare, *The prediction of mineral solubilities in natural waters - the $Na-K-Mg-Ca-H-Cl-SO_4-OH-HCO_3-CO_3-CO_2-H2O$ System to High Ionic Strengths at 25-Degrees-C.* Geochimica Et Cosmochimica Acta, 1984. **48**(4): p. 723-751.

38. Stock, D.I. and C.W. Davies, *The 2nd dissociation constant of magnesium hydroxide.* Transactions of the Faraday Society, 1948. **44**(11): p. 856-859.

39. Pitzer, K.S., *Ion Interaction Approach: Theory Data Correlation* in *Activity Coefficients in Electrolyte Solutions*, K.S. Pitzer, Editor. 1991, CRC Press: Boca Raton, FL. p. 75-153.

40. Linke, W., *Solubilities Inorganic and Metal-organic Compounds*. 4th ed. American Chemical Society. Vol. 1 & 2. 1965, Washington.

41. Christov, C., *Chemical equilibrium model of solution behavior and bishofite ($MgCl_2:6H_2O$(cr)) and hydrogen-carnallite (HCl: $MgCl_2:7H_2O$(cr)) solubility in the $MgCl_2 + H_2O$ and HCl-$MgCl_2 + H_2O$ Systems*

to High Acid Concentration at (0 to 100) degrees C. Journal of Chemical and Engineering Data, 2009. **54**(9): p. 2599-2608.

42. Krumgalz, B.S., *Temperature dependence of mineral solubility in water. Part I. Alkaline and alkaline earth chlorides.* Journal of physical and Chemical Reference Data, 2017. **46**(4).
43. Pabalan, R.T. and K.S. Pitzer, *Thermodynamics of concentrated electrolyte mixtures and the prediction of mineral solubilities to high temperatures for mixtures in the system Na-K-Mg-Cl-SO_4-OH-H_2O.* Geochimica Et Cosmochimica Acta, 1987. **51**(9): p. 2429-2443.
44. Dinnebier, R.E., D. Freyer, S. Bette, and M. Oestreich, *9Mg(OH)(2)center dot MgCl2 center dot 4H(2)O, a High Temperature Phase of the Magnesia Binder System.* Inorganic Chemistry, 2010. **49**(21): p. 9770-9776.
45. Phutela, R.C., K.S. Pitzer, and P.P.S. Saluja, *Thermodynamics of aqueous magnesium-chloride, calcium-chloride, and strontium chloride at elevated-temperatures.* Journal of Chemical and Engineering Data, 1987. **32**(1): p. 76-80.
46. Zhou, Z., H.S. Chen, Z.J. Li, and H.J. Li, *Simulation of the properties of MgO-$MgCl_2$-H_2O system by thermodynamic method.* Cement and Concrete Research, 2015. **68**: p. 105-111.
47. Robinson, W.O., Waggaman W. H. , *Basic magnesium chlorides.* Journal of Physical Chemistry, 1908. **13**: p. 673-678.
48. Dinnebier, R.E., M. Oestreich, S. Bette, and D. Freyer, *2Mg(OH)2:MgCl2: 2H2O and 2Mg(OH)2: MgCl2:4H2O, Two High Temperature Phases of the Magnesia Cement System.* Zeitschrift Fur Anorganische Und Allgemeine Chemie, 2012. **638**(3-4): p. 628-633.
49. Pannach, M., *Löslichkeitsgleichgewichte basischer Magnesiumchlorid- und Magnesiumsulfat-Hydrate in wässrigen Lösungen bei 25 °C bis 120 °C* 2019, Der Fakultät für Chemie und Physik der Technischen Universität Bergakademie Freiberg genehmigte Freiberg, Germany.
50. de Bakker, J., J. LaMarre, J. Peacey, and B. Davis, *The Phase Stabilities of Magnesium Hydroxychlorides.* Metallurgical and Materials Transactions B-Process Metallurgy and Materials Processing Science, 2012. **43**(4): p. 758-763.
51. GWB, *GWB Reference Manual, Release 15*. 2021, The Geochemist's Workbench.
52. Bodine, M.W., *Magnesium Hydroxychloride - Possible Ph Buffer in Marine Evaporite Brines.* Geology, 1976. **4**(2): p. 76-80.
53. Dinnebier, R.E., M. Pannach, and D. Freyer, *3Mg(OH)2·MgSO4·8H2O: A Metastable Phase in the System Mg(OH)2-MgSO4-H2O.* Zeitschrift Fur Anorganische Und Allgemeine Chemie, 2013. **639**(10): p. 1827-1833.
54. D'Ans, J. and W. Katz, *Magnesiumhydroxyd-Löslichkeiten, pH-Zahlen und Pufferung im System H2O–MgCl2–Mg(OH)2 Kali-Zeitschrift für Kali.* Steinsalz- und Erdölindustrie sowie Salinenwesen, 1941. **35**: p. 37-41.
55. D'Ans, J., W. Busse, and H.E. Freund, *Basic magnesium chloride* Kali u. Steinsalz, 1955. **8**: p. 3-7.
56. Blanc, P., A. Lassin, P. Piantone, M. Azaroual, N. Jacquemet, A. Fabbri, and E.C. Gaucher, *Thermoddem: A geochemical database focused on low temperature water/rock interactions and waste materials.* Applied Geochemistry, 2012. **27**(10): p. 2107-2116.
57. Nakayama, M., *A new basic triple salt containing magnesium hydroxide. Part IV. The quinary system KCl-K_2SO_4-$MgCl_2$-$MgSO_4$-$Mg(OH)_2$-H_2O at 50°.* Bulletin of the Agricultural Chemical Society of Japan, 1960. **24**(4): p. 362-371.
58. Nakayama, M., *A new basic triple salt containing magnesium hydroxide. Part II. The quaternary system KCl-$MgCl_2$-$Mg(OH)_2$-H_2O at 100 C.* Bulletin of the Agricultural Chemical Society of Japan, 1959. **23**(1): p. 46-48.
59. Chermak, J.A. and J.D. Rimstidt, *Estimating the thermodynamic properties (Δ Gof and Δ Hof) of silicate minerals at 298 K from the sum of polyhedral contributions.* American Mineralogist, 1989. **74**(9-10): p. 1023-1031.
60. Schindelholz, E. and R.G. Kelly, *Application of Inkjet Printing for Depositing Salt Prior to Atmospheric Corrosion Testing.* Electrochemical and Solid State Letters, 2010. **13**(10): p. C29-C31.

61. Bryan, C., A. Knight, R. Schaller, S. Durbin, B. Nation, and P. Jensen, *Surface Sampling Techniques for the Canister Deposition Field Demonstration*. 2021, Sandia National Laboratories. p. 34.

62. Jensen, P., S.R. Suffield, and B. Jensen, *Status Update: Deposition Modeling For SNF Canister CISCC*. 2020, Pacific Northwest National Laboratories: Richland, WA. p. 47.

63. Suffield, S.R., P.J. Jensen, B.J. Jensen, R. Ekre, J.A. Fort, W.A. Perkins, C. Grant, B.D. Hanson, and S.B. Ross, *Thermal and Deposition Modeling of the Canister Deposition Field Demonstration*. 2021, Pacific Northwest National Laboratories: Richland, WA. p. 88.

64. Bryan, C. and D. Enos, *Analysis of Dust Samples Collected from Spent Nuclear Fuel Interim Storage Containers at Hope Creek, Delaware, and Diablo Canyon, California*. 2014, Sandia National Laboratories: Albuquerque, NM. p. 281.

65. Tyree, C.A., V.M. Hellion, O.A. Alexandrova, and J.O. Allen, *Foam droplets generated from natural and artificial seawaters.* Journal of Geophysical Research: Atmospheres, 2007. **112**(D12).

66. Metals, A.C.G.-o.C.o., *Standard test method for determining atmospheric chloride deposition rate by wet candle method*. 2008: ASTM International.

67. Enos, D.G. and C.R. Bryan, *Final Report: Characterization of Canister Mockup Weld Residual Stresses*. 2016, U.S. DOE. p. 62.

68. Weirich, T.D., J. Srinivasan, J.M. Taylor, M.A. Melia, P.J. Noe, C.R. Bryan, G.S. Frankel, J.S. Locke, and E.J. Schindelholz, *Humidity effects on pitting of ground stainless steel exposed to sea salt particles.* Journal of the Electrochemical Society, 2019. **166**(11): p. C3477-C3487.

69. Srinivasan, J., T.D. Weirich, G.A. Marino, A.R. Annerino, J.M. Taylor, P.J. Noell, J.J.M. Griego, R.F. Schaller, C.R. Bryan, J.S. Locke, and E.J. Schindelholz, *Long-term effects of humidity on stainless steel pitting in sea salt exposures.* Journal of the Electrochemical Society, 2021. **168**(2).

70. Katona, R.M., J.C. Carpenter, A.W. Knight, C.R. Bryan, R.F. Schaller, R.G. Kelly, and E.J. Schindelholz, *Importance of the hydrogen evolution reaction in magnesium chloride solutions on stainless steel.* Corrosion Science, 2020. **177**.

71. Katona, R.M., J.C. Carpenter, A.W. Knight, R.S. Marshall, B.L. Nation, E.J. Schindelholz, R.F. Schaller, and R.G. Kelly, *Editors' Choice-Natural convection boundary layer thickness at elevated chloride concentrations and temperatures and the effects on a galvanic couple.* Journal of the Electrochemical Society, 2021. **168**(3).

72. Katona, R.M., J. Carpenter, E.J. Schindelholz, and R.G. Kelly, *Prediction of maximum pit sizes in elevated chloride concentrations and temperatures.* Journal of the Electrochemical Society, 2019. **166**(11): p. C3364-C3375.

73. Katona, R.M., A.W. Knight, E.J. Schindelholz, C.R. Bryan, R.F. Schaller, and R.G. Kelly, *Quantitative assessment of environmental phenomena on maximum pit size predictions in marine environments.* Electrochimica Acta, 2021. **370**.

74. Bryan, C. and E. Schindelholz, *FY18 Status Report: SNL Research into Stress Corrosion Cracking of SNF Interim Storage Canisters*. 2018, U.S. Department of Energy. p. 77.

75. Katona, R.M., J. Carpenter, E.J. Schindelholz, R.F. Schaller, and R.G. Kelly, *Cathodic kinetics on platinum and stainless steel in NaOH environments.* Journal of the Electrochemical Society, 2021. **168**(7).

76. Schaller, R., A. Knight, C. Bryan, and E. Schindelholz, *FY19 Status Report: SNL Research into Stress Corrosion Cracking of SNF Dry Storage Canisters*, U.S.D.o. Energy, Editor. 2019.

77. Katona, R.M., J.C. Carpenter, A.W. Knight, C.R. Bryan, R.F. Schaller, R.G. Kelly, and E.J. Schindelholz, *Importance of the hydrogen evolution reaction in magnesium chloride solutions on stainless steel.* Corrosion Science, 2020. **177**: p. 108935.

78. Katona, R.M., J.C. Carpenter, A.W. Knight, R.S. Marshall, B.L. Nation, E.J. Schindelholz, R.F. Schaller, and R.G. Kelly, *Natural convection boundary layer thickness at elevated chloride concentrations and temperatures and the effects on a galvanic couple.* Journal of the Electrochemical Society, 2021. **168**(3).

79. Katona, R.M., R.G. Kelly, C.R. Bryan, R.F. Schaller, and A.W. Knight, *Use of in situ Raman spectroelectrochemical technique to explore atmospheric corrosion in marine-relevant environments.* Electrochemistry Communications, 2020. **118**.

80. Katona, R.M., A.W. Knight, E.J. Schindelholz, C.R. Bryan, R.F. Schaller, and R.G. Kelly, *Quantitative assessment of environmental phenomena on maximum pit size predictions in marine environments.* Electrochimica Acta, 2021. **370**: p. 137696.

81. Maltseva, A., V. Shkirskiy, G. Lefèvre, and P. Volovitch, *Effect of pH on $Mg(OH)_2$ film evolution on corroding Mg by in situ kinetic Raman mapping (KRM).* Corrosion Science, 2019. **153**: p. 272-282.

82. Lojka, M., O. Jankovsky, A. Jiríckova, A. Lauermannova, F. Antoncik, D. Sedmidubsky, Z. Pavlik, and M. Pavlikova, *Thermal Stability and Kinetics of Formation ofMagnesium Oxychloride Phase3Mg(OH)2·MgCl2·8H2O.* Materials, 2020. **13**(767).

83. Dorrepaal, R.M. and A.A. Gowen, *Identification of Magnesium Oxychloride Cement Biomaterial Heterogeneity using Raman Chemical Mapping and NIR Hyperspectral Chemical Imaging.* Scientific Reports, 2018. **8**.

84. Liu, C.S., J.; Kelly, R. G, *Electrolyte film thickness effects on the cathodic current availability in a galvanic couple.* Journal of the Electrochemical Society, 2017. **164**(13).

85. Charles-Granville, U.E.L., C.; Scully, J. R.; Kelly, R. G., *An RDE approach to investigate the influence of chromate on the cathodic kinetics on 7XXX series Al alloys under Simulated thin film electrolytes.* Journal of the Electrochemical Society, 2020. **167**(11).

86. Amatore, C.S., S.; Thouin, L.; Warkocz, J. S. , *Mapping concentration profiles within the diffusion layer of an electrode: part III. Steady-state and time-dependent profiles via amperometric measurements with an ultramicroelectrode probe.* Electrochemistry Communications, 2000. **2**(5): p. 353-358.

87. Moraes, C.V.S., R. J.; Scully, J. R.; Kelly, R. G., *Finite element modeling of chemical and electrochemical protection mechanisms offered by Mg-based organic coatings to AA2024-T351.* Journal of the Electrochemical Society, 2021. **168**(5).

88. Porter, N.W.B., D.; Bryan, C.; Katona, R.; Schaller, R.F., *FY21 Status Report: Probabilistic SCC Model for SNF Dry Storage Canisters*, U.S.D.o. Energy, Editor. 2021.

89. Liya Guo, N.M., Haval Mohammed-Ali, Majid Ghahari, Andrew Du Plessis, Angus Cook, Steven Street, Christina Reinhard, Robert C. Atwood, Trevor Rayment, and Alison J. Davenport, *Effect of mixed salts on atmospheric corrosion of 304 stainless steel.* Journal of the Electrochemical Society, 2019. **166**: p. 3011-3012.

90. Cook, A.P., C.; Davenport, A., *Effect of nitrate and sulfate on atmospheric corrosion of 304L and 316L stainless steels.* Journal of the Electrochemical Society, 2017. **164**: p. C148.

91. Nishikata, A., Y. Yamashita, H. Katayama, T. Tsuru, A. Usami, K. Tanabe, and H. Mabuchi, *An electrochemical impedance study on atmospheric corrosion of steels in a cyclic wet-dry condition.* Corrosion Science, 1995. **37**(12): p. 2059-2069.

92. Schindelholz, E., B.E. Risteen, and R.G. Kelly, *Effect of relative humidity on corrosion of steel under sea salt aerosol proxies: I. NaCl.* Journal of the Electrochemical Society, 2014. **161**.

93. Street, S.R., N. Mi, A.J. Cook, A.B. Mohammed-Ali, L. Guo, T. Rayment, and A.J. Davenport, *Atmospheric pitting corrosion of 304L stainless steel: the role of highly concentrated chloride solutions.* Faraday Discussions, 2015. **180**: p. 251-265.

94. Bryan, C.R. and E.J. Schindelholz, *Properties of Brines formed by Deliquescence of Sea-Salt Aerosols.* NACE International, 2018.

95. Rebecca Schaller, A.K., Charles Bryan, Brendan Nation, Timothy Montoya, *SNF Interim Storage Canister Corrosion and Surface Enviroment Investigations*. 2020, Sandia National Lab.

96. Toloczko, M.B.C., F.C.; Bouffioux, R.A., *Results from PNNL SCC Testing: FY2021*, U.S.D.o. Energy, Editor. 2021.

97. Turnbull, A.M., L.; Zhou, S., *Modelling of the evolution of stress corrosion cracks from corrosion pits.* Scripta Materialia, 2006. **54**(4): p. 575-578.

98. Co, N.E.C. and J.T. Burns, *Effects of micro-scale corrosion damage features and local microstructure on fatigue crack initiation location.* International Journal of Fatigue, 2021. **150**.

99. Brewicka, P.T.D., V.G.; Geltmachera, A.B.; Qidwai, S.M., *Modeling the influence of microstructure on the stress distributions of corrosion pits.* Corrosion Science, 2019. **158**.

100. Donahue, J.R.B., J. T. , *Effect of chloride concentration on the corrosion–fatigue crack behavior of an age-hardenable martensitic stainless steel.* International Journal of Fatigue, 2016. **91**: p. 71-99.

101. Chen, Y.Y., H.C. Shih, L.H. Wang, and J.C. Oung, *Factors Affecting the Crack Growth Rates of Reactor Pressure Vessel Steels under Simulated Boiling Water Reactor Conditions.* CORROSION, 2006. **62**(5): p. 403-418.

102. James, L.A., H.B. Lee, G.L. Wire, S.R. Novak, and W.H. Cullen, *Corrosion fatigue crack growth in clad low alloy steels.* Journal of Pressure Vessel Technology, 1997. **119**(3).

103. ASTM international, *E8/E8M-16a Standard Test Methods for Tension Testing of Metallic Materials*. 2016.

104. ASTM International, *E1681 – 03 Standard Test Method for Determining Threshold Stress Intensity Factor for Environment-Assisted Cracking of Metallic Materials*. 2008.

105. ASTM International, *E399 −17 Standard Test Method for Linear-Elastic Plane-Strain Fracture Toughness KIc of Metallic Materials*. 2017.

106. ASTM International, *E647-15 Standard Test Method for Measurement of Fatigue Crack Growth Rates*. 2015.

107. Johnson, H.H., *Calibrating the electric potential for studying slow crack growth.* Materials Research Standards, 1965. **5**.

108. Chen, X., Nanstad, R., Sokolov, M., *Application of direct current potential drop for the J-integral Vs. crack growth resistance curve characterization* Materials Science and Technology Division; Oak Ridge National Laboratory, 2015.

109. Andersen, T.L., *Fracture Mechanics Fundamentals and Applications*. 3rd ed. 2005: CRC Press Taylor & Francis Group.

110. *E517-19 Standard Test Method for Plastic Strain Ratio r for Sheet Metal*. 2019, ASTM Internation.

111. Toloczko, M.B.S., J.E.; Deibler, J.E.; Seffens, R.J..; Bouffioux, R.A., *Chloride-Induced Stress Corrosion Cracking Test System Construction and Test Plan*, U.S.D.o. Energy, Editor. 2019.

112. Mills, W.J., *Fracture toughness of type 304 and 316 stainless steels and their welds.* International Materials Reviews, 1997. **42**(2): p. 45-82.

113. Bryan, C.R., A.W. Knight, R.F. Schaller, S. Durbin, B.L. Nation, and P. Jensen, *Surface Sampling Techniques for the Canister Deposition Field Demonstration*, in *Spent Fuel and Waste Disposition*. 2021, DOE SFWST. p. 34.

114. Enos, D. and C. Bryan, *Final Report: Characterization of Canister Mockup Weld Residual Stresses*. 2016, Sandia National Laboratories.

115. British Standards Institution, *BS 8571-2014 Method of test for determination of fracture toughness in metallic materials using single edge notched tension (SENT) specimen*. 2014.

116. Ross, K.A., H. Jiang, M. Alabi, and C. Enderlin, *Investigation of Cold Spray as a Dry Storage Canister Repair and Mitigation Tool*. 2020, Pacific Northwest National Laboratories: Richland, WA. p. 70.

Appendix A

Srinivasan, J., Weirich, T.D., Marino, G.A., Annerino, A.R, Taylor, J.M., Noell, P.J., Griego, J.J.M., Schaller, R. F., Bryan, C.R., Locke, J.S., & Schindelholz, E.J. (2021). Long-Term Effects of Humidity on Stainless Steel Pitting in Sea Salt Exposures. *Journal of the Electrochemical Socitey*, *168*, 021501.

Journal of The Electrochemical Society, 2021 **168** 021501

Long-Term Effects of Humidity on Stainless Steel Pitting in Sea Salt Exposures

J. Srinivasan,[1,*,z] T. D. Weirich,[1] G. A. Marino,[1] A. R. Annerino,[1] J. M. Taylor,[1] P. J. Noell,[2] J. J. M. Griego,[2] R. F. Schaller,[2,*] C. R. Bryan,[2] J. S. Locke,[1,*] and E. J. Schindelholz[1,z]

[1]*Fontana Corrosion Center, Department of Materials Science and Engineering, The Ohio State University, Columbus, Ohio 43210, United States of America*
[2]*Materials Science and Engineering, Sandia National Laboratories, Albuquerque, New Mexico 87185, United States of America*

Ground 304 stainless steel (SS) samples were exposed to sea salt particles at 35 °C and two relative humidity (RH) levels for durations ranging from 1 week to 2 years. For all exposure times, pit number density and total pit volume at 40% RH were observed to be considerably greater than those at 76% RH. Statistical analysis of distributions of pit populations for both RH conditions showed that pit number density and total pit volume increased rapidly at first but slowed as exposure time increased. Cross-hatched features were observed in the 40% RH pits while ellipsoidal, faceted pits were observed at 76% RH. Optical profilometry indicated that most pits were not hemispherical. X-ray tomography provided evidence of undercutting and fissures. Piecewise curve fitting modeled the 40% RH data closely, predicting that corrosion damage would eventually plateau. However, a similar treatment of the 76% RH data suggested that corrosion damage would continuously increase, which implied that the piecewise power-law fit was limited in its ability to model atmospheric corrosion generally. Based on these observations, the operative mechanisms determining long-term corrosion behavior were hypothesized to be different depending on the RH of exposure.

 [DOI: 10.1149/1945-7111/abdc75]

Manuscript submitted September 17, 2020; revised manuscript received January 6, 2021. Published February 1, 2021.

Supplementary material for this article is available online

Studies on controlled atmospheric exposures of stainless steels to both individual and mixed salts have shown that relative humidity (RH) is a key driver of both the extent and morphology of pitting due to its effects on droplet size, electrolyte volume, and electrolyte chemistry.[1–5] However, these studies have focused primarily on pitting under microliter-sized droplets, which are often orders of magnitude larger than the volumes created by microscopic sea salt particles[6–9] present on surfaces in marine atmospheres. Additionally, the duration of these atmospheric exposures correspond to the early stages of pitting (hours or days), and do not characterize the data over longer time periods (up to years).[10–12]

A recent study by Weirich et al.[13] on 304 SS pitting under seawater droplets for one year in controlled atmospheric exposures showed that RH had a distinct influence on pit morphology. Pits grown at 40% RH displayed an irregular, cross-hatched morphology visually similar to the near-surface deformation caused by grinding. Fissures resembling microcracks were also present in association with pits. On the other hand, pits that developed at 76% RH displayed no such irregular morphology, instead forming crystallographically faceted ellipsoids with no associated microcrack-like fissures. The authors proposed that these differences were largely due to available cathodic resources provided by the humidity-dependent electrolyte conditions. The irregular morphology at low RH was attributed to the limited volume of $MgCl_2$-rich electrolyte which restricted cathode throwing power. Consequently, pit growth proceeded at conditions close to critical pit stability/repassivation. The hydrogen evolution reaction was hypothesized to be accelerated on the cathode surface due to the presence of high $MgCl_2$ content,[14] and at the corroding surface of the pit due to the increasing contribution of the local cathodic reaction near repassivation.[15] This possibility was reasoned to potentially lead to local hydrogen uptake and hydrogen-induced microcracking. At high RH, the larger volumes of NaCl-rich electrolyte allowed for greater cathodic throwing power, leading to higher polarization of the pit resulting in growth in more aggressive conditions between critical pit stability and saturation. Overall, these results implied that RH played an influential role in determining susceptibility to pitting, microcracking, and possible eventual stress corrosion cracking (SCC).

Long-term pitting data are vital for corrosion-resistant design and management of various assets.[16,17] The design criterion of interest is a critical flaw size, such as depth of corrosion attack, that can be utilized in structural integrity analyses to assess susceptibility to mechanical failure due to SCC.[18] Statistically-based predictive models have typically generated estimates of this flaw size based on power-law relationships derived from regression of long-term empirical exposures to marine and industrial atmospheres.[10–12,19–23] However, the data for these models are usually based on outdoor exposures in uncontrolled conditions, which prevent a targeted study of how specific environmental variables affect corrosion damage. Consequently, the predictive power of these models is highly local to the environment in which the data were generated, and as such their utility in predicting long-term pitting is still debated.[24–26]

Weirich et al.[13] sought to determine the effects of RH on the evolution of corrosion kinetics and damage morphology. The current study focused on whether the distinct differences in corrosion damage due to RH identified in that work[13] were consistently reproduced over a range of exposure durations encompassing both the initial stages of pitting as well as the mature evolution of pit growth. Ground 304 SS specimens loaded with sea salt microparticles were exposed to 40% and 76% RH from 1 week up to 2 years. Pits that developed on these surfaces were quantified and characterized using profilometry, electron microscopy, and X-ray microtomography. Data from the study were fit to power-law based predictive models to estimate long-term atmospheric corrosion behavior, with subsequent commentary on the mechanistic implications of these results.

Experimental

Material.—The composition of the 304 stainless steel used in this study is shown in Table I and is identical to the material used in Weirich et al.[13] The parent material was a 4.76 mm-thick hot-rolled sheet (solution heat-treated at 1055 °C and water-cooled). The sheet

*Electrochemical Society Member.
zE-mail: srinivasan.82@osu.edu; schindelholz.2@osu.edu

Appendix B

Katona, R. M., Knight, A. W., Schindelholz, E. J., Bryan, C. R., Schaller, R. F., & Kelly, R. G., (2021). Quantitative Assessment of environmental phenomena on maximum pit size predictions in marine environments. *Electrochimica Acta*, *370*, 137606.

Electrochimica Acta 370 (2021) 137606

Contents lists available at ScienceDirect

Electrochimica Acta

journal homepage: www.elsevier.com/locate/electacta

Quantitative assessment of environmental phenomena on maximum pit size predictions in marine environments

R.M. Katona[a,b,*], A.W. Knight[a], E.J. Schindelholz[c], C.R. Bryan[a], R.F. Schaller[a], R.G. Kelly[b]

[a] Sandia National Laboratories, Albuquerque, NM 87123, United States
[b] Materials Science and Engineering, University of Virginia, Charlottesville, VA 22904, United States
[c] Materials Science and Engineering, The Ohio State University, Columbus, OH 43210, United States

ARTICLE INFO

Article history:
Received 9 September 2020
Revised 22 December 2020
Accepted 27 December 2020
Available online 31 December 2020

Keywords:
Maximum pit size predictions
Magnesium chloride
Sea-salt brines
Sodium chloride
Cathode precipitation
Water layer dehydration
Pit stability product

ABSTRACT

Maximum pit sizes were predicted for dilute and concentrated NaCl and $MgCl_2$ solutions as well as sea-salt brine solutions corresponding to 40% relative humidity (RH) ($MgCl_2$-rich) and 76% RH (NaCl-rich) at 25 °C. A quantitative method was developed to capture the effects of various cathode evolution phenomena including precipitation and dehydration reactions. Additionally, the sensitivity of the model to input parameters was explored. Despite one's intuition, the highest chloride concentration (roughly 10.3 M Cl^-) did not produce the largest predicted pit size as the ohmic drop was more severe in concentrated $MgCl_2$ solutions. Therefore, the largest predicted pits were calculated for saturated NaCl (roughly 5 M Cl^-). Next, it was determined that pit size predictions are most sensitive to model input parameters for concentrated brines. However, when the effects of cathodic reactions on brine chemistry are considered, the sensitivity to input parameters is decreased. Although there was not one main input parameter that influenced pit size predictions, two main categories were identified. Under similar chloride concentrations (similar RH), the water layer thickness (WL), and pit stability product, $(i \cdot x)_{cl}$, are the most influential factors. When varying chloride concentrations (RH), changes in WL, the brine specific cathodic kinetics on the external surface (captured in the equivalent current density (i_{eq})), and conductivity (κ_s) are the most influential parameters. Finally, it was noted that dehydration reactions coupled with precipitation in the cathode will have the largest effect on predicted pit size, and cause the most significant inhibition of corrosion damage.

1. Introduction

Marine and near marine environments are typically characterized by sea-salt aerosols containing high chloride concentrations [1], and they can lead to pitting corrosion of stainless steels (SS) when deposited and deliquesced on the alloy surface. The chemistry and concentration of a marine environments varies widely with relative humidity (RH) [1] and, thus, changes in RH can change the corrosivity of the brine. As such, seawater solutions become sodium chloride (NaCl) rich at high RH values (above 74% RH) and magnesium chloride ($MgCl_2$) rich at low RH values [1]. In this way, the RH along with salt load control the composition, volume, and other properties of the resultant brine, impacting anodic and cathodic corrosion kinetics [1,2]. It is necessary to understand the quantitative impacts of the brine properties and evolution on anodic and cathodic kinetics in order to inform upon SS degradation.

There is an increasing demand for the accurate prediction of localized corrosion damage and computational models can provide a powerful means to simulate the propagation of localized corrosion in multiple exposure environments. Various models have been developed to predict localized corrosion including analytical models [3–6], Finite Element Models (FEM) [7–12], and phase field models [13,14]. Each modeling technique has advantages and disadvantages that are beyond the scope of this paper to discuss. However, regardless of the method, the evolution of brine chemistry as corrosion occurs has proven to be difficult to capture. In atmospheric scenarios, oxygen reduction reactions (ORR) are typically assumed to be the cathodic reduction reaction and a by-product of such a reaction is the hydroxyl ion (OH^-) which causes a rise in cathodic pH [15]. In certain solutions, such as sea-salt brines or $MgCl_2$, a pH rise will cause the precipitation of hydroxide-containing species in the cathode [16,17]. Additionally, loss of brine components to solids results in the dehydration of the brine, influencing cathodic

* Corresponding author at: Sandia National Laboratories, Albuquerque, NM 87123, United States.
E-mail address: rmkaton@sandia.gov (R.M. Katona).

https://doi.org/10.1016/j.electacta.2020.137606
0013-4686/© 2021 Elsevier Ltd. All rights reserved.

Appendix C

Katona, R. M., Carpenter, J., Schindelholz, E. J., Schaller, R. F., & Kelly, R. G. (2021). Cathodic Kinetics on Platinum and Stainless Steel in NaOH Environments. *Journal of The Electrochemical Society*, *168*(7), 071509.

Journal of The Electrochemical Society, 2021 **168** 071509

Cathodic Kinetics on Platinum and Stainless Steel in NaOH Environments

R. M. Katona,[1,2,*,z] J. Carpenter,[1] E. J. Schindelholz,[3,] R. F. Schaller,[1,**] and R. G. Kelly[2,***]**

[1]*Sandia National Laboratories, Albuquerque, NM 87123 United States of America*
[2]*Materials Science and Engineering, University of Virginia, Charlottesville, Virginia 22904, United States of America*
[3]*Department of Materials Science and Engineering, The Ohio State University, Columbus, OH 43210 United States of America*

During typical atmospheric conditions, cathodic reduction reactions produce hydroxyl ions increasing the pH in the cathodic region. Therefore, cathodic reduction reactions are investigated on platinum and stainless steel 304 L (SS304L) in NaOH solutions ranging in pH from 13.6 to 16.5. It was found that in solution pHs less than 16.5 the cathodic reduction reaction on Pt and SS304L was ORR with an electron transfer number less than two due to superoxide formation as an intermediate. Increasing pH decreased the number of electrons transferred. At a pH of 16.5, the cathodic reduction reaction on SS304L is no longer ORR and the cathodic current on the surface of the alloy is due to oxide reduction occurring on the surface as indicated by the creation of multi-component Pourbaix diagrams. The results of this study have important implications for predicting corrosion in atmospheric environments.

 [DOI: 10.1149/1945-7111/ac1318]

Manuscript submitted March 22, 2021; revised manuscript received June 15, 2021. Published July 21, 2021.

Reduction reaction processes on stainless steel (SS) and platinum (Pt) alloys are important across a broad range of science and technology areas,[1,2] especially for corrosion processes.[3] Recently, multiple studies have explored cathodic reduction reactions in chloride-containing solutions at their equilibrium pH which could be present in marine and near marine corrosion environments.[3–5] By measuring and understanding these reactions, predictions regarding the extent of corrosion become possible. In NaCl solutions, the oxygen reduction reaction was determined to be dominant following a four electron transfer given by:[3]

$$O_2 + 2H^+ + 4e^- \rightarrow 4OH^- \quad [1]$$

As a result of Eq. 1, the pH in the cathode will increase. A pH rise of the cathode has been directly observed by Azmat et al. on zinc under marine solutions[6] and Schindelholz et al. on copper under NaCl electrolytes.[7] Additionally, ex situ analysis of electrolyte pools after SS coupon exposures are consistent with the formation of an alkaline electrolyte at cathodic sites due to the ORR reaction.[8] The production of hydroxyl ions from ORR will not only cause a rise in pH but will cause electro-migration to maintain electroneutrality. As such, a chloride-poor, alkaline solution can be present in the cathode.[8–11] This becomes particularly important in atmospheric scenarios where finite electrolyte volumes are present. A schematic of this phenomenon is presented in Fig. 1 for a droplet. For NaCl solutions, a common component of seawater brines at elevated relative humidities,[12] an NaOH rich brine would be present near the edge of the cathode or in micro-droplets around the original cathode (droplet)[8,10,11] and could potentially change cathodic reduction behavior.

Katona et al. made predictions of cathodic pHs (calculated through concentration of the hydrogen ion) under atmospheric conditions for common atmospheric solution chemistries and utilized these pH values to investigate precipitation reactions.[13,14] In order to make such pH predictions, the max pit model formulism presented by Chen and Kelly was utilized.[15] The analytical model relies on ohmic drop considerations in the thin electrolyte film to limit the cathode size and the cathodic current supply. Through the inherent coupling of the cathode and anode, a finite cathode implies a finite anode (i.e., a finite pit size).[15] As such, Katona et al. calculated total hydroxyl production based on the stoichiometric dissolution of SS304L. This was combined with the finite cathode radius to determine the cathode pH. The pH of SS304L exposed to 5.3 M NaCl under a loading density of 3 g m^{-2} (WL = 12 μm) is presented in Fig. 2. At the calculated maximum pit size (50% salt film saturation), the pH is over 14 and illustrates that high pHs that are possible in cathodic regions.[13,14]

While determining reaction mechanisms in chloride-containing solutions under natural pH conditions is crucial to understanding corrosion processes, it is also important to understand reaction mechanisms in an evolving cathode solution, specifically at elevated pH's. To date, information regarding the cathodic reduction behavior of SS or iron-based alloys in high pH is focused below a pH of 11. Generally, regardless of the solution composition, all researchers found a four electron transfer (Eq. 1) below a pH of 11.[2,16,17] The cathodic behavior of SSs has not been investigated in solutions of high pH values (nearing 13 and greater) which are possible at the cathode in some atmospheric corrosion scenarios (Fig. 2).[7,13] Additionally, SS cathodic behavior has not been established in pure NaOH solutions which could be possible in the surrounding edge of a cathode. To date, cathodic kinetics in pure NaOH solutions has focused on Pt.[1,18] In general, an increase in pH in pure NaOH solutions produces an electron transfer number nearing one on Pt electrodes. This can be described through the reduction of oxygen forming a superoxide anion as the rate limiting step (O_2^-, Eq. 2):

$$O_2 + e^- \leftrightarrow O_2^- \quad [2]$$

In basic media, a hydrogen peroxide anion is the following intermediate and produces a hydroxyl ion as the final product (Eqs. 3 and 4)[1].

$$O_2^- + H_2O + e^- \leftrightarrow HO_2^- + OH^- \quad [3]$$

$$HO_2^- + H_2O + 2e^- \leftrightarrow 3OH^- \quad [4]$$

As the hydroxyl concentration increases, the ORR reaction rate declines, and the protonation of the superoxide is suppressed; thus, the ORR shifts from a two-electron reduction pathway to a one-

*Electrochemical Society Student Member.
**Electrochemical Society Member.
***Electrochemical Society Fellow.
[z]E-mail: rmkaton@sandia.gov

Appendix D

Katona, R. M., Carpenter, J.C., Knight, A. W., Marshall, R.S., Nation, B.L., Schindelholz, E.J., Schaller, R. F., & Kelly, R. G., (2021). Editor's Choice – Natural Convection Boundary Layer Thickness at Elevated Chloride Concentrations and Temperatures and the Effects on a Galvanic Couple. *Journal of the Electrochemical Society*, *168*, 031512.

Journal of The Electrochemical Society, 2021 **168** 031512

EDITORS' CHOICE

Editors' Choice—Natural Convection Boundary Layer Thickness at Elevated Chloride Concentrations and Temperatures and the Effects on a Galvanic Couple

R. M. Katona,[1,2,*,z] J. C. Carpenter,[1] A. W. Knight,[1] R. S. Marshall,[3,*] B. L. Nation,[1] E. J. Schindelholz,[3,] R. F. Schaller,[1,**] and R. G. Kelly[2,***]**

[1]*Sandia National Laboratories, Albuquerque, New Mexico 87123, United States of America*
[2]*Materials Science and Engineering, University of Virginia, Charlottesville, Virginia 22904, United States of America*
[3]*Department of Materials Science and Engineering, The Ohio State University, Columbus, Ohio 43210, United States of America*

The natural convection boundary layer (δ_{nc}) and its influence on cathodic current in a galvanic couple under varying electrolytes as a function of concentration (1 – 5.3 M NaCl) and temperature (25 °C–45 °C) were understood. Polarization scans were obtained under quiescent conditions and at defined boundary layer thicknesses using a rotating disk electrode on platinum and stainless steel 304L (SS304L); these were combined to determine δ_{nc}. With increasing chloride concentration and temperature, δ_{nc} decreased. Increased mass transport (Sherwood number) results in a decrease in δ_{nc}, providing a means to predict this important boundary. Using Finite Element Modeling, the cathodic current was calculated for an aluminum alloy/SS304L galvanic couple as a function of water layer (*WL*) thickness and cathode length. Electrolyte domains were delineated, describing (i) dominance of ohmic resistance over mass transport under thin *WL*, (ii) the transition from thin film to bulk conditions at δ_{nc}, and (iii) dominance of mass transport under thick *WL*. With increasing chloride concentration, cathodic current decreased due to decreases in mass transport. With increasing temperature, increased cathodic current was related to increases in mass transport and solution conductivity. This study has implications for sample sizing and corrosion prediction under changing environments.
 [DOI: 10.1149/1945-7111/abeb29]

Manuscript submitted January 12, 2021; revised manuscript received February 22, 2021. Published March 16, 2021. *This paper is part of the JES Focus Issue on Characterization of Corrosion Processes in Honor of Philippe Marcus.*

Supplementary material for this article is available online

Metallic structures are commonly exposed to marine atmospheric conditions, characterized by thin electrolyte layers allowing for the formation an electrochemical or corrosion cell. The electrolyte can be formed through salt spray or deliquescence of salt as either a droplet or a thin water layer (*WL*) on the alloy surface and the chemical composition and thickness can vary widely.[1] As such, the rate and extent of corrosion on the alloy surface is dictated by the combination of environmental, physicochemical, and geometric variables, which include relative humidity (RH), temperature, electrolyte conductivity, electrolyte film thickness, in addition to the electrochemical kinetics on the alloy surface.[2–6] Due to the large potential variation in environmental conditions and *WL* thicknesses, modeling can serve as an important tool to evaluate environmental effects on the corrosion of alloys and galvanic couples.

One of the most important controlling factors for corrosion in atmospheric environments is the *WL* thickness. Tomashov initially recognized a corrosion rate dependence with *WL* thickness and qualitatively described four different reaction control mechanisms. Under bulk, full immersion conditions, a plateau in corrosion rate is seen and a constant diffusion layer is achieved. Decreasing the *WL* causes an increased corrosion rate which is due to more rapid diffusion of oxygen across the thinner *WL*. Further decreasing the *WL* thickness reduced dissolution due to anodic control (owing to lower corrosion product solubility in a smaller solution volume). Finally, once a continuous film is lacking, the final regime is reached and is characterized by a very low corrosion rate of dry chemical oxidation.[4] While useful conceptually, the outline presented by Tomashov lacked a demonstrated quantitative description between electrochemical kinetics and the film thickness.

Numerous authors have attempted to quantitatively determine the transition from bulk, full immersion kinetics to thin film kinetics.[4,7–34] The transition occurs at the natural convection boundary layer (δ_{nc}) and is formed on surfaces affected by convection or advection in response to thermally or compositionally driven spatially inhomogeneous density distributions.[32] This flow prevents a concentration gradient of the oxidized or reduced species from extending to large distances away from the electrode (i.e. the concentration gradient is finite and close to the surface). In the absence of natural convection, the diffusional boundary layer would continuously increase with time, lowering the diffusion-limited current density (i_{lim}) continuously[9]; however, an i_{lim} is observed in many cases. The quantification of δ_{nc} in solutions of various compositions has yielded values from near 250 μm[21,24–27,33] to between 500 and 1000 μm.[9,16,17,19,20,35] Several methods exist to quantify δ_{nc}; however, recently, Liu et al. utilized a rotating disk electrode (RDE) and quiescent cathodic polarization scans to quantify δ_{nc} in a dilute chloride-containing brine which could form under atmospheric conditions.[9] It was determined that in 0.6 M NaCl, in which the oxygen reduction reaction (ORR) is dominant and the diffusion of oxygen to the metal surface is the rate limiting process,[36] δ_{nc} was roughly 800 μm.[9] Below δ_{nc}, the flux of oxygen to the surface of the cathode is determined by the *WL* thickness. While the method presented provides a robust framework, there is still a gap in literature regarding δ_{nc} as a function of common environmental parameters such as brine composition, concentration, and temperature.

Models have been presented in literature to understand δ_{nc}.[21,24] Of particular note, Amatore et al.[24] described a micro-convection approach in which a diffusion-like term was used to account for natural convection. Dolgikh et al.[21] used this idea and extended it to multi-ion environments. While models exist to investigate natural convection, these models have not been widely applied, and the effects of δ_{nc} on the extent of corrosion in various environments have

*Electrochemical Society Student Member.
**Electrochemical Society Member.
***Electrochemical Society Fellow.
[z]E-mail: rmkaton@sandia.gov